UNIVERSITY OF CAPE TOWN
IYUNIVESITHI YASEKAPA • UNIVERSITEIT VAN KAAPSTAD

DEPARTMENT OF CHEMICAL ENGINEERING

Design of a Small-Scale System for the Growth of Artificial Sea Ice

PREPARED BY: MR BENJAMIN ANDREW HALL

DISSERTATION SUBMITTED TO THE UNIVERSITY OF CAPE TOWN IN PARTIAL FULFILMENT OF THE REQUIREMENTS FOR THE DEGREE OF:

MASTER OF SCIENCES IN CHEMICAL ENGINEERING

Supervisor:
Ms Tokoloho Rampai

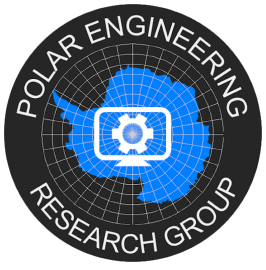

December, 2019

Plagiarism Declaration

I know the meaning of plagiarism and declare that all the work in the document, save for that which is properly acknowledged, is my own. This thesis/dissertation has been submitted to the Turnitin module (or equivalent similarity and originality checking software) and I confirm that my supervisor has seen my report and any concerns revealed by such have been resolved with my supervisor.

Signed:

Signed by candidate

Benjamin Hall
26 December 2019

Abstract

Sea ice plays a significant role in global climate systems, reflecting a significant portion of solar energy back into the atmosphere and maintaining ocean circulation currents. The effect of climate change on sea ice extent and seasonal changes is as yet unquantified. This is especially true for the initial growth processes and properties within the Antarctic Marginal Ice Zone (MIZ) front during the winter growth season.

The Polar Engineering Research Group (PERG) at the University of Cape Town has conducted several research expeditions to the Antarctic MIZ along the 0° line of longitude, collecting samples of first year sea ice. Artificial sea ice has been used as a supplementary area of study because of the advanced control it provides over variables such as cooling rate or initial solution salinity. This allows for the effect of individual variables to be analysed through repeated experiments while adjusting only the variable of interest. Due to the complex nature and conditions of formation for Antarctic sea ice, this study focusses on the key properties of sea ice formed in predominantly calm conditions. These are observed as vertically elongated ice crystals with a c-axis located randomly within the horizontal plane. The profile of ice thickness over time displays a $\sqrt{x}$ shape. Brine inclusions are located in vertically orientated, interconnected channels, contained within the intracrystalline planes. The crystal planes have spacings of about 1 mm. Lastly, the salinity profile of the ice displays a characteristic c-shaped curve with depth, with higher values of salinity found at the top and bottom of the ice. Ice fitting this description is referred to as columnar S2 ice.

The overall aim of this project is to design and test a small-scale system for the growth of artificial sea ice. This system will still enable method development of testing protocols for the testing of the Antarctic sea ice. Once this system has proven to reliably produce saline ice that can be termed as artificial sea ice with a columnar S2 structure, additional design implementations can then be undertaken to accomplish the growth of sea ice that more closely resembles the ice found in the Antarctic MIZ. The system is required to be large enough to produce samples of appropriate size and number to fit the testing protocols for mechanical testing set out by Schwarz et al. (1981), while being statistically sound. Secondary design objectives were to ensure the system is cost-effective, portable and simple.

A proof of design concept experiment, consisting of a 28 g kg^{-1} saline solution cooled at at a temperature of - 20 °C, was carried out in order to test the system design. The hypothesis is that the system design will be able to produce saline ice with properties similar to natural sea ice. Temperature profiles and ice growth within the tank were recorded, and ice samples were taken at the end of the run to determine in-ice salinity and crystal morphology.

With some refinement of the system to identify the cause of the extended granular and transition layer, the system can be used to provide the necessary test samples for method development for the mechanical testing of sea ice samples collected from the Antarctic MIZ. Following on from this initial design, additional design implementations can be undertaken to accomplish the growth of sea ice that more closely resembles the ice found in the Antarctic MIZ. This will aid in the determination of sea ice properties and studies of the underlying growth processes that cause them.

Acknowledgements

I was adamant in my decision not to study a Master's. Right up to the point I found myself on the SA Agulhas II, in the middle of the tempestuous Antarctic Ocean performing research on sea ice. Then a Master's seemed like a pretty "cool" idea.

Firstly, thank you to my supervisor, Ms Tokoloho Rampai for sending me on that initial trip that opened my eyes to the allure of Antarctica and research, as well as the financial and academic support. Thanks as well for creating the environment for me to develop my own ideas for this study.

I would like to acknowledge the financial contributions from the EBE faculty for the URC Block Grant and the Research Development Grant from the Research Office at the University of Cape Town for minor equipment funding and bursary top-ups.

Thanks go also to the wider Polar Engineering Research Group, A/Proff Sebastian Skatulla, Doctor Keith Machutchon, A/Proff Marcello Vichi and Dr Dyllon Randall. To my colleagues, Mark and Siobhan, as well as Emmanuel, Rutger and Andrea.

I would like to express my appreciation to the technical staff of the Concretes Lab in Department of Civil Engineering, for accommodating me in their space, and for all their valuable assistance. In addition, thank you to the technical staff of the Chemical Engineering Electronics Lab for the helpful discussions and advice on all things electrical, and for the loan of their tools. I would also like to extend my thanks to the finance and administration staff in the Chemical Engineering Department for making molehills out of paperwork mountains.

My gratitude to the CT Scanning Facility at Stellenbosch University for their adventurous attitude towards the new challenge of scanning sea ice and their willingness to tweak settings and provide recommendations for sample preparation. A very informative two weeks was spent at the Roland van Glasow Air-Sea-Ice Chamber within the Department of Environmental Sciences at University of East Anglia. My thanks to Professor Jan Kaiser for hosting us, and the invaluable advice and discussions concerning artificial sea ice set-ups and experimental techniques from Dr Max Thomas and Dr Odile Crabeck.

My gratitude goes to the Department of Science and Technology for financial contributions to the Antarctic research trips aboard the SA Agulhas II to obtain ice samples. For the captain and crew of the ship who were patient with the mad scientists and prepared to go the extra mile in the name of science.

Thank you as well to my family and friends for the encouragement, love and support during my Masters. You are all truly appreciated.

TO GOD BE THE GLORY

Contents

Plagiarism Declaration i

Abstract ii

Acknowledgements iii

Contents iv

List of Figures vi

List of Tables x

Nomenclature xi

1 Introduction 1

2 Literature Review 2

2.1 The Progression of Sea Ice Research . . . 2

2.2 Sea Ice Classifications . . . 3

2.3 The Thermodynamics of Sea Ice Growth . . . 4

2.4 Brine Inclusions, Channels and Brine Drainage . . . 11

2.5 Artificial Sea Ice . . . 14

2.5.1 Artificial Sea Ice for Study of Growth Processes and Ice Property Evaluation 14

2.5.2 Freezing Methods . . . 15

2.5.3 Tank Size and Material of Construction . . . 18

2.5.4 Water Circulation and Agitation . . . 20

2.5.5 Pressure Relief . . . 21

2.5.6 Saline Solution . . . 23

2.5.7 Seeding . . . 23

2.5.8 In-Situ Measurement Systems . . . 24

2.6 Literature Informed Design Route for Artificial Sea Ice Growth . . . 29

3 Design Objectives and Experimental Aims 31

3.1 Design Objectives . . . 31

3.2 Experimental Aims and Key Questions . . . 32

4 Methodology 33

4.1 Freezing Tank System Design Procedure . . . 33

4.2 Proof of Design Concept: Artificial Sea Ice Growth Experiment . . . 35

4.2.1 Experimental set-up . . . 35

4.2.2 Ice Analysis Techniques . . . 37

5 Freezing Tank System Design 39

5.1 Tank System Design . . . 39

5.1.1 Cooling Method . . . 39

5.1.2 Tank and Insulation . . . 41
5.1.3 Pressure Relief . . . 46
5.1.4 Bottom Heating . . . 50
5.1.5 Side Heating . . . 53
5.1.6 Agitation . . . 58
5.1.7 Manual Depth Measurement . . . 61
5.2 Control Centre System Design . . . 62
5.2.1 Temperature Measurement . . . 63
5.2.2 Tank Control . . . 67
5.3 HeatGen Program . . . 72
5.4 Temperature Derived Depth Measurement . . . 77
5.4.1 Model Development . . . 77
5.4.2 Validation Experiments for Temperature Derived Ice Depth Model . . . 79
5.5 Proof of Concept: Artificial Sea Ice Growth Experiment . . . 83
5.5.1 Temperature Profiles, Solution Salinity and Ice Depth . . . 84
5.5.2 Ice Salinity . . . 89
5.5.3 Ice Crystal Morphology and Brine Channel Structure . . . 90

6 Discussion **93**

7 Conclusions and Recommendations **102**
7.1 Conclusions . . . 102
7.2 Recommendations and Future Studies . . . 103

References **105**

A Appendix **115**
A.1 Control Centre System Design . . . 115
A.1.1 Temperature Measurement . . . 116
A.1.2 Tank Control . . . 118
A.2 HeatGen Method Development . . . 121
A.2.1 Temperature Smoothing . . . 121
A.2.2 Procedure for Temperature Grid Population . . . 123
A.3 Temperature Derived Depth Measurement . . . 125
A.4 Proof of Concept: Artificial Sea Ice Growth Experiment . . . 128

List of Figures

2.1 Pictomicrograph of small ice platelets known as frazil crystals (Fransson, 2009) . 3
2.2 Flow diagram of two predominant ice growth processes (TU Delft, 2016) with images of different ice types by Petrich and Eicken (2010) 4
2.3 Tetrahedral Arrangement of Water Molecules in Ice (Zhang et al., 2012) 5
2.4 Hexagonal Crystal Bonding Structure of Ice Ih (Weeks and Ackley, 1986) 5
2.5 Sea ice phase diagram (Bulk in-ice salinity of 5 g kg^{-1} derived from standard sea water composition (Millero et al., 2008). The precipitation temperatures of each of the main salt constituents are displayed with vertical lines, color-coded to the specified constituent. The black lines separate the individual phases of liquid, minerals and ice. The thin gray lines further split salt and H_2O contributions in the liquid and mineral phase. (Vancoppenolle et al., 2019) 7
2.6 Summary of heat fluxes occurring during sea ice growth (Wiese, 2012) 8
2.7 Modelled sea ice depth as a function of the cumulative number of freezing days (Anderson, 1961) 9
2.8 Plot showing the relationship of salt water density maximum to temperature and salinity (Chaplin, 2018) 9
2.9 Schematic showing the crystal structure of first year sea ice (Schwarz and Weeks, 1977) 10
2.10 Salinity profiles of sea ice obtained during winter 1977 to 1978 at Eclipse Sound, over two week intervals. Salinity scale is shown inserted, and a reference line of 6 g kg^{-1} is placed on each profile (Nakawo and Sinha, 1981) 11
2.11 Schematic of the Vertical Brine Channels and Diagonal Feeder Tubes Found in Sea Ice (Eide and Martin, 1975) 13
2.12 Fluctuating air temperatures experienced during an artificial sea ice growth experiment at the Sea ice Environmental Research Facility (SERF), University of Manitoba (Galley et al., 2015) 16
2.13 Cooling plate used for controlled cooling. Channels for ethylene glycol circulation is shown on the left, with the right showing the tank in operation (Schulson et al., 2015) 17
2.14 Round tank experimental set-up for ice artificial sea ice growth used by Marks et al. (2017) 19
2.15 Schematic of secondary radial flow pattern generated with tangential mixing in a round tank. The primary flow pattern (not shown) is tangential (Timmons et al., 1998) 21
2.16 Weeks (1962) experimental set-up showing pressure relief pipe on the right side of the tank 22
2.17 Nucleation categories and their regions in a supercooled solution (Randall et al., 2009) 24
2.18 Salinity Harp developed by Notz (2005) in operation in the experimental set-up of Garnett et al. (2019) 28

3.1 Objectives for the design of a system for the growth of artificial sea ice, as well as the assessment parameters for each objective 32

4.1 Design Process Pahl et al. (2007) 33
4.2 Artificial columnar S2 sea ice system sub-assemblies displaying their interlinkage and corresponding assessment parameters 34
4.3 Schematic of experimental set-up, showing locations of fan (F), pressure relief pipe (S_p), Pumps (P_{1-2}), manual ice depth measures (D_{1-2}), in-ice temperature chains ($T_{i,1-2}$), ambient temperature (T_a) and ice samples (I_{1-3}) 35
4.4 X-Ray CT Image of Brine Microstructure for making up total brine volume of 0.033 cm^3 dm^{-3} (Golden et al., 2007) 37

5.1 Schematic view of the insulation layers, as described in table 5.3 showing relative thicknesses, with the three temperature probes labelled as T_{Tank}, $T_{Insulation}$ and $T_{Ambient}$ with a blue dot and the red dots representing the location of the heater tape used for side heating. Surface areas of tank wall and outer insulation are also indicated using red arrows 44
5.2 Tank Layers: a) cut HDPE Tank b) insulated with 3mm rubber foam c) covered with foil for heat conduction from side heating d) final tank with outer 135 mm plastic wool insulation 45
5.3 Pressure relief pipe exiting from bottom of tank 47
5.4 Adjustment process for the manual heating of the pressure relief pipe 48
5.5 Bottom heating module, with heater tape mounted to plastic base 50
5.6 Comparison of low and high heating rates for bottom heating 52
5.7 Temperature profiles for average tank solution, outer insulation layer and ambient at high tank temperatures and no bottom heating, with side heating set to 20 % . . 54
5.8 Temperature profiles for average tank solution, outer insulation layer, tank bottom and ambient with solution at freezing point 55
5.9 Temperature profiles for average tank solution, outer insulation layer and ambient at high tank temperatures and no bottom heating, with side heating rates of 20 %, 10 % and "Off" 56
5.10 Interaction plot for effect of ambient cooling and its interaction with different rates of side heating 57
5.11 Interaction plot for effect of bottom heating and its interaction with side heating . 58
5.12 Temperature variation in tank with and without agitation 59
5.13 Comparison of temperature profile with and without agitation for bottom heating 60
5.14 3 Wire half bridge for Pt100 probes (Campbell Scientific, 2006) 64
5.15 Campbell CR5000 Data Logger with Additional Circuitry 65
5.16 Probe set-up for a) Focus on in-ice temperature measurement and b) Entire solution temperature measurement 66
5.17 Front view of the tank control center, with label overlay to show controls of each individual module 69
5.18 Temperature versus time of control box, controlled by heating circuit 70

5.19 The graphical user interface of the developed HeatGen program, with primary functions labelled from 1-11 72
5.20 Example temperature heatmap image sequence from HeatGen, over for a period of initial ice growth, shown for a duration of 42 hours, with images shown at 8 hour intervals. The small, white squares show the locations of the temperature probes . 76
5.21 Depth versus temperature profiles over time, showing the linear in-ice temperature profile, with the approximate ice-solution interface point shown with open circles 77
5.22 Example plot showing the temperature probe depths and associated temperatures (+) and the plotted linear lines of best fit used to calculated the temperature derived ice depth. The identified last probe within the ice is highlighted with a green circle 78
5.23 Freshwater experiment: manually measured ice depths, gradient calculated ice depths and the subsequent smoothed ice depth profiles 79
5.24 Correlation of the manually measured and the smoothed temperature derived ice depth profiles for the freshwater experiment. Perfect correlation shown by the solid black line, with $\pm$ 10 % bounds shown by the dashed lines 80
5.25 34 g kg^{-1} saline solution experiment: manually measured ice depths, gradient calculated ice depths and the subsequent smoothed ice depth profiles 81
5.26 Correlation of the manually measured and the smoothed temperature derived ice depth profiles for the 34 g kg^{-1} saline solution experiment. Perfect correlation shown by the solid black line, with $\pm$10 % bounds shown by the dashed lines . . 82
5.27 Temperature profiles for temperature probes at depths between 1 cm and 70 cm within the tank over experimental duration 84
5.28 Temperature versus depth evolution over the duration of the experiment showing ice growth as linear portion of temperature profile 85
5.29 Temperature versus depth profiles for select time intervals of 0, 32, 64, 95, 137 and 159 hours, showing difference in measured temperature between temperature string 1 and 2 86
5.30 Average temperature profile of temperature strings 1 and 2 over the duration of the experiment 86
5.31 Calculated ice depth and solution profiles over experimental duration, with measured initial and final solution salinity, as wells as final measured ice depth plotted (*) 87
5.32 Heat map profiles for select time intervals of 0, 32, 64, 95, 137 and 159 hours, showing tank temperature evolution, temperature deviation locations, and advancing ice front. The small, white squares show the locations of the temperature probes 88
5.33 Average in-ice bulk salinity profile from ice samples taken at end of experiment . 90
5.34 CT scan of 3 cm ice cubes from an artificial sea ice sample at a) Top in the X_3-X_2 plane, b) Top in the X_1-X_2 plane, c) Middle region in the X_3-X_2 plane, d) Middle region in the X_1-X_2 plane, e) Bottom in the X_3-X_2 plane, f) Bottom in the X_1-X_2 plane. Items of interest are highlighted as follows: red - pore spaces, yellow - brine inclusions, purple - crystal orientation in X_1-X_2 plane. 92

6.1 A schematic of the completed small scale system for the growth of artificial columnar sea ice 93
6.2 Salinity profiles of young sea ice from Nakawo and Sinha (1981), originally displayed in Section 2.4. Salinity scale is shown inserted, and a reference line of 6 g kg^{-1} is placed on each profile 97

A.1 Insulated box used to house control centre 115
A.2 Circuit Diagram for additional PT100 Temperature Measurement Circuitry for Campbell Logger 117
A.3 Tank System Circuit Diagram 118
A.4 Control Center Circuit Diagram 119
A.5 Control Center Rear with Schematic Overlay 120
A.6 Comparison of smoothing methods where a) shows unsmoothed temperature profiles, b) shows the cubic spline method and c) shows the linear smoothed temperature profile 121
A.7 Calculation steps for population of example temperature grid for Heatmap generation 123
A.8 Completed example temperature grid for Heatmap generation 124
A.9 28 ppt Experimental Run: Smoothing of Temperature Profiles 128
A.10 28 ppt Experimental Run: Solution Temperature Profile 128
A.11 28 ppt Experimental Run: Temperature and Salinity Data from 3 Samples used for Salinity Trend Calculation 129
A.12 28 ppt Experimental Run: Ice Melting and Subsequent Brine Drainage Due to Defrost Cycles 130

List of Tables

2.1 Summary of ice properties used to categorise saline ice as "Artificial Columnar S2 Sea Ice" 14

2.2 Precipitating minerals during the freezing of sea water, with their highest temperature of precipitation as well as their final mass fraction at the eutectic point (-36.2 °C) (Vancoppenolle et al., 2019) with the proposed freezing temperature cut-off of -20 °C shown in blue 15

2.3 Comparison of Thermistor, RTD and Thermocouple properties taken from Omega (2019) and a survey of their previous uses in artificial sea ice-systems . . 25

5.1 Decision matrix table for the cooling method for the artificial sea ice, with the chosen method outlined in red 40

5.2 Decision matrix table for tank material and configuration, with the chosen configuration outlined in red 41

5.3 Description of insulation layers including their material of construction, thickness and the layer conductivity 44

5.4 Decision matrix table for pressure relief system 46

5.5 Comparison of low and high heating rates for bottom heating 52

5.6 Heating rates comparison 61

5.7 Decision matrix table for temperature probe selection 63

5.8 Fit parameters for the correlation between the manually measured and the smoothed temperature derived ice depth profiles for the freshwater experiment . . 80

5.9 Fit parameters for the correlation between the manually measured and the smoothed temperature derived ice depth profiles for the 34 g kg^{-1} saline solution experiment 82

A.1 Example data showing the linear line fitting and associated error that provided cut-off point for ice depth. Last known point in ice shown by red line 125

Nomenclature

$\mathrm{c\text{-}axis}$: The optical axis of the crystal, through which light passes through unaltered. The c-axis is orientated normal to basal plane.

H : Ice depth (cm)

m : Constant for freezing point depression created by sea salt in water (0.05 °C (g kg^{-1})$^{-1}$)

PSU : Practical Salinity Units (dimensionless)

$\mathrm{Q_a}$: Atmospheric heat flux, from ice to environment (W m^{-2})

$\mathrm{Q_{c,b}}$: Conductive heat flux at the bottom of the ice (W m^{-2})

$\mathrm{Q_{c,t}}$: Conductive heat flux at the top of the ice (W m^{-2})

$\mathrm{Q_e}$: Heat loss through evaporation (W m^{-2})

$\mathrm{Q_L}$: Latent heat released during ice formation (W m^{-2})

$\mathrm{Q_{lw}}$: Heat loss from long wave radiation to surrounding atmosphere (W m^{-2})

$\mathrm{Q_{lw}}$: Incoming heat in the form of from short wave radiation from the sun (W m^{-2})

$\mathrm{Q_w}$: Oceanic heat flux from water to ice (W m^{-2})

$\mathrm{T_{ambient}}$: Temperature of the ambient air

$\mathrm{T_i}$: Ice temperature

$\mathrm{T_{freeze}}$: Freezing point temperature (°C)

$\mathrm{T_w}$: Freezing point temperature of pure water (0 °C)

Θ : Cumulative number of freezing days

$\mathrm{S_B}$: Bulk in-ice salinity in g kg^{-1}

$\mathrm{S_{br}}$: Ice brine salinity in g kg^{-1}

υ_B : Relative brine volume in cm^3 dm^{-3}

1 Introduction

Sea ice conjures an image of vast frozen deserts, sitting on a frigid sea far to the North or South where most will never venture. Yet sea ice has global relevance, providing a unique habitat for organisms ranging from microorganisms to polar bears. It acts as an insulating and reflective barrier between the atmosphere above and the ocean below, limiting heat and moisture exchange to curb the formation of severe weather systems. In addition, it plays an important role in the global ocean circulation system, with the formation of cold, dense water that migrates to the poles.

Sea ice forms as a thin floating layer on top of the ocean, with a temperature relatively close to its melting point (Weeks, 2010). This makes it particularly susceptible to changes in atmospheric temperatures, which have been seen to be steadily increasing since the late 1980s (IPCC, 2007). This has led to very active research within the last few years to improve our knowledge of sea ice and to incorporate its effect on the Earth's climate system and as well as the feedback mechanisms into global climate models (Notz, 2005).

Predictive computational models of Antarctic sea ice and metocean thermodynamics are used as input to these climate models and enable analysis of sea ice extent and break up. In order for these models to be accurate, there needs to be a sufficient quantity of data on ice properties to act as input parameters as well as for calibration and verification (Feltham et al., 2006). Sea ice properties vary drastically over area, due to its dependency on oceanic and meteorological conditions. Thus, sea ice sampling and the determination of its physical and mechanical properties needs to be undertaken across a huge spatial region. This is especially true of the Antarctic Marginal Ice Zone (MIZ), where data is limited (Lange et al., 1989).

The Polar Engineering Research Group at the University of Cape Town has carried out three research trips into the Antarctic MIZ, obtaining samples of pancake and pack ice for analysis of physical and mechanical properties. To formulate the testing protocols, and better understand the results obtained from such tests, it is advantageous to perform similar testing on artificial sea ice. Laboratory-grown artificial sea ice enables controlled studies of specific sea ice properties, studied in isolation under repeatable conditions, where the full growth history is known (Haas, 1999).

To grow artificial sea ice, a system is required that is able to mimic the key environmental and thermodynamic conditions under which sea ice is formed. The overall objective of this study is to design, build and test a small-scale tank system for the growth of artificial sea ice. This system will consist of the freezing tank and associated modules to enable accurate simulation of the key metocean conditions required the formation of sea ice, along with the associated electronic control and measurement systems.

This study begins with a literature view of sea ice properties, as well as previous artificial sea ice systems and all the required components. The design objectives and experimental aims are outlined in Section 3. The design procedure and experimental methodology is presented in Section 4. The system design process is described in Section 5 and the results of an ice growth experiment are presented as a proof of concept. Section 6 contains the discussion of the system feasibility with Section 7 presenting the conclusions of the study and possible improvements.

2 Literature Review

2.1 The Progression of Sea Ice Research

Sea ice growth occurs in both the Northern and Southern hemispheres during the winter months. While the total volume of sea ice is insubstantial compared to the seawater volume, its surface area is extensive, accounting for as much as 7 % of global surface area in winter months (Weeks, 2010). This has a huge effect on global climate systems, due to its reflectivity, causing as much as 40 % of radiation to be reflected back into the atmosphere (Rinke et al., 2006). Sea ice at the earth's poles create and maintains global ocean circulation systems with the cold, dense water generated from the sea ice being circulated to the low latitudes. Within the last few decades, steadily increasing global air temperatures have resulted in a rapid yearly decrease in sea ice extents (IPCC, 2007). Additionally, the rate of decrease in sea ice extent will continue to accelerate as sea ice extents decrease, due to the positive ice-albedo feedback effect (Rinke et al., 2006). Considering the effect of sea ice on the global climate system, such changes are cause for concern and have resulted in increased research to accurately predict and incorporate sea ice decreases into global climate models.

Extensive research on sea ice was carried out predominantly in the Arctic between the 1960s to late 1990s, motivated primarily by exploration for offshore oil and gas operations (Weeks, 2010). The properties of sea ice are fairly well understood for this region, and many of the early papers from this era are still seen as valid and referred to frequently. However, advances in technology and the accuracy of instruments, as well as non-intrusive analysis techniques such as those presented by Galley et al. (2015) and Crabeck et al. (2016) provides a means for properties such as brine distribution to be re-examined, with an eye to confirming original results and better understanding mechanisms leading to their formation. In addition, research in the Antarctic has been less prevalent, with the extreme seasonal change in ice extents meaning only some 15 % survives beyond a single season (Weeks, 2010). The initial growth processes and properties of early ice stages such as so-called pancake ice and its growth cycle in what is known as the advancing Marginal Ice Zone (MIZ) front during the winter season has received very little attention (Lange et al., 1989). Doble et al. (2003) examined these properties and found them to vary hugely and to be far more complex than pancakes found in the Arctic by Wadhams et al. (1996).

It is common to supplement studies undertaken on natural sea ice by using laboratory grown artificial sea ice. Haas (1999) provides a succinct summary of the advantages of using an ice tank for ice experiments over field experiments. Tank grown sea ice has a greater degree of homogeneity, allowing multiple samples to be taken with comparable properties. Natural sea ice has been shown to have a high degree of variation even on a scale of a few metres (Eicken et al., 1991). The full history of the ice growth can be recorded by monitoring of air and water temperatures and controlling the temperature forcing. An ice tank allows the separation of primary processes due to ice formation from the secondary processes that follow, namely algal activity. This results in an isolation of the effects of biological activity. The development of these ice communities can also be easily monitored throughout their entire life cycle. Haas (1999) and Weeks and Cox (1974) also note that the logistics for tank experiments are much simpler and cheaper than those for field experiments.

2.2 Sea Ice Classifications

Sea ice begins as small ice platelets called frazil ice, which form when the surface layer of the ocean is supercooled (Weeks and Ackley, 1986). Figure 2.1 shows a pictomicrograph of frazil crystals.

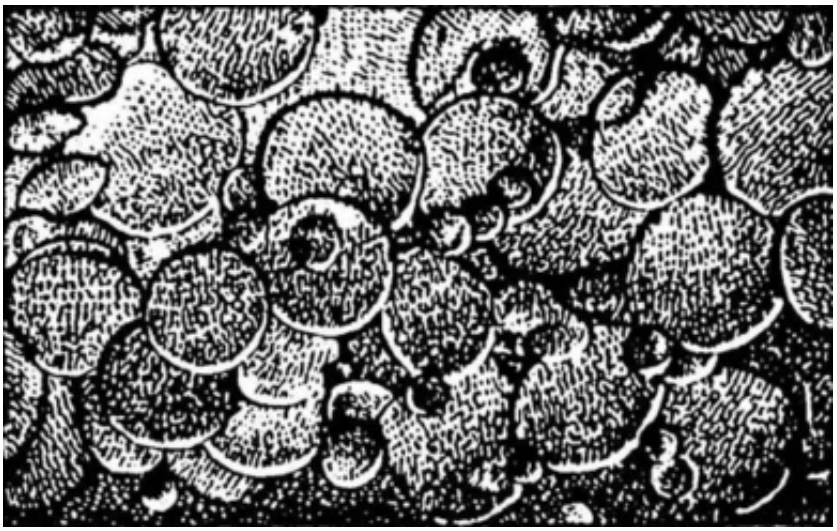

Figure 2.1: Pictomicrograph of small ice platelets known as frazil crystals (Fransson, 2009)

The size of these crystals range from 4-8 mm in diameter and are approximately 0.1 mm thick (Fransson, 2009). From these crystals, sea ice growth pathways and its physical appearance is strongly influenced by one of two sets prevailing environmental conditions. The first set of environmental conditions, is that of calm conditions with a calm sea-state. Under these conditions, the frazil crystals freeze together and form a thin, flexible sheet called nilas. While the nilas is less than 5 cm in thickness, it is almost fully transparent, causing only a slight sheen to the surface of the water. This stage is called dark nilas, with the latter thicker stage called light nilas as it increases in opacity (Weeks, 2010). Both frazil and nilas are categorised as new ice. As ice growth continues, it is categorised as young ice. Young ice is less flexible than new ice and under pressure, young ice sheets will break and move over each other rather than flexing. The movement of two ice sheets over each other is known as rafting. When the ice reaches a thickness of 30 cm and beyond, it is termed as first-year ice. Weeks (2010) explains that the depth of 30 cm is used for this classification separation since there is a significant change in how quickly the mean salinity decreases with time at around this thickness.

Under turbulent conditions, with a rough sea state and high winds, sea ice follows a different growth process, with the frazil ice crystals growing through consolidation rather than a growth in the individual ice crystal size. The frazil crystals are churned into a thick, soupy layer known as grease ice. The crystals are not bonded together well, and would not hold their shape if removed from the water (Weeks, 2010). Grease ice continues to thicken, while the crystals begin to freeze together, forming small conglomerate masses of ice. These conglomerates grow through adherence of frazil crystals, while bumping into each other due to the rough sea state. This bumping rounds the edges of the ice, giving them a disc shape. Ice of this type is known as pancake ice. Pancake ice continues to grow predominantly through agglomeration and rafting,

though Doble et al. (2003) found that there is variation in the structure of pancake ice, where some also increase in depth through the downward growth of ice crystals, known as "columnar ice growth". The pancakes continue to increase in size, increasing in diameter up to 5 m, until the wave motion is damped enough to allow the pancakes to freeze together, forming a cohesive sheet of first year ice. The exact growth processes and pathways that sea ice within the Antarctic MIZ follows is still relatively unknown and not well understood. Weeks (2010) believes this is primarily due to the small crystal sizes that limit the implementation of the normal methods for analysis of crystal structure used within the Arctic. Another reason is that initial data from pancakes studied in the Arctic suggested that pancakes were reliably formed through bottom accumulation (Wadhams and Wilkinson, 1999). However, a recent study by Doble et al. (2003) suggested that this was not the dominant pathway, and that a variety of morphologies commonly occur.

Sea ice formed in both calm and turbulent conditions progress to first year ice, though with very different ice structures along the way. Figure 2.2, from TU Delft (2016) summarises the stages discussed above, with images from Petrich and Eicken (2010) provided as clarification.

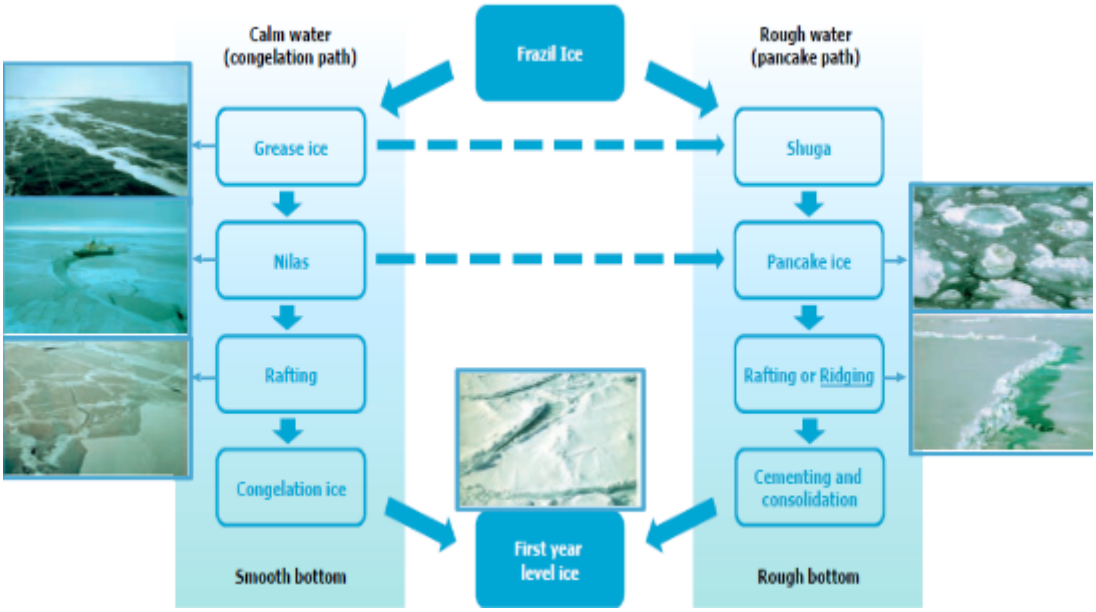

Figure 2.2: Flow diagram of two predominant ice growth processes (TU Delft, 2016) with images of different ice types by Petrich and Eicken (2010)

At any stage during the process, weather conditions can change, shifting the development to the other environmental pathway. This is shown by the dashed horizontal lines between grease ice and shuga, and for nilas and pancake ice.

2.3 The Thermodynamics of Sea Ice Growth

While there are at least nine different polymorphs of ice, only ice Ih exists at atmospheric pressure and in the temperature range of -80 °C to 0 °C (Weeks and Ackley, 1986). Thus, all sea ice and naturally formed ice upon the earth's surface will be of the form Ih. Ice Ih has a hexagonal crystal structure, consisting of a tetrahedral arrangement of H_2O molecules, seen in Figure 2.3.

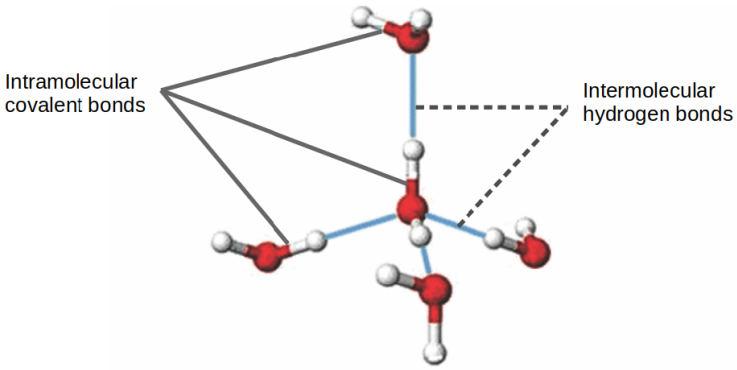

Figure 2.3: Tetrahedral Arrangement of Water Molecules in Ice (Zhang et al., 2012)

A central H_2O molecule bonds to four other H_2O molecules through hydrogen bonding between the electronegative oxygen atom (shown in red) of one H_2O molecule and the hydrogen atom (shown in white) of the adjacent H_2O (Zhang et al., 2012). A continuation of the tetrahedral bonding pattern leads to the hexagonal crystal structure as shown by Weeks and Ackley (1986) in Figure 2.4.

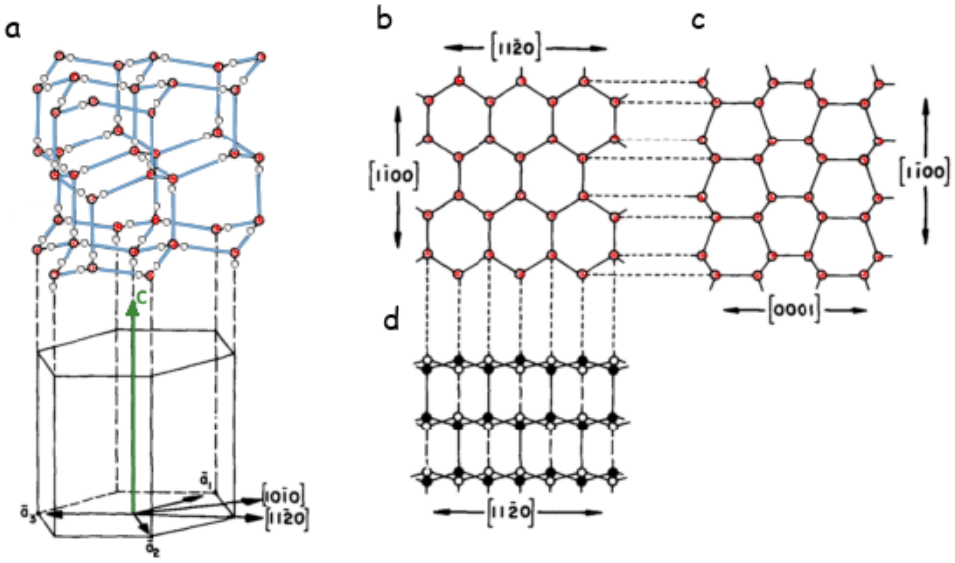

Figure 2.4: Hexagonal Crystal Bonding Structure of Ice Ih (Weeks and Ackley, 1986)

The crystal face showing hexagonal symmetry is known as the basal plane. The axis normal to the basal planes is known as the crystallographic axis of ice (shown in green), or c-axis. The c-axis is the same as the optical axis, where light will pass through without diffraction (Fransson, 2009). The oxygen to oxygen bonding distance is 0.276 nm at 0 °C, creating an open, low density structure. It is this configuration that leads to ice being less dense than its melt, causing it to float (Petrich and Eicken, 2010). Within the basal planes, fracture requires the breaking of four bonds, while between the basal planes, only two bonds need to be broken (Weeks and Ackley, 1986). An analogy of a deck of cards can be used, with each sheet strong within itself, but weak at the interfaces between each card and vulnerable to shear forces (Fransson, 2009).

Sea ice has the additional complication due to the presence of salt in solution. Sea water composition varies with location, but not to a great degree (Talley, 2002). In order to provide a standard, surface water from the Atlantic is referred to as "standard sea water". This has a salt content of 35.17 g kg^{-1} (Millero et al., 2008). While fresh water has a freezing point of 0 °C, the salts present in sea water create a freezing point depression. The approximate freezing point can be found as a function of the salinity (Grae Worster and Rees Jones, 2015):

$$\mathrm{T_{freeze}} = \mathrm{T_w} - \mathrm{m} \cdot \mathrm{S_{br}} \tag{2.1}$$

Where $\mathrm{T_{freeze}}$ is the expected freezing point, $\mathrm{T_w}$ is the freezing point of pure water (0 °C), m is a constant for salt in water (0.05 °C (g $\mathrm{kg}^{-1})^{-1}$) and $\mathrm{S_{br}}$ is the salinity of the brine in g kg^{-1}. Using this equation, one can estimate that the freezing point of standard sea water (35.17 g kg^{-1}) (Millero et al., 2008) is -1.7 °C. Ice has a very selective lattice, which does not allow the incorporation of salts. As the salt water solidifies, the salts are rejected from the crystal structure, increasing the salinity of the surrounding seawater. In theory, this should produce a pure ice phase, with no salt inclusions. However, it is found that sea ice retains a proportion of these salts. These salts are rejected from the ice phase, but are trapped as liquid or solid inclusions along the grain boundaries of ice platelets that make up sea ice crystals (Weeks, 2010). Since the brine pockets have a higher salinity than seawater, their freezing point is further depressed, keeping them liquid. As the temperature is decreased further, more ice continues to form while the brine pockets get smaller and concentrated. At some point, the salt within the brine reaches its saturation point, and further decrease of temperature results in the precipitation of solid salt as well as ice formation (Marion et al., 2010). This delicate phase balance between solid ice, solid salts and brine is further complicated by the presence of several different salts within sea water, each with their own saturation point and effect on freezing point depression.

Assur (1960) developed a phase diagram for sea ice derived from algorithmic chemical computations, based off a study of ion concentrations in brine presented by Nelson and Thompson (1954) . The results from these studies have been used extensively for brine salinity and brine volume calculations (Cox and Weeks, 1983, 1986; Griewank and Notz, 2015; Moreau et al., 2015; Notz and Grae Worster, 2009).

The method used by Nelson and Thompson (1954) of documenting the chemical evolution of brine from freezing down to eutectic point results in a calcium precipitate of antarcticite along the Ringer-Nelson-Thompson (RNT) pathway. However, it has been proven that this is not the equilibrium pathway that naturally occurs in sea ice (Butler and Kennedy, 2015; Butler et al., 2016; Geilfus et al., 2013). Instead, calcium precipitates as gypsum along what is known as the Gitterman pathway (Gitterman, 1937). The eutectic temperature for the RNT pathway is -54 °C as opposed to -36.2 °C along the Gitterman pathway. While the resultant deviation of sea ice composition and thermodynamic properties in Assur's results have been found to be negligible for most use cases compared to later models that incorporate the correct pathway (Butler and Kennedy, 2015; Marion et al., 2010), an accurate and more rigorous phase composition for sea ice has been presented by Vancoppenolle et al. (2019) and can be seen in Figure 2.5.

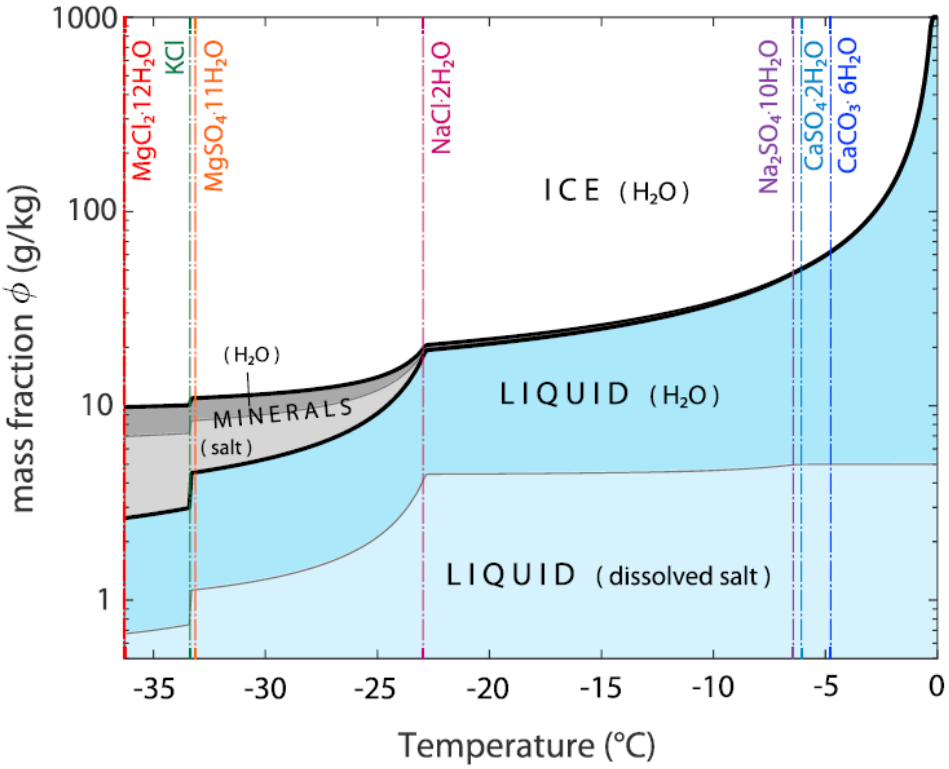

Figure 2.5: Sea ice phase diagram (Bulk in-ice salinity of 5 g kg^{-1} derived from standard sea water composition (Millero et al., 2008). The precipitation temperatures of each of the main salt constituents are displayed with vertical lines, color-coded to the specified constituent. The black lines separate the individual phases of liquid, minerals and ice. The thin gray lines further split salt and H_2O contributions in the liquid and mineral phase. (Vancoppenolle et al., 2019)

The diagram allows for the calculation of mass fraction of each of the constituents over the displayed temperature range between the eutectic temperature of the Gitterman pathway at -36.2 °C and 0 °C. It also clearly shows the precipitation temperatures of each of the major minerals found during the freezing process. This will be discussed further in Section 2.5.2. Since this is specifically for "standard" sea water, if another salinity is being examined, the values of salt and brine must be reduced accordingly for accurate results.

Now that the components and their effects upon the system have been discussed, we can examine the freezing process itself more closely. Sea ice formation occurs due to atmospheric cooling, occurring predominantly during the winter months within the polar regions. The heat fluxes of this atmospheric cooling can be approximated as being in the vertical direction only (Maykut and Untersteiner, 1971), with negligible horizontal gradients. This is illustrated in Figure 2.6. Figure 2.6 shows the prevailing heat flux direction occurring at the air-ice/ice-water interface. Where Q_w is the oceanic heat flux from water to the layer of new ice, where is is currently forming. Q_L is the latent heat released during ice formation, which is summed with Q_w to give $Q_{c,b}$, the conductive heat flux at the bottom of the ice required to be removed through the existing ice layer for continued ice formation. This ice layer also decreases in temperature with time and ice formation, thus $Q_{c,t}$ is the conductive heat flux off the top of the ice sheet to atmosphere. Q_a is the atmospheric heat flux.

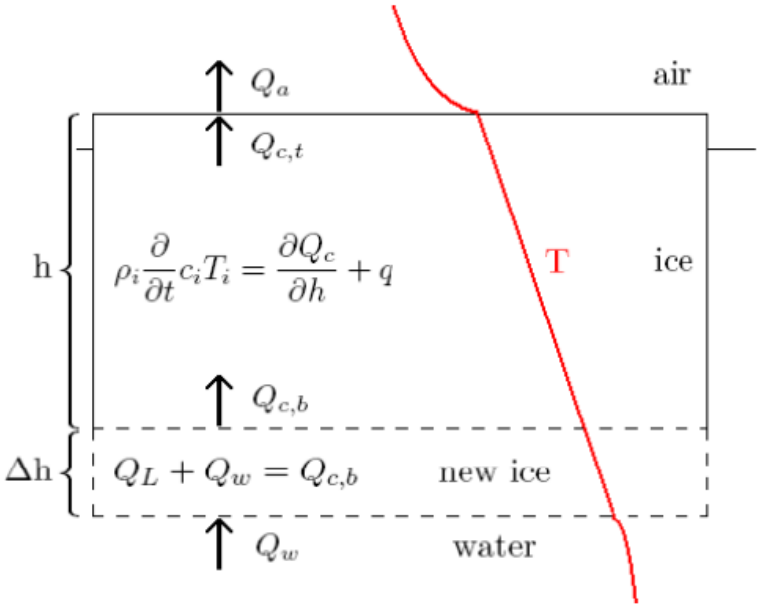

Figure 2.6: Summary of heat fluxes occurring during sea ice growth (Wiese, 2012)

Williams (1963) describes the net heat flux from natural water surfaces to atmosphere as:

$$\mathrm{Q_a} = \mathrm{Q_{co}} + \mathrm{Q_{lw}} + \mathrm{Q_e} - \mathrm{Q_{sw}} \tag{2.2}$$

Where $\mathrm{Q_a}$ is the total heat loss from the water/ice surface, $\mathrm{Q_{co}}$ is the convective heat loss, $\mathrm{Q_{lw}}$ is the long wave radiation from water/ice surface to surrounds, $\mathrm{Q_e}$ is the heat loss through evaporation, and $\mathrm{Q_{sw}}$ is the heat gain through incoming short wave radiation from the sun. $\mathrm{Q_e}$ can be significant, even when there is ice present and ambient temperatures are below freezing, due to sublimation. Ice sublimation occurs as a function of air temperature, wind speed, air humidity (Das et al., 2013). Regarding $\mathrm{Q_{sw}}$ and $\mathrm{Q_{lw}}$, the large zenith angles near the poles, combined with the high surface albedo of ice and snow means that up to 95 % of the incoming short wave radiation is reflected back into the atmosphere (van den Broeke et al., 2004). As with most natural surfaces, it also has a high long wave emissivity, meaning it loses heat to the surrounds. Using the net heat flux, one can derive the theoretical rate of sea ice growth.

An initial study on sea ice growth rate was carried out by Anderson (1961) in North Star Bay, Thule, Greenland. Over the winter of 1956-1957, ice samples with thicknesses between 20 - 150 cm were taken, all with very little snow on the surface. The ice depth was evaluated as a function of the cumulative number of freezing days (Θ), where Θ is given by

$$\Theta = \int_0^{\mathrm{t}} (\mathrm{T_{freeze}} - \mathrm{T_{ambient}})\,\mathrm{dt} \tag{2.3}$$

Where $\mathrm{T_{freeze}}$ is the freezing point temperature and $\mathrm{T_{ambient}}$ is the ambient air temperature. The resultant log-log plot of ice thickness versus cumulative freezing days is shown in Figure 2.7.

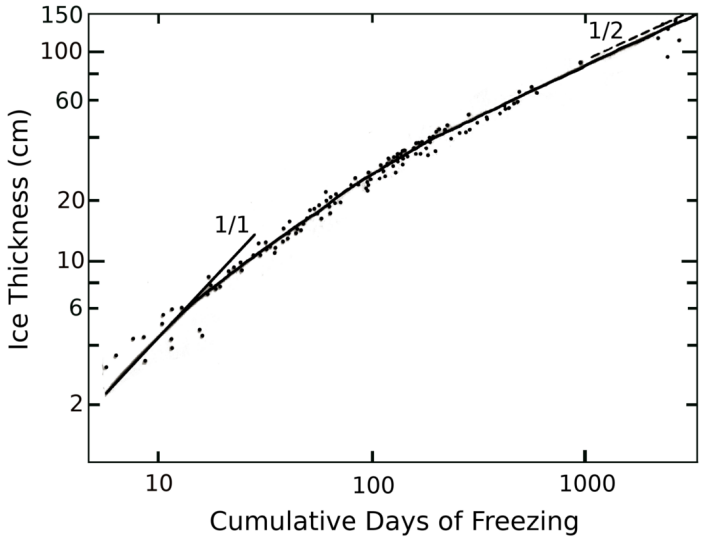

Figure 2.7: Modelled sea ice depth as a function of the cumulative number of freezing days (Anderson, 1961)

The profile shows an initial, linear relationship of ice growth with time, that over a longer term, resembling the form $\sqrt{x}$. The decrease in ice growth rate over time is due to the insulating nature of ice, which slows the conductive heat flux from the growth location at the ice-ocean interface.

With fresh water, which has a density maximum at 4 °C, cooling at temperatures close to the freezing point of 0 °C would cause a decrease in density, resulting in a cooled, stable top layer. Further cooling takes place only via conduction, much more inefficient than convection. Thus, the very surface layer would freeze first, while lower layers are still at temperatures of 4 °C (Weeks, 2010). However, the addition of salt in seawater increases the density of the solution, as well as causing a freezing point depression. The increase in the maximum density of water as its salinity increases is shown in Figure 2.8, showing the temperature at which this maximum temperature occurs, as well as the corresponding line of freezing point as a function of salinity.

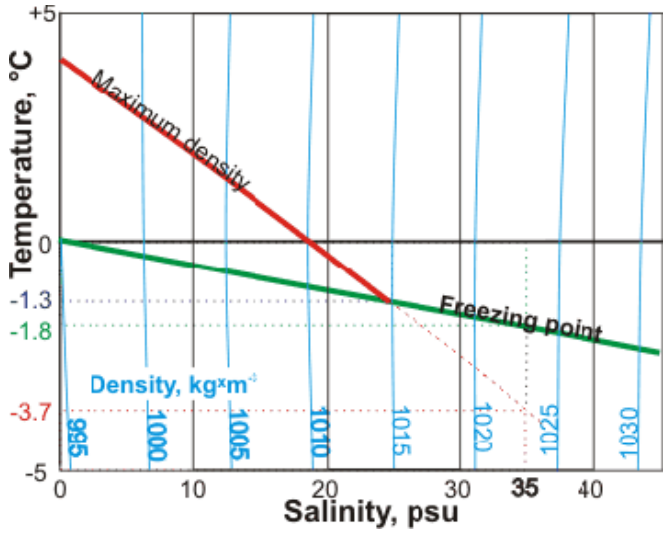

Figure 2.8: Plot showing the relationship of salt water density maximum to temperature and salinity (Chaplin, 2018)

Figure 2.8 shows that the line of maximum density and freezing point intersect at a salinity of 25 g kg^{-1}. Since seawater has a salinity close to 34 g kg^{-1}, it does not reach its maximum density before freezing. The upper, cooler layer of seawater is always more dense than the underlying layer, causing an overturning due to convection. Thus, the entire upper layer of the water column needs to reach the freezing point of -1.8 °C before ice formation begins. The thickness of this upper layer ranges from 10 to 40 m (Weeks, 2010). Initial ice formation is frazil ice platelets, which was shown by Arakawa (1954) to grow from spherical nuclei to a discoidal shape. Ice formed during this time through agglomeration of the crystals is called granular ice. Granular ice is categorised as isotropic, in that its properties do not vary according to direction of measurement. The crystal grain sizes of both frazil and pancake ice (which is predominantly granular) are less than 1 x 10^{-1} mm thick, with a length of less than 10 x 10^{-1} mm (Eicken and Lange, 1989).

Schwarz and Weeks (1977) provides a detailed schematic (Figure 2.9) which shows the structure of first year sea ice throughout the various stages of growth. The initial granular ice skim has crystal c-axes predominantly vertical.

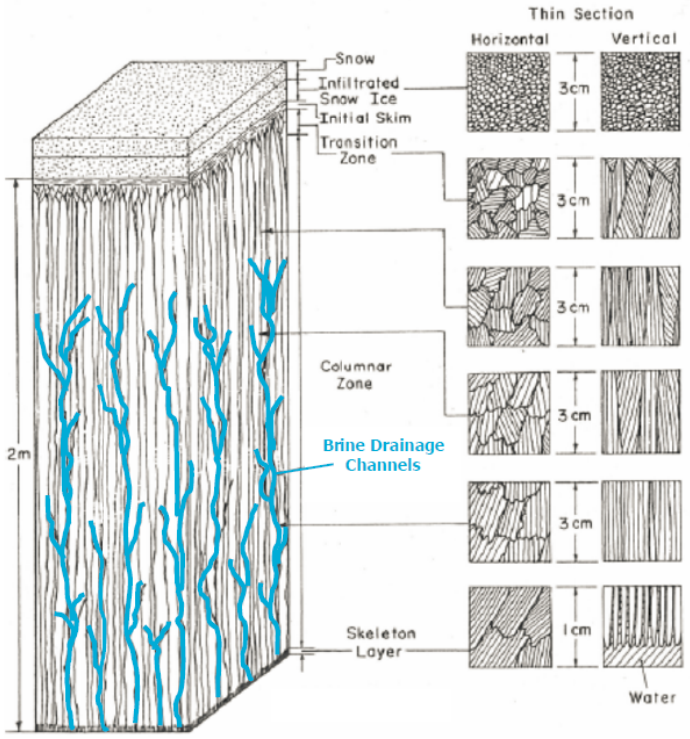

Figure 2.9: Schematic showing the crystal structure of first year sea ice (Schwarz and Weeks, 1977)

In calmer conditions, or where the ice layer is thick enough to damp the churning effect of the waves, the alignment of the c-axes begin to shift through a process of geometric selection (Weeks, 2010). Since the heat flux is in the vertical direction, crystals with their c-axis aligned closer to perpendicular to the flux direction grow faster. These intersect with the surrounding crystals of a less favourable direction and eliminate further growth. The layer where this shift of c-axes orientation takes place is known as the transition layer and generally occurs over a vertical distance of less than 10 cm (Weeks and Ackley, 1986). The layer following the transition layer is called the columnar layer, wherein the preferred direction of downward crystal growth is

dominant, and the crystals are elongated downwards, with all c-axes in the horizontal direction (Weeks and Ackley, 1986). Columnar ice can be placed in two categories. In the first, the horizontal c-axes are randomly orientated, termed "columnar S2" ice. In the second, the c-axes are not only located but also aligned in the horizontal plane (Timco and Weeks, 2010). This is shown to occur in the presence of a dominant water current (Langhorne and Robinson, 1986; Stander and Michel, 1989) and is termed "orientated columnar" or "S3" ice. Lofgren and Weeks (1969) found the dendrite crystal diameters of columnar ice to be in the range of 1 to 7 x 10^{-1} mm. The lengths of these crystals can extend down the entire thickness of the ice sheet (Timco and Weeks, 2010). Concentrated brine is entrapped during initial growth throughout the sea ice structure as intracrystalline brine pockets between ice platelets (Petrich and Eicken, 2010). These brine inclusions can develop into interconnected brine drainage channels, which can be seen within the columnar section of sea ice in Figure 2.9 as the highlighted blue lines. Brine inclusions shall be discussed in detail within the following section.

2.4 Brine Inclusions, Channels and Brine Drainage

In granular ice, brine and salt inclusions occur between the ice crystals, trapped by the surrounding ice crystals (Weissenberger et al., 1992). In columnar ice, brine and salt inclusions occur within the crystals at grain boundaries, in vertically orientated planes. These inclusions grow or shrink as a function of temperature and can develop into interconnected brine channels. These channels allow for the convection of brine through the ice, and young sea ice is found to experience significant brine drainage (Notz and Grae Worster, 2008). There are several theories for how this brine transport out of the ice takes place, however, it is theorised by Weeks and Ackley (1986) that gravity drainage is the only transportation mechanism of significance during ice growth. The result of this brine drainage is that columnar sea ice bulk salinity follows a C-shaped curve, with high values for salinity being found both in the uppermost surface layer as well as near the ocean-ice interface. The demonstration of the C-shaped salinity profiles for sea ice was best measured by Nakawo and Sinha (1981) in the Canadian Arctic (Figure 2.10).

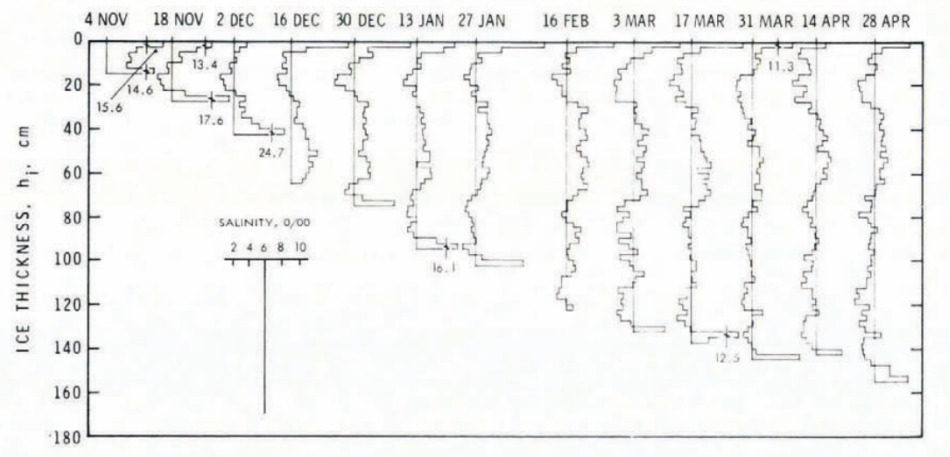

Figure 2.10: Salinity profiles of sea ice obtained during winter 1977 to 1978 at Eclipse Sound, over two week intervals. Salinity scale is shown inserted, and a reference line of 6 g kg^{-1} is placed on each profile (Nakawo and Sinha, 1981)

While this profile is specifically for Arctic sea ice, the profile is similar for Antarctic sea ice, though known to be more complicated (Weeks, 2010). Freezing experiments by Weeks and Assur (1967) and Cox and Weeks (1975) proved that ice salinity was a linear function of the growth rate. This would account for the high surface salinity, since ice growth is fastest during initial formation before decreasing as the ice depth increases. Eicken (1992) identified additional factors such as upward brine expulsion and flushing as to why the surface layer experiences high salinity. The high salinity at lower depths is due to the open structure of the lower ice layer, as well as the brine from above draining downwards (Petrich and Eicken, 2010). The salinity profiles from pack ice samples, which included pancake ice, in the Antarctic have been found to exhibit four possible trends, with the two most prevalent being the same C-shape curve as found in the Arctic (51 %), and an S-shaped curve which experiences a salinity decrease near the ice-ocean interface (33 %) (Eicken, 1992).

A general expression for the bulk salinity (S_B) of growing sea ice derived from its thickness (H) was developed by Kovacs (1996), using data sets of first year sea ice from both the Arctic and Antarctic:

$$S_B = 4.606 + \frac{91.603}{H} \tag{2.4}$$

As mentioned previously, there is a large variation within sea ice properties over spatial areas, yet this relationship was found to possess a correlation coefficient of R^2 = 0.73. This correlation should fit reasonably well for sea ice grown both under calm and turbulent conditions, though it should be noted that higher salinities will be expected for sea ice grown in turbulent conditions by 2 to 3 % (Weeks, 2010). Doble et al. (2003) conducted field sampling in the Weddell Sea MIZ where turbulent conditions are common. Frazil salinities ranged from 9.5 to 18.9 g kg^{-1}, while pancake ice (formed from frazil ice consolidation) had salinities between 5.4 and 12.5 g kg^{-1}. The values for lower salinities in pancake ice corresponded to pancakes from stations further into the ice field, implying they had been formed at an earlier date.

Bulk salinity of the ice is not an accurate method of determining the distribution of the salt and brine within the ice, since it is not a homogeneous mix, but rather consists of pure ice and concentrated pockets or channels of brine that migrate downwards over time. Based on Assur's phase diagram and data published in 1960, Frankenstein and Garner (1967) created an equation to determine the brine volume for a given bulk salinity and temperature:

$$v_B = S_B \cdot (\frac{49.185}{T_i} + 0.532) \tag{2.5}$$

Where v_B is the relative volume of brine in cm^3 dm^{-3}, S_B is the bulk salinity in g kg^{-1} and T_i is the absolute ice temperature of the sample in K. Equation 2.5 is valid for temperatures between -0.5 °C and -22.9 °C and has a correlation coefficient of 0.9995. Within the sea ice, the voidage is made up of brine but also entrapped gas. Though this gas volume is often small for young ice, if highly accurate voidage results are required then it should also be included. Cox and Weeks (1983) developed equations for the calculation of the gas volume, finding that ice with a salinity of 10 g kg^{-1} had a maximum gas volume of 0.05 %. It should be noted that their method requires very accurate measurements of density to be taken, which is difficult to obtain (Timco and Frederking, 1996).

Initial attempts to determine the shape and distribution of brine pockets and drainage channels were accomplished by the slicing of thin vertical sections of ice wherein the drainage channels would be visible (Eide and Martin, 1975). The channels were found to be tree-shaped, with slanted feeder tubes joining together to form large vertical channels which drain downwards. A schematic of these channels can be seen in Figure 2.11.

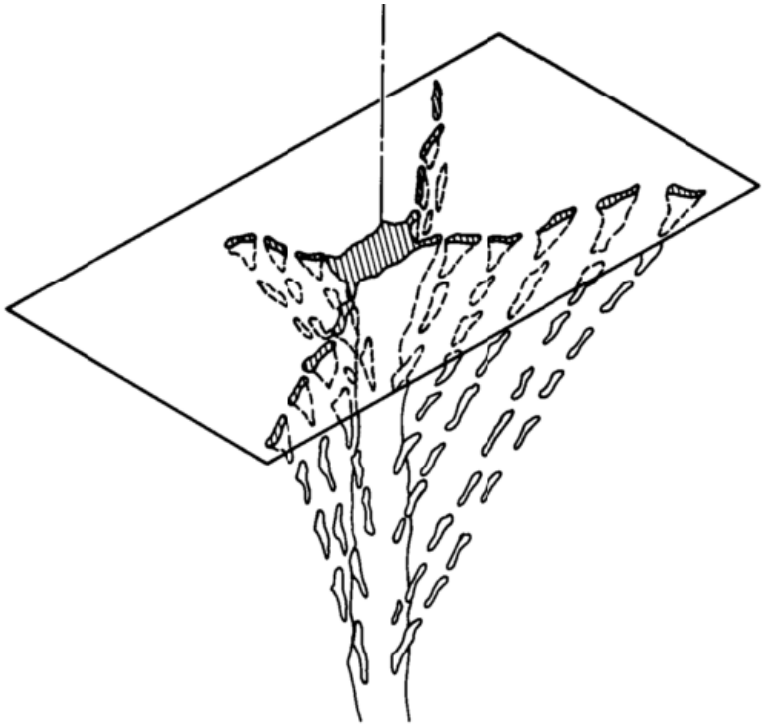

Figure 2.11: Schematic of the Vertical Brine Channels and Diagonal Feeder Tubes Found in Sea Ice (Eide and Martin, 1975)

It was also noted by Eide and Martin (1975) that brine channels have a characteristic neck at the exit point. This neck is thought to be caused by a buoyancy force from below and a pressure gradient force from above. This is a useful feature to note, since it allows for the loss of brine during shipping and storage of samples to be minimised by storing and transporting at low temperature (<-23 °C) (Cox and Weeks, 1986). This open structure and long, vertical tubes means that sea ice is, to some extent, a permeable structure. However, while the permeability, k is a function of the brine volume within the ice, the exact relationship has not received much study (Golden et al., 2007). For columnar sea ice, it is generally accepted that ice with a brine volume of 5 % and a salinity of less than 5 g kg^{-1} is effectively impermeable at temperatures of -5 °C or lower. This relationship was discovered by Golden et al. (1998) and dubbed "The Law of Fives". The voidage and brine channels are of interest due to their effect on the mechanical strength of the ice (Frankenstein and Garner, 1967) and their use as a habitat by microorganisms (Krembs and Deming, 2011). The difficulty with analysing the pore structure within the ice is the small size of the inclusions (Weeks and Ackley, 1986) and temperature dependence. Methods of analysis need to be able to go down to a sub-millimetre scale, and preferably do so in a non-intrusive manner at low temperature.

2.5 Artificial Sea Ice

2.5.1 Artificial Sea Ice for Study of Growth Processes and Ice Property Evaluation

Artificially grown sea ice has been used as an analysis tool because of the advanced control it provides over variables such as cooling rate or initial solution salinity, allowing for the effect of individual variables to be analysed through repeated experiments while adjusting only the variable of interest (Weeks, 1962). It has been used for the determination and analysis of a vast array of properties and characteristics of sea ice including mechanical properties, brine inclusions and brine drainage, thermal properties, optical properties, and gaseous exchange. In order to be used for such purposes, it is important that the artificially grown sea ice closely resembles natural sea ice. But achievement of this aim can sometimes be difficult to judge, especially in light of the immense variation in the properties of sea ice as highlighted by Maykut et al. (1992). The focus of previous artificial sea ice set-ups has been on the growth of artificial columnar S2 sea ice, since this is the most prevalent form of sea ice (Weeks and Ackley, 1986). Considering these studies, a list of key properties have been identified that is used to categorise the laboratory grown saline ice as artificial columnar S2 sea ice (Table 2.1).

Table 2.1: Summary of ice properties used to categorise saline ice as "Artificial Columnar S2 Sea Ice"

Property	Columnar S2 Sea Ice	Previous Mentions
Temperature Profile	Vertically orientated, linear temperature profile	Cottier and Wadhams, 1999 Haas, 1999 Marks et al., 2017 Wiese, 2012
Ice Growth Rate	Ice thickness as function of time has shape of $\sqrt{x}$	Cox and Weeks, 1975
Crystal Morphology	Vertically elongated ice crystals, with c-axes all located in horizontal plane, but with random orientation within horizontal plane	Haas, 1999 Schulson et al., 2015
Brine Location	Vertical, brine inclusions located in intra-crystal planes with 1 - 1.5 mm spacing between planes	Eide and Martin, 1975 Galley et al., 2015 Golden et al., 2007
In-Ice Salinity Profile	C-shaped salinity profile, with highest salinity found at the top and bottom of the ice	Cottier and Wadhams, 1999 Notz et al., 2005

As discussed in the preceding sections, the properties of the ice stem from the metocean conditions prevalent during formation. The largest influence on the ice properties is the direction of the heat flux (Lepparanta, 1993). The property most popularly referred to is temperature profile, with Weeks and Cox (1974) stressing the importance of the measurement this variable, as it affects all other properties. These properties include the ice growth rate, seen to be of the form $\sqrt{x}$ in natural sea ice (Anderson, 1961) and was found by Cox and Weeks (1975) to show the same trend in artificial sea ice. This is once again attributed to the uni-directional, top-down heat flux, since the thickening ice causes a corresponding increasing insulation effect, causing the ice growth to slow down. The directional heat flux furthermore affects the ice crystal morphology, with the vertical elongation of the crystals in the direction of heat flux. However, the c-axes have been shown to be randomly orientated within the horizontal plane, termed as "S2 columnar sea ice" (Timco and Weeks, 2010). This is usually analysed using thin sections of ice under cross-polarized light, and was used by Haas (1999) and Schulson et al. (2015) to classify the artificial sea ice grown in their studies. This is different from sea ice formed in the presence of a dominant current, where the c-axes within the horizontal plane are all aligned, as seen in the artificial sea ice growth study performed by Cottier and Wadhams (1999) and Langhorne and Robinson (1986).

As the columnar ice forms, it grows downwards in needle-like dendrites that create planar channels in which the excluded salt from the freezing process is forced into. This results in concentrated brine, located in these vertical planes within the sea ice crystal itself, referred to as brine inclusions. The spacing of these brine inclusions is normally within the order of 1-1.5 mm. The planar spacing was measured by Eide and Martin (1975) during his artificial sea ice study for the purposes of comparison to the spacings observed in natural sea ice. These inclusions can develop into interconnected brine channels, with the brine draining into the underlying solution (Schwarz and Weeks, 1977). Using non-intrusive imaging techniques, Galley et al. (2015) and Golden et al. (2007) observed the presence of these channels within artificial sea ice. Due to this brine drainage, the salinity profile of the ice changes over time. Natural sea ice commonly exhibits a c-shaped salinity profile through the ice depth (Nakawo and Sinha, 1981), with the same profile observed for artificial sea ice (Cottier and Wadhams, 1999; Notz, 2005).

2.5.2 Freezing Methods

The growth of artificial sea ice has been carried out in temperatures ranging from -5 °C (Naumann et al., 2012) to -30 °C (Perovich and Grenfell, 1981). Roscoe et al. (2011) grew artificial sea ice in temperatures as low as -40 °C, however, this was specifically to examine the growth of frost flowers, which have been shown by Barber et al. (2014) to form at very cold atmospheric temperatures. It is known that there is a linear relationship between atmospheric temperature and growth rate, with a lower atmospheric temperature creating a greater temperature gradient and therefore a higher growth rate (Anderson, 1961), with the growth rate affecting the ice properties such as crystal size and ice salinity (Weeks and Assur, 1967). A temperature of -20 °C is a popular choice of temperature (Cox and Weeks, 1975; Middleton et al., 2016; Schulson et al., 2015; Wiese et al., 2015), since it mimics natural average winter air temperatures measured within the polar regions, and allows for reasonably fast ice growth. Another consideration for the choice of freezing temperature is the possible precipitation of solid salts at low temperatures. These solid salts can affect the physical, mechanical and optical properties of sea ice (Assur, 1960; Light et al., 2009; Perovich and Gow, 1996). Table 2.2 shows the temperatures and mass fractions of precipitating minerals during the sea ice freezing process, as shown in the sea ice phase diagram (Figure 2.5) discussed in Section 2.3 (Vancoppenolle et al., 2019).

Table 2.2: Precipitating minerals during the freezing of sea water, with their highest temperature of precipitation as well as their final mass fraction at the eutectic point (-36.2 °C) (Vancoppenolle et al., 2019) with the proposed freezing temperature cut-off of -20 °C shown in blue

Mineral	Chemical Formula	Highest Temperature Of Precipitation (°C)	Mass Fraction at Eutectic Point (g kg^{-1})
Ikaite	$CaCO_3 \cdot 6H_2O$	-4.9	2
Gypsum	$CaSO_4 \cdot 2H_2O$	-6.2	36
Mirabilite	$Na\ S0_4 \cdot 10H_2O$	-6.4	105 @ -22.9 °C
Proposed Freezing Temperature of -20 °C			
Hydrohalite	$NaCl \cdot 2H_2O$	-22.9	754
Sodium Bromide	NaBr	-22.9	0.4
Meridianite	$MgSO_4 \cdot H_2O$	-33.3	62
Sylvite	KCl	-33.4	11
Magnesium chloride dodecahydrate	$MgCl_2 \cdot 12H_2O$	-36.2	135

The most prevalent salt on a mass basis is hydrohalite, which begins to precipitate at -22.9 °C. A freezing temperature of -20 °C stays above the precipitation point of hydrohalite, with only the possibility of ikaite, gypsum and mirabilite precipitating out. The maximum combined mass fraction of these three minerals is just 143 g kg^{-1}. Thus, a temperature of -20 °C stays below the precipitation temperature of the majority of the salt, negating any effects that this would have on the ice properties.

Early artificial sea ice experiments made use of freezer chests, where the freezing vessels were placed inside the freezer surrounded by insulation to ensure uni-directional cooling (Nelson and Thompson, 1954). However, this limits both the size of the freezing vessel, and the instrumentation that can easily be included in the set-up. It also makes access to the vessel difficult during the experiment, since the small space would ensure a rapid increase in temperature if the freezer needed to be opened to make any adjustments to the set-up or monitor ice growth.

Larger tank sizes will be more expensive and require more intensive, heavy-duty cooling methods if the tank is not located in an area of the world where ambient temperatures are below freezing. The Sea-ice Environmental Research Facility (SERF) at the university of Manitoba is located outdoors and uses natural cooling for ice growth (Hare et al., 2013). Using natural cooling is cheaper since no cooling equipment or duties are required, however it does result in a more variable and uncontrolled ambient temperature profile, as seen in Figure 2.12

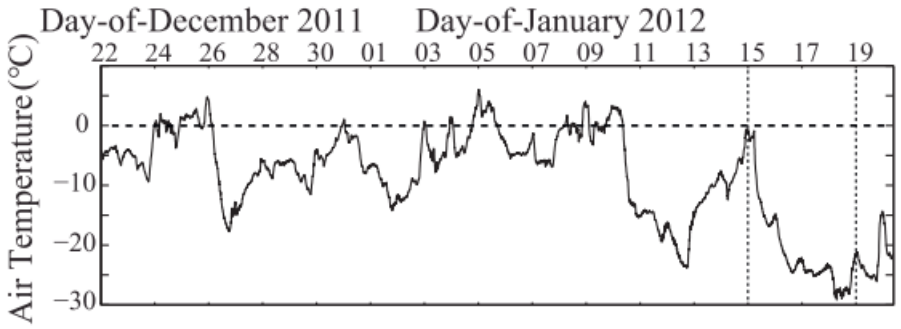

Figure 2.12: Fluctuating air temperatures experienced during an artificial sea ice growth experiment at the Sea ice Environmental Research Facility (SERF), University of Manitoba (Galley et al., 2015)

This could be seen as an advantage if the tank-grown ice is attempting to exactly mimic the growth conditions experienced by natural sea ice, where conditions will fluctuate. While examining the effect of a single variable upon ice properties, it would be preferable to have tighter control over the cooling temperature.

It is now common practice to make use of a temperature controlled room, where the temperature can be adjusted to the desired freezing temperature (Cottier and Wadhams, 1999; Loose et al., 2009; Roscoe et al., 2011; Weeks, 1962). This could be used as the primary freezing mechanism, with heat transfer taking placed between the cold ambient air and the solution surface. The disadvantage of this method is the slow heat transfer properties of air, resulting in a low ice growth rate and a variable air temperature when measured right above the solution surface (Nomura et al., 2006). To negate this, many experimental set-ups include a fan which blows the cold air above the tank surface and enhance circulation, improving the heat transfer rate (Marks et al., 2017; Perovich and Grenfell, 1981).

Wiese et al. (2015) and Marks et al. (2017) mentioned another issue to overcome when using chillers to maintain the desired freezing temperature. Chillers require a warming period every few hours in order to remove ice-build up. Marks et al. (2017) noted an increase in the room temperature of up to 6 °C. Many of these rooms used floor-based air circulation, as seen in the experimental set-up of Marks et al. (2017), requiring the use of thick insulation at the bottom and sides of the tank to ensure the cooling occurs from the tank surface only.

Another method of ensuring greater control over the heat transfer and cooling rate is to use a metal cooling plate that is in direct contact with the solution. This has been used by researchers such as Cox and Weeks (1975), Notz et al. (2005), Eide and Martin (1975) and Middleton et al. (2016). Schulson et al. (2015) provides a look at the inner channels of such a cooling system and is shown in Figure 2.13.

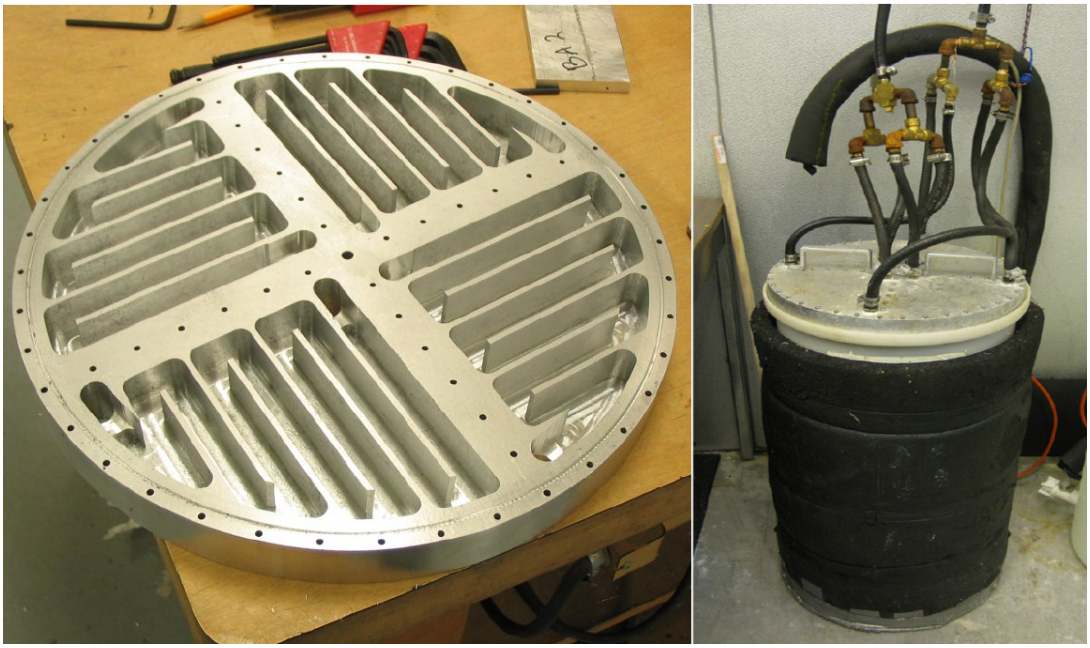

Figure 2.13: Cooling plate used for controlled cooling. Channels for ethylene glycol circulation is shown on the left, with the right showing the tank in operation (Schulson et al., 2015)

Cooling liquid such as ethylene glycol is circulated through the plate and has been successfully used to maintain the desired cooling temperature within 0.1 °C (Golding et al., 2014). In addition to the consistent cooling temperature, it has the advantage of natively ensuring uni-axial cooling, and can be used within a room where the ambient temperature can be as high as -1 °C (Middleton et al., 2016).

This allows for a more comfortable work environment and means that instrumentation that would otherwise be at risk in lower temperature environments can perhaps be used. However, the disadvantage of such a system is that it is more expensive to set up, since it involves the machining of a cooling plate (shown in Schulson et al. (2015)) and acquisition of a cooling circulation system, in addition to a temperature controlled room to keep ambient temperatures of -1 °C. The cooling plate also does not allow a natural ice freeboard, and requires a pressure relief system to account for the density change during ice growth (Notz, 2005).

In addition to cooling from the top surface, it is usual to install temperature control or a constant heating rate for the underlying solution (Marks et al., 2017; Roscoe et al., 2011; Weeks and Cox, 1974; Wiese et al., 2015). This is to simulate the oceanic heat flux, a highly variable value, shown to be as low as 1 W m^{-2} in the Arctic by Li and Riska (2002) or averaging between 10 to 15 W m^{-2} in the Antarctic across the growth season (Allison, 1979). The heat input prevents super-cooling from occurring, so that the ice formation only occurs at the ice-solution interface. Wiese et al. (2015) found that a heat input of 15 W m^{-2} was sufficient to prevent supercooling.

2.5.3 Tank Size and Material of Construction

The choice of tank size, and material of construction is largely influenced by research direction and budget. Since the properties of interest are primarily the physical and mechanical properties of the ice, this section shall focus on tank set-ups for this purpose. Artificial sea ice studies have been conducted in vessels ranging from a few litres (Notz, 2005) to tanks greater than 1 million litres, for example, the ice tank at the Hamburg Ship Model Basin (Haas, 1999). However, for budget and simplicity, smaller tanks tanks are generally preferred. However, small tanks can also be complex and expensive, designed for precision experiments to analyse intricate interactions such as gaseous exchange through sea ice. Examples of these advanced chambers include the Sea Ice Chamber at the University of Leeds (Shaw et al., 2011), and the Roland van Glasow Air-Sea-Ice Chamber, School of Environmental Sciences (Garnett et al., 2019).

Smaller tanks are useful for analysis of structure and chemical composition where the focus is on the growth process itself, where few ice samples required for ex-situ analysis (Weeks and Cox, 1974). Schwarz et al. (1981) outlined the requirements for samples used for testing either compressive or tensile strength. The samples need to be sufficiently large to be independent of the ratio of sample size to crystal size. It has been found that in order to be independent of this ratio, sample widths need to be greater than 12 times the crystal diameter. Lengths need to 2 to 3 times the sample diameters in order to be long enough for the midsection to be free of end-stress-effects. This translates to sample diameters of between 6 cm (Jones, 1997) to 7.62 cm (Assur, 1960) and lengths of approximately 20 to 25 cm (Weeks, 2010). Therefore, mechanical testing usually requires larger tanks, especially since it is important to obtain multiple samples to ensure statistical significance. Tank sizes that have been used to grow samples for mechanical testing seem to be within the range of 800 to 1000 dm^3 (DeFranco and Dempsey, 1991; Golding et al., 2014; Gratz and Schulson, 1997; Schulson et al., 2015). The likely reason for this size choice is because it allows the best compromise between a tank large enough to yield sufficient samples to provide statistical significance, while minimising the growth time, experimental complexity and the required amount of salt and water. There are tanks much greater in size, such as the ice tank at the Hamburg Ship Model Basin (Haas, 1999), with a volume of 1 950 000 dm^3, the CRREL facility including a tank of 799 000 dm^3 (Buist et al., 2011) or the 1 340 000 dm^3 Sea-ice Environmental Research Facility (SERF) (Hare et al., 2013). However, a tank of similar size is out of the budget restraints of this project and so they are not discussed further.

Round tanks have been found to minimise the stress on the tank walls (Perovich and Grenfell, 1981). A variety of materials can be used for their construction. Marks et al. (2017) and Golding et al. (2014) Schulson et al. (2015) chose to construct their tanks from plastic, since this is a cost-effective, lightweight and non-reactive material (Figure 2.14).

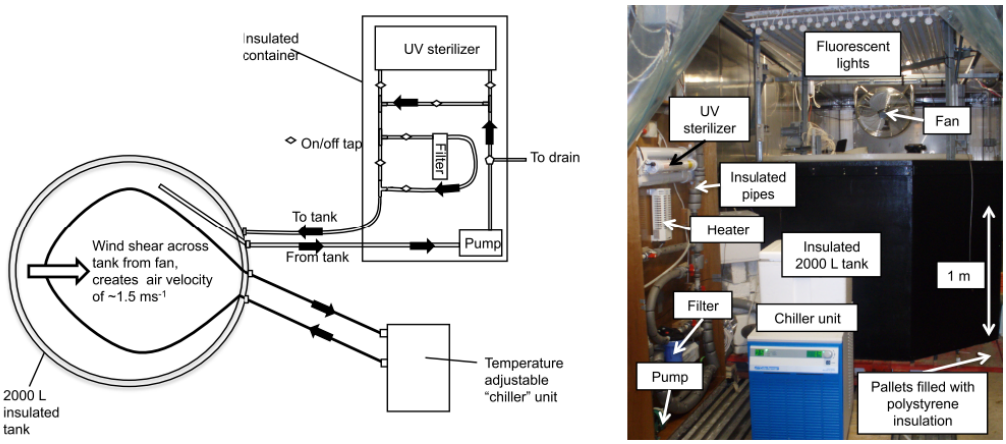

Figure 2.14: Round tank experimental set-up for ice artificial sea ice growth used by Marks et al. (2017)

Weeks (1962) used a steel tank, however, the tank needed to be coated in an anti-corrosion paint due to the salt. The metal would also have conducted temperatures extremely well, which may exacerbate any effects at the tank sides. Indeed, it was mentioned by the authors in a later paper (Cox and Weeks, 1975) that the ice was thicker at the tank sides, suggesting an greater degree of cooling near the walls. It is most likely that a steel tank was used since plastic was less ubiquitous as it is nowadays. Shaw et al. (2011) is seen to use a square stainless steel tank to examine the diffusive transport of atmospheric halocarbons through sea ice. It is suspected that stainless steel is used since it will not not interact with the halocarbons. Therefore, the choice of this material is for a specialised case. Insulating round tanks provides some challenge, with the insulation required to be flexible in order to tightly fit around the curved sides. Both Weeks (1962) and Marks et al. (2017) used neoprene sheets adhered to the tank wall to provide a first insulation layer. However, their next layers differ, with Weeks using glass wool and tar paper, while Marks et al. built up a square wooden box fitted with polystyrene sheets. A simple and novel solution to both tank and insulation was used by Light et al. (2015), who grew saline ice in a commercially available, insulated square tank primarily used for food transport. No information was given on the physical properties of the produced ice, so it is difficult to know how accurately the set-up was able to mimic natural sea ice, but it is indeed an interesting and attractively simple approach.

Square tanks have also been commonly used, either made of glass (Garnett et al., 2019; Wiese et al., 2015) or plexiglass (Middleton et al., 2016; Newyear and Martin, 1997; Shazly et al., 2009).. The advantage of these materials is that the transparent surface allows easy visual inspection of ice growth, and can be used to check for supercooling and spontaneous nucleation of ice crystals within the underlying water column. These materials also share similar thermal properties to sea ice (Eide and Martin, 1975) which is useful since the cooling rate will be the same through the advancing ice front and the tank wall next to it. This will help prevent different ice thicknesses near the tank walls, if any external temperature influence can be negated

on the tank sides. This is not too difficult to accomplish however, with insulation easily accomplished for a square tank using polystyrene boards of between 5 to 20 cm thick (Carns et al., 2015; Style and Grae Worster, 2009; Weissenberger, 1998; Wettlaufer et al. 1997). A method for insulation to allow an unobstructed view is construction of what is known as a Hele-Shaw cell (Middleton et al., 2016). This involves double walling the plexiglass or glass tank and using a sealed air gap inside in order to provide insulation and an unobstructed view. Such an insulation technique is only desired when visualisation is important, since it does not provide optimal insulation (Eide and Martin, 1975). It is also a more expensive and complex tank design. A simple solution for quick checks of the ice would be a removable insulation panel. Another advantage of a square or rectangular tank design is that it allows for the generation of waves. Two dimensional waves can be generated in rectangular wave flumes, where the tank width is much less than its length. Square basins allow for the generation of three dimensional waves. Larger tanks are also preferred for experiments on wave-ice interaction where effects of wave amplitude to ice scale are important and the tank needs to be large enough to allow for full wave development and decay. Indoor wave tanks are preferred since the effect of wind can be controlled.

2.5.4 Water Circulation and Agitation

Most artificial sea ice set-ups use a system to circulate or agitate the underlying solution and prevent temperature and salinity stratification. As mentioned in Section 2.3, the location of the solution density maximum at 4 °C should ensure convective mixing of ocean water takes place. However, Haas (1999) points out that growth rates and temperature gradients for artificial sea ice set-ups are much greater than those found in naturally occurring sea ice. This may account for the need for mixing greater than the rate that natural convection will provide. While Lake and Lewis (1970) and Niedrauer and Martin (1979) found that underlying solution temperatures were very stable under natural sea ice, Haas (1999) measured a large degree of temperature variation in the saline solution underneath artificial sea ice grown without water circulation or agitation. This mixing can be provided by using a pumped water circulation system (Marks et al., 2017) or aquarium impeller pumps (Garnett et al., 2019; Roscoe et al., 2011; Wiese et al., 2015).

The geometry of tanks have an effect on mixing, and different geometries will require different mixing set-ups and pump placements to ensure optimal mixing. Circular mixing works best in round tanks with even single pumps able to provide good mixing when placed tangentially to the tank wall to create a circularly orientated flow (Timmons et al., 1998). The primary tangential flow pattern generates a secondary, radial flow that creates circulation towards the tank center. However, Timmons et al. (1998) did note that there could be a dead zone formed near the center of the tank, termed an irrotational zone, where low fluid velocities result in poor mixing (Figure 2.15). Square tanks do not work well with circular flow and have dead zones in their corners (Lekang, 2013). A general configuration for the pump placement in a square tank is to use two pumps, and to place them diagonally across from each other in the tank corners (Garnett et al., 2019; Shaw et al., 2011).

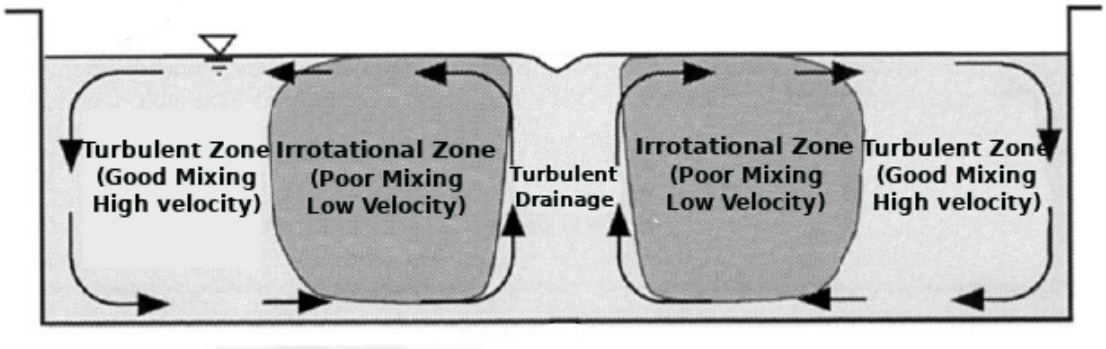

Figure 2.15: Schematic of secondary radial flow pattern generated with tangential mixing in a round tank. The primary flow pattern (not shown) is tangential (Timmons et al., 1998)

The agitation rate is quite important, since Langhorne and Robinson (1986) found that a significant degree of horizontal alignment within the crystal c-axes could be seen under growth conditions with currents faster than 10 mm s^{-1}. This crystal alignment due to current was confirmed by Stander and Michel (1989) and Cottier and Wadhams (1999). Current also affects pores in the ice, with stronger currents resulting in smaller pores but greater pore densities (Eicken et al., 2000). Horizontally aligned c-axes in columnar sea ice does occur naturally, but is not common (Timco and Weeks, 2010) and thus should only be replicated if it is desired to specifically examine the effect of this alignment. Otherwise, it would be desired to prevent this alignment, either through currents lower than the threshold rate or by creating a varying current direction.

2.5.5 Pressure Relief

Sea ice has a density lower than that of its melt, instigating a volume increase upon freezing (Weeks, 2010). The lower density ice floats, maintaining a certain freeboard. The optimum method of replicating this freeboard in laboratory grown sea ice is to maintain free-floating ice. To do this, one can provide heating to side of tank, to prevent ice from freezing to walls (Wiese et al., 2015). This heating needs to be as minimal as possible since too much heating would prevent any ice formation at all or would alter the heat flux through the ice. The tank material will play a role in this, with a rough material such as cement creating a higher coefficient of friction between the walls and the ice, meaning more heating will be required to ensure the ice is free enough to float. Glass tanks, being much smoother, will enable the ice to slide up and down with a lower heat input. Such methods have been used by Wiese et al. (2015) and in the ice tank mentioned by Garnett et al. (2019). The heating rate was not mentioned by either, though the heating film used in ice tank spoken of by Garnett et al. (2019) is capable of outputting 130 W/m^2. This would likely be far in excess of the required amount. The choice of free floating ice also affects placement of instrumentation, since free floating ice will cause the surface level of the ice to move upwards due to volume increase. Not only could this upward movement affect delicate instrumentation or cables that pass through the ice, but in ice measurements such as temperature or salinity need to be placed in such a manner as to allow upwards movement with the ice so that probe locations measured from surface level remain in a fixed position and no stress build up is created between upwards floating ice and fixed instrumentation.

If the experimental set-up does not maintain free-floating ice, a pressure relief pipe or mechanism is required to prevent excess stress on the tank walls. This also prevents an unnatural pressure build up beneath the ice that would result in a reversal of the brine drainage phenomenon and subsequent flooding of the ice surface with brine (Style and Grae Worster, 2009). Systems with capped, top down cooling plates cannot, by default maintain free floating ice and so make use of pressure relief pipes. Cox and Weeks (1975), Notz et al. (2005) and Schulson et al. (2015) used such a system, and included a simple pipe connected at the bottom of the tank to allow pressure relief. No valve is required, since as long as the height of the relief pipe is above the water surface, no drainage will occur. The water head will increase above ice level to equalise pressure as the ice grows downwards. The exact same system of pressure relief has been used in open tanks where the ice is constrained against the tank walls such as in Figure 2.16 in the set-up of Weeks (1962).

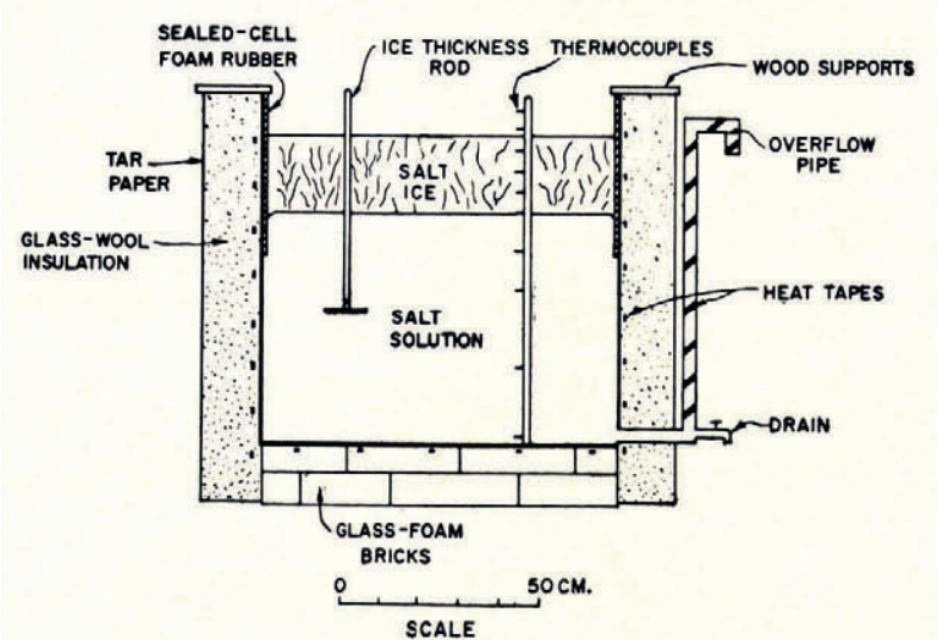

Figure 2.16: Weeks (1962) experimental set-up showing pressure relief pipe on the right side of the tank

The overflowing water in the pressure relief pipe is routed into a secondary tank or basin. It is crucial that this pipe is insulated, to prevent freezing and subsequent blockage of the pressure relief pipe (Schulson et al., 2015; Weeks, 1962). Weeks (1962) found that insulation was insufficient to prevent freezing of the pressure relief pipe, and used a heated wire wrapped around the pipe to the draining solution liquid. Roscoe et al. (2011) believes that the only system capable of preventing any pressure build-up, is a system introduced by Style and Grae Worster (2009). This system made use of a collapsible bag placed at the bottom of the tank. This bag was filled with methanol, which will remain liquid despite the temperature, and connected to an external reservoir, allowing full control and adjustment of the pressure. However, Roscoe et al. (2011) did not use the aforementioned system. Rather, the authors introduced two systems of their own. One uses bicycle inner tubes partially inflated with air and placed at the bottom of the tank, while the other consisted of plastic envelopes filled with bubble wrap and clamped to the tank walls slightly below ice growth. The second method was found to better minimise the pressure build up. Shaw et al. (2011) used a similar air-compressible system for pressure relief in his set-up.

2.5.6 Saline Solution

The formulation of artificial sea ice requires a solution of salt and brine, ideally a solution that mimics the natural sea water found in the polar regions. The simplest method of doing this is through the use of natural sea water, and has been used by researchers such as Nomura et al. (2006) and Weissenberger et al. (1992). However, as noted by Weeks and Cox (1974), this can be expensive if one is located far from the coast. Additionally, the surface salinity of seawater in the polar regions is known to be in the range of 30 - 33 g kg^{-1}, which may be different to the region where the seawater is collected from. A further complication when using natural sea water is that small tanks require a lower starting salinity to obtain the same natural salinity of sea ice (Schulson et al., 2015). This is due to the brine drainage from the newly grown ice increasing the salinity of the underlying solution. Therefore, using natural sea water would still require the measurement of the salinity and subsequent dilution with deionised water to bring it down the the required starting salinity.

To overcome the concerns of using natural seawater, one can formulate the saline solution using deionised water and salts. Deionised water is used so that the water does not add any additional undesired components to the system. Some experimental set-ups have used single component salts, such as NaCl for the formulation of their saline solution (Weeks, 1962). The NaCl mass fraction accounts for over 60 % of the salts within seawater (Millero et al., 2008). Therefore, the ice formed from an NaCl solution should closely resemble the natural sea ice and has the advantage that the simple composition will aid the modelling and prediction of the variation of properties as a function of temperature and composition. If the aim is to produce ice that most closely resembles natural sea ice, the most ubiquitous method is to use synthetic sea salt mixtures commonly used in aquariums (Cottier and Wadhams, 1999; Hare et al., 2013; Marks et al., 2017; Papadimitriou et al., 2004). The exact composition of commercially available aquarium salts are readily available, allowing for an exact analysis and chemical balance on an ionic level to be performed if required.

The solution can easily be formulated to provide a lower starting salinity to account for the salinity increase experienced in smaller tanks. Typical values for the starting solution salinities range from 17.5 g kg^{-1} (Schulson et al., 2015) to 32 g kg^{-1} (Marks et al., 2017). The resultant ice salinities within these studies show a much smaller range, with the aforementioned solution salinities resulting in bulk in-ice salinities of 5 g kg^{-1} and 7 g kg^{-1} respectively. Comparing differences in parameters of the above experimental set-ups, it was not possible to establish a trend between initial solution salinities and tank parameters that led to such similar ice salinities. Schulson et al. (2015) recommends that the required solution salinity that results in natural in-ice salinities should be experimentally determined, with it varying for different experimental set-ups.

2.5.7 Seeding

The commonly quoted "freezing point" of saline solutions refers to the thermodynamically defined temperature at which ice will begin to form. In reality, a solution can remain in liquid form to a temperature lower than what the thermodynamic limit predicts (Freitag, 1999). In order for ice to form, a process of nucleation needs to occur. Figure 2.17 shows the different types of nucleation and the regions which they occur in (Randall et al., 2009).

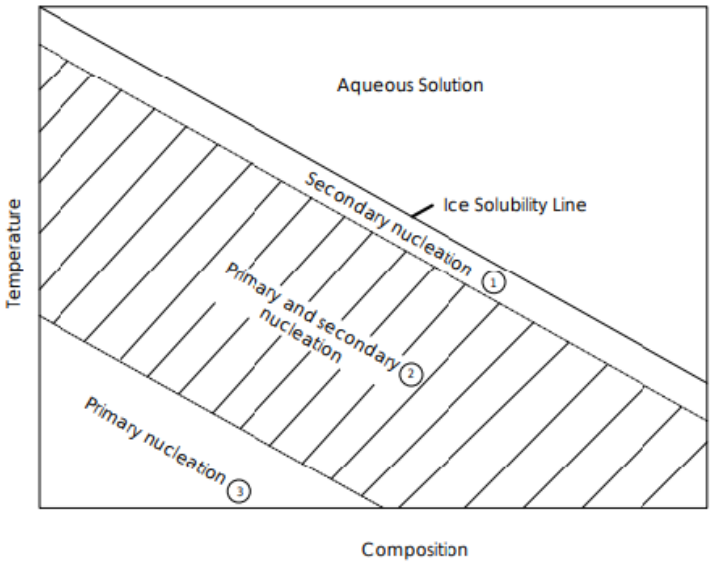

Figure 2.17: Nucleation categories and their regions in a supercooled solution (Randall et al., 2009)

Nucleation can take place as either primary or secondary nucleation. Primary nucleation refers to the spontaneous nucleation of ice from solution, and takes place unpredictably at temperatures much lower than than the thermodynamically predicted crystallization temperature. Secondary nucleation involves the addition of a small amount of ice crystals into the solution, providing a site for ice nucleation. Secondary nucleation is possible within a very small degree of supercooling. This process of adding small amount of ice crystals, or parent material is known as seeding (Randall et al., 2009). The formation of natural sea ice commonly occurs through a natural process of secondary nucleation from readily available heterogeneous nuclei (Weeks, 2010). Tucker III et al. (1987) reports that an absence of this natural seeding has been found to occasionally occur on lakes and in Arctic melt ponds. In these instances, it was found that the dominant ice form was large crystals orientated with a vertical c-axis. This is contrary to natural sea ice where the c-axis is orientated horizontally (Weeks and Ackley, 1986). Therefore, in artificial sea ice, where the natural secondary seeding is not present, it is common to artificially seed the solution at the predicted freezing point to promote columnar ice growth and control grain size (Cottier and Wadhams, 1999; Golding et al., 2014; Kim et al., 2006). This has been accomplished using two methods. Spray seeding was used by both Cottier and Wadhams (1999) and DeFranco and Dempsey (1991), where a spray bottle of supercooled deionised water is sprayed over the water surface. The water droplets crystallise upon contact with the cold ambient air and provide ice seed for nucleation to occur. Another method is crush ice made from deionised water and pass it through a sieve with a fine mesh size (Barrette and Jordaan, 2001; Golding et al., 2014).

2.5.8 In-Situ Measurement Systems

Since one of the greatest advantages of laboratory grown sea ice is the ability to measure and record the entire growth history the ice, the in-situ measurement systems are of paramount importance. Measurements taken during ice growth are important for later characterization and recording of ice history, in order to contextualise results (Schwarz et al., 1981). This subject is

undoubtedly where the early paper by Cox and Weeks (1975) is most in need of an update. The advance in technology and the introduction of the microprocessor has enabled a whole host of measurement capabilities that would have previously been unobtainable, inaccurate or very expensive. Products such as micro-controllers and microcomputers have enabled the design of powerful, yet cheap logging systems to be designed, with 3D printers providing a simple and quick path for custom fabrications (Rabault et al., 2019). Pearce (2014) is very descriptive on both the philosophy of open source design as well as providing explanations for how to take advantage of the aforementioned technologies to easily design measurement systems with only a basic understanding of electronics and coding. Commercially available dataloggers such as the systems used by Wiese et al. (2015), Notz (2005), or Eicken et al. (2000) provide off the shelf systems capable of reading either analogue or digital signals from probes such as temperature, salinity, pressure, current or wind speed and log these measurements either independently or through coupling to a computer. These systems provide fairly accurate results for most purposes, with temperature accuracies of ± 0.2 °C.

2.5.8.1 Temperature

Temperature is one of the most important variables to record during ice growth. With many of the ice properties such as growth rate, brine volume, and its strength strongly dependent on temperature, a record of temperature enables a good description of the history of the ice, which allows for a better understanding of its properties. Haas (1999) remarks that the ability to so easily record this temperature history is one of the greatest advantages of artificial sea ice growth. Temperature of both the underlying solution and the in-ice temperature can be measured using one of three popular probes types, depending on the property of interest and the degree of accuracy required. These probes are thermocouples, thermistors and Resistive Temperature Detectors (RTD's). A comparison between the properties of the three probe types is shown in Table 2.3.

Table 2.3: Comparison of Thermistor, RTD and Thermocouple properties taken from Omega (2019) and a survey of their previous uses in artificial sea ice-systems

	Thermistors	RTD's	Thermocouples
Range	-100 °C to +325 °C	-200 °C to +650 °C	-200 °C to +2300 °C
Accuracy	0.05 °C to 1.5 °C	0.1 °C to 1 °C	0.5 °C to 5 °C
Passive/Active	Active	Active	Passive
Footprint/Size	Small	Moderate	Large
Stability	0.2 °C a^{-1}	0.05 °C a^{-1}	Variable
Linearity	Exponential	Linear	Non-Linear
Response Time	0.12 s to 10 s	I s to 50 s	0.12 s to 10 s
Cost	Low to moderate	High	Low
Previous Use Cases	Cottier and Wadhams, 1999 Eide and Martin, 1975 Haas, 1999 Kawamura et al., 2006 Kotovitch et al., 2016 Lake and Lewis, 1970 Maus and De La Rosa, 2012 Notz, 2005 Perovich and Grenfell, 1981 Roscoe et al., 2011 Thomas, 2018 Wiese, 2012	Barrette and Jordaan, 2001	Galley et al., 2015 Marks, 2017 Nomura et al., 2006 Shokr et al., 2009 Weeks, 1962

The most common probe type used for temperature measurement in artificial sea ice set-ups is a thermistor. Thermistors contain a ceramic or polymer resister that has an exponential and well-known relationship with temperature (Texas Instruments, 2019). These can be either have a Negative Temperature Correlation (NTC) or a Positive Temperature Correlation (PTC), with NTC thermistors being the most common (Omega, 2019). Thermistors are active components, requiring an excitation current or voltage to be applied over the resistor and the resultant voltage drop being used to determine the resistance and thus temperature. Considering the properties of the resistors shown in Table 2.3, one can see the reason for their popularity. The high accuracy, and fast response time means that temperature fluctuations can be closely tracked. Combined with their small physical size, thermistors have even been used by Lake and Lewis (1970) to track brine movement by analysing temperature fluctuations occurring at precise location points within ice. It is common to find systems with upwards of 30 thermistors for measurement, easily accomplished due to their simple circuit design and low cost (Garnett et al., 2019; Roscoe et al., 2011; Wiese, 2012). Unfortunately thermistors do experience drift over time, in the region of 0.02 °C a^{-1}. They therefore require frequent calibration to ensure their measurement accuracy (Garnett et al., 2019; Wiese, 2012).

RTD probes consist of a fine metal wire wrapped around a ceramic or glass core. The wire is most often platinum, since it has a well-characterised resistance/temperature relationship. The length of this wire is chosen so that the probe has a very precise, known resistance at 0 °C. They are also active components, requiring an excitation current/voltage. However, the resistances of RTD's are usually higher than thermistor resistances, and the relationship to temperature is linear rather than exponential. The higher resistance requires a higher excitation current, leading to self-heating. This is a problem with RTD probes, and the excitation current needs to be carefully chosen in order to limit the effect of self-heating (Texas Instruments, 2019). The two most common types of RTD probes are Pt100 or Pt1000 probes. The PT stands for platinum, and the "100" or "1000" indicates the known resistance in ohms at 0 °C. RTD's are not commonly used, with only Barrette and Jordaan (2001) advocating their use. This is probably due to their complicated additional circuitry requirement and high cost (Omega, 2019). They also have long response times, taking between 1- 50 seconds to respond to temperature changes. However, they can be an accurate, with class A Pt100's rated to an accuracy of $\pm$ 0.15 °C. In addition, their measurement is highly stable over time, with a drift of just 0.05 °C a^{-1}.

Thermocouples are passive components, consisting of two wires of different metals joined together at the measurement end. Temperature can be measured due to the Seebeck effect; when the open and closed ends are at different temperatures, a small voltage is generated between the two wires at the open end (Siren et al., 2001). Thus, by measuring the voltage difference and the temperature at this junction point, the temperature at the measurement end can be calculated (Texas Instruments, 2019). The benefits of thermocouples are that their simple and robust design allows for measurement across a large range of temperatures (Omega, 2019). Thermistors themselves are extremely simple, consisting of the simple two-wire pair with one end fused. The measurement circuit is somewhat complicated due to the required thermistor or RTD at the junction point for reference temperature, however, only one such reference probe is required

regardless of the number of thermocouples need to be measured. This advantage was put to use by Galley et al. (2015), Marks et al. (2017) and Shokr et al. (2009), with their measurement systems consisting of more than 30 thermocouples each. However, the additional temperature measurement adds inaccuracy to the system and thus the associated error is $\pm$0.5 °C at best (Omega, 2019).

2.5.8.2 Salinity

The measurement of salinity is just as important as temperature, since the combination of temperature and salinity combined is what determines the freezing point of seawater and brine solutions and the properties of the sea ice (Cottier and Wadhams, 1999).

Salinity is commonly calculated by measuring the conductivity and temperature, using the Practical Salinity Scale developed in 1978 (PSS-78). This method measures the conductivity and compares it to the conductivity of a solution of potassium chloride (KCl) where the mass fraction of KCl is 32.4356 x 10^{-3}, at a temperature of 15 °C and pressure of 1 bar (Lewis and Perkin, 1981). This solution gives the conductivity of seawater of exactly 35 g kg^{-1}. Ideally, the measured sample should also be at a temperature of 15 °C but that is not always possible. The temperature measurement allows for an adjustment to be made, such that measurements can now be taken at temperatures between -2 °C and 35 °C (Lewis and Perkin, 1981).

In-situ solution salinity has been measured using a number of different methods. The most common method is the use of a CTD, an oceanographic instrument array that measures conductivity, temperature and pressure (Cottier and Wadhams, 1999; Garnett et al., 2019; Wiese, 2012).. These are precise, commercially available instruments, providing a very accurate measurement of the solution salinity and temperature which can be used to calibrate the measurements of temperature and solution for other instruments within the solution (Garnett et al., 2019; Wiese, 2012). Another method to measure in-situ solution salinity is the use of small sampling tubes placed at the desired measurement location (Garnett et al., 2019; Notz, 2005). These tubes are then run to outside of the tank, where a syringe can be used to suck up a sample that can then be measured using a portable conductivity meter or a salinometer to determine salinity. While simple and low cost, this method requires the sample lines to be kept heated to prevent ice formation and requires the extracted volume to ideally be added back into the system so as not to have any undue effects (Garnett et al., 2019). The simplest solution is that recommended by Weeks and Cox (1974). If the solution is well mixed during ice growth, and at constant pressure, the solution can be assumed to be at freezing point and thus salinity can be calculated using the linear temperature-salinity relationship (Figure 2.8). While very simple, it does involve a number of assumptions such as the absence of supercooling or ice formation at the measurement point and can only be used once ice formation has begun.

Unlike temperature, the measurement of salinity becomes much more difficult in ice than in the underlying solution (Notz and Grae Worster, 2008). The ice inhibits both sample line and conductivity measurements. The salt content in the ice is also concentrated within brine channels and pockets, surrounded by pure ice (Weeks and Ackley, 1986). This further complicated measurement methods. Cox and Weeks (1975) presents a method that used radioactive tracer added to the initial saline solution. By using a scintillation detector, the location and relative

concentration of the brine within the ice could be determined. A concern with this method are the additional safety concerns and precautionary measures instigated by the radioactive element. Another non-intrusive detection method is presented by Aussillous et al. (2006), who placed a freezing vessel containing sucrose solution into an MRI machine. The liquid sucrose solution produces a vastly stronger signal than the solid ice, allowing for the detection and concentration of brine within the ice to be measured. The disadvantage of the MRI measurement system is that the strong magnets prohibit the use of any metal, which makes temperature measurement very complicated. Notz and Grae Worster (2008) notes that the disadvantages to both these systems is that their complicated and delicate measurement systems do not allow such methods to be used in the field. The salinity harp (Figure 2.18) developed by Notz et al. (2005) has become the instrument of choice for in-situ salinity measurement (Eicken et al., 2010; Garnett et al., 2019; Wiese et al., 2015).

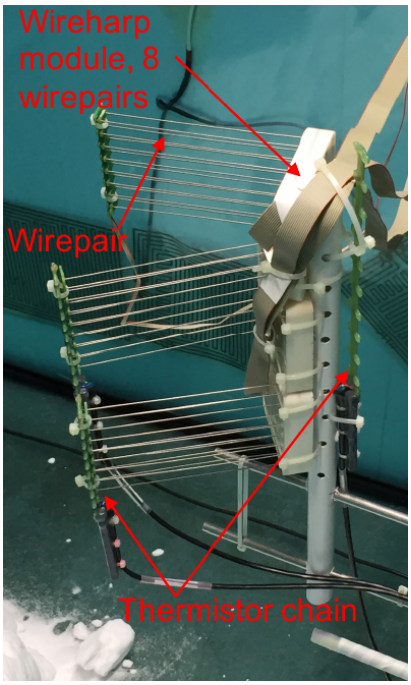

Figure 2.18: Salinity Harp developed by Notz (2005) in operation in the experimental set-up of Garnett et al. (2019)

The salinity harp consists of a vertical array of platinum wire pairs that are closely spaced horizontally. The conductivity between each wire pair can be measured, with a temperature sensor at the same point allowing a conversion to salinity. Notz (2005) explains that the measurement of conductivity is possible despite the insulating effect of the surrounding ice because the wire lengths are longer than the typical ice grain size, allowing the conductivity through the interstitial brine channels to be measured, and the resultant inhomogeneities of the brine distribution to be averaged out.

In absence of an in-situ method, the in-ice salinity can be measured only at the end of the experiment, by removing an ice sample, cutting it into vertical sections and melting each section down before using a portable conductivity meter or salinometer to to measure the bulk salinity of the melt (Weeks, 2010). The advantage of this method is in its simplicity and that the temperature

profiles of the ice will in no way be affected by the placement of materials with different thermal properties into the ice, as experienced by Wiese et al. (2015). In addition to the loss of the temporal evolution of the in-ice salinity profile, this method's primary drawback is the loss of brine during extraction, which affects the accuracy of the result (Notz and Grae Worster, 2008).

2.5.8.3 Ice Depth

Measurement of the ice depth is important so as to determine the ice growth rate as well as to determine the end point of the freezing experiment. It is noted by Weeks and Cox (1974) that the salinity of the underlying solution gradually increases as the ice depth increases, with a recommendation that the ice depth should never exceed 50 % of the tank depth. However, more recent artificial sea ice growth experiments are seldom continued to more than 20 % of the tank depth (Cottier and Wadhams, 1999; Hare et al., 2013; Wiese et al., 2015). The simplest method of measuring ice depth is by visual inspection. This is method can be used if the tank is made of transparent material such as glass or plexiglass (Wiese et al., 2015). A removable square of the insulation can be cut, allowing for a measurement to be taken using a ruler stuck to the side of the glass. However, if the tank is opaque or the insulation cannot easily be removed, then an equally simple method is presented by Weeks (1962), where a metal rod with cross bar was frozen into the ice. The rod could be heated to enable it to slide freely within the ice, and by pulling the cross bar up to the underside of the ice surface, a measurement of ice depth could be obtained. The instrument designed by Notz et al. (2005) described in Section 2.5.8.2 also allows for the measurement of ice depth and records the data continuously, allowing a greater resolution of the data and without requiring human input.

Feltham et al. (2006) also mentions that the linear temperature profile within sea ice provides a reasonable approximation up to depths of 0.8 m. This linear trend is seen in artificial sea ice as well, with temperature being used by Marks et al. (2017) as a means of continuous ice depth approximation.

2.6 Literature Informed Design Route for Artificial Sea Ice Growth

A review of literature provided a detailed understanding of sea ice properties and the underlying growth processes. However, it has been identified that the initial stages of sea ice growth within the Antarctic MIZ are still relatively unknown and express a large degree of variation in their properties (Doble et al., 2003).

It was additionally highlighted that sea ice studies are greatly supplemented by the use of artificial sea-ice set-ups to allow greater control over the input variables as well as with a higher degree of repeatability (Haas, 1999). There are high costs and risks involved in the collection of sea ice samples (Weeks and Cox, 1974), especially within the harsh sea conditions within the Antarctic MIZ during winter. Therefore, artificial sea ice set-ups allow for a larger sample group for studies. These studies could be on the effect of metocean conditions on physical or mechanical properties of the sea ice. Previous studies of artificial sea ice mostly focussed on the growth of artificial columnar S2 sea ice, since it is the most prevalent form of naturally occurring

sea ice (Timco and Weeks, 2010). The relatively simple growth conditions allow for consistent ice growth properties over multiple experiments (Haas, 1999). Studying artificial columnar sea ice provides an opportunity to begin to understand the simple growth mechanisms experienced during the growth for a variety of sea ice types. Thereafter the effects of additional variables such as turbulent conditions and high winds as experienced within the Antarctic MIZ can be incorporated.

An analysis of previous studies of artificial sea ice provided direction for the key properties that need to be focussed on in order to create saline ice that can be termed as artificial columnar S2 sea ice. It was found that other than one early review paper on the growth of artificial sea ice by Weeks and Cox (1974), there is a lack of published resources that detail the design aspects for the equipment required for the growth of artificial sea ice. Papers primarily describe the simulated metocean conditions used for the growth of artificial sea ice, with less detail given on the equipment and instrumentation. An exhaustive analysis of literature resulted in a coalition of the key design features, components and instrumentation of a system for the growth of artificial sea ice. These are as follows; freezing method, tank, water circulation, pressure relief, saline solution, ice seeding and the in-situ instrumentation for temperature, salinity and ice depth measurements. The aforementioned aspects of an artificial sea ice growth tank system are investigated within the scope of this project for the growth of artificial columnar S2 sea ice.

3 Design Objectives and Experimental Aims

The Polar Engineering Research Group at the University of Cape Town has a 6 m x 3 m mobile cold laboratory which was commissioned for the analysis and testing of Antarctic sea ice. Coupled with testing of the natural sea ice, there is a need to grow and test artificial sea ice as it allows for tighter control of the growth conditions and a detailed history of the ice growth to be recorded. The overall aim of this project is to design and test a small-scale system for the growth of artificial sea ice. There is a precedent for such systems, using air-cooled refrigerated rooms for artificial sea ice growth such as the systems described by Wiese et al. (2015), Light et al. (2015) and Marks et al. (2017). The designed system will be used for method development of testing protocols for the Antarctic sea ice. It will also enable controlled studies of specific sea ice properties, studied in isolation under repeatable conditions. This will enable the determination of sea ice properties such as crystal size and orientation, brine volume and internal ice structure as well as mechanical properties such as compression strength, elastic modulus and poisson's ratio.

The properties of Arctic and Antarctic sea ice are known to be different, due to the dominant environmental conditions during formation. Antarctic sea ice is also known to be more complex, with a variety of possible morphologies (Doble et al., 2003). Therefore, this system design focusses on the growth of columnar sea ice formed in the calm conditions found predominantly within the Arctic (Weeks and Ackley, 1986). While this will likely result in a different morphology to the Antarctic sea ice, it will still enable method development of testing protocols since the properties still fall within the same scale. Once this system has proven to reliably produce saline ice that can be termed as artificial sea ice with a columnar S2 structure, additional design implementations can then be undertaken to accomplish the growth of sea ice that more closely resembles the ice found in the Antarctic MIZ. The project is predominantly focussed on the system design, with a secondary component being an artificial sea ice growth experiment to assess the properties of the produced ice and determine if the system is successfully able to grow artificial sea ice.

3.1 Design Objectives

Figure 3.1 outlines the primary and secondary objectives for the design of the system, as well as the parameters that will be used to assess the accomplishment of each of the objectives. The first primary objective for the system is to produce saline ice with properties typical of columnar S2 sea ice. An experiment will be carried out at the end of the design to test the system, and the properties of the artificial sea ice will be compared to the key properties listed in Table 2.3. The second primary objective relates to the intended use of the tank for the growth of samples for the purposes of mechanical testing. Therefore, the second primary objective is that the tank is large enough to allow samples of suitable size, as well as a suitable number of samples, to fulfil the requirements outlined by Schwarz et al. (1981) for the standardized mechanical testing study.

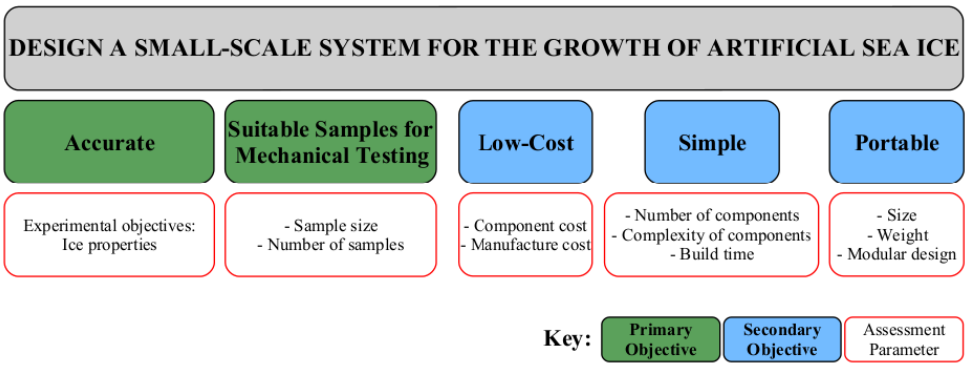

Figure 3.1: Objectives for the design of a system for the growth of artificial sea ice, as well as the assessment parameters for each objective

The secondary objectives of the design is to minimise cost, keep it simple, and also portable. The cost of the system will be minimised during the conceptual design phase where each concept variant and possible component choice will be assessed using both component cost and manufacture cost as a factor. Simplicity of design will be assessed by the number of components, the complexity of each component, and the build time of each sub-assembly. The system needs to be portable since laboratory space is limited, and there may be occasions where the system needs to be removed to make space for other projects. Thus, the size and weight shall be minimised while still ensuring the system accomplishes its primary aim of producing samples of sufficient size and quantity to be used for mechanical testing in future projects.

3.2 Experimental Aims and Key Questions

The overall aim of the experiment was to confirm that the freezing tank system designed above does produce saline ice with the properties that allow it to be termed ”artificial columnar S2 sea ice” as seen in Table 2.1. This was tested using the following methods:

- Temperature probe strings located within the tank to record the temperature of the ice and underlying solution.
- Sectioning and melting of ice samples taken at the end of the growth experiment to determine an in-ice salinity profile.
- CT scanning of ice samples to analyse the ice crystal morphology and the brine channel distribution.

Several key questions were identified to assess the experimental aim and the above parameters:

- Does the ice experience the same linear temperature profile seen in Arctic sea ice?
- What is the rate and model ft for the ice growth rate of the saline ice?
- Does ice crystal morphology of the saline ice compare well with that seen in columnar sea ice?
- Are the brine inclusions located within intracrystal, vertically orientated planes as seen in columnar sea ice?

4 Methodology

4.1 Freezing Tank System Design Procedure

The design procedure of the freezing tank system shall be carried out using the design process laid out by Pahl et al. (2007). This design process is summarised graphically in figure 4.1.

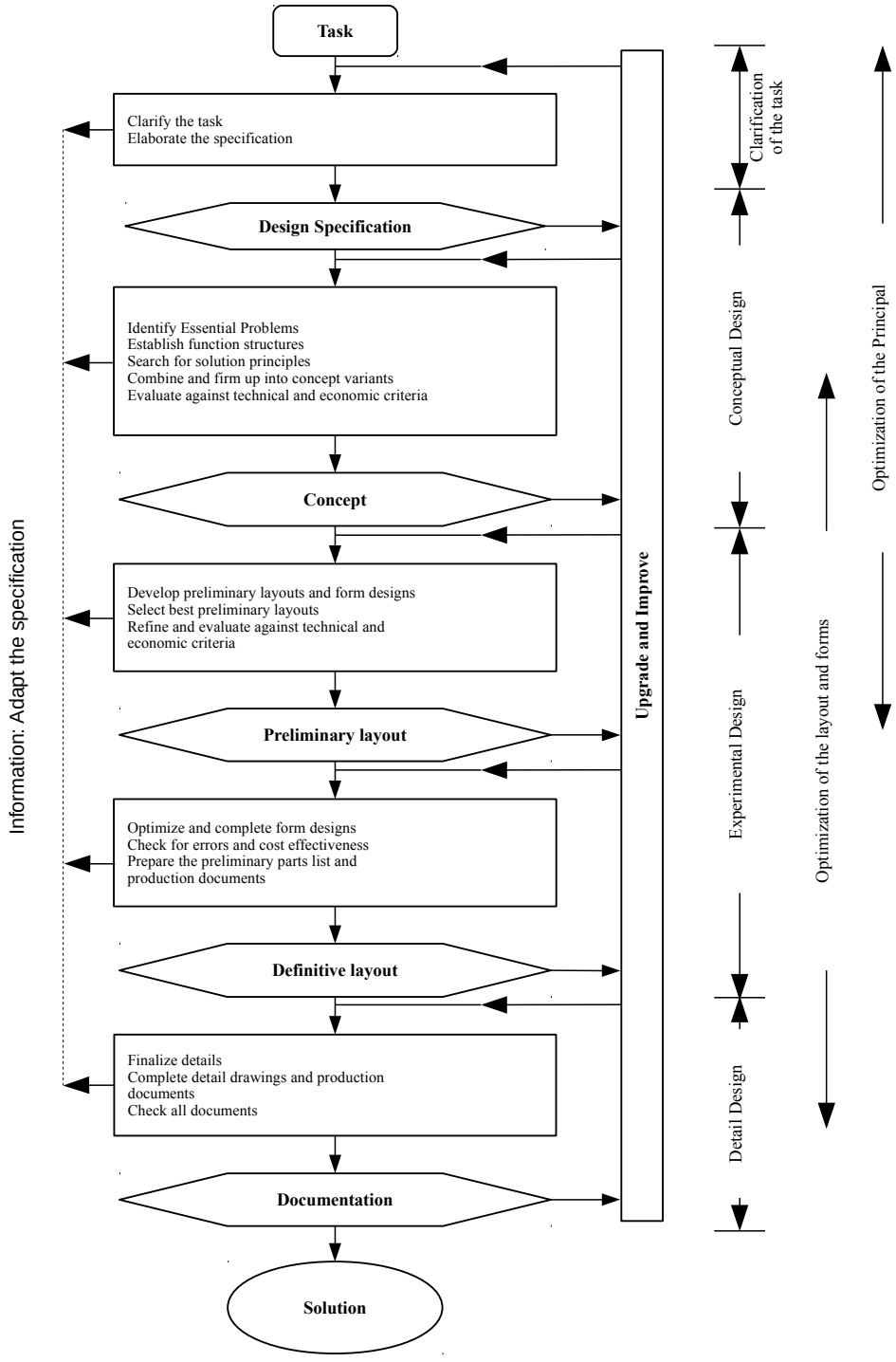

Figure 4.1: Design Process Pahl et al. (2007)

The task clarification, design objectives and elaboration of the specifications are elaborated in Section 3.1. The system can be broken down into sub-systems, each of which required individual detailed design. From the literature research, the following sub systems shown in Figure 4.2 are required to make up the freezing tank system to produce the desired artificial columnar S2 sea ice.

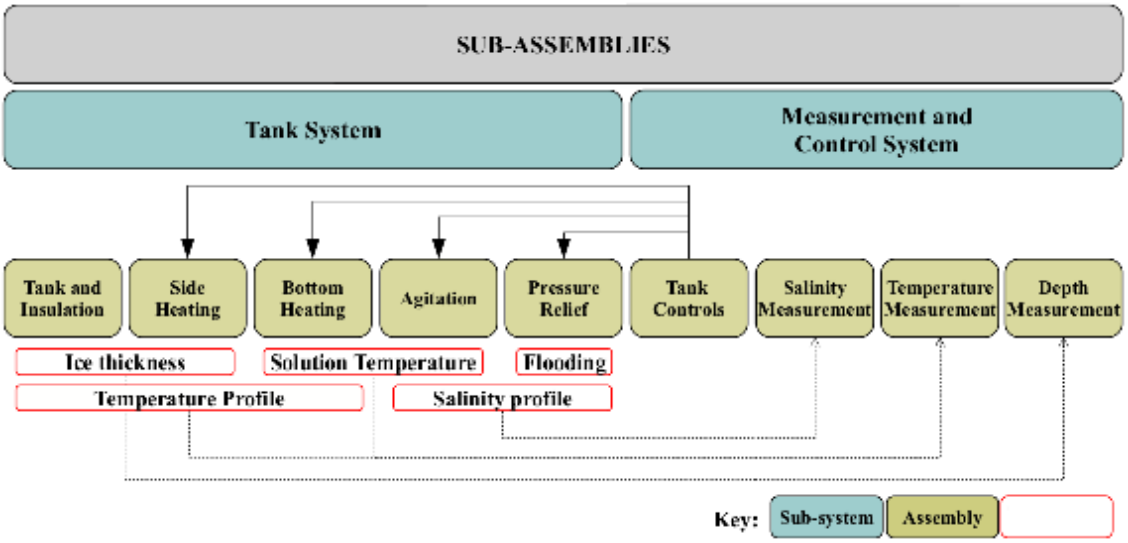

Figure 4.2: Artificial columnar S2 sea ice system sub-assemblies displaying their interlinkage and corresponding assessment parameters

The system design can be broken up into two systems; the freezing tank system which includes the tank and insulation, side heating, bottom heating, agitation and pressure relief, as well as the measurement and control system which includes controls for the tank system and measurement systems for salinity, temperature and depth. The initial design work shall be focused on analysis of concept variants as found through literature research. These variants shall be evaluated against the design objectives using a decision matrix method (Eatas and Jones, 1993). This method places all possible design paths in a table with columns for each of the design objectives.

For each design choice, a rating is assigned against each design objective, according to how well it fulfils it. Each design objective can be weighted differently according to its priority. These results can be tallied for each design choice, and the design choice with the highest total fulfils the objectives best. The chosen concept variants will become the design concept, with detailed specifications of each sub-assembly. Each sub-assembly will require evaluation to determine whether it works successfully. The assessment parameters shown in 4.2 shall be used to assess the functionality of the chosen each sub-assembly. These assessments will be carried out at a modular level, enabling the performance of the sub-assembly to be assessed in isolation before being added to the system. Once the system design is complete, an experiment of artificial sea ice growth will be carried out, as proof of design concept.

4.2 Proof of Design Concept: Artificial Sea Ice Growth Experiment

4.2.1 Experimental set-up

The proof of design concept experiment was carried out in the freezing tank designed according to the methodology presented in 4.1. The experimental set-up is shown in Figure 4.3.

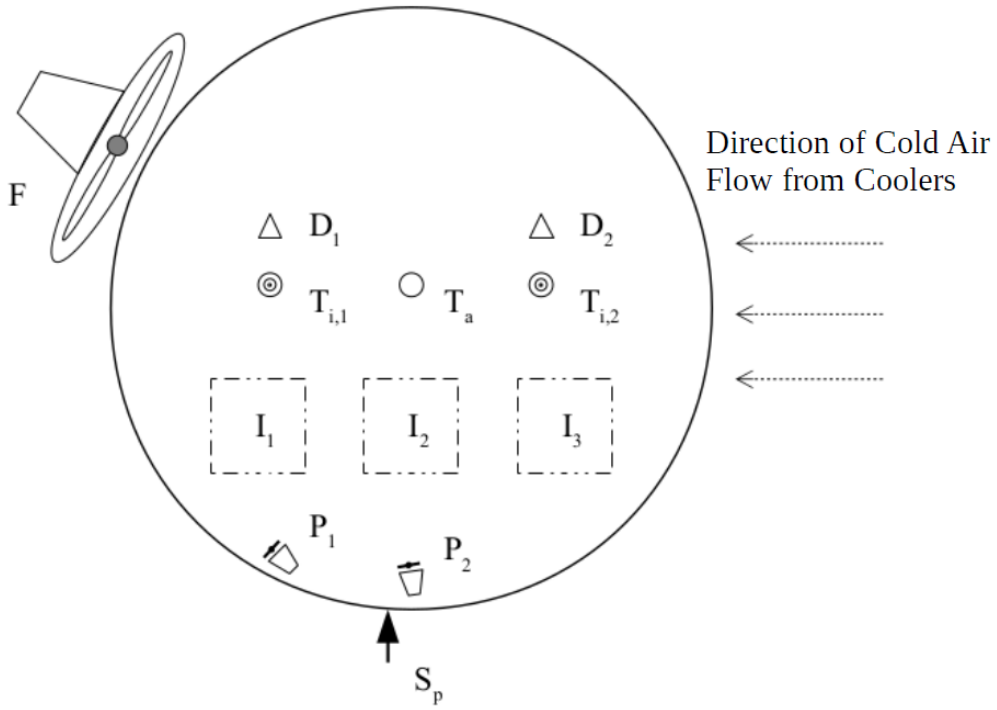

Figure 4.3: Schematic of experimental set-up, showing locations of fan (F), pressure relief pipe (S_p), Pumps (P_{1-2}), manual ice depth measures (D_{1-2}), in-ice temperature chains ($T_{i,1-2}$), ambient temperature (T_a) and ice samples (I_{1-3})

The direction of cold air flow shows the location of the cooling unit to the right of the tank, such that predominant cooling was from this direction. In order to equalise this, a fan was placed from the opposite direction, providing constant air flow of 12 m s^{-1} over the tank surface. Aquarium pumps were located at a depth of 45 cm and 70 cm, with P_1 at a depth of 70 cm located tangentially to provide tangential mixing as described by Timmons et al. (1998). P_2 at a depth of 45 cm was directed radially, on a pulse cycle to create turbulence and introduce random flow to prevent S3 ice growth and counteract the formation of dead zones that may occur from tangential flow patterns (Timmons et al., 1998). Pump flow rates were set to 100 dm^3 h^{-1} for P_1 and 50 dm^3 h^{-1} for P_2. Ambient temperature was measured 1 cm above the solution surface. The ice temperature was measured with two temperature chains shown at position $T_{i,1\&2}$. These chains consisted of 8 temperature probes, at depths of 1 cm, 3 cm, 5 cm, 8 cm, 13 cm, 18 cm, 25 cm and 30 cm. Further probes were located at 45 cm and 70 cm, to measure solution temperature. All temperature probes were class A Pt100 (± 0.15 °C) and connected to Campbell Scientific CR5000 datalogger. The measurement accuracy of this system was $\pm$0.2°C. Temperature was recorded every 6 seconds, with the values averaged over 5 minute intervals, and only the 5 minute average values being stored. The pressure relief pipe was located at the position indicated by S_p, at 70 cm. Water samples were taken from this pipe and used to measure solution salinity.

A secondary 500 dm^3 tank in the cold laboratory was used to mix the artificial seawater solution. 370 l of deionised water was placed into the tank, and 10.36 kg of aquarium seasalt (Aquaforest Sea Salt) added to make up a 28 g kg^{-1} solution. Aquarium pumps were used to mix the solution for 12 hours to dissolve the salt. The conductivity and temperature of the solution was measured using a conductivity meter (AZ instruments, model 8301 - Conductivity accuracy of ± 2 µS cm^{-1}, Temperature accuracy of ± 0.6 °C). This was converted to a value for salinity using the PSS-78 standard (Lewis and Perkin, 1981). During this time, the temperature was set to 4 °C, pre-cooling the solution. The saline solution was transferred to the freezing tank and the room temperature was set to -10 °C. The bottom heating was set to -1.6 °C, the freezing point of a 28 g kg^{-1} solution. Side heating was set to a rate determined iteratively during the initial system design to prevent cooling from the side of the tank. Pressure relief pipe heating was turned on to prevent freezing. The pumps were set to maximum flow rate of 260 dm^3 h^{-1} to ensure fast mixing and prevent ice growth. Once the solution was at freezing point, the room temperature was set to -20 °C and the pumps were decreased to a flow rate of 100 dm^3 h^{-1}. The solution surface was seeded with ice crystals according to the method by Golding et al. (2014). Ice growth was allowed to continue for 160 hours with data collection occurring every 2 days. Salinity samples from the pressure relief were taken at the same time. Further entry to the cold lab was limited in order to prevent temperature fluctuation. Once ice depth had reached 25 cm, the room temperature was set to -10 °C for ice sampling.

Ice sampling was carried out at 3 points within the ice tank, as shown by I_{1-3} on Figure 4.3. Power to the tank system was turned off. Holes were made with a wood auger bit (l=30 cm, dia=2 cm) attached to an electric drill at the four corners of a sample location, creating a square outline of 10 cm. A saber saw was inserted into the holes and used to cut the sample clear. A ”U” shaped wire was inserted under the ice and used to lift the sample clear.

Cottier and Wadhams (1999) describes a method for ice sampling to limit the brine drainage that occurs during sample removal. The method involves the cutting of a hole located adjacent to the desired sample location. A container with a removable plug can be inserted through this hole and placed underneath the sample. The sample and the container can then be removed together, with the container retaining the underlying solution and preventing brine drainage from the sample. The captured solution is allowed to drain through the plug hole in the container until the sample is floating just above the container bottom. Then the plug is replaced and the container with sample and solution can be placed in the freezer at -20 °C. This will freeze all of the surrounding solution, and the entrapped brine, preventing its escape. The sample can then be processed and analysed, with the frozen solution easily due to its composition and structure distinguished from the original sample (Garnett et al., 2019). Unfortunately, due to the size of the tank, the above method could not be used, since the creation of lateral holes to allow the bucket to be inserted would result in the destruction of too large an area of ice, thus limiting the number of samples available for study. Previous studies suggest that the above method does not reliably result in greater brine retention than sampling without the container (Thomas et al., 2020). The chosen method of collecting ice samples sans container is still used extensively (Galley et al., 2015; Golding et al., 2014; Marks et al., 2017; Schulson et al., 2015; Wiese et al., 2015).

4.2.2 Ice Analysis Techniques

4.2.2.1 Bulk Ice Salinity

The bulk salinity refers to the average salinity of the entire ice sample. This includes both the pure ice component and highly concentrated brine located in the brine channels (Weeks and Ackley, 1986). Two samples from each of the three sample points were used to assess the salinity distribution and variation as a function of ice depth. The samples consisted of rectangular sections roughly 3 cm x 6 cm in length and width with a vertical height of the total ice depth. These were sectioned vertically into 2 cm blocks using a handheld cross cut saw. The saw was wiped after every cut, to avoid any cross-contamination of brine volume into other sections. Each cut section was placed in a sealed plastic container and labelled with sample location and section height. The plastic containers were placed in a room at ambient temperature and allowed to melt overnight. The salinity of the solution was measured using the handheld conductivity meter and converted to salinity using the PSS-78 standard (Lewis and Perkin, 1981).

4.2.2.2 Computerized Tomography (CT) Scan

A CT Scan combines data from an array of X-ray images to build a 3-D image of the density distribution of a substance. This is a non-intrusive method, allowing a large sample to be analysed without disturbance to its internal structure. Golden et al. (2007) used X-Ray CT on laboratory grown sea-ice single crystals to track thermal evolution of the pore structure. Figure 4.4 shows a sea ice crystal with a brine volume of 0.033 cm^3 dm^{-3}.

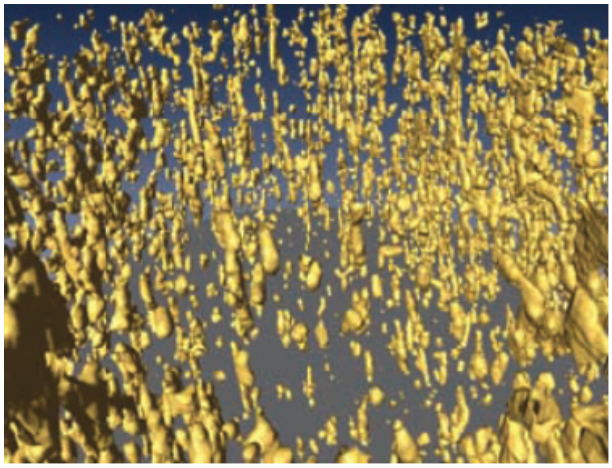

Figure 4.4: X-Ray CT Image of Brine Microstructure for making up total brine volume of 0.033 cm^3 dm^{-3} (Golden et al., 2007)

The crystal was doped with CsCl to improve the brine/ice contrast. Using the images, they were able to qualitatively correlate the relationship between temperature, porosity and brine channel interconnectivity. This technique is particularly useful in analysing small scale intra-crystalline brine layer connectivity and its evolution with temperature.

For the purposes of ice texture and fabric analysis, a simple and popular method is the use of cross-polarised imaging on a universal stage (Cottier and Wadhams, 1999; Crabeck et al., 2016; Schulson et al., 2015; Sinha, 1986). However, the equipment necessary for this technique was not available at the time of study and the preparation methodology had not been developed within

the research group. Due to time constraints, the procurement of the necessary equipment and development of the preparation and measurement methodology for cross-polarised imaging was deemed to be outside the scope of this study. A Phoenix v|tome|x micro X-ray CT scanner was readily available for sample analysis, and the required methodology for sample preparation was simple and well-established. Thus, an analysis of ice texture and fabric was performed using CT scanning. CT scanning is capable of resolutions allowing an in-depth analysis of the the gas volume in sea ice at bubble sizes < 1 mm (Crabeck et al., 2016). Since the desire in this study's case was to perform crystal analysis and measure the planar spacings, the desired resolution is more within the range of 0.1 - 10 cm, which is on the upper limit of the capability of CT scanning. However, through the scanning of multiple regions and constructing a cumulative image of the sample, one can use CT scanning for the purposes of crystal analysis and measurement of the planar spacings while simultaneously having good enough resolution ($<$1 mm) to enable the analysis of entrained brine (Crabeck et al., 2016).

The Phoenix v|tome|x micro X-ray CT scanner used in this study did not allow for active cooling of the sample during imaging. However, this was not necessarily cause for concern, since room temperature imaging has been used for sea ice measurements in previous studies (Crabeck et al., 2016; Galley et al., 2015).In addition, it is known that temperature changes primarily affect the brine volume and pore spaces (Golden et al., 2007; Pringle et al., 2009; Eicken et al., 2000). Light et al. (2003) found that ice crystals are much less affected even by temperature changes from -30 °C to -2 °C. Since focus of these measurements is on ice texture and fabric analysis, it leaves room for a fairly large temperature increase to still be acceptable. However, a number of measures were taken to reduce temperature effects on the ice. The samples were insulated with bubble wrap, felt and polystyrene to maintain their sub-zero temperatures, the scan times were limited to under 20 minutes to reduce exposure to room temperature conditions, and the temperature of the sample was measured before and after scanning to ensure that the temperature change was under 2 °C within the ice sample.

Ice samples taken from the artificial sea ice growth experiment for CT scanning were wrapped in felt and bubble wrap for insulation and stored at -20 °C. CT Scanning was conducted using a Phoenix v|tome|x micro X-ray CT scanner. Prior to CT scanning, samples were taken out of the freezer and allowed to slowly warm to a temperature of -5 °C. Cox and Weeks (1986) theorise that storage at temperatures lower than -20 °C and subsequent reheating to the original temperature will return the ice structure to its original state. Thus, scanning at -5 °C was seen as a representative analysis of the brine volumes and channels experienced in natural sea ice at this temperature. The temperature was measured using a digital MT605 Major thermometer ($\pm$1 °C) by drilling a small hole through the insulation. When the sample was at the correct temperature, it was removed from the bubble wrap and placed in a polystyrene sample holder, which insulated the sample and limited the temperature change to under 2 °C. This sample holder was placed in the scanner. The scan duration was 16 - 19 minutes and gave a voxel size of 35 µm. Temperature was re-measured after removal from the scanner to obtain an average temperature increase during scanning. The sample was sectioned for salinity measurements in the same method described previously.

5 Freezing Tank System Design

5.1 Tank System Design

For this project, a small-scale system was designed for the growth of artificial sea ice. The system consists of two sub-systems subdivided into modules; the freezing tank system which includes the tank and insulation module, side heating module, bottom heating module, agitation module and pressure relief module, as well as the measurement and control system which includes controls for the tank system and measurement systems for salinity, temperature and depth. This design was assessed through an artificial sea ice growth experiment. Artificial sea ice was grown using an initial solution salinity of 28 g kg^{-1}, and the properties of the ice were compared to the key properties highlighted within Table 2.1 to determine the effectiveness of the system design. This section details the design process and assessment criteria for each of the aforementioned modules, as well presenting the results from the proof of design concept experiment.

5.1.1 Cooling Method

As discussed in Section 2.5.2, there are a number of freezing methods that can be used to grow artificial sea ice, namely, using environmental temperatures in regions of the world where this is a possibility, using convective cooling through the use of a temperature controlled room and chillers, and lastly using a cooling plate that has refrigerated ethylene glycol or similar coolant pumped through it. The cooling method is discussed first, since it will influence all subsequent decisions regarding tank size, insulation and heating requirements, as well as instrumentation possibilities.

To determine the optimum cooling method for the tank, a decision matrix table as described by Eatas and Jones (1993) was used. A decision matrix table assesses each possible design choice against the design objectives given in section 3. For each objective, the design choice is given a minimum score of 0 and a maximum score of 4. A different weighting can be applied to each of the objectives in order to increase its influence on the outcome. Therefore, in each case, the primary objectives received a higher weighting than the secondary objectives.

For the primary objectives of obtaining ice with properties resembling sea ice and provision of suitable samples for mechanical testing, it was decided that the cooling method needs to be able to provide cooling accomplishes three goals. It needs to provide cooling that is representative of that which occurs during high latitude winter conditions (Wiese et al., 2015) and it needs to provide cooling that is repeatable over multiple experiments (Haas, 1999). Lastly, for the purposes of mechanical testing, it is optimum to procure samples that are grown at a single, stable temperature such that the effect of temperature can either be selectively examined, or discarded as a variable (Schwarz et al., 1981). Therefore, each of the cooling methods were assessed against its ability to provide representative, repeatable and stable temperatures. Each of these primary objectives, received a weighting of 2. The secondary objectives of the design is to keep the system low-cost, simple and portable. Only cost and manufacture simplicity can be assessed for the cooling method choice, since the portability of the system will be independent of the cooling method. The secondary objectives received a weighting of 1, Therefore a total score of 32 was possible. The assessment of the three cooling methods is shown in table 5.1.

Table 5.1: Decision matrix table for the cooling method for the artificial sea ice, with the chosen method outlined in red

Cooling Method	References	Primary Objectives			Secondary Objectives		Sum
		Representative (x2)	Repeatable (x2)	Stable (x2)	Cost (x1)	Manufacture Simplicity (x1)	
Environmental	Galley et al., 2015 Hare et al., 2013 Weissenberger, 1998	3	1	0	4	0	12
Convective	Cottier and Wadhams, 1999 DeFranco and Dempsey, 1991 Loose et al., 2009 Marks et al., 2017 Roscoe et al., 2011 Weeks, 1962 Wiese et al., 2015	2	3	3	3	3	22
Cooling Plate	Cox and Weeks, 1975 Eide and Martin, 1975 Golding et al., 2014 Middleton et al., 2016 Notz et al., 2005 Schulson et al., 2015	2	4	4	1	0	21

Environmental cooling is advantageous since it precisely replicates the natural conditions under which sea ice forms. The obvious caveat to this advantage is that to achieve this, the research facility must be located in the high latitudes. The location of the laboratory at the University of Cape Town, South Africa ruled out the possibility of using natural cooling, since the climate is too mild. In addition, environmental cooling has the disadvantage of fluctuating temperatures, with the likelihood of the exact same conditions occurring for multiple experiments also being fairly low (Hare et al., 2013). Convective cooling was possible at the research group facilities, which consisted of a refrigerated shipping container with dimensions of 3 m wide, 6 m long and 2 m high similar to those used by Marks et al. (2017) and Wiese et al. (2015). This cold laboratory was capable of reaching temperatures as low as -30 °C and therefore provided an adequate cooling method for the study. It was noted by both Marks et al. (2017) and Wiese et al. (2015) that the chillers used in refrigerated containers have a defrost cycle that results in temperature increases of up to 6 °C at regular intervals. However, compared to environmental cooling, a temperature increase of 6 °C every 12 hours is considered a very small fluctuation. The temperature control allows for stable and repeatable cooling over multiple experimental runs.

In order to overcome any degree of temperature fluctuation and ensure the temperature at the ice interface is precisely as desired, a cooling plate in direct contact with the solution can be used. While this method scored very highly under the objectives of repeatability and stability, it is not a simplistic design, resulting in high cost and manufacture complexity. In addition, it does not replace the need for convective cooling, but rather complements it, since the tank is still required to be located in a temperature-controlled room at a maximum of 0 °C so that excess heat is not absorbed through the sides other than where the cooling plate is located. Additionally the cooling plate does not allow a natural ice freeboard and adds complexity to the measurement systems since they have to pass through either the cooling plate or tank sides to measure tank conditions, rather than the exposed water surface.

Therefore, for the purposes of this study, convective cooling was used as the method of artificial sea ice growth. If the additional accuracy and stability of the cooling plate method is desired at a later date, this can always be added since the addition is not affected by the design choice within this study.

5.1.2 Tank and Insulation

The first module was the tank itself. The tank was used as the vessel for holding the initial saline solution, and combined with insulation, promotes uni-directional, top-down cooling. The choice and design of the tank is the first module discussed since it influences the design of all the other modules. The first design choice to consider for the tank was the approximate size range, between the 20 dm^3 size such as that used by Notz (2005) to tanks greater than 1 x 10^6 dm^3, such as the ice tank at the Hamburg Ship Model Basin (Haas, 1999). The method of cooling chosen in Section 5.1.1 restricts this range, since the tank would be required to fit within the dimensions of the cold laboratory. The choice for the tank size was strongly influenced by the three secondary objectives of the design, to keep the system low-cost, simple and portable. The primary objectives of producing ice with properties similar to sea ice and obtaining suitable samples for mechanical testing can be achieved within a greater size range and so does not constrain the design choice.

It was decided to consider a tank within the range of 300 - 800 dm^3. Many artificial sea ice set-ups within literature fall into this size range (Light et al., 2015; Marks et al., 2017; Schulson et al., 2015; Weeks and Cox, 1974; Wiese, 2012), which provides points of reference for both the design and the resultant artificial sea ice properties. It should be possible within this size, given the volume, to obtain suitable samples for mechanical testing, and enough of them for statistical relevance. This would enable compliance with the standardization of testing protocols presented by Schwarz et al. (1981). The size should allow the system to fulfil the secondary objectives of being low-cost, simple and portable. However, this was additionally affected by the choice of materials for the tank.

A survey of literature on artificial sea ice growth systems and their tanks was undertaken, and an assessment against the design objectives was carried out. Table 5.2 shows the considered tank materials and configurations, and assessment results.

Table 5.2: Decision matrix table for tank material and configuration, with the chosen configuration outlined in red

Configurations	References	Primary Objectives		Secondary Objectives			Sum
		Surface Smoothness (x3)	Ease of Insulation (x3)	Cost (x2)	Portability (x2)	Manufacture Simplicity (x1)	
Round							
Perspex	Perovich and Grenfell, 1981 Salomon et al., 2017	4	3	1	2	1	28
Plastic	Golding et al.,2014 Marks et al., 2017 Schulson et al., 2015	3	3	4	4	3	**37**
Ready-made (Plastic M.o.C.)	Light et al., 2015	3	4	3	3	4	**37**
Stainless steel	Roscoe et al., 2011 Weeks, 1962	2	1	2	2	3	20
Square							
Perspex	Newyear and Martin, 1997	4	4	1	1	2	30
Glass	Thomas, 2018 Wiese et al., 2015	4	4	2	1	2	32

The primary objectives of obtaining ice with properties resembling sea ice and provision of suitable samples for mechanical testing cannot really be assessed just through tank configuration. The objective of samples suitable for mechanical testing was dictated primarily by tank size, which has already been discussed. Ice properties cannot be directly assessed from tank configuration, but rather how the properties of materials influence the ice properties.

The material properties that will affect the ice properties are surface smoothness and ease of insulation. Surface smoothness will limit ice adherence to the vessel side and help promote free floating ice. Ease of insulation is important to ensure one-dimensional cooling. The primary objectives were weighted more heavily than the secondary objectives, with their scores being multiplied by 3. Cost and portability were multiplied by 2, and manufacture simplicity was the classified as lowest priority, with its score having a relative weighting of 1. Therefore, a total score of 44 was possible.

Square tanks are predominantly made from glass or perspex since the shape requires stronger side walls with additional frame support. However, while glass or perspex score well for surface smoothness and ease of insulation, it was expensive and heavy, and has additional manufacture complexity. Thus, round tanks were the better option, despite the rounded sides being more difficult to insulate. Rounded perspex tanks are also expensive and heavy, and it was also difficult to obtain them in the size necessary to hold 300 - 800 dm^3. The choice of a stainless steel tank scored very poorly, at 20 / 44, since it is expensive and heavy. The thermal conductivity of the metal adds to the insulation difficulty. It is also susceptible to corrosion, even with the metal being corrosion resistant. A plastic tank was chosen as the tank configuration and material of choice. Both ready-made, such as that used by Light et al. (2015) and plastic tanks obtained the best score, of 37 / 44. A ready-made solution proved difficult to obtain and thus a plastic tank was chosen. A round plastic tank was the most ubiquitous tank configuration and material according to literature, reinforcing the design choice. Plastic tanks in a variety of sizes are readily available for applications of water storage.

A closed-top plastic tank of 500 dm^3 was bought. The top was cut off, leaving an open surface and a working volume of 400 dm^3. The dimensions of the tank are 0.8 m diameter, with a height of 0.8 m. Leaving a 10 cm gap between the tank walls and potential sample area to account for edge effects, this results in an area large enough to obtain 18 samples of 10 cm x 10 cm. These squares could be used either as they are or cut into cylinders of 9 cm diameter, as recommended by Schwarz et al. (1981). This diameter was the same as of the Antarctic ice samples obtained using the Kovacs Mark II ice corer.

It was crucial that a tank system attempting to grow ice that can be termed artificial sea ice has insulation on the sides and bottom of the tank so as to accomplish the one-directional, top-down cooling seen during natural sea ice growth (Schulson et al., 2015; Wiese, 2012). For the insulation necessary to accomplish this, flexible insulation materials similar to those used by Weeks (1962) and Marks et al. (2017) were considered. However, it was first necessary to consider the total heat transfer of the system. This would enable a comparison of the heat losses from the tank surface compared to the walls and base. Thereafter, the effect of adding insulation can be measured. Insulation will not completely negate heat loss through the sides and base of the tank, but with enough insulation, the relative rates of heat transfer compared to that from the surface would allow the heat loss from base and sides to be taken as negligible.

Using the net heat transfer equation presented in Section 2.3 by Williams (1963), but adding a term for the heat transfer through the tank walls and base gives:

$$\mathrm{Q_a} = \mathrm{Q_{co}} + \mathrm{Q_{walls}} + \mathrm{Q_{base}} + \mathrm{Q_{lw}} + \mathrm{Q_e} - \mathrm{Q_{sw}} \tag{5.1}$$

Where $\mathrm{Q_a}$ is the total heat loss from the water/ice surface, $\mathrm{Q_{co}}$ is the convective heat loss, $\mathrm{Q_{walls}}$ is the heat loss through the tank walls, $\mathrm{Q_{base}}$ is the heat loss through the tank base, $\mathrm{Q_{lw}}$ is the long wave radiation from water/ice surface to surrounds, $\mathrm{Q_e}$ is the heat loss through evaporation, and $\mathrm{Q_{sw}}$ is the heat gain through incoming short wave radiation from the sun.

It was assumed that the heat transfer through the tank base was zero. The bottom was raised from the floor on concrete blocks and 5 cm thick wooden chip board, with a 1 cm thick rubber neoprene layer between tank and wooden boards. In addition, Section 5.1.4 shall discuss bottom heating in the tank to control solution temperature. Since the system was indoors, the incoming short wave radiation and outgoing long wave radiation can be assumed as 0. Since the ambient temperature will be below freezing, the heat loss from evaporation can be taken as 0. This was not quite accurate, since it was known that ice sublimation can occur (Das et al., 2013). However, this would only occur at the ice surface, which would further separate the relative rates of heat transfer from tank surface and the tank sides. Therefore, this term can be discarded for now. Therefore we are left with a simplified expression of heat flux of the tank as:

$$\mathrm{Q_a} = \mathrm{Q_{co}} + \mathrm{Q_{walls}} \tag{5.2}$$

Where we desire $\mathrm{Q_{co}} >> \mathrm{Q_{walls}}$. The convective heat transfer can be described as:

$$\mathrm{Q_c} = \mathrm{h_0 A(T_{ice} - T_a)} \tag{5.3}$$

Where $\mathrm{h_0}$ is a bulk heat transfer coefficient, A is the surface area, $\mathrm{T_{ice}}$ is the ice surface temperature and $\mathrm{T_a}$ is the ambient temperature. Ashton (1989) provides several possible values for $\mathrm{h_0}$ while determining an alternate method of thin ice growth on cold lakes. The author recommends estimating a constant value for $\mathrm{h_0}$ based on the wind speed. He uses values of 10 W $\mathrm{m^{-2}}$ $\mathrm{K^{-1}}$ for calm conditions and 30 W $\mathrm{m^{-2}}$ $\mathrm{K^{-1}}$ for high wind conditions. This larger value was taken as appropriate for forced cooling as experienced in the cold lab, especially since a fan will be used to promote air flow, further increasing heat transfer rate.

The heat flux through the tank walls is taken as conductive, and is described as:

$$\mathrm{Q_{walls}} = \frac{\mathrm{kA(T_w - T_a)}}{\mathrm{L}} \tag{5.4}$$

Where k is the thermal conductivity of the insulation, A is the surface area, and L is the insulation thickness. Table 5.3 shows the total insulation layers used for the tank sides, including the plastic walls of the tank itself. The layers, their thicknesses and their respective conductivities are described in Table 5.3 and are shown graphically in Figure 5.1.

Table 5.3: Description of insulation layers including their material of construction, thickness and the layer conductivity

Sub-Assembly	Layer	Material	Thickness (mm)	k (W m^{-1} k^{-1})	Reference
Tank	**1: Tank**	Polyethylene Terephthalate (PET)	8	0,29	SpecialChem, 2019
	2: Rubber	Closed-cell Neoprene	10	0,05	Engineering Toolbox, 2003
	3: Foil	Aluminium	0,2	235	Engineering Toolbox, 2003
Outer Insulation	**4: Foil**	Aluminium	0,2	235	Engineering Toolbox, 2003
	5: Plastic Sheet	Low-density Polyethylene (LDPE)	0,25	0,35	SpecialChem, 2019
	6: Plastic Wool	Polyester	135	0,043	Isotherm, 2015
	7: Plastic Sheet	Low-density Polyethylene (LDPE)	0,25	0,35	SpecialChem, 2019
	8: Rubber	Closed-cell Neoprene	3	0,05	Engineering Toolbox, 2003
Total			**156,9**	**0,046**	

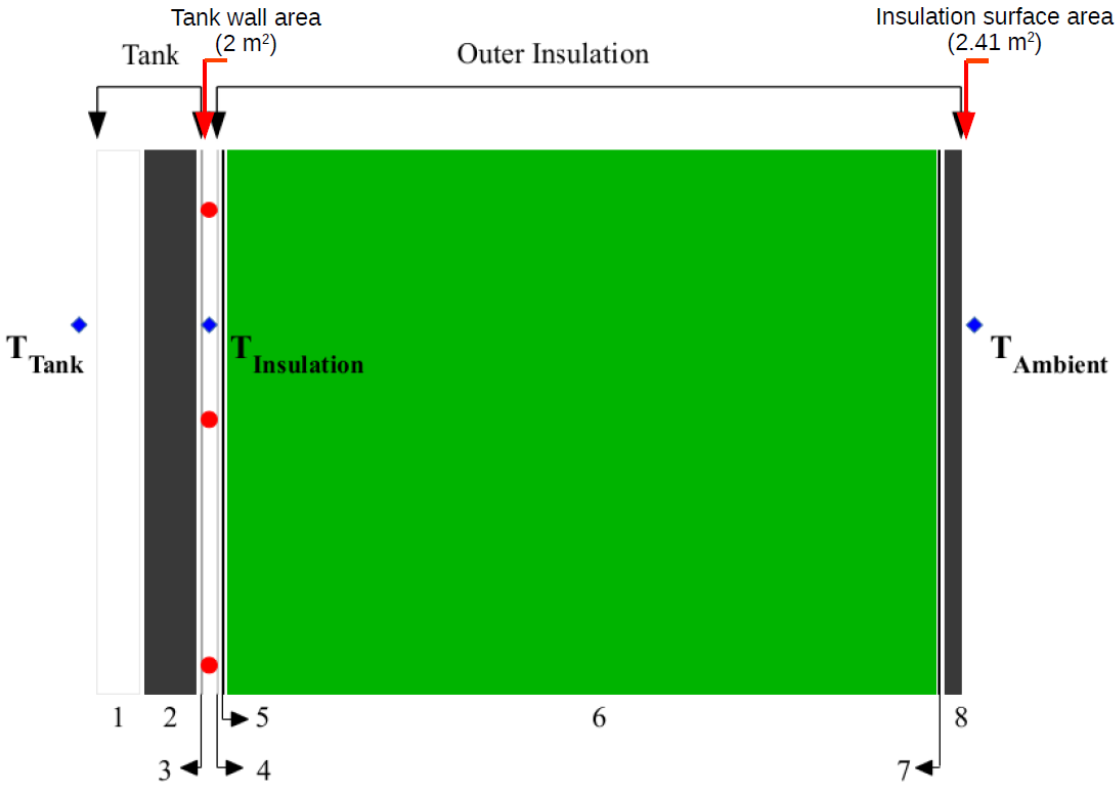

Figure 5.1: Schematic view of the insulation layers, as described in table 5.3 showing relative thicknesses, with the three temperature probes labelled as T_{Tank}, $T_{Insulation}$ and $T_{Ambient}$ with a blue dot and the red dots representing the location of the heater tape used for side heating. Surface areas of tank wall and outer insulation are also indicated using red arrows

The insulation was divided into two "sub-assemblies". The tank sub assembly consists of the tank wall, with a layer of thin closed-cell neoprene adhered to it, with a layer of foil over the outside. The foil layer was present to promote an even heat distribution by the side heating element, shown in Figure 5.1 by the red dots. Additionally, the blue dots labelled as T_{Tank}, $T_{Insulation}$ and $T_{Ambient}$ are temperature probes used during the assessment of the insulation and side heating.

The design, operation and assessment of the side heating element shall be discussed further in Section 5.1.5. The outer insulation sub assembly is removable so as to increase portability and allow easy access to the side heating elements and pressure relief pipe (discussed in Section 5.1.3).

The main insulation is a 135 mm thick layer of plastic wool. This has similar insulation properties to the glass wool used by Weeks (1962) but is non-toxic and is not an irritant to skin. This plastic wool is covered by a layer of plastic sheeting to waterproof it and prevent influx of water, which would negate its insulating effect. The outer layer of the plastic sheet is covered by a thin rubber neoprene layer, to protect the plastic sheeting from rips or tears.

Converting the thermal conductivity of each layer to an R-value using $\mathrm{R} = \frac{\mathrm{L}}{\mathrm{k}}$, where L is the thickness of the layer, allows the total R value to be calculated using $\mathrm{R} = \mathrm{R}_1 + \mathrm{R}_2 + \mathrm{R}_3 + ... + \mathrm{R}_\mathrm{n}$. This R value is found to be 3.43 K $\mathrm{W}^{-1}\,\mathrm{m}^2$. Using $\mathrm{C} = \frac{1}{\mathrm{R}}$ gives a total conductance of 0.046 $\mathrm{W\,m^{-1}\,K^{-1}}$ through the insulation. Comparing this value to the conductivity of the plastic wool, one can see it is very similar, confirming that the plastic wool was the layer contributing most to the insulation. Comparing the heat flux through the tank walls and from the top surface, one obtains: $30\mathrm{A}(\mathrm{T_{ice}} - \mathrm{T_a}) >> 0.30\mathrm{A}(\mathrm{T_w} - \mathrm{T_a})$. Per unit area, the rate of heat transfer is roughly 100 times greater at the tank surface than through the walls. However, the side walls do consist of a greater surface area. The tank top surface has an area of 0.50 m^2. Using an average radius of halfway between the thickness of the outside insulation and the inner tank radius, the area of the tank walls is 2.41 m^2. Taking this difference in surface area into account, the heat transfer rate is only 21 times greater at the tank surface than the tank walls. To ensure one-dimensional cooling, the heat transfer rate ratio of tank top surface compared to the side walls should be as high as possible. Therefore, this ratio can be increased to greater than 21 using the side heating introduced in Section 5.1.5 to compensate for heat loss from the tank sides.

Figure 5.2 shows the tank construction and insulation process, where a) shows the 500 dm^3 tank with the top cut open, b) shows the neoprene layer adhered to the tank sides c) shows the addition of the foil layer and side heating tape, with d) showing the tank with the outer insulation layer.

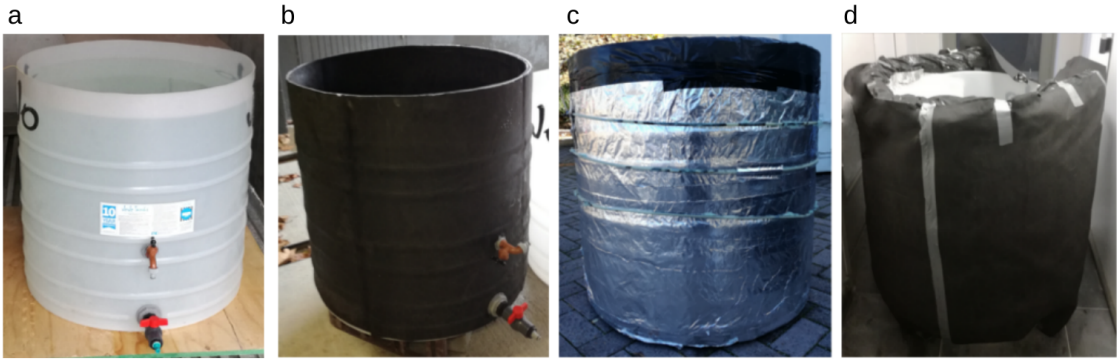

Figure 5.2: Tank Layers: a) cut HDPE Tank b) insulated with 3mm rubber foam c) covered with foil for heat conduction from side heating d) final tank with outer 135 mm plastic wool insulation

The taps shown in a) of Figure 5.2 were removed, with the upper tap replaced by a stopper, and the lower inlet being used for installation of the pressure relief pipe.

5.1.3 Pressure Relief

A system of pressure relief was required due to decrease in density of ice compared to its melt, causing a volume expansion upon phase change. In an artificial sea ice system, this volume expansion can cause a pressure build-up if the ice adheres to the side of the freezing vessel. Besides causing possible damage to the system, pressure build up was undesired since it forces the underlying solution back through the porous ice layer, preventing brine drainage and creating an unnatural salinity profile as well as surface flooding (Roscoe et al., 2011). A decision matrix was used to assess pressure relief systems used in artificial sea ice systems from literature, to find the best system to maintain a realistic freeboard. The primary objective of the pressure relief system was to ensure accurate sea ice properties, predominantly, a natural salinity profile. The primary objective of achieving the correct size and number of samples for mechanical testing was not affected by the pressure relief system since it does not affect tank area. Therefore, the possible design choices are not assessed against this objective. The three secondary objectives are used to assess the design choices. The possible design choices and the decision matrix assessment results are shown in Table 5.4.

Table 5.4: Decision matrix table for pressure relief system

Method	References	Primary Objectives	Secondary Objectives			Sum
		Accuracy (x3)	Cost (x2)	Portability (x2)	Manufacture Simplicity (x1)	
Separate tank (passive)	Thomas, 2018	2	2	1	3	15
Pressure relief pipe (passive)	Schulson et al., 2015 Weeks, 1962	1	3	4	4	**21**
Free-floating ice (passive)	Thomas, 2018 Wiese, 2012	4	2	1	1	19
Air-filled bladder (passive)	Roscoe et al., 2011	2	2	4	2	20
Methonol-filled Bladder (active)	Style and Worster, 2009	3	1	2	1	16

Free-floating ice was advantageous since it ensures the most realistic ice freeboard and therefore should result in the most realistic ice salinity profiles. Free floating ice has been accomplished by Wiese (2012) and Garnett et al. (2019). Their systems consisted of glass-walled tanks with heated side panels to partially melt ice near the walls and prevent adherence. However, both authors report difficulties in consistently accomplishing free-floating ice. In addition, free-floating ice would work best in a glass tank where wall smoothness was optimum. Thus, though desirable, it was unlikely to be accomplished in this system design. Roscoe et al. (2011) commends the system by Style and Grae Worster (2009), who used an active pressure relief system consisting of a methanol filled balloon within the tank. The methanol's low freezing point keeps it liquid, and by linking it to a small external reservoir, the pressure can be controlled by adjusting the reservoir level. However, this was deemed to be an expensive and complicated system, with the additional reservoir and components reducing portability as well. Thus, it received a low score.

A simplistic system consisting of a heated pressure relief pipe was considered the best design choice. While it scored lowest on system accuracy, its simplicity, low cost and portability enables it to score highly. It should be noted that the rating of accuracy was purely a relative one, therefore a pressure relief pipe was quite capable of enabling adequate pressure relief, and has been used successfully by researchers such as Weeks (1962) and Schulson et al. (2015). The installed pressure relief pipe is shown in Figure 5.3.

Figure 5.3: Pressure relief pipe exiting from bottom of tank

The pressure relief pipe consists of a flexible, transparent PVC pipe with wire reinforcing and an internal diameter of 25 mm. The pipe was routed between the tank and the outer insulation layer, to a second smaller vessel to allow draining of the solution overflow. Where the pipe exits the tank insulation, it was covered by a 28 mm thick foamed polyethylene insulation sleeve. Flexibility of the pipe was advantageous since it allows the pipe to be easily routed through the insulation and into the smaller vessel, with the maximum height of the pipe set to the water level in the tank. The transparency enables the pipe to be checked for ice build-up to ensure pressure relief was not impeded. The pressure was naturally regulated through the pressure head of the water, the pipe was open to the atmosphere and regulates to atmospheric pressure, therefore allowing any pressure build-up within the tank to be dissipated by increasing the height of the water column within the pipe.

This ensures that the correct freeboard within the ice was maintained. It uses the same principal as the separate reservoir tank used by Garnett et al. (2019), however, it was preferred since it does not require the whole reservoir to remain liquid in order to regulate pressure. Additionally, adjusting the height of the pressure relief pipe allows finer control of the pressure relief. If the highest point of the pipe was level with the tank surface, any pressure build-up will increase the water level within the pipe, which will immediately overflow into the secondary vessel. Since the ice was porous, a consistently large head difference between overflow pipe and the tank over an extended time could still result in an percolation of solution up through the ice, upsetting the natural salinity drainage and profile. However, by adjusting the pipe bend to a slightly lower point, one can decrease the necessary pressure build-up before it overflows, thus allowing the adjustment of the ice freeboard. However, this was difficult to do since it would require a knowing the exact ice depth and a constant lowering of the pressure relief pipe height as the ice depth increases. Therefore, the pressure relief pipe level was set to the level of initial solution, and only adjusted downwards by a 1 - 2 cm if it was noted that flooding has occurred on the ice surface.

One risk with the pressure relief pipe was the potential to siphon the water from the tank, since the outlet was lower than the tank water level. The risk of this can be negated by ensuring that a pipe of large enough diameter was used so that even at a maximum rate of ice growth, the pipe diameter will not be flooded with water, but rather drain over the maximum height point while maintaining open volume within the pipe. The internal diameter of 25 mm was found to be sufficient, even with the internal heating cable. The heating cable was waterproof with a silicone outer layer resistant to temperatures between -40 °C and 180 °C. The nichrome wire heating element was capable of supplying up to 65 W m^{-1} at constant wattage, and runs off 230 V. The heating rate was adjustable, however, there was no feedback loop or temperature measurement, which makes control of the temperature difficult. While the heating rate may be constant, factors such as ambient temperature, the solution temperature and side heating rate will affect the temperature of the pressure relief pipe. The difficulties are made simpler since the exact temperature of the pressure relief pipe system was unimportant, as long as it was not low enough to result in freezing of the overflow, or too high that it melts the pipe or causes excess heat to be transferred back into the tank.

To determine the required heating rate, a temperature probe was inserted into the pressure relief pipe, and placed in what was identified as the section most vulnerable to freezing. While within the tank insulation, the pipe was well insulated, however, near to the drainage point into the secondary tank, the pipe will be most exposed to freezing, due to the influx of cold air into the open end of the pipe, and with only the foam insulation sleeve. The tank was filled with saline solution of 34 g kg^{-1}, therefore allowing the temperature of the solution to be within the expected range for normal artificial sea ice growth. The cold laboratory temperature was decreased to -20 °C and ice was allowed to grow within the tank over a period of 13 days. The air temperature of the cold laboratory was monitored, hereafter termed as the "ambient temperature", as well as the temperature of the solution within the tank and the temperature within the pressure relief pipe. The heating rate within the pressure relief pipe was adjusted until it was found to be within the proper range. The results of the freezing experiment are shown in Figure 5.4.

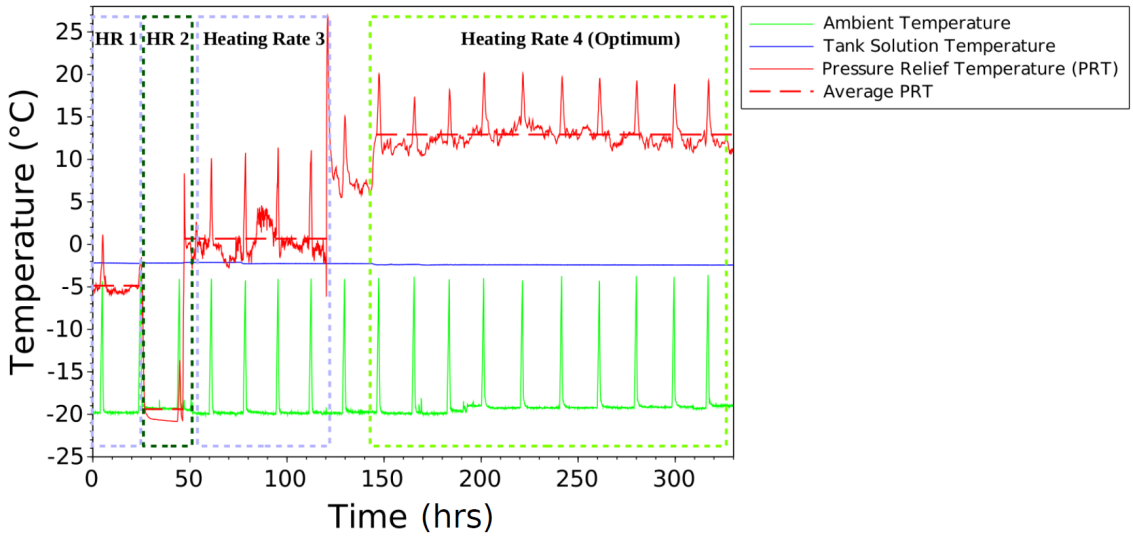

Figure 5.4: Adjustment process for the manual heating of the pressure relief pipe

The regular upward temperature spikes seen within the ambient temperature profile is caused by the defrost cycles of the chiller within the cold laboratory, also experienced by Marks et al. (2017) and Wiese (2012). These defrost cycles and temperature increases caused corresponding temperature increases within the ice temperature profile. This is an undesired fluctuation but unfortunately it was not possible to turn off the defrost cycles without causing possible damage to the chiller due to ice-build up.

The defrost cycles added additional complexity to the heating rate control of systems without temperature feedback mechanisms. A heating rate that may be ideal during normal ambient temperatures of -20 °C may provide too high of a heat input during a defrost cycle. Figure 5.4 shows that four different heating rates were tested. The optimum heating rate needs to reliably keep the temperature within the pressure relief pipe above the estimated freezing point of solution (-1.54 °C for 28 g kg^{-1} saline solutions) without providing too much heat input into the tank. The first tested heating rate was too low, and then the heating was turned off entirely so as to establish a baseline heat loss. The third heating rate was deemed to be close to optimum, with an average temperature of 0.7 °C. However, single measured temperature points were measured as below that of the solution freezing point temperature. The last heating rate that was tested had an average temperature of 12.9 °C, with a maximum of 20.2 °C and a minimum of 10.4 °C. This provided a heat input that kept the solution within the pressure relief pipe well above the freezing point of the solution, regardless of the chosen solution salinity.

The relatively warm temperature of the water in the pipe will result in a lower density than the tank solution which will be at the solution freezing point of -1.54 °C. This low density should prevent the transfer of the heat from the pressure relief pipe back into the system, since the primary means of heat transfer in water is convective, and the direction of convective heat transfer is away from the tank. However, as a further assessment, the total energy of the water within the pressure relief pipe can be calculated. Using the pipe dimensions (l = 2.5 m, dia = 0.025 m), the maximum temperature measured in the pressure relief pipe of 20.2 °C and the heat capacity of seawater (Talley, 2002), the maximum energy available for addition to the system would be 104 kJ. If this was transferred back into the tank containing 400 dm^3 of solution at -1.54 °C, the temperature change would be 0.06 °C. In addition, Section 5.1.4 discusses the design of a temperature-controlled heating system for the bottom of the tank to simulate the oceanic heat flux, capable of outputting 650 W. Therefore, any possible heat input from from the pressure relief pipe is negligible and would in addition, be accounted for by the temperature controlled bottom heating.

The last heating rate was deemed to provide an optimum heat input to the pressure relief pipe that would prevent freezing of the solution within the pipe while not experiencing too high a maximum temperature during a defrost cycle. This heating rate was recorded and was used for all subsequent experiments.

5.1.4 Bottom Heating

The bottom heating module is important for temperature control of the solution, and to simulate the oceanic heat flux. Prevention of solution supercooling and simulation of the oceanic heat flux will be accomplished through a submerged heating element at the bottom of the tank, capable of supplying 15 $\mathrm{W\ m^2}$ such as those used by Wiese et al. (2015) and Roscoe et al. (2011). The amount of heat input should be adjustable in order to tune it for growth conditions. The same waterproof heating tape as used for pressure relief heating, capable of supplying 65 $\mathrm{W\ m^{-1}}$ was used for the bottom heating module. The heating tape was mounted to a circular plastic board, which allowed for easy removal from the tank, while enabling the tape to be laid out to accomplish even heating distribution across the tank area. The plastic disc had holes drilled into it, in order to allow water to pass through it, to make it easier to take into and out of the tank even when the tank was filled with water (Figure 5.5).

Figure 5.5: Bottom heating module, with heater tape mounted to plastic base

The total length of the heating cable used was 9.6 m, and was therefore capable of supplying a total 650 W, or 1300 $\mathrm{W\ m^2}$. While this seems extremely excessive, it should be noted that control of the heating rate does allow this to be adjusted down to the desired rate. In addition, the desired oceanic heat flux of 15 $\mathrm{W\ m^2}$ mentioned by Wiese et al. (2015) is a constant rate, whereas the heating module discussed herein was temperature controlled. Therefore, even if the measured heat rate at an instant was much greater than 15 $\mathrm{W\ m^2}$, the temperature controller turns this heating off as soon as the setpoint temperature (solution freezing point) was reached, and thus the average heat rate over time will be much lower.

It was seen as advantageous to have the ability to increase the heating rate to a much greater level, since it also enabled the melting of the ice and resetting of the tank to be accomplished much quicker, reducing time between experiments. The cable has a small surface area, therefore the high heat output of 65 $\mathrm{W\ m^{-1}}$ results in a high temperature. While this should dissipate quickly

in water, especially if well-mixed, the extreme temperature gradient was undesired, and could result in undue wear of the components. Using a greater length of cable allowed a much lower heating rate per metre, as well as a more even distribution of heating over the tank base area. While heating pads such as those used by Garnett et al. (2019) have a greater surface area and a maximum heating rate much closer to the desired value required for the oceanic heat flux, it was decided not to use them, since Garnett et al. (2019) notes that they did not perform well in salt water, with a high failure rate due to corrosion. It was also decided to stick to systems running at 230 V. The reasons for this will be discussed in Section 5.2.2.

It is known that in a well-mixed, small-scale system the solution temperature should be at freezing point (Weeks and Cox, 1974). This is seen in the ocean as well, where the entire upper layer of between 10 m to 40 m deep is at freezing point before ice formation begins (Weeks, 2010). Thus, for a given solution salinity, the desired temperature set-point is known. Therefore, it was decided to use a temperature controller to control bottom heating. The controller was connected to a NTC temperature probe (accurate to ± 0.6 °C within expected range of solution temperature) which was mounted 3 cm above the bottom heating element.

The controller has control only over whether the heating was on or off, with no control over the heating rate, therefore no PID control was possible. The hysteresis level was set to 0.1 °C, the maximum resolution of the controller. The hysteresis setting prevents over-switching of the heating, so that it was not being turned on and off too often, which shortens the operation life of the relay. However, with adjustment of the heating rate to the correct level it was determined that a change of 0.1 °C took an average of 15 minutes to occur. Therefore, this was deemed more than adequate and would keep the temperature close to the set-point. A temperature controlled setpoint was decided to be a cheaper, simpler solution than a constant power input controller, especially since the required heat input would need adjustment to account for individual system heat fluxes. However, since the temperature controller does not record when it was turned on, the heat input from the bottom heating was difficult to quantify. When it is necessary to have an exact budget of the heat input, the controller can be bypassed and the bottom heating can be set to a constant rate.

To determine the required heat input, a freezing experiment was carried out, where a 34 g kg^{-1} saline solution was placed in the tank and allowed to reach freezing point. The temperature of the underlying solution was monitored near the bottom heating element at several locations, and these temperatures were averaged to obtain the average solution temperature. The setpoint temperature of the bottom heating controller was set to the freezing point of solution, as -1.9 °C, note that the actual calculated freezing point was -1.87 °C. The controller resolution was only 0.1 °C. In addition, the freezing point decreased slightly due to ice formation leading to an increase in the solution salinity. The heating rate was adjusted and allowed to stabilise, with the average solution temperature from all probe points recorded over time. Figure 5.6 shows the summarised results of the heating rates.

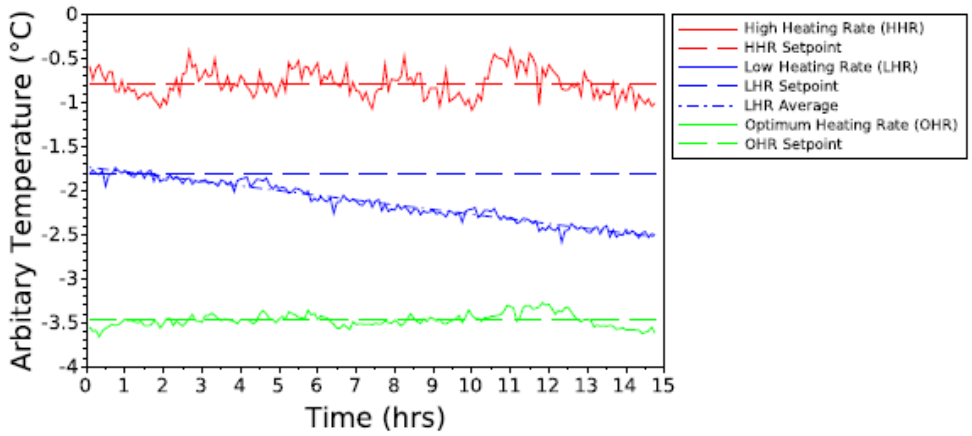

Figure 5.6: Comparison of low and high heating rates for bottom heating

The y-axis is shown as nominal temperature, since all three profiles were measured at a setpoint temperature of -1.9 °C. The y-axis is useful to show the scale of the fluctuations for each of the profiles only. The high heating rate profile was shifted up and the optimal heating rate profile was shifted down so that they can all be placed on one axis for comparative purposes. Table 5.5 shows the analysis of each of the heating rates.

Table 5.5: Comparison of low and high heating rates for bottom heating

Parameter	High Heating Rate		Low Heating Rate		Optimum Heating Rate	
	Low	High	Low	High	Low	High
Oscillation Range	-0.41	0.30	-0.13	0.18	-0.19	0.17
Percentage Split	47.5%	52.5%	48.6%	51.4%	50.3%	49.7%
Standard Deviation of Oscillations	0.158		0.050		0.073	

The initial heating rate proved to be unsatisfactory. While it was able to maintain the set point temperature, with an almost even distribution around the mean, The standard deviation from the set point was 0.16 °C and the oscillations were too great, with a maximum temperature of 0.30 °C higher than the setpoint, and a negative oscillation of 0.41 °C. The oscillations are greater than the accuracy of the NTC temperature probe connected to the bottom heating temperature controller. However, it was suspected that the high heating rate results in a quick temperature increase in the heater tape and the nearby water. This increase takes place at a greater rate than either convective or conductive heat transfer through the water. Therefore, by the time the temperature at the location of the NTC temperature probe, located 3 cm above the heating module increases to the setpoint, the bottom heater module has transferred an excess of heat into the tank. Even when the heating module measures that the setpoint temperature has been reached and switches off, the comparatively warm water near the bottom heater module and the heat retained in the heater tape continues to dissipate through the rest of the solution, causing a continued increase in average solution temperature. Thus, a lower heating rate was preferred.

Too low of a heating rate resulted in the bottom heating unable to maintain the solution at the set point temperature. The oscillations are measured against a trendline of the temperature profile in this case, since they would mean little if calculated as oscillation against the setpoint. The small oscillations do suggest a fairly even temperature distribution within the tank.

Increasing the heating rate slightly resulted in the optimum temperature profile. The temperature controller was able to maintain the solution temperature at the setpoint, with a standard deviation of 0.07 °C. It was evenly distributed around the mean, with oscillations of ±0.2 °C. Since a lower heating rate meant the bottom heating module was not able to maintain the temperature setpoint it, this was deemed to be the optimum heating rate for the system when considering no additional factors. However, a means of further increasing the ability of the system to maintain temperature setpoint is discussed in section 5.1.6

5.1.5 Side Heating

A means of heat input from the sides of the tank was added to negate heat loss through the insulation. This side heating is found in many artificial sea ice set-ups such as those described by Weeks (1962), Wiese (2012) and Garnett et al. (2019). As described in Section 5.1.2, the side heating was installed between the tank and outer insulation layer. It consisted of the same 65 $\mathrm{W\ m^{-1}}$ waterproof heating tape used in the pressure relief and bottom heating modules. Seen in Figure 5.2 c), a total length of 9.5 m of heater tape was wrapped around the upper half of the tank, between the foil layers which would assist in attaining a more even heat distribution. The side heating module was therefore capable of supplying a total heat input of 652 W, or 652 $\mathrm{W\ m^{-2}}$ (over half of the tank wall surface area). As mentioned for the bottom heating module, this was also far in excess of what would be required and can be reduced to the desired level. The heater tape was used since it simplifies the system, reducing the number of different components and making it easier to replace if broken. It also enabled all the designed electrical components within the tank to run off 230 V, the reason for this will be discussed in Section 5.2.2.

The amount of heat input from the side heating needed to be carefully balanced. While it was required to negate possible heat loss from the side walls, as well as promoting free-floating ice, it should not provide enough heat to result in a positive heat flux into the tank. The side heating could not be controlled using a temperature controller as used for the bottom heating module, since there was no temperature at any point within the system that the side heating was required to keep constant. A small, but constant, heat input was therefore necessary. However, the value of this heat input was difficult to empirically determine. Based on the calculated heat conductivity through the insulation, the heat loss can be estimated as $\mathrm{Q_{walls}} = 0.30\mathrm{A}(\mathrm{T_w} - \mathrm{T_a})$. Taking the area of the side walls as 2.41 $\mathrm{m^2}$, the calculated heat loss through the tank walls was 0.72 $\mathrm{W\ m^{-2}\ \Delta T^{-1}}$. To validate this heat loss, one would need to isolate the heat loss through the side of the tank from the much greater heat loss from the top of the vessel. While all these heat losses can be calculated theoretically and the temperature within the tank at various locations over time can be measured and used to fit to the modelled heat losses, it was decided a simpler method could be used to determine the required heat input from the side heating.

The tank was placed in the cold laboratory and filled with saline solution at 34 $\mathrm{g\ kg^{-1}}$. Temperature probes were placed to measure the ambient temperature, temperature within the

insulation layer at the point where the side heating element was located, and the solution temperature at various locations within the tank. It should be noted that the location of the side heating element, and the temperature probe was close to the tank, with the bulk of the insulation lying between the probe located at the side heating and the ambient temperature probe. These probes will be termed as "Ambient", "Insulation" and "Tank" for the remainder of this section. In the case where the bottom heating module was switched off, the temperature values from the probes within the solution were averaged to obtain one value. If the bottom heating module was switched on, solution temperatures close to the bottom heating module were averaged and compared to an average value from temperature probes further away. This enabled a proxy reading of when the bottom heating module was heating the solution, since the temperature reading close to the bottom heating module would be warmer than the value further up the tank (seen in Figure 5.7).

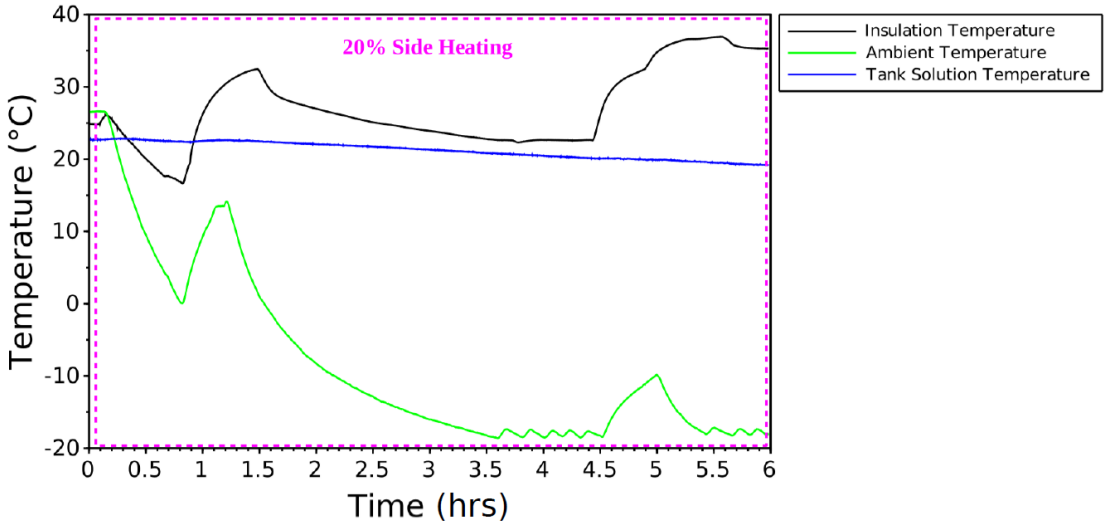

Figure 5.7: Temperature profiles for average tank solution, outer insulation layer and ambient at high tank temperatures and no bottom heating, with side heating set to 20 %

In order to establish a baseline setting and determine the direction of adjustment, a quick initial experiment was run for 20 % side heating. The solution was initially at room temperature of 23 °C. The ambient temperature was set to -20 °C and the heating rate for side heating set to an arbitrary initial rate of 20 % (for description of heating control method see Section 5.2.2). The bottom heating module was initially turned off. The tank was allowed to cool for 6 hours while temperatures were recorded. The ambient temperature, insulation temperature and average solution temperature profiles during this time are depicted in Figure 5.7.

Within these initial 6 hours of cooling seen within Figure 5.7, the heat loss was at a maximum, since the temperature difference between the ambient and solution temperature was greatest. During this period, it can be seen that the insulation temperature, which can be used as a proxy to assess the approximate side heating rate undergoes an upward spike at 1 hour and again at 4.5 hours. Graphically this is deceiving, since it suggests an adjustment to the rate of side heating. However, in reality, these spikes are due to the cold laboratory undergoing a defrost cycle. This can be seen by a corresponding spike occurring within the ambient temperature

profile. The average tank solution temperature decreased for the duration of the test where the side heating was set to 20 %. This indicates that the side heating rate was not large enough to result in a net positive heating flux into the tank. However, the temperature difference between the insulation and the ambient was close to 60 °C near the end of the 6 hours, which suggests a heating rate that was too high.

Once this initial test had established a baseline and an approximate range for the correct heating settings, a more rigorous, secondary test (Figure 5.8) was carried out at a lower tank solution temperature with ice formation. The lower tank solution temperature creates a smaller temperature gradient between the tank solution and the ambient temperature, lowering the heat flux from the tank surface. This heat flux was further inhibited by the ice growth. Therefore, the heat input from the side heating module will make up a larger proportion of the total heat flux, even if the heating rate was reduced. The side heating rate was adjusted to a value of 10 % and the bottom heating was turned on to prevent ice formation from the tank bottom and prevent supercooling.

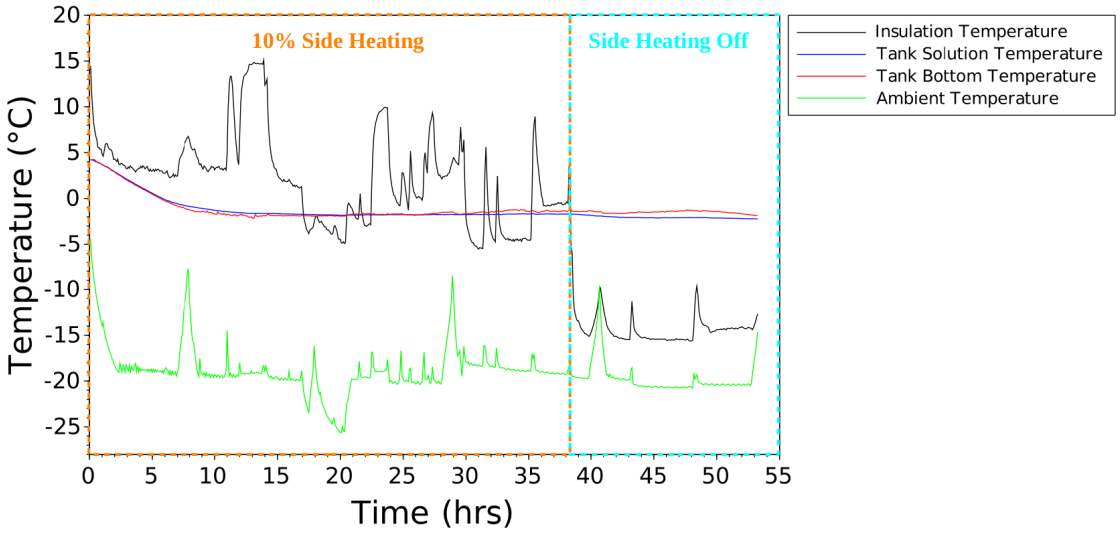

Figure 5.8: Temperature profiles for average tank solution, outer insulation layer, tank bottom and ambient with solution at freezing point

The second test duration was 55 hours so as to test the stability of the heating rates and temperature control. At 38 hours, the side heating was switched off to obtain temperature profiles when no side heating was present. A graphical representation of the cross-section through the insulation for a heating rate of 20 %, 10 % and no side heating is displayed in Figure 5.9. The respective temperatures at each location were taken from the end values of the 20 % heating rate and from average values for each of the 10 % heating rate and when side heating was switched off. This enables some extrapolation of the temperature gradients through the side of the tank, though an exact value of the temperature at the surface point of the inside tank wall and the outer edge of the insulation could not be precisely measured. Thus, the tank solution temperature was used as a proxy for the inside tank wall and the ambient temperature was used as a proxy for the outer insulation surface.

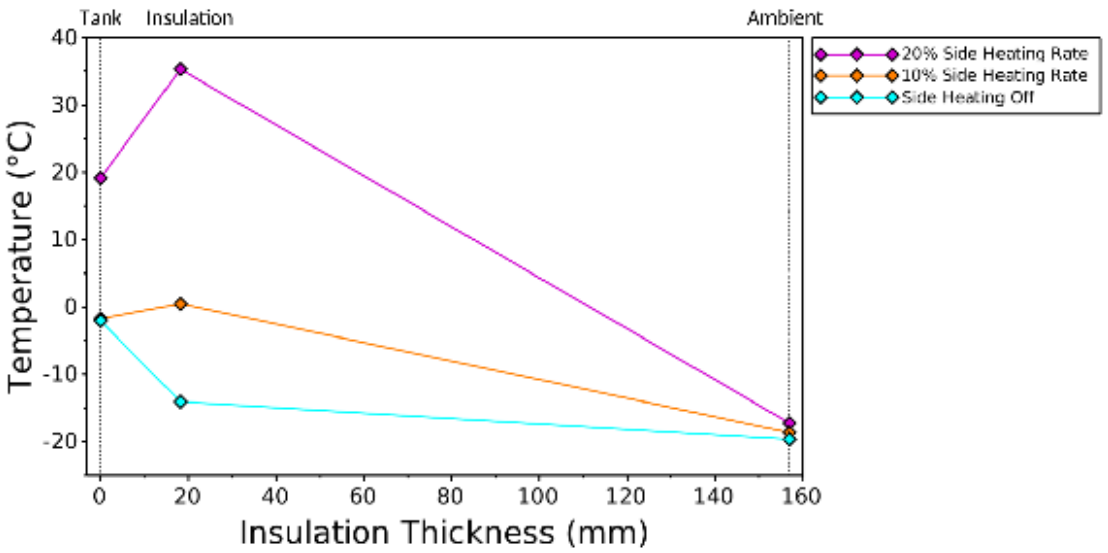

Figure 5.9: Temperature profiles for average tank solution, outer insulation layer and ambient at high tank temperatures and no bottom heating, with side heating rates of 20 %, 10 % and "Off"

The profile of "Side Heating Off" shows a baseline temperature difference between the tank, insulation temperature and ambient. It can be seen that there was a temperature difference of $>$10 °C between the tank solution temperature and the temperature within the insulation layer. Since the point of measurement happens close to the tank, with the bulk of the insulation located between the insulation temperature probe and the ambient temperature probe, there should be a negligible temperature gradient between the solution in the tank and the insulation temperature if insulation layer was perfectly insulating. The observed $>$10 °C temperature difference implies that the insulation was not sufficient to prevent heat loss through the side walls. This was as expected from the calculation of heat loss in Section 5.1.2. The initial heating rate tested was 20 %. The 20 % Side Heating Rate profile in Figure 5.9 was taken from the profiles seen in Figure 5.7. Thus, the tank solution temperature was close to 20 °C rather than at freezing point as seen in the temperature profiles of 10 % Side Heating Rate and Side Heating Off. However, the positive temperature difference of $>$15 °C between Tank and Insulation, combined with the $>$50 °C temperature difference between Insulation and Ambient confirms the earlier surmise that a 20 % side heating rate may be too high. Considering the profile for 10 % Side Heating Rate, there was a temperature difference between tank and insulation of about 2 °C. This temperature gradient was small, with a slightly positive heat flow into the tank. However, it was decided further analysis of the effect of the side heating was required, since the measured temperatures within the profiles from Figure 5.9 are proxies only and cannot be used in an actual calculation of heat flux.

Further analysis was accomplished using interaction plots. An interaction plot is a visual statistical method to determine the effect of, and interaction between, two variables, each with two levels. The first assessment was performed to determine the change of cooling rate with and without active ambient cooling, for different side heating rates (Figure 5.10).

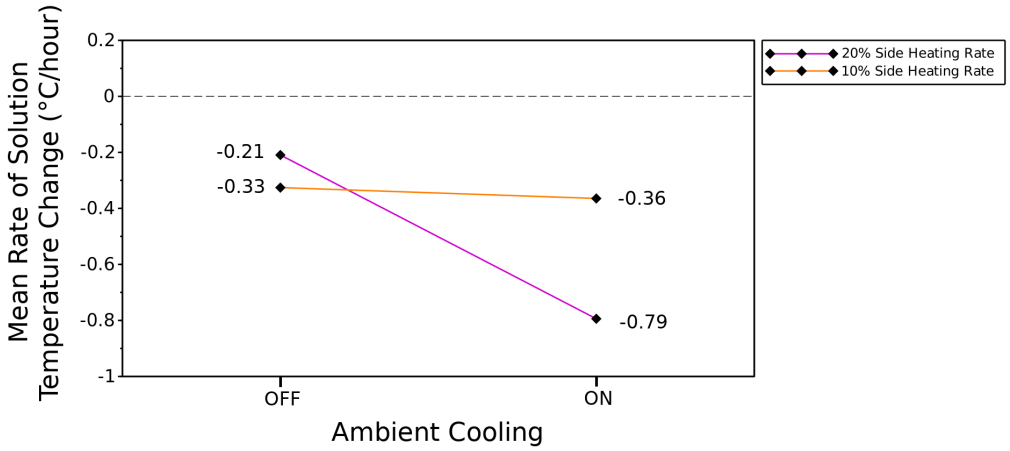

Figure 5.10: Interaction plot for effect of ambient cooling and its interaction with different rates of side heating

The ambient cooling was assigned as "off" during a defrost cycle. While this still would imply an ambient temperature lower than tank solution temperature, and therefore a heat loss from the solution to ambient, the temperature gradient and degree of forced convection was much reduced. Thus, assessing the difference between net cooling rate when ambient cooling was on or off should distinguish the contribution of heat from the side heating.

While it was already established that the 20 % side heating rate was too high, it is shown in Figure 5.10 for comparative purposes. The assessment of the 20 % side heating rate took place when the tank solution temperature was initially at 22 °C. Therefore, it was expected that the cooling rate would be much greater than the cooling rate for the 10 % side heating rate where the tank temperature decreased to -2 °C. This was observed when ambient cooling was on, with an average tank cooling rate of -0.79 °C compared to -0.36 °C. However, there was a drastic change in the solution cooling rate when the ambient cooling was not active for the 20 % side heating rate. The high tank temperature during the 20 % side heating rate assessment should imply the magnitude of the cooling rate experienced at the tank surface should dominate the net heat balance, regardless of whether the ambient temperature was on or off, since there was still a large temperature difference between tank and ambient. However, the 0.58 °C reduction in average cooling rate when the ambient cooling was switched off suggests that the side heating heat input plays a significant role in the overall heat balance, with the heat input from side heating being proportionally greater with the reduction in cooling rate experienced when ambient cooling was off. This change was not seen for the 10 % side heating rate, where the cooling rate experiences a change of 0.03 °C when ambient temperature was turned on or off. Therefore it implies that the contribution of the side heating to the overall heat balance was much smaller, and should not affect the system too greatly. To further explore the extent of heat input from the side heating, the contributions to overall heat flux from a side heating rate of 10 % compared to the bottom heating was assessed (Figure 5.11).

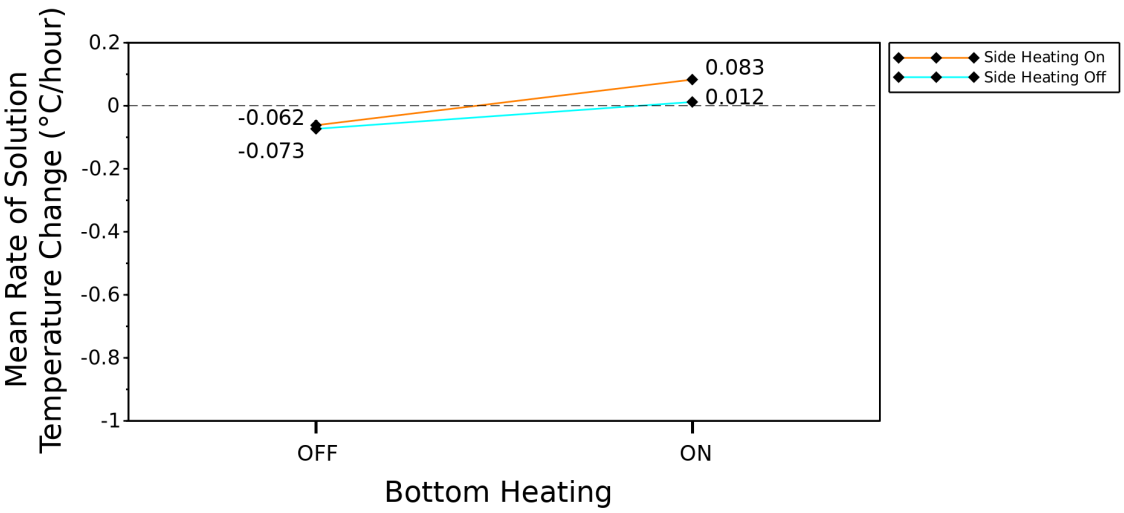

Figure 5.11: Interaction plot for effect of bottom heating and its interaction with side heating

This assessment took place when the solution temperature was at freezing point. Therefore the majority of the heat removed from the system by the ambient cooling was the latent heat required for phase change from liquid solution to ice. Ideally, in this stage, with constant solution salinity the solution temperature will remain constant, regardless of the cooling rate. However, the brine expulsion from the recently formed ice, does cause a slight solution salinity increase over time, with a resultant freezing point temperature decrease. Thus there can be a small mean rate of solution temperature change. This negative solution temperature rate of change occurs where bottom heating was turned off, and was negative both when side heating was turned on or turned off. Switching the bottom heating on results in a change of heat flux direction, bottom heating on causing a positive mean rate of solution temperature change. This proves that the bottom heating operates as desired, and does not cause a drastically positive heating rate.

In summary, it was surmised from temperature profiles that a side heating rate of 10 % will counteract heat loss from the side of the tank unaccounted for by the insulation, and indeed result in a slight heat input from the tank sides. However, the emphasis is on “slight”, with the level of heat input determined to have a negligible impact on the overall tank heat balance, which was net negative in the direction of the tank surface, as desired.

5.1.6 Agitation

During the determination of the optimum bottom heating rate, it was identified that the natural convection within the tank was insufficient to ensure a uniform solution temperature (seen in Figure 5.12). In order to prevent stratification of temperature and salinity within the tank, a means of agitation within the tank was required. It was also theorised that this would result in a more stable control of the temperature setpoint, since the forced mixing would distribute the heat generated from the bottom heating element much more efficiently than natural convection, preventing overheating. A comparison of tank temperature profiles was performed (Figure 5.12) between two freezing experiments, both with bottom heating active, where the first experiment had no agitation (shown in a)) and the second experiment (shown in b)) had activation agitation using aquarium pumps (Boyu Wave Maker, 40-260 $\mathrm{dm}^3\ \mathrm{h}^{-1}$).

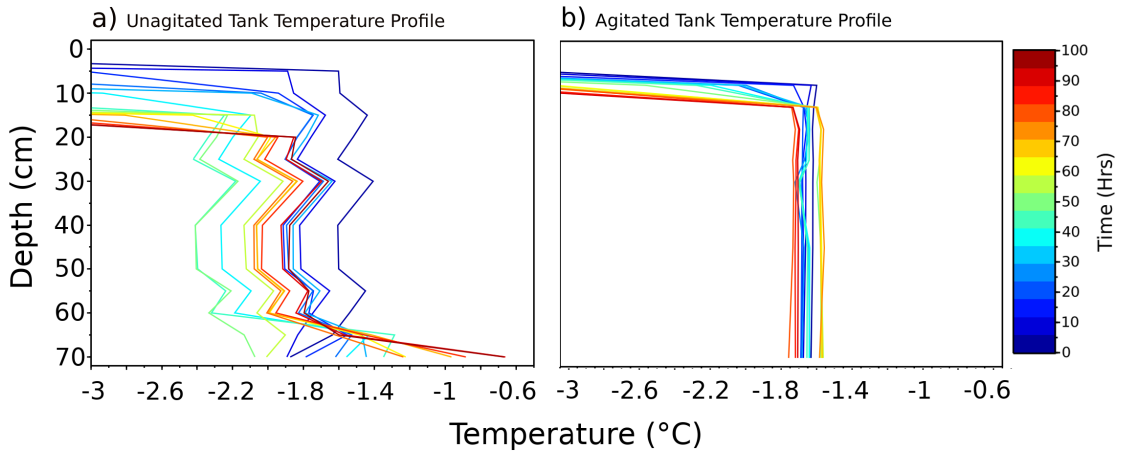

Figure 5.12: Temperature variation in tank with and without agitation

Figure 5.12 shows the temperature profiles within the tank before and after agitation. 0 cm represents the surface of the tank, and it can be seen in these profiles that the temperature near the top surface was much lower than the range shown in these plots. These lower temperature indicate the presence of ice near the tank surface, with the shift of the profile from a near horizontal line to a near vertical line indicating the location of the ice-solution interface and thus, the ice depth. It can be seen that the ice temperature tends toward the solution temperature near the ice-solution interface, since this will represent the freezing point of the solution.

It can be seen in Figure 5.12 a) that before agitation, the temperature in the solution within the tank varied with depth, fluctuating by upwards of 0.2 °C per 10 cm. This fluctuation was even larger at the bottom of the tank, with the lowest measured temperature point warmer by over 1 °C, especially later on near the end of the experiment. The bulk solution temperature can also be seen to vary over time, despite the bottom temperature setpoint, with the solution portion (excluding top most ice layer) of the temperature profiles displayed in a) plotted within a range of -0.6 °C to -2.4 °C.

In comparison, the temperature profiles of an experiment carried out with agitation, shown in Figure 5.12 b), are consistent over time, with all the profiles falling within a much tighter temperature range of between -1.5 °C to -1.7 °C. The solution temperature measured at different temperature profiles show variations lower than 0.1 °C. The agitation method and considerations are discussed below, followed by further analysis of the effect on the solution temperature temperature setpoint.

No decision matrix assessment was performed for the method of agitation, since it seemed that the preferred method according to the surveyed artificial sea ice systems found in literature was to use aquarium impeller pumps (Garnett et al., 2019; Roscoe et al., 2011; Wiese, 2012). Aquarium pumps with a control over the flow rate are available, enabling adjustment of the agitation level and generated current. They are inexpensive and self-contained, thus fulfilling the secondary objectives of being cost-effective, portable and simple. Two such pumps were procured (Boyu Wave Maker, 40-260 $\mathrm{dm}^3\ \mathrm{h}^{-1}$). The placement of these pumps were carefully considered to prevent ensure

consistent mixing without the creation of dead zones. Timmons et al. (1998) recommends placing pumps in a direction creating flow tangential to the tank walls, since it results in a circular flow pattern, with a secondary radial flow pattern. This ensures good mixing in the tank, with no dead zones. However, it was known that currents over 10 mm s^{-1} can result in horizontal alignment of the c-axis in the ice (Langhorne and Robinson, 1986). Working from the minimum current necessary to align the c-axis, gives a required fluid velocity of 36 m h^{-1}. Considering circular flow, one can derive a rough estimate of fluid velocity from the tank area. The tank radius was 0.4 m, and when ice growth has reached its maximum, the minimum remaining water depth can be assumed as 0.4 m (30 cm of ice growth). Thus the area for circular flow was 0.16 m^2. For the maximum pumped flow rate flow rate of 260 dm^3 h^{-1}, the resultant fluid velocity was 1.63 m h^{-1}. This was much less than the lower current limit that would result in horizontal alignment of the c-axis in the ice crystals.

One pump was placed 10 cm above the tank base, directed tangentially. This pump was set to a constant flow rate of 100 dm^3 h^{-1}, with the second pump placed 45 cm above the tank base, facing radially with a pulsed flow of 50 dm^3 h^{-1}. This pulsed flow was to add turbulence to the system, further improving the mixing. The pumps are situated within the temperature-controlled underlying solution, and therefore should not be at any risk of freezing. The impeller has a magnetic drive, reducing the damage to the pump even if it does ice up. With the addition of agitation enhancing mixing beyond that of natural convection, it was possible to perform a secondary analysis upon the bottom heating rate (Seen in Figure 5.13).

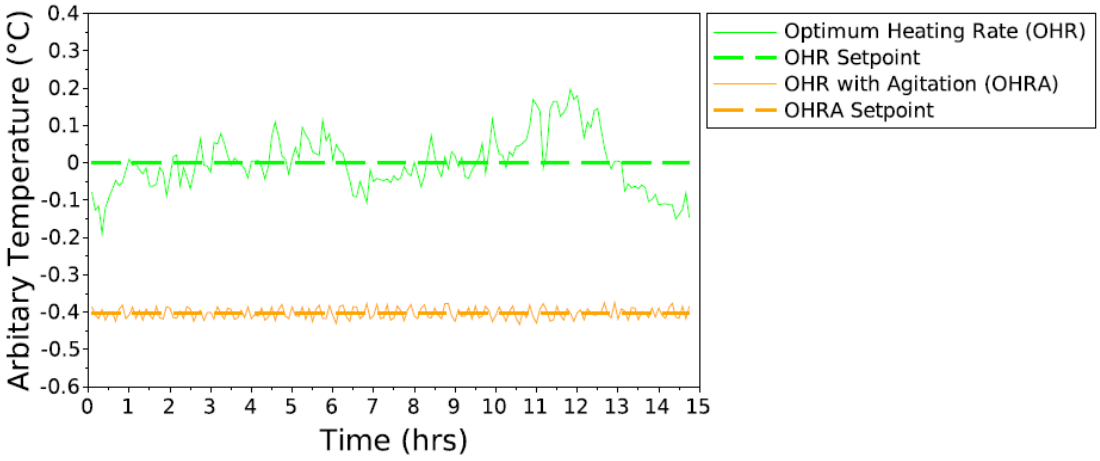

Figure 5.13: Comparison of temperature profile with and without agitation for bottom heating

For this analysis, adjustment of the heating rate from what was determined to be optimum within Section 5.1.4. Rather, the effect that the addition of agitation had on the temperature profile was examined. The optimum heating rate determined in Section 5.1.4 is shown again with y axis displaying a smaller range. It can be seen that the profile, which had a comparatively small oscillation range when shown on the larger axis scale against the higher heating rates, now shows a much greater degree of oscillation than when agitation is added. Table 5.6 shows the analysis of the two temperature profiles.

Table 5.6: Heating rates comparison

Parameter	Optimum Heating Rate		Optimum Heating Rate with Agitation	
	Low	High	Low	High
Oscillation Range	-0.19	0.17	-0.03	0.03
Percentage Split	50.3%	49.7%	48.0%	52.0%
Standard Deviation of Oscillations	0.073		0.015	

The addition of agitation resulted in an oscillation range of just 0.03 °C compared to 0.2 °C without agitation. The standard deviation from the setpoint temperature was 0.015 °C. At first this may seem an impossible level of control with a temperature probe that is only accurate within ±0.6 °C. However, there is a difference between accuracy and repeatability of a sensor. While accuracy refers to the absolute measurement compared to the physical value, the repeatability of a sensor refers to how small a range the measurements lie in for the same physical value (Celera Motion, 2019). The low standard deviation of the solution temperature over time suggests that while the NTC sensor used to control the temperature setpoint was only rated to an accuracy of ±0.6 °C, it had a very good repeatability. It was also noted that when comparing results of the temperature read from the temperature controller to that recorded by the temperature measurement system (discussed in Section 5.2.1 from which these profiles were generated , the difference between the NTC sensor and the tmeperature measurement system was seldom greater than 0.1 °C, the maximum resolution shown by the controller. This in turn suggests that the accuracy of the NTC sensor is greater than its rating would suggest, which is advantageous for accurate solution temperature control.

Overall, when considering Figure 5.12 and the oscillation range and standard deviation of the system after the addition of agitation, it can be seen that the addition of agitation was advantageous to the system in preventing thermal stratification, by which it can be inferred that saline stratification was also prevented. It resulted in a very stable solution set point temperature, allowing the solution to be set to the freezing point, despite the changing ambient temperature due to the defrost cycles within the cold laboratory.

5.1.7 Manual Depth Measurement

During the initial design, a method was required to determine the ice depth throughout the growth process. The lack of transparent side walls did not allow visual inspection as used by Wiese (2012). To disturb the system as little as possible, drilling a hole every time it is desired to know the ice depth was deemed unsuitable. Therefore, a similar system to that described by Weeks (1962) was designed. This consisted of two 1 m lengths of heater tape, with a cross-bar at the end of each of them. Measurement striations starting at the cross-bar as zero point were marked along their length. These could be suspended above the water surface level, with the cross-bars below the expected ice depth. In order to measure the ice depth, the heater tape can be simply switched on, melting the surrounding ice and allowing the cross-bar to be slid upwards until it contacts the underside of the ice. The first visible measurement striation above the ice gives the ice depth. Once this has been recorded, the heater tap can be slid back through the ice, ensuring

that the cross-bar is deep enough below expected ice level that it will not freeze in. Two depth measures are used since it is known that ice depth variation even over a small area is possible, with two measures giving some idea of the horizontal variation, and creates redundancy in case one depth measure is frozen in. No heating rate control was deemed necessary for the ice depth measure system. The 65 W heating rate allows for fast melting of the surrounding ice, quickly freeing the depth measures up. Once ice depth measurements have been taken, the heating can be turned off, freezing the depth measures back in and limiting the effect the depth measures have on the surrounding ice.

This system does not enable a continues monitoring of the ice depth, since it relies on human input for measurement. The duration of the freezing experiment means there are large gaps in measurements since it is not possible to be present or visit at regular, frequent intervals over a period of 8 - 16 days. It was also discovered that regular entrance and exit of the cold lab can cause similar temperature spikes to a defrost cycle, as well as increasing the necessary number of defrosts due to the influx of humid air causing an ice-build up on the chillers. Therefore a continuous, automated means of measuring the ice depth was also implemented and will be discussed in Section 5.4.

5.2 Control Centre System Design

All of the electronic modules within the tank such as the pressure relief heating, bottom heating, side heating require power input and a central housing. Weeks and Cox (1974) also mention the importance of temperature measurement within the system, thus, a data logger capable of measuring and recording temperature inputs from multiple probes was also necessary. Thus, the control centre system design consists of the design and procurement of a system and data logger for the temperature measurement within the tank, as well as the design of the tank controls panel. These two sub-modules will be discussed in the following sections.

All of these systems require housing. The location of the cold laboratory dictates that this housing, hereafter termed the “control centre” will need to be housed within the cold laboratory itself. This increases the complexity of the systems, since not all electrical components will be capable of operation at temperature extremes of -20 °C. The data logger was identified as being particularly vulnerable. Therefore, the housing needs to be well-insulated and also capable of maintaining a consistent, moderate temperature. While the design of the control centre does not necessarily affect the primary objectives of creating accurate artificial sea ice or with the required samples for mechanical testing, it was constrained by the secondary objectives of being low cost, simple, and portable.

An insulated box was re-purposed to house the controls for the electrical tank modules as well as the data logger. This can be seen in Appendix A.1 Holes were cut into the side for the mains power inlet, the power connections for the bottom heating, side heating, pressure relief heating and depth measurement modules, as well as a hole for all the temperature probe cables. A data cable was run externally to the box from the data logger, allowing data collection without having to open the box.

A perspex inner lid was added, such that the box could be open to allow viewing of the front control panel and indicator lights while limiting the internals to exposure from the cold temperature. If adjustments to any of the heating rates or switching of any of the modules was required, then the perspex lid can be removed. Further discussion of the Control Centre System internals and design of all the associated circuitry will be discussed in Section 5.2.2.

5.2.1 Temperature Measurement

The measurement and logging of temperature during ice growth is ubiquitous in ice growth studies (Marks et al., 2017; Notz, 2005; Weeks, 1962; Wiese et al., 2015) , with the logging of a complete temperature record over the entire ice growth history cited as one of the biggest advantages of artificial sea ice set-ups (Haas, 1999). Accurate, closely-spaced temperature measurement during ice growth also enables the calculation and inference of other properties such as ice depth (Markset al., 2017; Wiese et al., 2015),, salinity (Notz, 2005) and even brine drainage (Lake and Lewis, 1970).

Thus, the choice of datalogger and temperature probes was crucial to ensure that the most accurate temperature record during ice growth can be kept. Keeping in mind the design objectives for the study, the chosen temperature measurement module needs to primarily ensure accurate measurement of temperature, with the ability to measure and log many temperature probe inputs simultaneously. The system also needs to be cost effective, durable and simple to manufacture. Temperature probes were identified as the first design option to decide upon, since they generally account for the largest degree of measurement error within the temperature measurement system. For the measurement of in-situ temperature within the saline solution, the growing ice, and ambient temperature, three possible probe options were identified from literature. A decision matrix was constructed to assess the options (shown in Table 5.7).

Table 5.7: Decision matrix table for temperature probe selection

Probe Type	References	Primary Objectives	Secondary Objectives			Sum
		Accuracy (x3)	Cost (x2)	Durability (x2)	Manufacture Simplicity (x1)	
Thermocouples	Weeks and Cox, 1974 Marks et al., 2017	1	3	4	4	21
Thermistors	Notz et al., 2005 Wiese et al., 2015	4	2	3	0	22
Platinum Resistance (RTD)	Barrette and Jordaan, 2001	4	2	2	3	23

The accuracy of the possible probe options was assessed on a general basis, since thermocouples, thermistors and platinum resistance probes all have a large possible range of accuracy, and depend on the quality of the chosen probe. However, it was generally noted that higher accuracies are possible using thermistor or platinum resistance probes (known as RTD's) (Texas Instruments, 2019). The higher accuracy does imply a higher cost per probe, since it consists of a more complex system with added measurement circuitry required.

Thermistors scored highly in accuracy, cost and durability, however, it proved impossible to locate them or acquire the components necessary to manufacture them. Therefore, they received a manufacture simplicity score of 0. Therefore, the outcome of the assessment showed that

platinum resistance probes, specifically Pt100's, were the best choice, ensuring high accuracy and were easily obtainable.

A datalogger capable of reading and recording the inputs from the Pt100 was required. A Campbell Scientific CR5000 datalogger was procured. The datalogger measurement was accurate to within 0.1 % of the probe reading for RTD probes. Full specifications of the CR5000 datalogger can be found in Appendix A.1. The logger memory is capable of storing over 240 000 values, which allows for logging and recording temperature results at 5 minute intervals for the duration of 1 month. The results can accessed via a USB cable and a laptop. This logger is capable of connecting to and measuring inputs from thermocouple, thermistor or RTD temperature probes. Therefore, the option was open to switch to thermistors at a later stage if these can be sourced.

The datalogger had 20 analogue differential (voltage) measurement channels. While this would natively allow up to 20 thermocouples to be connected to be connected and measured simultaneously, matching this number with RTD probes has an additional challenge. Thermocouples are passive components requiring only a measurement of voltage using the analogue differential channel and a temperature reading from a reference thermistor contained within the datalogger. RTD's are referred to as active components, requiring a voltage to be applied over their temperature dependent resistor, and the resultant voltage drop being measured using the analogue differential channel. The CR5000 datalogger only has four voltage excitation channels, each capable of supplying a excitation voltage to a maximum of four probes at once. Thus, the datalogger can natively only supply excitation voltage to a maximum of 16 RTD probes. In addition, RTD probes require a slightly more complex connection with additional components in order to accurately measure temperature. Figure 5.14 taken from the CR5000 User manual (Campbell Scientific, 2006) shows the required three wire half bridge circuit for connection of each RTD probe to the datalogger.

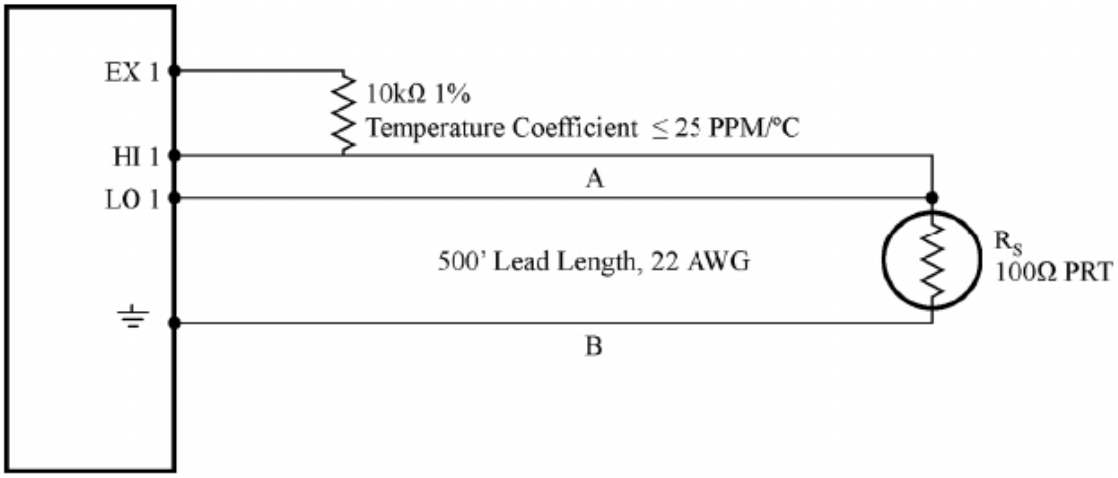

Figure 5.14: 3 Wire half bridge for Pt100 probes (Campbell Scientific, 2006)

The circuit involves an additional highly stable resistor, which is used as a reference point for the measurement. A simple circuit was designed (See Appendix A.1.1), using a relay to enable one voltage excitation channel to excite an additional four RTD probes, allowing all 20 RTD

probes to be connected. Calculation of the required excitation voltage and initial input parameters for conversion of the measured voltage to temperature was carried out using the directions given in the user manual. The conversion equation used by the CR5000 datalogger is based on the Callendar-Van Dusen equation (Fernicola and Iacomini, 2008).

The CR5000 datalogger with additional circuitry is seen in Figure 5.15. The additional circuit also included plugs for quick connection of the RTD probes. The relay is switched using one of the controller channels on the datalogger, with a small piece of additional code written in the measurement program. The customization of this measurement program allowed for additional tasks to be carried out by the datalogger, such as the heating and temperature control of the control center box, the connectors for this system can be seen in Figure 5.15 labelled "H.Box-Fan" and "H.Box-Heat". This box heating system will be further discussed within the next section.

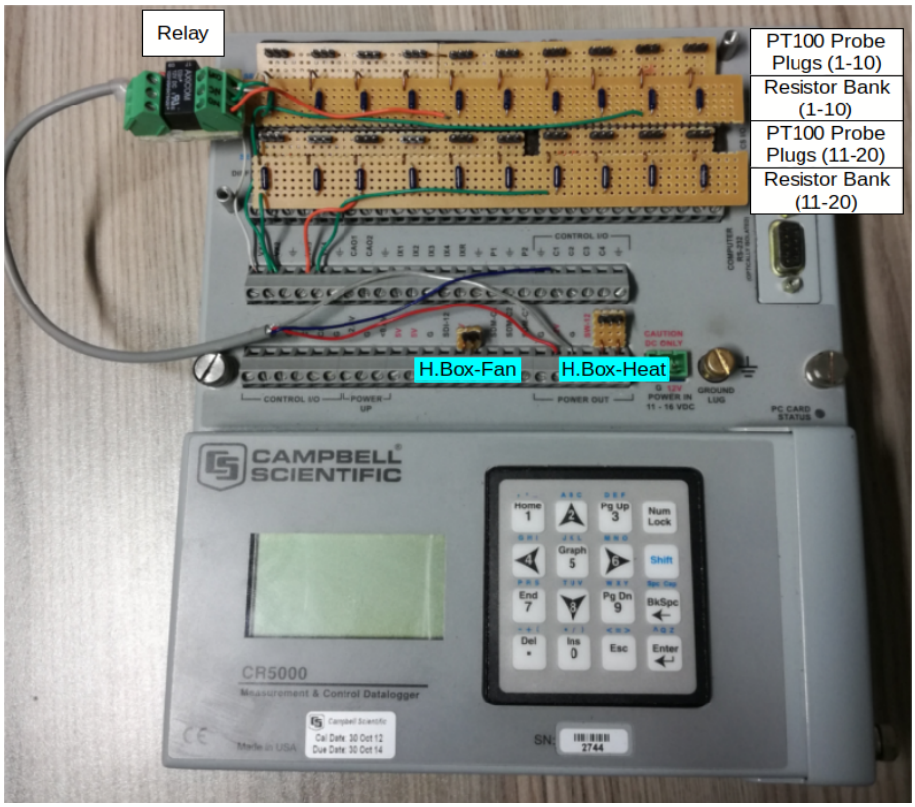

Figure 5.15: Campbell CR5000 Data Logger with Additional Circuitry

Calibration of the probes was carried out using a two-step process which was verified by similar calibration methods in literature (Garnett et al., 2019; Wiese, 2012). The temperature probes are placed in an agitated beaker of pure-ice water slush, where the temperature will be exactly 0 °C. Temperature measurements are taken at a 6 second interval, a safe minimum interval ensuring that the sequential measurement of each probe, and switching of the voltage excitation relay was safely carried out. The measurements were taken for a duration of three minutes. The temperature results from each probe were averaged, and both the average temperature and maximum deviation from 0 °C was assessed for each probe. If the result of the average measurement error was greater than ± 0.2 °C, or the single maximum deviation was greater than ± 0.5 °C, the probe was identified

as faulty and discarded. While some adjustment may have been possible, it was a tedious process and identified as too risky, with too many possible causes of the error to ensure that the adjustment had a high chance of success.

The second calibration step was carried out at the beginning of each experiment, while the solution was at room temperature. The tank agitation was set to maximum and the temperature measurements interval was set to the minimum 6 second interval. The temperatures were recorded for a duration of 5 minutes. The mean deviation for each probe was calculated by taking the temperatures for all 20 probes over 5 minutes and averaging the results to one value, and comparing this value to the average temperature for each individual probe. This calculated deviation, or offset, for each probe was then added to the respective probe for all temperature measurements during the subsequent freezing experiment.

A frame was required to hold all the temperature probes in placed during the freezing experiment. Additionally, the planned layout of the probes required consideration, since 20 probes was a limited number with which to retain a good resolution of the temperature evolution within the tank. The temperature probe set-up was dictated by the two focus areas. Namely, ice focus or tank focus. Ice focus was the primary focus area, where the priority was placed on small vertical spacings of temperature probes within depth where ice growth was located, allowing for maximum resolution and analysis of in-ice temperatures and ice growth rate. Tank focus was useful for measurement of temperature evolution throughout the entire tank, used for when there was no agitation and therefore thermal stratification was expected. PVC piping was used to create scaffolds (Figure 5.16) for holding the temperature probes at their desired location within the tank.

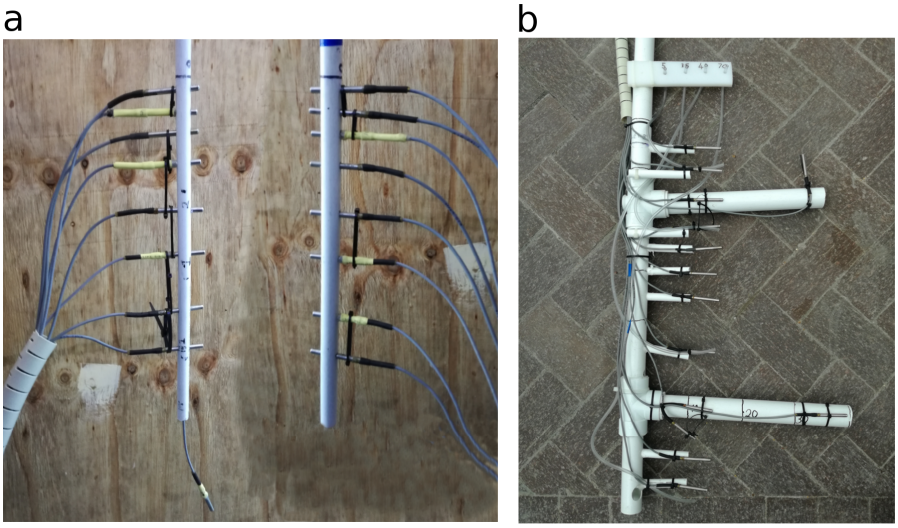

Figure 5.16: Probe set-up for a) Focus on in-ice temperature measurement and b) Entire solution temperature measurement

PVC was used since it is inert and will not corrode in saline water. It is light, low cost and easy to work with. It has a low thermal conductivity, which was very important so as not to disturb the temperature gradients within the ice and saline solution. The ice focus probe set-up consists of

two identical temperature strings, which are hung from above the tank, with each consisting of 8 probes located at depths between 0-30 cm , where maximum ice growth was expected. A probe was placed at 45 cm within one of the strings , with a final two probes(not shown) being placed to measure the ambient temperature above the tank and one at the bottom of the tank, at 70 cm depth. The 20th probe was used to measure ancillary temperatures such as pressure relief, side heating, or areas of interest within the tank. The set-up can use fewer probes at lower depths, since the agitation will ensure uniform solution temperatures. Two probe strings are used for redundancy and so that any variations in temperature and cooling rates experienced across the tank can be measured. The vertical spacings within this range are not consistent, with a higher concentration of probes near the surface. This configuration of varied vertical spacing has been used by set-ups such as those described by Notz (2005). This allowed the highest resolution of temperature measurement describing initial ice growth, when the growth rate was fastest.

The probe are located at depths of 1, 3, 5, 8, 13, 18, 25 and 30 cm. The smallest vertical spacing, at the probes at depths of 1, 3 and 5 cm give good resolution for the initial ice growth. Unlike thermocouples, RTD's have a fairly large physical footprint, with the electronics being insulated and protected in a rounded metal cylinder 3 mm in diameter. The physical footprint of the probe limited how closely spaced they could be and also implied that the measured temperature was the average temperature conducted from any water/ice making contact with the metal cylinder of the probe, rather than a point measurement such as those used by Lake and Lewis (1970). Point probes were not used since the degree of location accuracy was not deemed to be necessary.

The tank focus probe set-up was not used with agitation but may be useful for experiments where thermal stratification was to be analysed. It consists of an adjustable PVC scaffold where probes can be placed at any depth with 5 cm intervals, and two adjustable cross bars that can be set to measure the horizontal temperature variation at any desired vertical depth. The scaffold slots into a base on the bottom heating module, allowing it to easily be vertically mounted within the tank.

5.2.2 Tank Control

The tank control consists of the all of the electronic modules within the tank such as the pressure relief heating, bottom heating, side heating and depth measure modules discussed in Section 5.1. Also included within this system was the datalogger power circuit, temperature control for the control centre and mains power for all of these modules.

After consideration of the required power input for the heating modules, the decision was made to use 230 V AC electrical systems. Moving to a lower voltage DC system would have required higher currents in order to obtain the same power as well as additional transformers and rectifiers. The safety implications of this decision were carefully considered. Lower voltage DC current is generally deemed safer since the resistance of our skin prevents lower voltage from causing electrical shock. However, in the presence of moisture, especially conductive salt water, even lower voltage can cause shock, as experienced with a 9 V battery on the tongue. Since the required power remains constant, lowering the voltage would have required a corresponding increase in current (P = VI). The electrical current is what causes shock, with AC currents higher than 20 mA rated as potentially fatal and 500 mA for DC (NIOSH, 1998). Therefore, using either

of these voltage sources would have resulted in currents potentially deemed fatal. Many household appliances also require currents exceeding these limits, requiring safety systems to prevent injury or death. Therefore, by using the same 230 V AC power delivery, as used by household appliances, the same safety systems can be implemented. These consist of a fuse located within the designed control system, which will break in the event of a short circuit, shutting off electrical supply. Secondly, the tank was grounded through the earth of the power input. If a current greater than 30 mA passes through the earth line, the circuit breaker will immediately trip. This grounding line is the preferred path of current flow, and thus would identify and trip any short circuits occurring within the tank due to waterproofing breakdown before an accidental touch of the "live" water would occur. Connection points between the electrically operated tank modules such as the bottom heating, side heating and pressure relief module to the control box were identified as vulnerable points of electrical safety. These connection points were necessary in order to allow the modules to be easily moved and disconnected. To combat this vulnerability, IP68 waterproof connectors were used. All powered systems were switched off and disconnected before ice sampling took place, in case cutting of the ice severs heating element. With the implemented safety measures, the tank electrical system was deemed as safe for laboratory use when the correct safety procedures are followed. The layout of the control centre is shown in Figure 5.17.

The system circuit diagrams and image of rear electrical wiring panel can be found in Appendix A.1.2. Considering the objectives of being low cost, simple and portable, the control systems were kept as simple, using off the shelf components that are easily available. If it was identified that more advanced control of a module was necessary, components could always be upgraded at a later stage. Thus, as a means of controlling the heating rates, Silicon Controlled Rectifier (SCR) dimmers commonly used for the dimming of light bulbs were used. This allowed an adjustable, predictable means of controlling the heating rate by turning of a dial. However, this method does not provide an indication of the level of heating, and the dial control was not linear. Therefore, it was necessary to experimentally determine the required levels of heating by measurement of the resultant temperature increase induced by each module, with the correct heating rates and dial positions being marked.

Not shown in Figure 5.17 is the 230 V AC input (C1), which is delivered to the back panel before being routed to each control module. Each module has an indicator LED which shows when the module was turned on and providing heat input. The datalogger is the only system running of 12 V DC, requiring a power supply to convert the 230 V AC input (C2). The bottom heating controls (C4) consist of the temperature controller, shown by H.B Temp Relay, and the dimmer controlling heating rate. The temperature controller in C4 is individually powered. through C3 which is shown within Appendix A.1.2. The pressure relief system consists of a heat rate controller and a time relay (C3). Initially the time relay was used so that the module was only periodically on, adjustable to 15 minute intervals. However, it was decided that a constant low heat rate was adequate and thus this relay was bypassed. The side heating (C6) module consisted of a dimmer for adjustable heating rate and switch. The circuit to provide heat to the depth measurement system to free it from the ice, (C7) consisted only of a switch, since it is only powered for short intervals and the maximum heating rate during was desired.

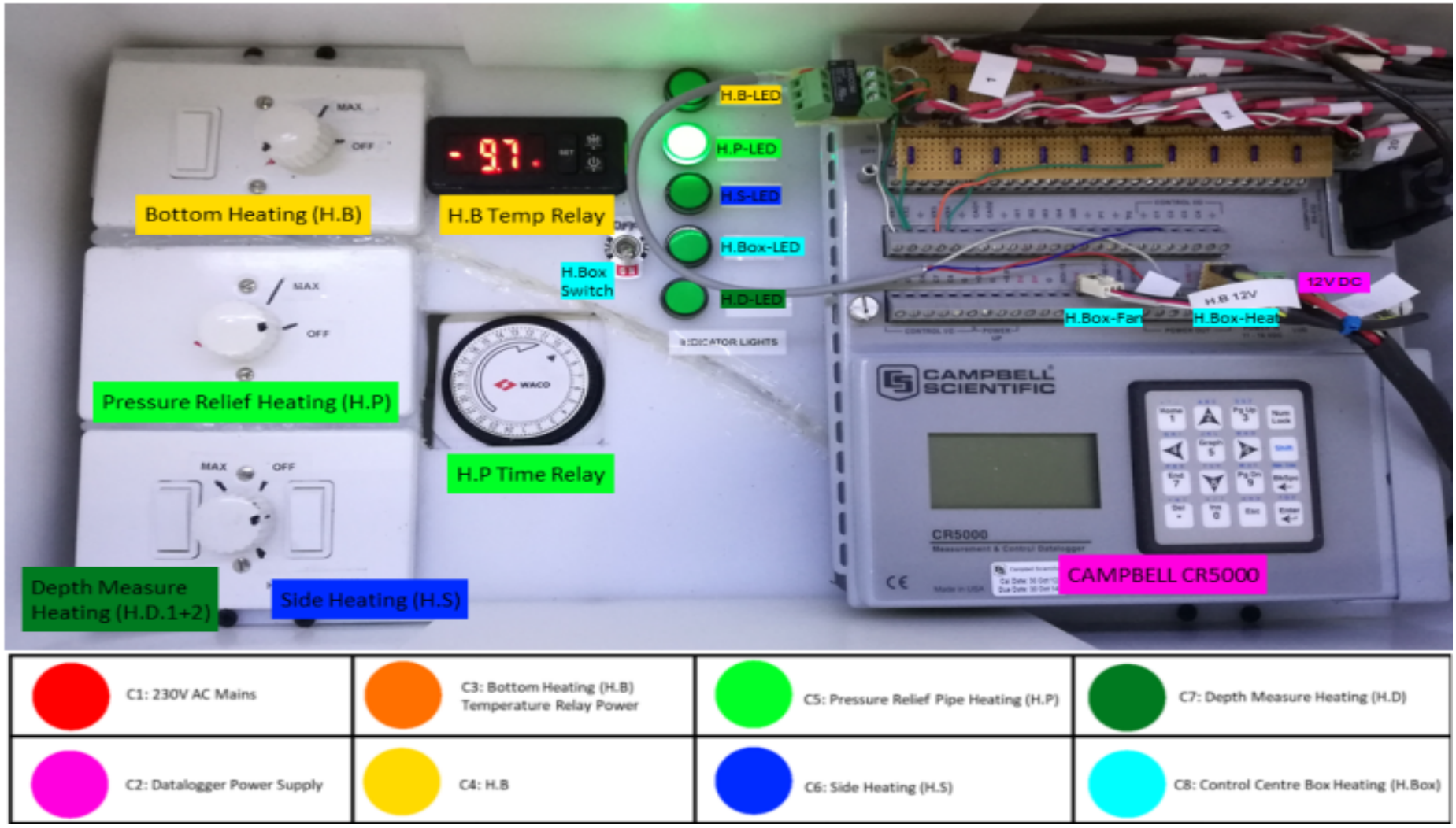

Figure 5.17: Front view of the tank control center, with label overlay to show controls of each individual module

The design of the control box heating circuit (C8) shall be discussed in greater detail since it has not been previously introduced. The box heating was required to maintain moderate temperatures within the box, primarily to protect the more sensitive electrical components within the datalogger and bottom heating temperature controller. To accomplish this heating, 1.2 m of heating tape producing a maximum of 80 W with a rate controller was situated within the box, underneath the front panel shown in Figure 5.17. The rate controller was not made accessible since after initial set-up, since it should not require adjustment, and accidental adjustment could have detrimental effects. The box heating relied heavily on the abilities of the datalogger to provide switched and constant low voltage power, and its internal temperature sensor. A small computer fan was connected to the constant power supply (H.Box-Fan), and blown over the heater tape, so as to aid in heat dispersion. The fan was always on, however, the heating was switched on and off as required.

A simple program was written on the datalogger, that would record the internal temperature of the datalogger, and switch a small relay with 12 V DC if the temperature was less than 9.3 °C. The small relay would in turn switch the 230 V AC heating tape on. The system would then switch off when the temperature reached 10 °C. A temperature profile of the internal box temperature over time is shown in Figure 5.18, where the ambient temperature in the cold laboratory was set to -20 °C.

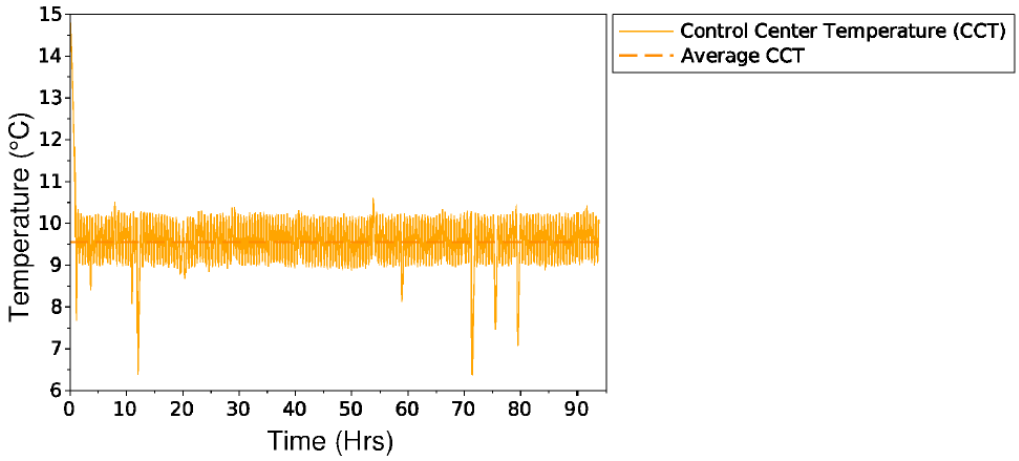

Figure 5.18: Temperature versus time of control box, controlled by heating circuit

The average temperature within the box was 9.56 °C over the 96 hour duration. Sharp decreases shown within the profile where the temperature drops below 9.3 °C indicate when the box was opened to adjust something inside, exchanging a significant portion of box air volume with the ambient -20 °C air. The internal datalogger temperature sensor is not directly exposed, and therefore would not directly record the air temperature. Rather, it reflects the cooling effect on all the components within the box, and will be affected at a slower rate than the air temperature. Thus, due to the insulating properties of air and its low heat capacity, a decrease to -20 °C was not seen, despite the opening of the control center. The maximum negative deviation from the low setpoint was 2.5 °C. This temperature drop required a time of around 50 minutes to return within range. Even without the opening of the control center, a high degree of fluctuation can be seen within the temperature profile. Despite this high degree of oscillation and the 50 minutes to

return the box temperature to its desired range, a higher heating rate was not considered.

Primarily, this was a safety consideration. While it was not ideal, the datalogger and all the components within the box are capable of withstanding -20 °C temperatures. However, if the heating control was to over-heat the box, the datalogger could be affected, and in extreme cases the high temperatures could cause a fire-risk. The temperature was not measured at the point of heat generation, and therefore there was a delay in the measurement time of the temperature increase caused by the heating. It was not know whether the temperature at the source has risen higher than acceptable levels, which could begin to heat electrical components, causing possible damage or risk of short circuiting caused by melting insulation. Placing a temperature probe closer to the heat source would not solve the problem, since this would mean the heating system would turn off pre-emptively before the entire space and all the components were within the desired temperature range.

Another issue with a higher heating rate was if the feedback system fails, the system could fail open, and continue to heat the box, with a higher heating rate having the aforementioned concerns of component damage and fire-risk. With the present heating rate, the system was tested at fail-closed, where the heating remains on and it was found that if ambient temperature was at -20 °C, the internal box temperature would stabilise at about 35 °C. The datalogger was rated for operation in a temperature range of - 25 to 50 °C. Therefore the maximum temperature of 35 °C was deemed to be low risk.

Additional fail-safes were added at software level, to shut off the heating in the event of any anomaly in temperature readings within the box, as well as hardware level with a fuse to trip in the event of any electrical short. A higher heating rate would also result in greater upward temperature oscillations. The system could potentially experience the same initial problem as seen with the bottom heating system, where the temperature, since it was measured at a different location from where it was the heat was generated from, would continue to rise even after the upper limit has been reached and the heating has been switched off. It would also mean the relay was being switched more rapidly. This would cause additional wear, decreasing its lifetime.

At the same time, it could be argued that a lower heating rate would be advantageous, since it this would further increase the lifetime of the relay by limiting its cycles. If a constant heating rate could be found to combat the heat loss, the relay could be removed entirely. However, this would not be able to reheat the system when the box was open, nor would the constant heat rate be able to account for ambient temperature changes or if the ambient cooling was shut off entirely.

In summary, the control center provided a simple, low-cost and portable means of housing the tank control modules as well as the datalogger for temperature measurement. The internal temperature of the control center was regulated, and the feedback circuit was found to keep the system within the desired temperature range, with an average temperature of 9.56 °C.

5.3 HeatGen Program

A record of temperature readings taken at a variety of locations throughout the tank enables a detailed picture of the temperature temporal evolution. This allows 2D or even 3D temperature profiles and ice development over time to be generated, which is crucial for the analysis and explanation of ice properties. To aid in the processing of the raw temperature data from the datalogger and to assist in standardising the most useful temperature analysis plots, a program was developed in Scilab. This program, named ”HeatGen”, is essentially a Graphical User Interface (GUI), for performing some useful processing steps and generating a variety of different temperature profiles for the data analysis step. The name stems from the initial, primary function of the program, the generation of temperature heatmaps. The GUI simplifies and speeds up the generation of useful temperature derived profiles, and was also advantageous in that it does not require users to be capable of programming in Scilab to easily access functions written within the program. As long as Scilab is installed on the computer, the HeatGen program can be opened independently, with no need to load and run it by first opening Scilab and using the console. Simultaneously, it still consists of easily accessible Scilab modules, so that users that are competent in Scilab are able to adjust the functions and easily make changes to the internal parameters if desired. The HeatGen GUI is shown in Figure 5.19.

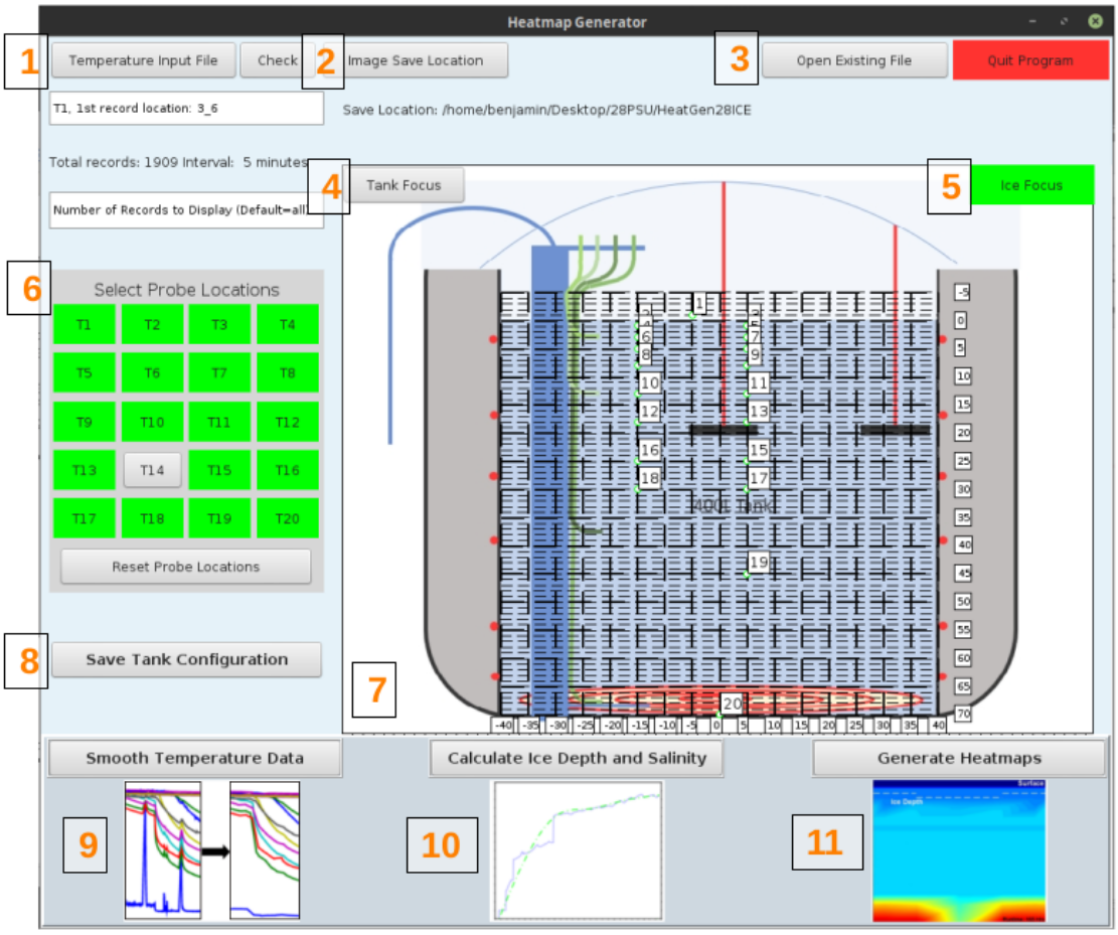

Figure 5.19: The graphical user interface of the developed HeatGen program, with primary functions labelled from 1-11

The functions of HeatGen program (labelled from 1-11 within Figure 5.19) are described below.

1. Input of the raw temperature files in .csv format from the datalogger. The location of the desired first record for the analysis is entered in the block contained "T1, 1st Record Location", which provides the ability to filter out unwanted initial data which may occur before the start of the desired measurement time. Using the "Check" button then shows the user the number of records the file contains as well as the measurement interval.

2. Save location for the profiles and generated data from the program. This save location is then shown below for confirmation. Open an existing file. The settings and input files for HeatGen, including the temperature probe locations seen in #8 can be saved to a file using function #3 which is stored for subsequent re-opening at a later time.

3. "Tank Focus" allows the selection of a wide grid spacing for temperature probe placement on the schematic. The location of each temperature probe used during the experiment can be mapped by the user on the tank schematic shown by #7. Depending on the temperature probe set-up used (discussed in Section 5.2.1), a location grid of different spacings can be selected. Tank focus is a macro scale grid, used for experiments where the temperature measurement focus is over the entire tank, and has grid spacings representing 5 cm of distance within the tank.

4. "Ice Focus" is a grid for mapping of temperature probe locations with fine spacing, and is shown selected in Figure 5.19. It is used primarily when the focus is on the temperature profiles within the ice, therefore requiring a larger number of temperature probes to be placed in a smaller space, with smaller spacings between them. This grid enables a much finer control over the mapping of temperature probes, with the grid spacing representing 1 cm vertical distances within the tank. The horizontal spacing remained at 5 cm, since the exact horizontal location of the probe was not considered of primary importance. This shall be discussed in greater detail later in this section.

5. "Select Probe Locations" allows the probes used within the experiment to be selected for mapping onto the tank schematic shown by #7. The user selects the desired focus on the tank, using functions #4 or #5, which then displays the desired mapping grid. It is then possible to click on the probe number from the list in #6 and select its location on the schematic in #7. Once the probe is selected it is displayed in green, and its location is displayed on the schematic is shown by a green dot and a label with the probe number on it. If a mistake in placement is made, the "Reset Probe Locations" is used to remove all mapped probes so that the placement can be inputted correctly.

6. Tank schematic for plotting of the temperature probes listed in #6.

7. Allows for the saving of the mapped temperature locations, raw temperature input file and other settings to be saved for later use. Once saved, a user can re-use the settings at a later stage by clicking on #3. This will automatically repopulate all settings and temperature probe locations for the generation of further profiles or regeneration of old profiles.

8. Smoothing of the temperature profiles to remove anomalies and defrost cycle spikes.

9. Calculation of the ice depth and salinity profiles over time, which can be inferred from temperature data. The method development for this calculation shall be discussed in further detail in Section 5.4.

10. Generation of the tank temperature heatmaps, outputted as both PNG and video format.

Mapping the temperature probe position through a GUI interface enabled a faster, more intuitive method over manual, console entry. This also results in a reduced error in probe placement, since the eye will more easily notice a mistake in placement in a visual map rather than numeric matrix. The temperature mapping is used for many of the temperature profiles that HeatGen can output, and is crucial for use in the calculation of ice depth as well as the heat map image sequence.

While the temperature results from the freezing experiments were mostly averaged values of readings taken every 6 seconds over the course over 5 minutes, they still contained a large degree of temperature fluctuation. This is not indicative of faulty temperature measurement, since these fluctuations in temperature over time occur even in field experiments (Lake and Lewis, 1970). If anything, it may suggest an inconsistency of the cooling unit to maintain a precise temperature. Combined with the defrost cycles, the raw temperature profiles are extremely noisy. While this may accurately represent the temperature experienced within the tank, and should always be consulted and referred to when considering the ice history, it does not allow for the accurate fitting of trend lines, or data modelling. Therefore, further calculations such as those of ice depth based on the data becomes difficult to accomplish. Therefore, a function to smooth the data was developed. A cubic spline smoothing function was investigated using the Scilab function "smooth". However, it was found that the function smoothed temperature decreases that were deemed to be important for the subsequent calculation of ice depth, solution salinity and the temperature heatmaps. Therefore, a linear smoothing function was developed that would identify and remove temperature increase spikes that were classified as a defrost cycle. A comparison between the cubic and linear smoothing functions, as well as the Scilab code for the utilized linear smoothing function can be found in Appendix A.2.

Incorporated into the HeatGen program was the function that modelled ice growth based on the assessment of a linear temperature profile. This is a reasonable assumption and has been used by Marks et al. (2017) to determine ice depth. The development and accuracy of this model is shown in Section 5.4. In addition, by knowing the temperature of the well-mixed solution and assuming that pressure is constant, the bulk solution salinity can be determined, since the solution is deemed to be at freezing point (Weeks and Cox, 1974) and the temperature-salinity relationship is linear (Figure 2.8). While more accurate methods of real-time salinity measurement can be used, such as a CTD deployed at the bottom of the tank, this method was deemed adequate for this small scale system where the aim is for samples grown for mechanical testing. If more detailed ice growth studies are intended, then a CTD for bulk solution salinity measurement and indeed a more advanced ice depth measurement system, such as sonar, is recommended.

During temperature analysis, a need was identified for a method to visualise the temperature evolution throughout the tank area. To accomplish this, a heatmap of the temperature within the tank for each point in time was generated. These heatmaps could then be spliced together into a video clip, showing the temperature evolution over time and enabling a qualitative analysis and aiding in the identification of anomalies which can then be explored in greater detail using other plots. To generate these heatmaps, a Scilab function called "Sgrayplot" was used. This function requires the input of an r x c matrix the size of the area in question, in this case the size of the tank, with a temperature value for each location within the matrix. The chosen r x c matrix was base on the chosen grid at function #4 and #5 seen within Figure 5.19. If the tank focus was chosen, the 5 cm tank spacing resulted in a 17 x 16 matrix. If the 1 cm grid was chosen, the resultant matrix which needs to be populated with temperature values is 17 x 76. With a maximum of 20 temperature probes, it was not possible and highly impractical to measure the real temperature for each of these location points. Thus, a significant step of in the heatmap generation is the population of this grid from the maximum of 20 known values. The grid population is based on a number of assumptions that were made about the tank properties and heat fow characteristics. These were necessary in order to model the heat fluxes and populate the grid (see Appendix A.2 for grid population). These are as follows:

1. The insulation and side heating results in no horizontal heat flux. Therefore, unless the temperature at two points along the same horizontal line are specifically measured, it can be assumed that all locations along the same horizontal line will be uniform.

2. The primary temperature gradient is in the vertical direction, with the direction of heat flow out the top of the tank.

3. There is a linear temperature gradient between any two known temperature values.

4. The ambient temperature will be uniform across the entire tank surface

While it is known that in reality these assumptions will not hold true, it still should enable a good representation of the heat flow within the tank, and improves with the number of temperature probes placed in the tank. Once the grid has been populated, the matrix is passed through the "Sgrayplot" function, the colors and associated temperature range is chosen to provide maximum detail at the range close to where phase change occurs. With ambient temperatures of -20 °C and freezing point of a 34 g kg^{-1} solution at -1.8 °C, representation of the entire range would not show good detail of what is occurring at the ice-solution interface. Therefore, the ambient temperature and colder ice is shown at the lower limit of the range, even though they are actually at much lower temperatures. A plot is generated for each time interval throughout the ice growth. The user can select extra information to show within the plots, such as temperature probe location, a line representing ice depth which can either be from manually measured values or from the calculated ice growth method which is discussed in Section 5.4 and is also incorporated in the HeatGen program. An example image sequence of the heatmaps generated by HeatGen is shown in Figure 5.20.

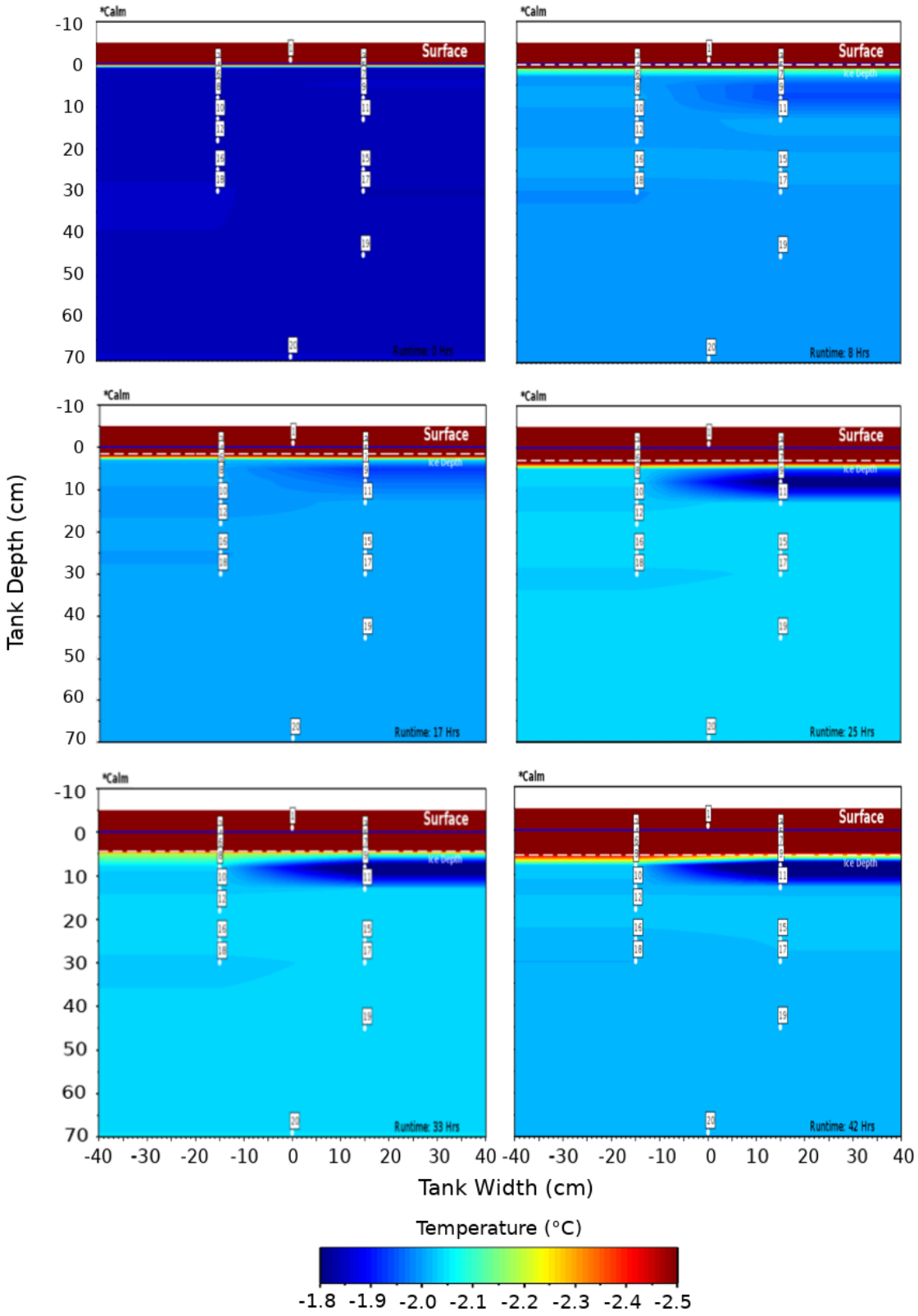

Figure 5.20: Example temperature heatmap image sequence from HeatGen, over for a period of initial ice growth, shown for a duration of 42 hours, with images shown at 8 hour intervals. The small, white squares show the locations of the temperature probes

5.4 Temperature Derived Depth Measurement

It is known that sea ice displays a temperature profile that can be well-approximated as a linear function of depth (Weeks, 2010). Therefore, it was possible to use the temporal evolution of the temperature profiles seen in Figure 5.21 to determine ice depth by identifying the point of gradient change, which represents the ice-solution interface.

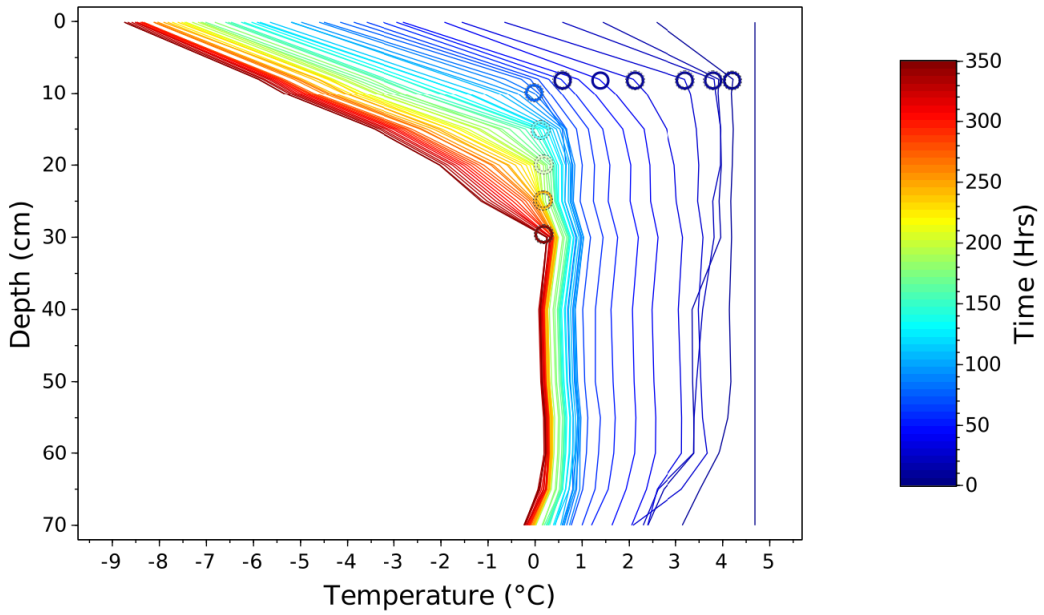

Figure 5.21: Depth versus temperature profiles over time, showing the linear in-ice temperature profile, with the approximate ice-solution interface point shown with open circles

This linear assumption will not entirely hold true, since brine drainage moves colder brine down through the ice towards solution, which can be picked up by the temperature probes as temperature fluctuations (Lake and Lewis, 1970). However, it has the advantage of being a continuous, non-intrusive measurement system. A disadvantage with this system, was that the calculation was carried out using the temperature results taken off the datalogger, which were only collected at the end of the experiment. Therefore, while the temperature measurement was continuous, neither the temperature nor the resultant ice depth can be monitored in real time. Nevertheless, this method has an advantage over the manual depth measurement system, since it does not disturb the ice formation by lab entry, and does provide continuous, rather than intermittent monitoring.

5.4.1 Model Development

The model of the temperature derived ice depth measurement was developed in Scilab since it incorporates well with the existing HeatGen program also developed in Scilab. This allows for the easy carry-over of probe locations and depths and for the subsequent incorporation of the calculated ice depth into other plots such as heatmaps.

Using the straight line approximation of temperature within the ice, one can use the gradient change between the ice portion of the temperature profile and the underlying solution temperature profile so as to identify the last known probe depth in which ice occurs. By using gradient change,

rather than identifying the depth at where the expected freezing point temperature was exceeded, the model should be valid for any starting solution salinity.

The model plots points of temperature as a function of depth. Using the Scilab function "datafit" , a straight line was fitted between a successively greater number of data points (Figure 5.22).

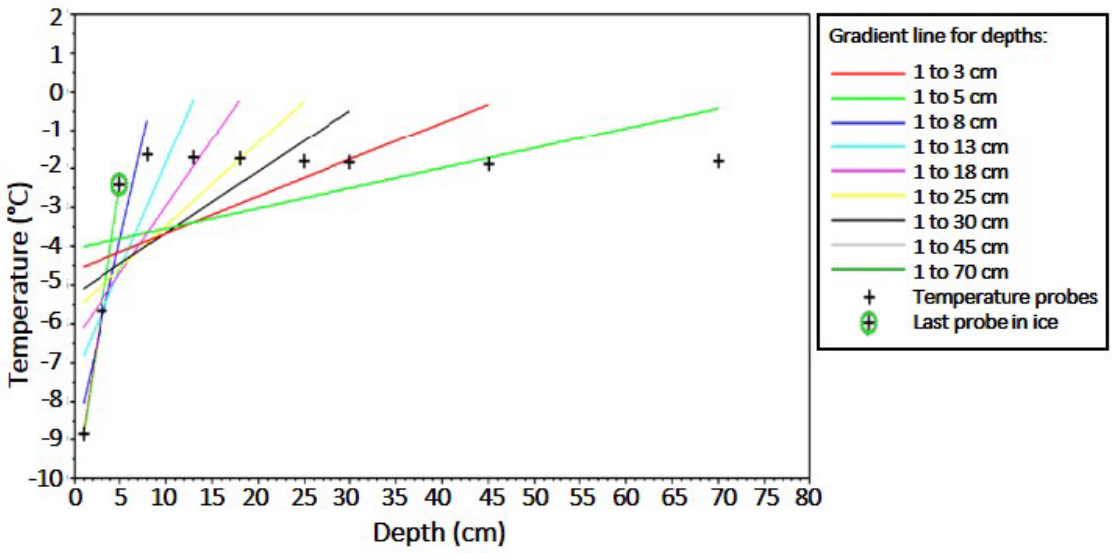

Figure 5.22: Example plot showing the temperature probe depths and associated temperatures (+) and the plotted linear lines of best fit used to calculated the temperature derived ice depth. The identified last probe within the ice is highlighted with a green circle

The least squares error for each straight line fit was stored. It was found that a simple limit for the error could be established, such that an error greater than the limit value represents the fit of a line to points that are no longer solely within ice. Thus, the equation of the linear line can be found using the gradient and constant value calculated up to the last value within the ice. However, the last probe within the ice does not give the full ice depth. To determine the actual location of the ice-solution interface, the average solution temperature was first determined using the results from all the underlying probes. Subsequently, by equating the linear equation of ice depth to the average solution temperature, the depth of the ice-solution interface can be estimated. The Scilab code for the temperature derived depth function can be found in Appendix A.3, along with the data for three time points as an example.

The model does require a high probe resolution to accurately calculate ice depth. A minimum of two probes are required within the ice in order for the model to begin predicting ice depth, since a gradient function requires at least two points. To ensure that the model accurately predicts initial ice growth rates, the frst two probe depths need to be spaced as close as possible to one another. The model output was subsequently passed through a cubic spline Scilab smoothing function to phase out anomalies and provide a more consistent growth rate. The results of two validation experiments of the model is discussed below.

5.4.2 Validation Experiments for Temperature Derived Ice Depth Model

In order to validate the model, two ice growth experiments were conducted, one using freshwater and one using a saline solution of 34 g kg^{-1}. During each experiment, the solution was placed in the tank and the ambient temperature was set to -20 °C. Temperature was measured using the datalogger and the ice-focus probe set-up (Discussed in Section 5.2.1). The ice depth was measured throughout the experiments using the manual system of depth measurement presented in Section 5.1.7. to measure the ice depth in the middle of the tank between the two temperature probe strings. The results for the freshwater ice growth experiment of the manually measured ice depths, gradient calculated ice depths and the subsequent smoothed ice depth profiles are shown in Figure 5.23.

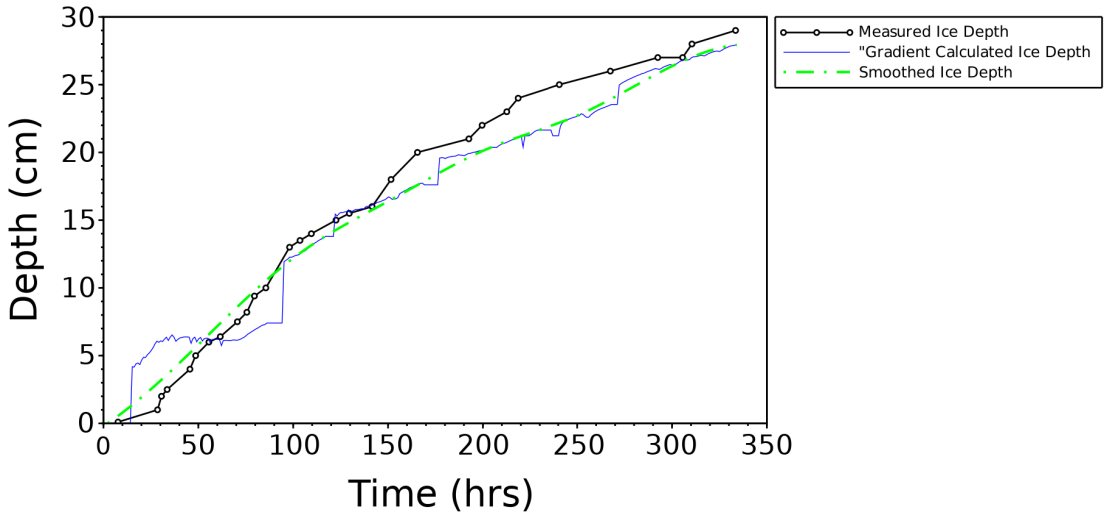

Figure 5.23: Freshwater experiment: manually measured ice depths, gradient calculated ice depths and the subsequent smoothed ice depth profiles

The overall trend of the three different ice depth profiles are seen to have a $\sqrt{x}$ shape, which is similar to that found in a previous study of artificial sea ice (Cox and Weeks, 1975). The gradient calculated ice depth shows rapid increases at 10 hours and again at 100 hours. This did not correspond with any rapid increases within the manually measured ice depth profile. It was postulated this increase was a result of the incorporation of a new probe point into the linear line of best fit, once the ice had reached a new probe depth. The probes only measure the temperature at discreet depths within the tank. When ice growth is between these probe at different depths, the model needs to predict the ice-solution interface using the equation of linear fit from the last known probe situated within the ice. If the temperature gradient of the previous probes produce a line of best fit with a low gradient, the predicted ice growth rate may reflect a slow increase until it is corrected by the incorporation of the next probe. This incorporation of the next probe resulted in the sudden increase in depth. The smoothed ice depth profile adjusts for these sudden increases in depth due to this inadequacy of the model to predict to predict change in ice depth between two probes. Visually, this smoothed ice depth profile matches the manually measured ice depth profile reasonably well. However, statistical confirmation of this was also carried out.

Shown in Figure 5.24, the smoothed temperature derived ice depth profile was plotted against the manually measured ice depth profile. A perfect direct correlation between the calculated and the manually measured ice depth profiles would fall directly on the y=x line, indicated by the sold black line. The bounds defining a correlation within $\pm$ 10 % are shown with black dashed lines.

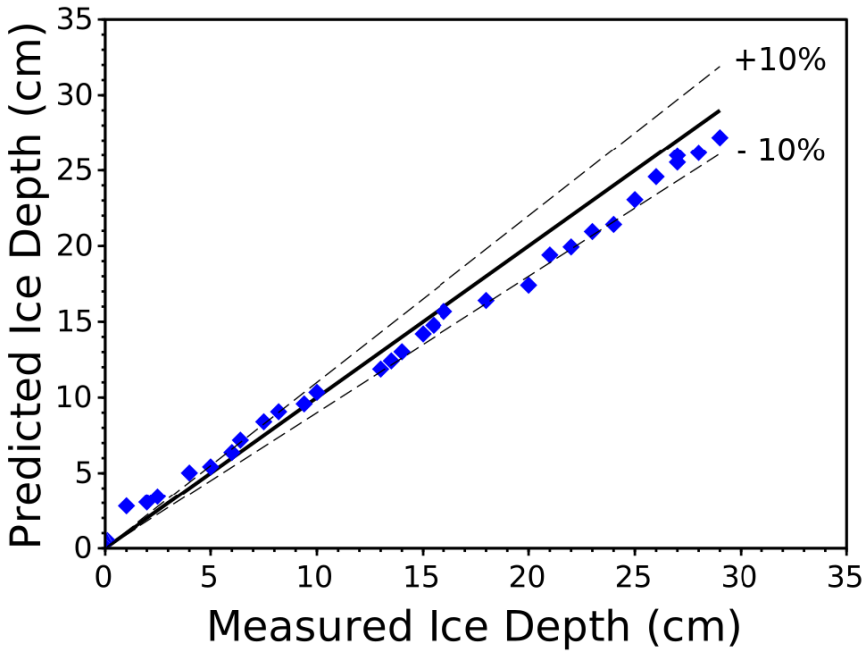

Figure 5.24: Correlation of the manually measured and the smoothed temperature derived ice depth profiles for the freshwater experiment. Perfect correlation shown by the solid black line, with $\pm$ 10 % bounds shown by the dashed lines

The smoothed temperature derived ice depth profiles showed a good correlation, within $\pm$ 10 %, to the manually measured ice depth profile. Table 5.8 shows fit parameters for the correlation.

Table 5.8: Fit parameters for the correlation between the manually measured and the smoothed temperature derived ice depth profiles for the freshwater experiment

Parameter	Low	High
R^2 Value	0.977	
Standard Deviation Of Error	0.665	
Error Range	-2.59	1.80
Percentage Split	60.0%	40.0%

The R^2 was 0.977, which was indicative of a good fit. The standard deviation of error was calculated as 0.666 cm, which, given the minimum distance between probe locations of 2 cm, was quite small. Considering maximum ice growth was 27 cm, this resulted in an error of 2.4 %. There seemed to be a switch after a depth of 10 cm from over-estimating the ice depth profile to under-estimating the ice depth profile. The error appeared to be larger for the under-estimation as well, with the maximum negative deviation being 2.6 cm. The positive deviation was found to be a maximum of 1.8 cm.

The results for the 34 g kg^{-1} saline ice growth experiment of the manually measured ice depths, gradient calculated ice depths and the subsequent smoothed ice depth profiles are shown in Figure 5.25

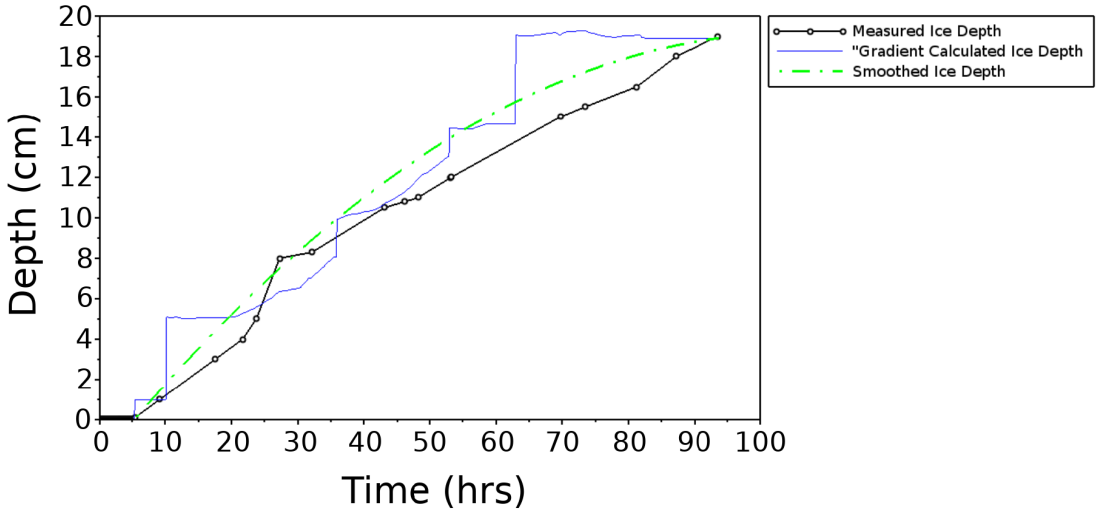

Figure 5.25: 34 g kg^{-1} saline solution experiment: manually measured ice depths, gradient calculated ice depths and the subsequent smoothed ice depth profiles

The experiment using the 34 g kg^{-1} saline solution was stopped after 100 hours, compared to the freshwater run that was stopped after 350 hours. This was due to the increasing underlying solution salinity to $>$ 40 g kg^{-1} that created a further freezing point depression and therefore was deemed to no longer represent a freezing experiment of 34 g kg^{-1} saline solution. Visually, the manually measured ice depth profile and the smoothed temperature derived ice depth profile displayed a linear trend, rather than the $\sqrt{x}$ shape displayed by the freshwater profile. However, this was primarily due to the different experimental timescales. If one examines the profiles found within Figure 5.24, it can be seen that the profiles also display a linear trend. This trend was also observed by Anderson (1961) during the early growth of natural sea ice. The 34 g kg^{-1} saline ice growth was capped at 100 hours due to the small capacity of the tank, with longer studies possible within tanks where a deeper underlying water column is present, so that the increase in underlying solution salinity is not as large for ice depths within this range of 0 - 30 cm. The rapid increases in temperature derived ice depth at 10 and 100 hours within the freshwater experiment occurred much more frequently within the 34 pp saline solution experiment over the same time scale. The cause of the increases are the same as discussed above in connection with the freshwater experiment. The cause of the greater number of increases was not certain, yet it was noted that the ice growth rate was faster within the 34 g kg^{-1} saline solution experiment. The measured ice depth was 19 cm for the 34 g kg^{-1} saline solution compared to 12 cm for the freshwater experiment. When the freshwater ice growth had also reached $\pm$ 20 cm at 170 hours, four such temperature increases had occurred. This suggests that the temperature increases are purely a function of the temperature probe locations, with an adjustment to the linear equation line taking place each time a subsequent probe was found to be within the ice. It was also noted that the manually measured ice depths, gradient calculated ice depths and the subsequent smoothed ice depth profiles all correlated exactly at the end of the experiment.

Shown in Figure 5.26, the smoothed temperature derived ice depth profile was plotted against the manually measured ice depth profile. A perfect direct correlation between the calculated and the manually measured ice depth profiles would fall directly on the y=x line, indicated by the sold black line. The bounds defining a correlation within ± 10 % are shown with black dashed lines.

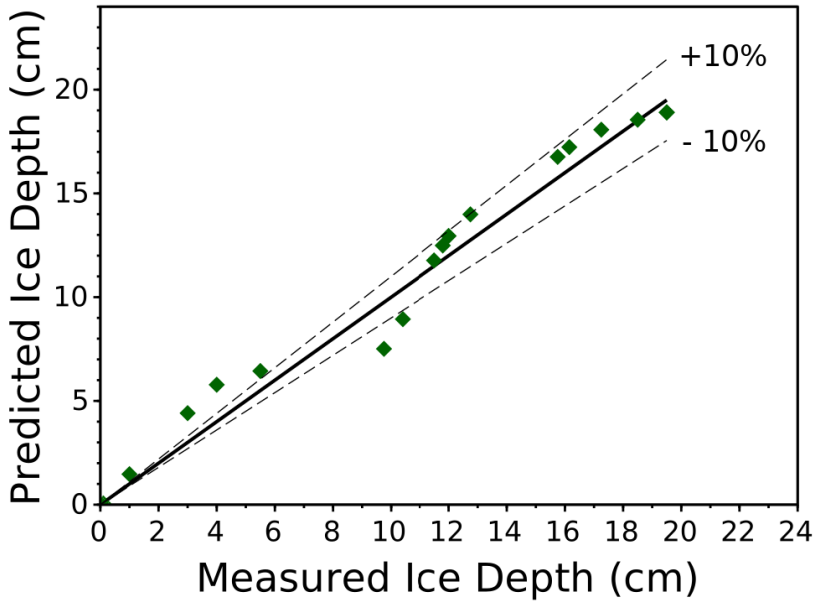

Figure 5.26: Correlation of the manually measured and the smoothed temperature derived ice depth profiles for the 34 g kg^{-1} saline solution experiment. Perfect correlation shown by the solid black line, with ± 10 % bounds shown by the dashed lines

The smoothed temperature derived ice depth profiles show a reasonable approximation, however, up to depths of 12 cm, the predicted values fall outside of the 10 % bounds from the manually measured ice depth. The error also appears to have a sinusoidal shape, where initially the ice depth was over-estimated, then between 10 - 12 cm it was under-estimated, before being over-estimated again for the remainder of the experiment. Table 5.9 shows fit parameters for the correlation.

Table 5.9: Fit parameters for the correlation between the manually measured and the smoothed temperature derived ice depth profiles for the 34 g kg^{-1} saline solution experiment

Parameter	Low	High
R^2 Value	0.993	
Standard Deviation Of Error	0.613	
Error Range	-2.24	1.78
Percentage Split	33.3%	66.7%

The R^2 was 0.993, which was indicative of a good fit, however, it also shows the limitations of the R^2 value, since it suggests that the smoothed temperature derived ice depth for the 34 g kg^{-1} saline solution better fits the manually measured ice depth profile than what was seen during the freshwater experiment. This was primarily due to the greater number of data points taken during the freshwater experiment. In addition, the absolute error at greater ice depths can be larger but still fit within the 10 % bounds of the correlation window. Calculating the R^2 for the freshwater

experiment over the same duration as the total time of the 34 g kg^{-1} saline solution experiment resulted in a R^2 of 0.991. The R^2 for the two freezing experiments are very similar when calculated over the same time frame. The standard deviation of error for the 34 g kg^{-1} saline solution experiment was calculated as 0.613 cm, which was similarly small compared to the freshwater experiment which was 0.666 cm. However, it was found that the smoothed temperature derived ice depth of the 34 g kg^{-1} saline solution experiment over-estimated the manually measured depth for 66.7 % of the time. This may be due to the difference between the interfaces for fresh and saline water, with fresh water being flat Gold (1977), while saline solution experiences dendritic ice growth resulting in an interfacial layer several centimeters in depth Schwarz and Weeks (1977). It is suggested that the stepwise jumps in gradient calculated ice ice depth may also be due to phenomenon. It can be seen that the smoothed profile follows the lower limit of the steps, which would be at the beginning of this interfacial layer. The temperatures over the entire interfacial layer are generally very similar, due to the open nature of the ice structure at this point. While the extended layer could cause an uncertainty in the exact location of the interface as it moves between probes, the method of assessing the gradient between successive probes would limit this uncertainty, with the smoothed ice depth potentially removing the overestimate factor. When the identical initial 100 hour time frame was once again compared in isolation, the results are similar in their overestimation for both fresh water and the saline solution.

Taking into account the results from both validation experiments, it was observed that the temperature derived ice depth measurement function, which uses gradient as an assessment parameter, provided similar goodness of fits regardless of the salinity of the solution. It therefore provides a model that was independent of the freezing point temperature. The average standard deviation of the smoothed temperature derived ice depth measurement from the manually measured ice depth for both experiments was 0.648 cm. This degree of fit was deemed sufficient within the context of the aim of the study, which was to design a small-scale system for the growth of artificial sea ice. The temperature derived ice depth results are used to provide an indication of whether the general growth trends observed agree with those reported in literature. A greater degree of accuracy of ice depth was not required for the development of current system design. The temperature derived depth measurement function was successful in providing a non-intrusive, continuous means of reasonably accurate ice depth estimation that can be calculated at the end of the experiment upon retrieval of the temperature results from the datalogger.

5.5 Proof of Concept: Artificial Sea Ice Growth Experiment

To confirm that the designed system is able to grow saline ice with the properties of sea ice, an ice growth experiment was conducted. Using the designed system, a saline solution of 28 g kg^{-1} was cooled at -20 °C until an ice depth of close to 25 cm was reached. During the experiment, temperatures inside the tank were recorded for analysis of temperature profiles and to calculate ice depth and solution salinity. At the end of the experiment, the salinity of the underlying solution was measured and ice samples were taken. The ice samples were used to determine in-ice bulk salinity and the crystal morphology. This section details the results of the ice growth experiment.

5.5.1 Temperature Profiles, Solution Salinity and Ice Depth

The experiment was stopped at 160 hours. The tank focussed temperature profiles were analysed using the developed HeatGen program. Temperatures of probes within the tank were first smoothed using the linear smoothing method. This removed defrost cycle spikes and other anomalies so that further analysis of temperature could be accurately performed. The results of the temperatures profiles before and after smoothing is shown in Appendix A.4. The results from the two temperature strings were averaged for probes at the same depth. Figure 5.27 shows the temperature evolution of the tank over the growth period for probes at different depths.

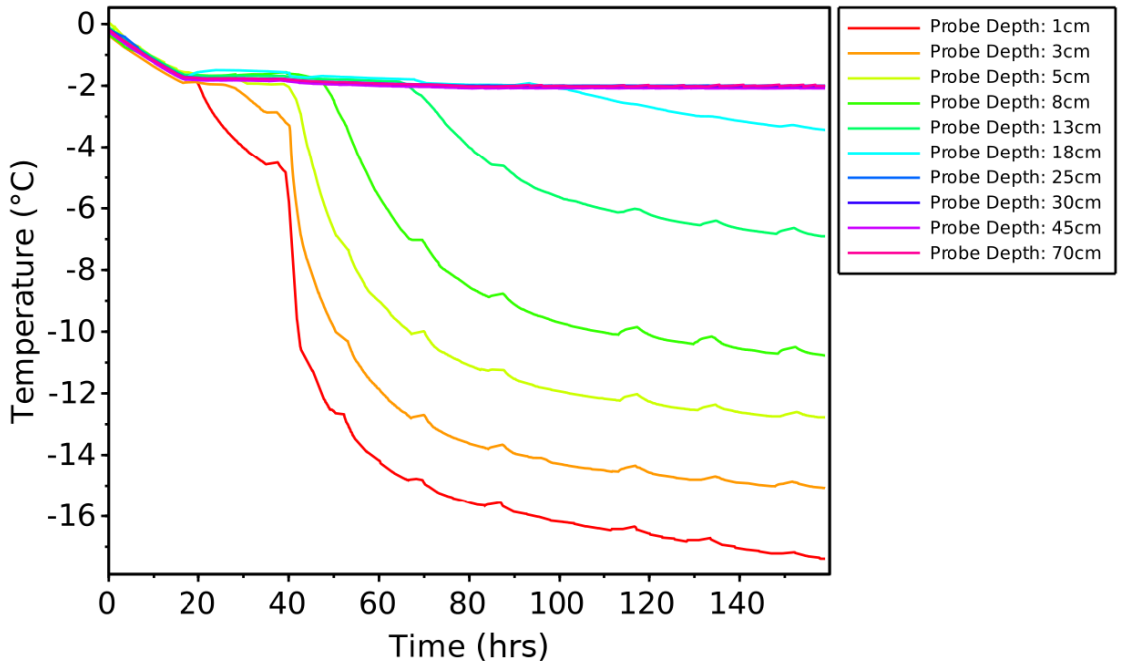

Figure 5.27: Temperature profiles for temperature probes at depths between 1 cm and 70 cm within the tank over experimental duration

The solution cooled uniformly, with identical temperatures at all depths within the tank and the same cooling rate. After 20 hours, the solution reached freezing point, as seen by levelling off of the solution temperature. The expected freezing point of the solution was -1.54 °C, based on the measured initial salinity of 28.3 g kg^{-1}. However, the solution temperature experienced a plateau at -1.72 °C. After this time, the temperature at each depth changes only when ice growth has occurred and the growth interface has moved past this point. It can be seen that the ice growth occurred in sequence, with ice forming first at a probe depth of 1 cm and last at a probe depth of 18 cm. There is a significant temperature decrease seen at a depth of 1 cm and 3 cm just after 40 hours. This is due to the fan that was switched on at this point. The fan was only switched on once the ice had formed a cohesive sheet so that the ice crystals were not pushed to the side of the tank from the force of the air flow. The small temperature increases seen at regular intervals within the temperature profiles of depths with ice formation is due to the defrost cycles of the laboratory which occurred every 18 hours. These small increases are what remains after smoothing.

A temperature versus depth profile was also generated showing the evolution over the duration of

the experiment. This is shown in Figure 5.28. As with Figure 5.27, Figure 5.28 shows the initial uniform cooling of the solution before the freezing point is reached, represented by the vertical profiles decreasing in temperature. After ice growth begins at 20 hours, the vertical profile remains for the underlying solution and shows only a small decrease in temperature. In Figure 5.28, the linear temperature profile within the ice can be clearly seen. As the experiment progresses, the linear portion of the profile increases in depth, showing the growth of the ice.

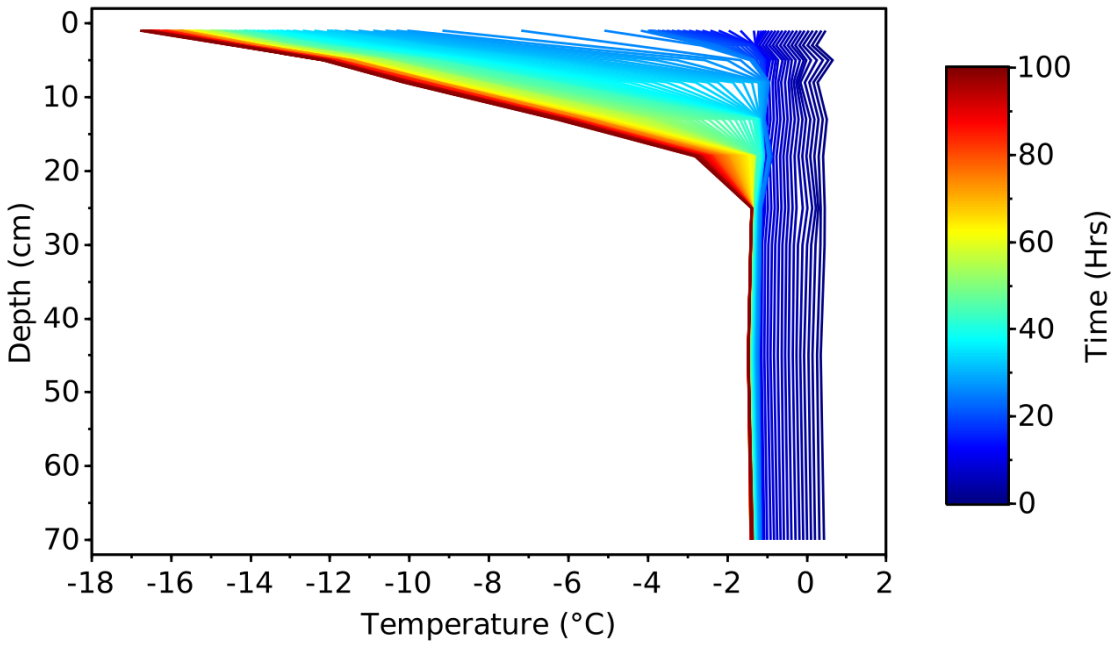

Figure 5.28: Temperature versus depth evolution over the duration of the experiment showing ice growth as linear portion of temperature profile

It was observed that there is a lower gradient occurring near the ice-solution interface, which could be due to the skeletal layer, where the ice is highly permeable, allowing enhanced mixing with the underlying solution. The profile taken at the end of the experiment, shown in red, shows a gradient change between 18 cm and 25 cm before the vertical temperature profile of the underlying solution. The intermediate gradient change is due to the ice depth being below 25 cm, with the linear in-ice temperature profile stopping before 25 cm. These intermediate gradients can be seen in earlier profiles at higher depths. These profiles are taken from the average temperatures of the two temperature strings. However, there was a clear difference in temperatures measured for each of the two strings. Figure 5.29 shows the difference in temperature versus depth profiles of the two strings, for 6 equally spaced time intervals throughout the experiment duration.

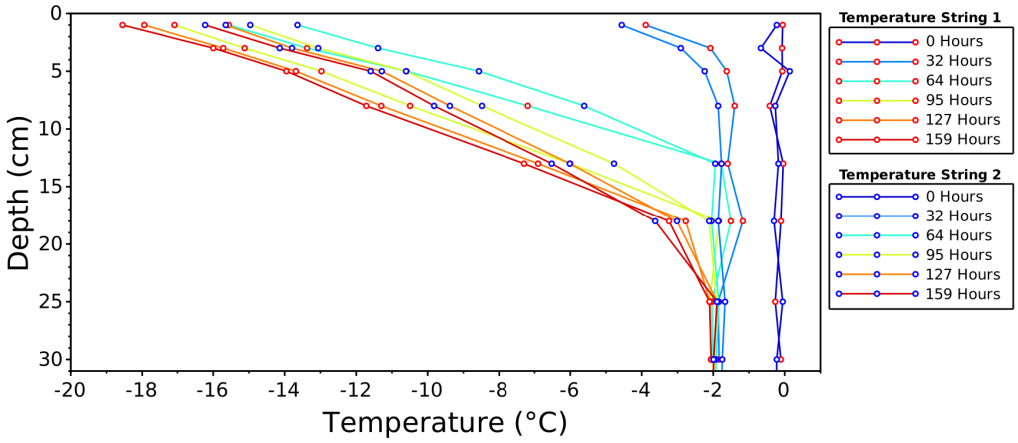

Figure 5.29: Temperature versus depth profiles for select time intervals of 0, 32, 64, 95, 137 and 159 hours, showing difference in measured temperature between temperature string 1 and 2

The difference in measured temperatures between the two strings occur predominantly within the depths where ice has grown, with the underlying solution temperature being measured as near equal for both strings. The exception to this is a depth of 18 cm at both 32 hours and 64 hours, where temperature string 1 records a temperature 0.9 °C higher than temperature string 2. The experimental set-up shown in section 4.2.1 shows that temperature string 1 is closest to the fan, and temperature string 2 is closest to the cooling unit. Initially, the temperature profile recorded at the location of temperature string 2 was colder, however, this was reversed between 32 hours and 64 hours, and for the remainder of the experiment, the temperature profile at the location of temperature string 1 was colder. Within each time point, the largest difference was always seen at the probes closest to the ice surface. The difference also increased over time, with a temperature difference of 2.3 °C between the probes at 1 cm below the ice surface measured at the end of the experiment. The recorded temperatures for each of the entire probe strings were averaged and plotted over time to identify the source of the discrepancy. This plot is shown in Figure 5.30.

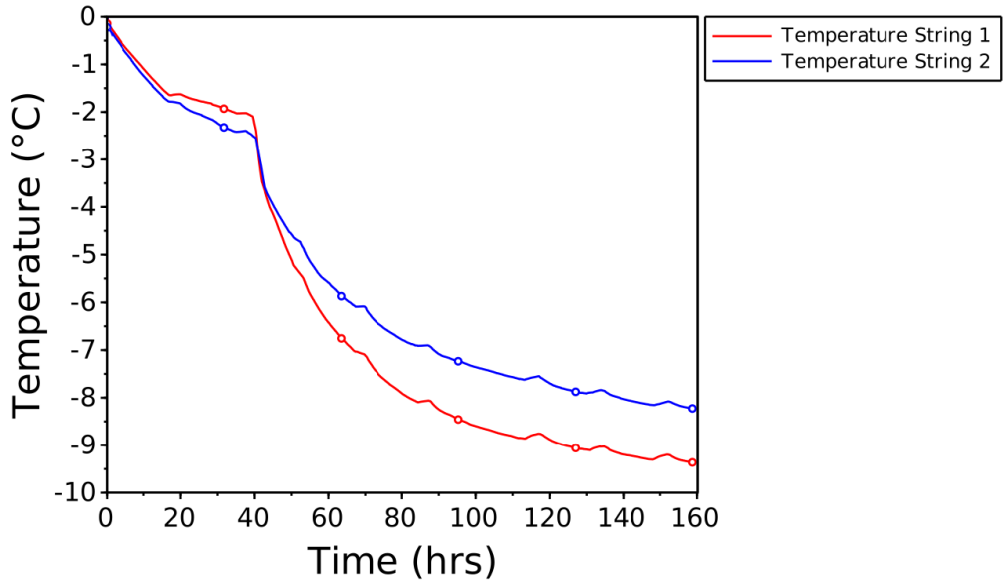

Figure 5.30: Average temperature profile of temperature strings 1 and 2 over the duration of the experiment

The average temperatures between the two string are identical at the beginning of the experiment, confirming that the differences are seen predominantly within depths where ice is present. The profiles cross over each other at 40 hours, the time that the fan was switched on. The developed HeatGen program was also used to calculate the ice depth, solution temperature and solution salinity profiles from the recorded temperature data. The solution temperature is calculated only to derive the solution salinity and is shown in Appendix A.4. The profile of solution salinity and ice depth over the duration of the experiment is shown in Figure 5.31.

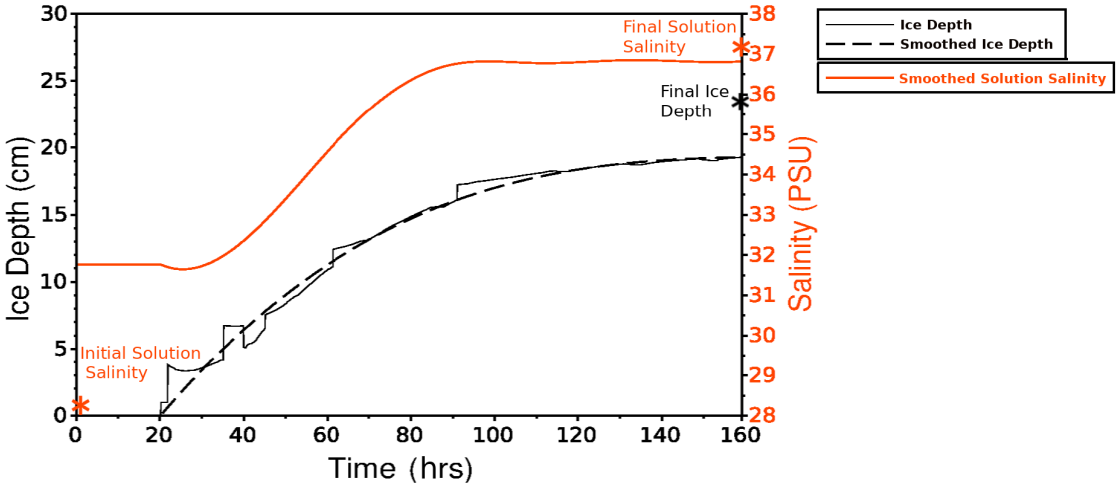

Figure 5.31: Calculated ice depth and solution profiles over experimental duration, with measured initial and final solution salinity, as wells as final measured ice depth plotted (*)

The initial and final solution salinity was measured using a conductivity meter and converted to salinity using the PSS-78 standard. The final average ice depth was measured from the extracted ice samples. As discussed in section 5.1.7, manual depth measurement system has some drawbacks which make them disadvantageous to use over an extended freezing experiment or when a very stable cooling temperature is required. Therefore, for the validation experiment, where the properties and temperature profile of the artificial ice was prioritized, it was decided to forego the manual depth measurement system and make use of only the temperature derived ice depth model. Since the calculation of ice depth does experience some noise and fluctuations, a smoothed plot of ice depth is generated since it is unlikely that the fluctuations are representative of the ice growth. The initial measured solution salinity of 28.3 g kg^{-1} is markedly lower than the calculated solution salinity of 31.7 g kg^{-1}, with a difference of 3.4 g kg^{-1}. The calculated and measured salinity values were closer at the end of the experiment, with a difference of 1.0 g kg^{-1}. The final calculated ice depth was 5 cm less than the measured result of 23 cm.

Tank heatmap profiles (Figure 5.32) were plotted for the same 6 equally spaced time intervals throughout the experiment duration, namely 0, 32, 63, 95, 137 and 159 hours. The temperature is represented by the colour, with dark red representing a temperature of -2.5 °C or lower, while dark blue represents a temperature of -1.8°C or higher. This range was chosen to provide maximum color range for temperatures within the tank, with focus upon the ice-solution interface temperatures. The locations of the temperature probes are displayed on the plots, with temperature string consisting of even numbered probes between 2 and 18 and temperature string

2 consisting of odd numbered probes between 3 and 17. The temperature above the tank surface is shown as dark red, the colour of the minimum temperature, however, the recorded temperature exceeds the range limit of -2.5 °C and was set at -20 °C.

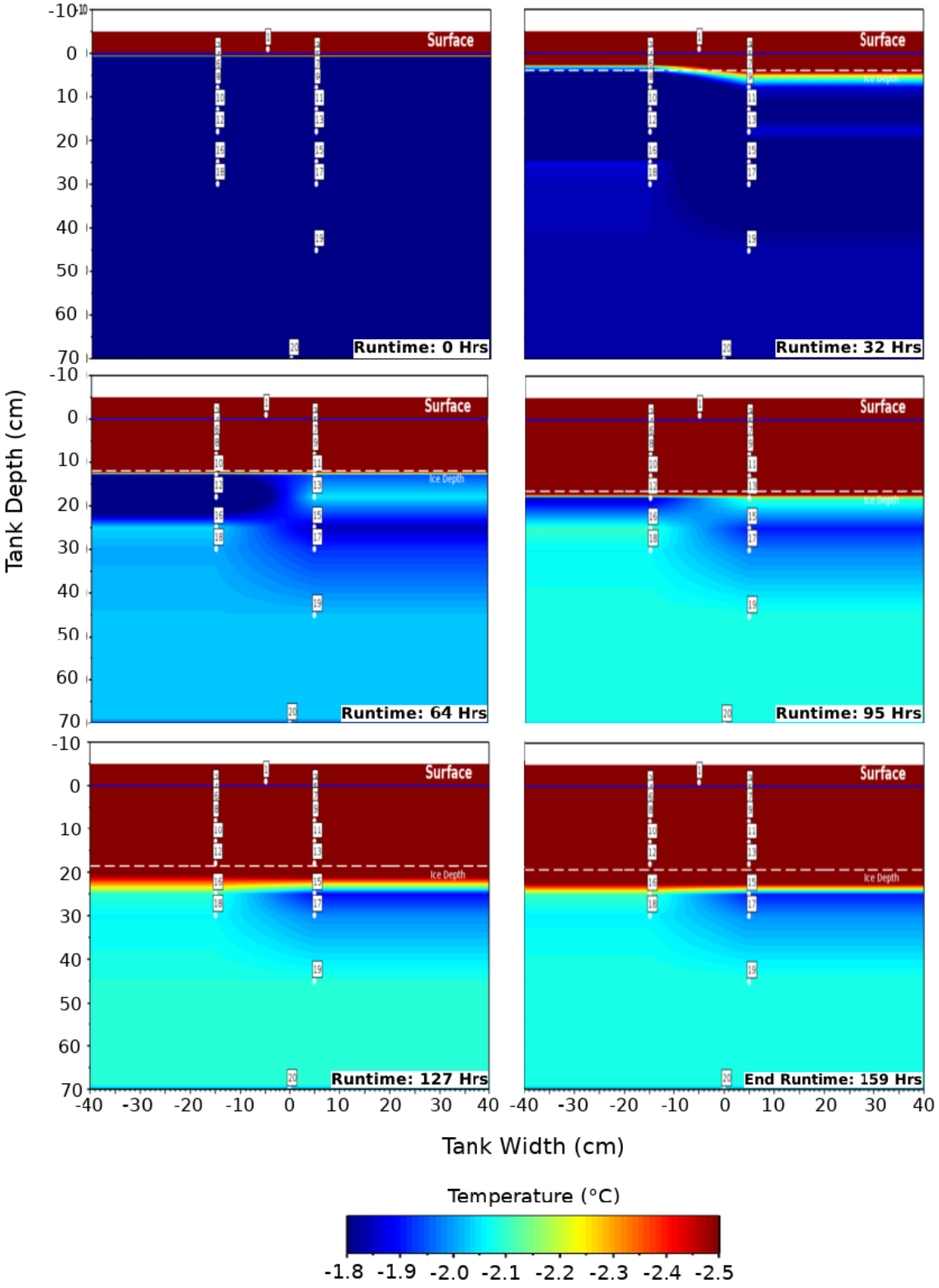

Figure 5.32: Heat map profiles for select time intervals of 0, 32, 64, 95, 137 and 159 hours, showing tank temperature evolution, temperature deviation locations, and advancing ice front. The small, white squares show the locations of the temperature probes

The temperature variation between the two temperature strings can be seen within the heat map profiles, with cooler temperatures extending deeper for temperature string 2 at 32 hours. At 64 hours the temperature measured at 18 cm is still higher for temperature string 1 than temperature string 2. However, at the location of temperature string 2, an underlying warmer area of solution persists from a depth of 25 cm to beyond 30 cm. This warm layer remains for the duration of the experiment. After the experiment, probes 15 and 17 were checked to ensure that the underlying warm area was not as a result of probe malfunction. The probes had been calibrated at the beginning of the experiment and found to measure the solution temperature accurately at the end of the experiment and thus ruled out the possibility of probe malfunction. It is theorised the location of the fan leading to the temperature anomalies shown in Figure 5.29 is the cause of the underlying warm area seen in Figure 5.32.

Ice depth calculated using the temperature derived method is also shown in the heat map profiles as a dotted white line. This is first seen at 32 hours, where the ice has reached a depth of 3 cm. The chosen color range of the heat maps highlight the temperatures experienced at the ice-solution interface, around the observed temperature plateau of between 1.7 °C and -2.0 °C. Thus, the profiles themselves provide a secondary, rough estimate of ice depth, seen by the colour shift from a temperature below -2.5 °C (dark red colour) to the temperature of the underlying solution, which is -1.72 °C (dark blue, seen at 32 hours and 64 hours) at the beginning of ice growth and decreases to -2.06 °C (teal, seen from 95 hours until 159 hours) by the end of the experiment. It should be noted that the calculated ice depth is averaged between the two temperature strings, and so will always display a uniform ice depth. However, the ice-solution interface colour better shows ice depth differences between the two tank sides, as can be seen at 32 hours. The calculated ice depth is an overestimate for ice depth on the side of the tank where temperature string 1 is located, and an underestimate for where temperature string 2 is located. However, the two methods show fairly similar ice depths. This agreement of ice depth is also shown at 64 hours and 95 hours. However, the two methods differ for the profiles of 127 hours and 159 hours. The calculated ice depth is about 5 cm less than the location of the ice solution interface point displayed by the colour shift. The ice-solution interface displayed by the heat map at 127 hours agrees well with the measured ice depth of 23 cm.

5.5.2 Ice Salinity

The in-ice bulk salinity was measured to determine the salinity profile for comparison with literature results of other artificial sea ice growth set ups and the salinity profiles found in sea ice. Three ice samples were removed from the tank, the location of these samples is shown in section 4.2.1. The samples were sectioned into horizontal slices of 3 cm for the upper slice, and there after 2 cm. The samples for the lower two sections were always combined to increase fluid volume, since the dendrites at the interface meant the last samples contained a low fluid volume making salinity measurement difficult. The salinity profile can be seen in Figure 5.33.

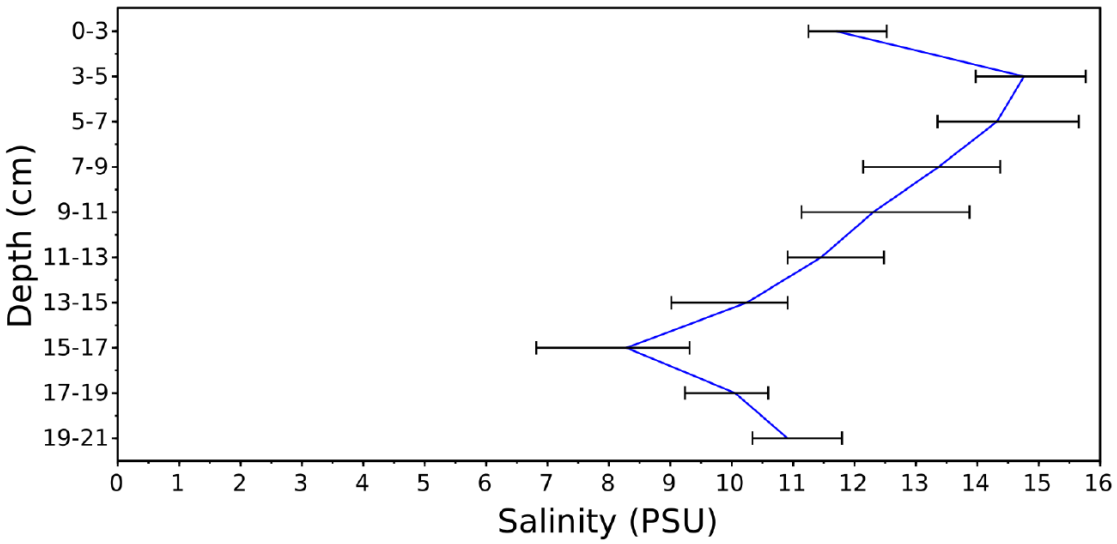

Figure 5.33: Average in-ice bulk salinity profile from ice samples taken at end of experiment

The data for these measurements can be found in Appendix A.4. The sample lengths experienced fairly low variation, with lengths of 21, 22 and 23 cm respectively. The profile represents the average values of salinity for three samples taken from the tank. The error bars represent the range of the variation between the three samples for each of the depth intervals. The values are plotted at the middle limit of each of the slices.

5.5.3 Ice Crystal Morphology and Brine Channel Structure

CT scanning was used to examine the crystal morphology including size, orientation and spacing. It also allowed for a cursory examination of the brine inclusions. Detailed analysis of these inclusions was not possible due to the duration of the scan which was performed at room temperature. This could have resulted in an undesired volume change due to the temperature increase. However, a detailed analysis of the brine inclusions was outside the scope of this study and therefore the shortcoming was not a cause for concern.

A CT scan was performed on 3 cm cubed samples of ice from the top, middle and bottom of a 23 cm ice specimen from the tank. The result is shown in Figure 5.34. The greyscale image represents density, with the most dense components, which is the brine, displayed as light grey or white, while the least dense, which is open space, showing up as black. The ice is displayed as a dark grey. Images a) and b) are the image pair of the sample from the top of the ice, images c) and d) are the image pair in the middle of the sample, and images e) and f) are taken from the bottom of the sample. Images a), c) and e) are taken down the length of the specimen and therefore orientated within the vertical X_3 and horizontal X_2 plane. Images b), d) and f) are located in the horizontal X_1 and horizontal X_2 plane and represent a horizontal slice of the images of a), c) and e) respectively. Since each sample is only 3 cm in length, the captured length from the specimen is only 9 cm. Therefore a), c) and e) cannot be fitted directly together to provide a continuous examination of the crystal structure down the length of the specimen. The images of b) and d) were initially captured to provide a higher resolution examination of the pore and brine inclusions and therefore the total image size is smaller than the other images seen here.

All images are shown at the same scale so as to allow meaningful comparison between them, with the scale bar representing 7.5 mm shown at the bottom of the image set.

Images a) and c), showing the X_3-X_2 plane for the top and middle of the sample show pore spaces generally round in shape, of less than 1 mm diameter with the exception of the pores highlighted in red. The grain boundaries for the ice crystals cannot be identified at this resolution implying their size both horizontally and vertically is > 0.5 mm. The median brine inclusions are similarly difficult to determine, however, there are many outliers of larger size that can be identified, with a few highlighted in yellow for demonstration. These brine inclusions are generally horizontally orientated, with lengths 2 ± 0.5 mm.

The X_1-X_2 images of the top and middle samples, shown by b) and d), display similar results, with no identification of the grain boundary or median brine inclusions possible. The outlying brine inclusion which were shown to extend horizontally are also seen in the X_1-X_2 plane, extending in the same direction with a thickness in the X_1 plane of 0.5 ± 0.2 mm.

The bottom sample image pair shows a markedly different crystal structure in comparison to the top and middle. Image e), located in the vertically orientated X_3-X_2 plane, shows the planar boundary spacings of vertically orientated crystals, which are highlighted by the bright brine inclusions occurring at the boundaries (examples shown in yellow). The spacings of the planar brine inclusions seen e) are measured as 0.5 ± 0.2 mm. The length of the majority of these crystals within the X_3-X_2 extend beyond the image bounds, meaning they are longer than 3.3 cm. The bottom of e) shows the bottom of the sample, where vertically elongated voids can be seen extending up into the ice from the bottom of the sample. The largest of these voids are highlighted in red.

Image f) shows a horizontal image slice within the X_1-X_2 plane, taken from the lower section of e). It should be noted that the bright white dot surrounded by concentric circles is a ring artefact that occurs as a function of the rotation of the CT scanning machine, and is not a feature within the sample. The open, porous structure of the ice at this depth is displayed again, especially on the right of the image. The planar boundaries can again be identified, with brine inclusions located at the boundaries. In this orientation, once can identify a variation in the crystal orientation, with four orientations identified and shown by the purple rectangles. Individual ice dendrites can be seen in the bottom right of the image, highlighted in blue.

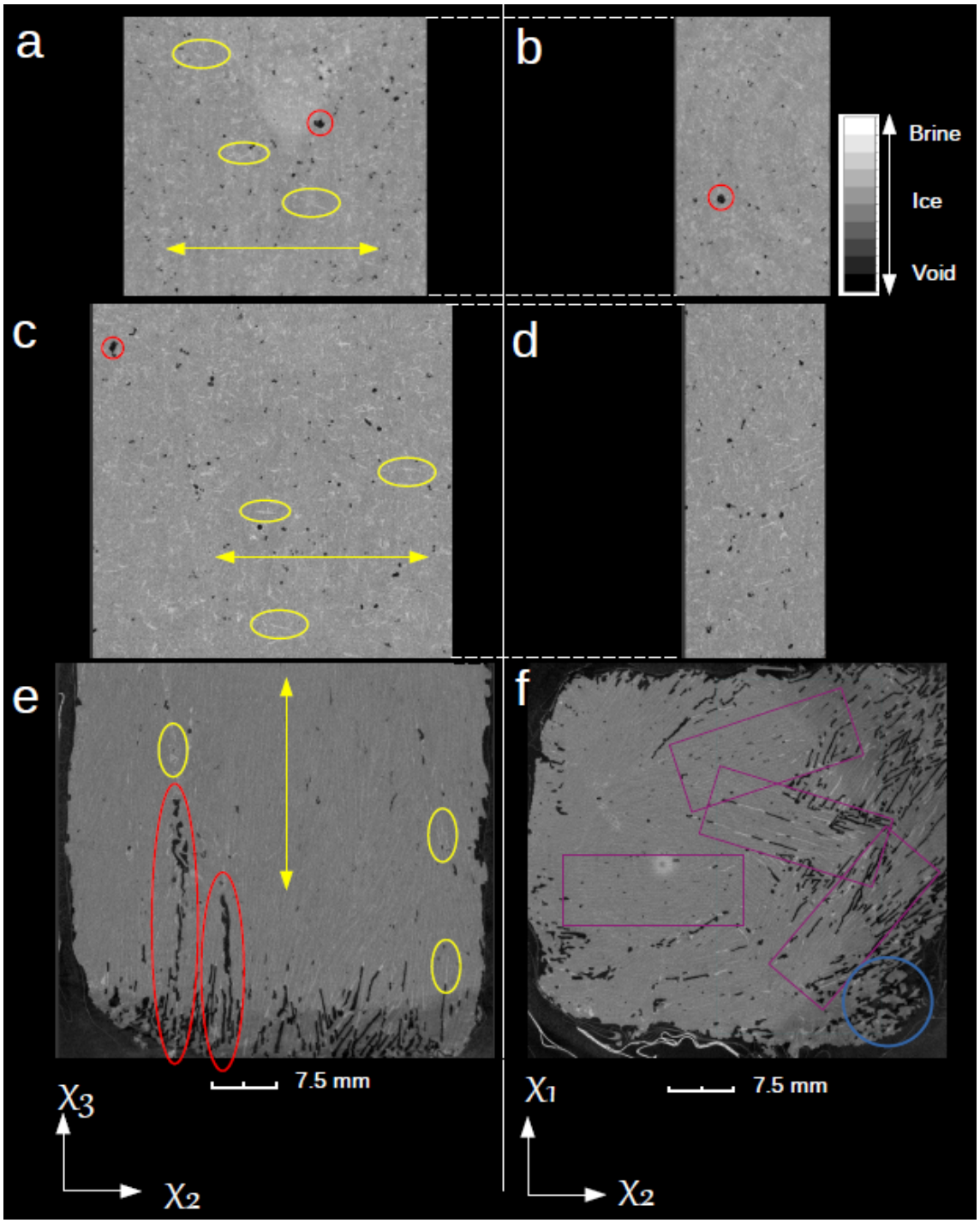

Figure 5.34: CT scan of 3 cm ice cubes from an artificial sea ice sample at a) Top in the X_3-X_2 plane, b) Top in the X_1-X_2 plane, c) Middle region in the X_3-X_2 plane, d) Middle region in the X_1-X_2 plane, e) Bottom in the X_3-X_2 plane, f) Bottom in the X_1-X_2 plane. Items of interest are highlighted as follows: red - pore spaces, yellow - brine inclusions, purple - crystal orientation in X_1-X_2 plane.

6 Discussion

The overall aim of this project was to design, build and test a small-scale system for the growth of artificial columnar sea ice. The system was designed to be used for method development of testing protocols for the Antarctic sea ice. It was also designed to enable controlled studies of specific sea ice properties, which can be studied in isolation under repeatable conditions. These sea ice properties include crystal size and orientation, brine volume and internal ice structure as well as mechanical properties such as its compression strength, elastic modulus and Poisson's ratio.

This project was predominantly focussed on the system design. The objectives of the design was to create a system that enables the growth of saline ice with properties similar to those of natural sea ice. The system was required to be large enough to produce samples of appropriate size and number to fit the testing protocols for mechanical testing set out by Schwarz et al. (1981), while being statistically sound. The secondary design objectives were set to ensure the system remains cost-effective, portable and simple.

The system design was split into different modules, where each of the modules could be designed and improved individually by qualitatively assessing all the possible design options against their predicted ability to fulfil each of the objectives. A schematic of the completed system is shown in Figure 6.1.

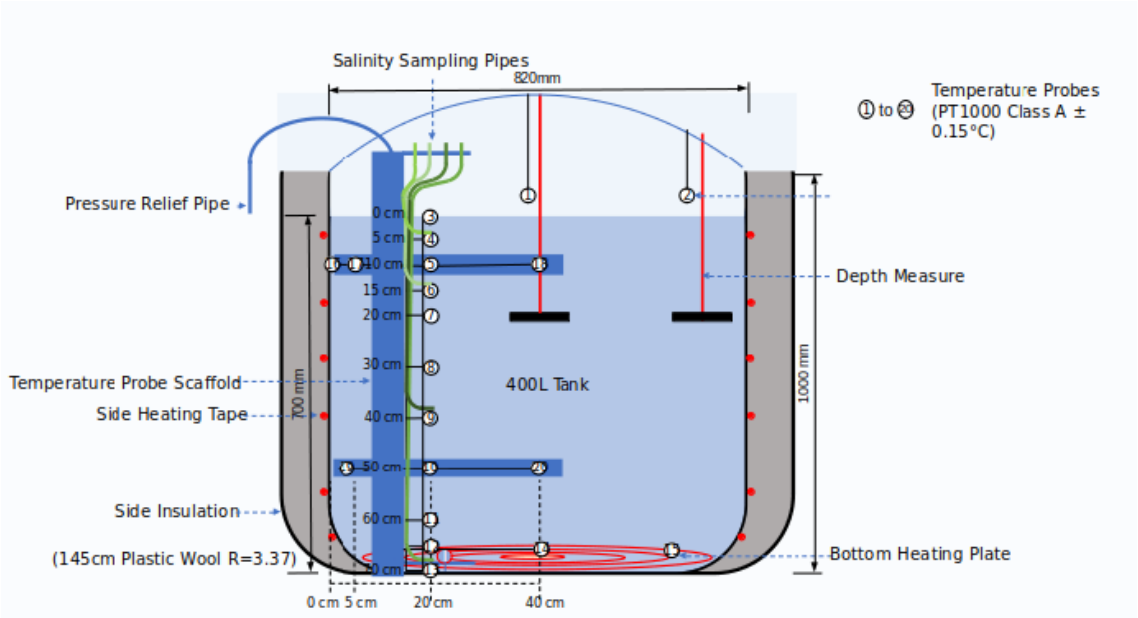

Figure 6.1: A schematic of the completed small scale system for the growth of artificial columnar sea ice

The completed system consists of a 400 dm^3 plastic tank with insulated sides and an electrically heated pressure relief pipe routed from near the bottom of the tank to account for ice volume expansion. The insulation on its own was found to be insufficient to prevent heat loss from the sides of the vessel and thus a side heating module was added negate any heat loss. A temperature controlled bottom heating module was installed, which, in conjunction with the agitation system, provided a uniform and constant solution temperature set at the freezing point (-1.9 °C).

Both ice depth and temperature measurement systems were included in the design. Manual ice

depth measures were installed. A temperature measurement system consisting of 20 RTD temperature probes ($\pm$ 0.15 °C) was installed for monitoring the ambient, ice and solution temperatures within the tank system. The datalogger for temperature measurement was housed in an insulated control centre box, which contained all of the tank control systems such as the heating rate controllers. The control centre box was also temperature controlled, with the temperature kept constant at 9.6 ± 0.4 °C to prevent any ice formation on the electrical components.

A proof of design concept experiment, consisting of a 28 g kg^{-1} solution at -20 °C, was carried out in order to test the system design. The hypothesis was that the system design will be able to produce saline ice with properties similar to natural sea ice under the same conditions. Temperature profiles and ice growth within the tank were recorded, and ice samples were taken at the end of the run to determine in-ice salinity and the crystal morphology of the ice. The results of this experiment are discussed below in order to compare the properties of the ice grown within this tank to key properties of columnar S2 sea ice. If the ice properties of ice grown within this study matches the aforementioned key properties, the system can be declared successful in its aim to grow artificial columnar S2 sea ice.

The temperature profiles within the ice followed a linear trend (Figure 5.28) with depth as described in both artificial sea ice growth experiments by Marks et al. (2017); Notz (2005); Weeks (1962) and Wiese (2012) as well as that found in natural sea ice (Notz, 2005; Timco and Weeks, 2010).. This suggested an accurate representation of the uni-directional top down heat flux as experienced under real metocean conditions (Maykut and Untersteiner, 1971). This uni-directional cooling was substantiated to some extent by results shown in f) of Figure 5.34. This kind of columnar ice has been observed in sea ice formed under calm ocean conditions (Schwarz and Weeks, 1977). The crystals display elongation in the direction of the heat flux (Timco and Weeks, 2010), which further confirms that the heat flux was primarily vertical. However, only the bottom sample from the last 3 cm of ice showed columnar ice growth within vertically orientated grains. Figure 5.34 shows that the top and middle sections of the ice displayed granular ice, with no distinguishable heat flux direction. The ice displays typical isotropic properties,indicative of granular ice (Timco and Weeks, 2010).

Granular ice forms in the initial stage of ice growth, formed from supercooled ice crystals in the atmosphere Fransson (2009). This initial granular layer (a), c) in Figure 5.34) with random c-axis alignment begins to shift through a process of geometric selection towards a vertically aligned direction during the transition layer (Weeks, 2010). This transition layer depth has been measured to generally occur within less than 10 cm (Weeks and Ackley, 1986). The location of the transition layer and the beginning of the columnar zone displayed in e) of Figure 5.34 is not seen within Figure 5.34 and must therefore occur between Figure c) and e). Therefore, the length of the granular and transition zone cannot be calculated but is known to be greater than 10 cm when accounting for the length of the samples displayed in a) and c) and the gap between them. In addition, artificial sea ice normally has even less of a transition zone, since the process of selective seeding at the appropriate time should influence an effectively instant growth of

columnar ice Schulson et al. (2015). Therefore, while columnar ice can be seen within the lower 3 cm of the sample, the experiment was not successful in producing samples of completely columnar ice. It is known that granular ice continues to form at lower depths in turbulent conditions (Eicken and Lange, 1989). It is suggested that the flow rate and location of the pumps may have been one of the reasons that contributed to increased length of the transition zone, and these variables should be examined in a proceeding study. Another possibility is that the phenomenon was caused by supercooling, where ice crystals spontaneously occur within solution as reported by Thomas et al. (2020). This could have happened as a result of improper seeding time or too high of an initial cooling rate at the top surface. The fan could been the cause of a high initial cooling rate, with other effects caused by the fan being discussed during analysis of the seeding method.

While CT scanning as a method of crystal analysis was partly successful since it enabled the identification of crystal boundaries, crystal orientation and the location of brine inclusions, the limitation in sample size did not allow for a cohesive assessment of the ice macro-structure along the length of the sample. This made it impossible to identify the beginning and length of the columnar zone of ice growth seen only within e and f) in Figure 5.34. It also made the assessment of the S2 nature of the columnar zone difficult to confirm, since it only shows a small area of ice growth. It is acknowledged that cross-polarised imaging on a universal stage such as described in Cottier and Wadhams (1999), Crabeck et al. (2016), Schulson et al. (2015) and Sinha (1986) is a better method to use, and it is recommended that the necessary equipment is procured and the methodology is developed for use in future studies. The spacings (0.5 ± 0.2 mm) between these vertical planes of the ice were found to be within the range of plane spacings (1 mm) measured within sea ice (Timco and Weeks, 2010). Since it is known that the spacings are influenced by the growth rate of the ice Jeffries et al. (1993); Nakawo and Sinha (1981), it can be postulated that the chosen freezing temperature of -20 °C and the subsequent growth rate is similar to that which occurs in the ocean.

The temperature profiles indicate that insulation and side heating of the system was sufficient to ensure the overall heat flux was correctly orientated. This is corroborated by the growth of columnar sea ice near the bottom of the sample, as shown in Figure 5.34. The temperature profile and presence of columnar ice at lower ice depths also suggest that it may be the surface cooling rate or agitation rate that caused the extended granular and transition zone, rather than the tank insulation or heating control. Additionally, the demonstration of the vertical heat flux validates the assumption of uni-directional cooling made within the HeatGen development, and this corroborates the validity of the modelled heatmap temperature profiles.

The ice growth rate fits the form of a $\sqrt{\mathrm{x}}$ function with respective to time, with the fastest growth rate experienced initially after which it gradually slows. This was the same curve of growth rate as observed both in previous artificial sea ice set-ups (Cox and Weeks, 1975) and in natural sea ice (Weeks, 2010). The slowing down of the ice growth rate was caused by the insulating effect of the thickening ice. Additionally, artificial sea ice systems also experience a salinity increase in the underlying solution during ice growth due to brine drainage (Weeks and Cox, 1974). This

could also cause a slowing in ice growth, since the increased salinity would result in a further depression of the freezing point of the system. The final ice depth measured off one of the ice samples cut from the tank was 24 cm compared to 19 cm predicted by the temperature derived ice depth model. This is an error of 21 %, which is greater than expected and suggests that the temperature derived model of ice depth cannot be used with confidence until further validation has been done. Interestingly, it can be noted that the visual, qualitative indication of ice depth seen in the heatmap temperature profile was much more accurate and the final interface was shown to be at 24 cm. This suggested that it may be more accurate to assess temperature gradients found between individual probes rather than taking the cumulative average, despite the discrepancies experienced at an individual probe location.

Analysis of the temporal evolution of the temperature profiles and the heatmap image sequence (Figure 5.28 and Figure 5.32) showed that the solution temperature was very similar at all the measurement points. This result confirmed that the agitation worked well, enabling a uniform solution temperature. Analysis of the horizontal plane's c-axis alignment (Figure 5.34f) showed that there was a variation, suggesting that the current was not greater than the lower limit given by Langhorne and Robinson (1986). This is consistent with the observations of natural sea ice in the absence of a current (Timco and Weeks, 2010). However, as discussed previously, the size of the sample used to assess this orientation is too small to entirely confirm this conclusion, with cross-polarised imaging of a thin horizontal section at least 6 x 6 cm better able to confirm the above conjecture (Schulson et al., 2015). The temperature of the solution was seen to decrease uniformly until the freezing point was reached, after which it remained stable. This indicated that the bottom heating module was successful in preventing any supercooling and maintaining the solution at its freezing point as experienced during natural sea ice formation (Weeks, 2010).

During the early design stages, a method used by Garnett et al. (2019) was tested for the measurement of solution salinity. The measurement end was located next to a temperature probe within the tank to allow correlation of measured salinity with the measured temperature. The pipes were routed through the heated pressure relief pipe to prevent ice formation in the sample lines and consequent blockage of the line. These pipes could be attached to a syringe to obtain a water sample through suction. However, since the pressure relief pipe terminated within the cold laboratory, it was found that the exposed ends of the sample lines froze closed. Precautions were taken by forcing out the leftover solution within the pipes by using an air filled syringe. A heat gun was also used to gently warm the pipes prior to sampling. However, the precautions failed to prevent blockage of the pipes by ice formation. Therefore this system of solution sampling for salinity was discarded. In addition, it was decided to move towards autonomous measurement systems to limit the number of physical disturbances to the system.

The method recommended by Weeks and Cox (1974) whereby the solution salinity can be calculated directly from the solution temperature was used. The system was well-mixed and the underlying solution was assumed to be at freezing point. However, there was a large difference between the salinity measured using this method and from the results of salinity measurement taken using the handheld conductivity meter. The initial solution salinity was measured by the

portable conductivity meter as 28 g kg^{-1}, while the temperature predicted salinity at the point of initial growth was 32 g kg^{-1}. Likewise, a sample of the solution salinity measured at the end of the experiment was measured as 37.5 g kg^{-1}, while the temperature derived solution salinity was predicted as 36.5 g kg^{-1}. The error at the end of the experiment was much smaller at the beginning. This shed suspicion on the accuracy of the handheld conductivity meter, and it was suggested that this, rather than the temperature derived salinity, may have been the cause of the largest error. The Campbell Scientific temperature measurement system had an accuracy of $\pm$ 0.2 °C. The calculation of salinity from temperature is a straightforward, linear relationship. The error of 0.2 °C carried through the salinity calculation according to the PSS-78 standard (Lewis and Perkin, 1981) gives a systematic error of 0.12 g kg^{-1}. The difference between the salinity result measured using the handheld conductivity meter and the temperature derived salinity is 4 g kg^{-1}. This is quite significant when considering the associated freezing point depression and effect on the in-ice salinity.

Examining the in-ice salinity profile, one can see that the average salinity of 12 g kg^{-1} is much higher than the 4 - 7 g kg^{-1} given by Schulson et al. (2015). However, the average salinity agrees well with the salinities of young, natural sea ice presented by Nakawo and Sinha (1981) of similar depths as grown in this study, shown in Figure 6.2.

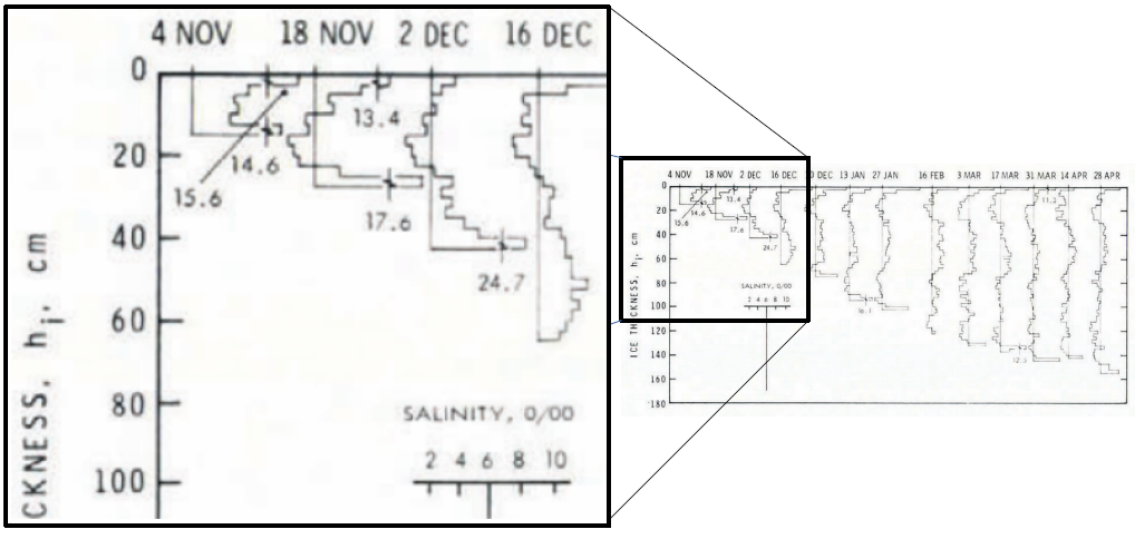

Figure 6.2: Salinity profiles of young sea ice from Nakawo and Sinha (1981), originally displayed in Section 2.4. Salinity scale is shown inserted, and a reference line of 6 g kg^{-1} is placed on each profile

Figure 6.2 shows that for ice of about 15 cm, the average salinity was measured as 14.6 g kg^{-1}), and after a further two weeks of growth, at a depth of 25 cm, the average salinity was 13.4 g kg^{-1}). Therefore, the average salinity for 23 cm ice grown in this study of 12 g kg^{-1} is close to these initial values. This is one of the observations of Haas (1999), that the drawback to artificial sea ice is the time period over which it was grown, therefore the portrayed properties are often of very young sea ice. The measured salinities were also found to be similar to the salinity measured by Wiese et al. (2015) during a study on the growth and melt rate of artificial sea ice.

Many studies do seem to concentrate on the growth of artificial sea ice that displays salinities seen in ice of much greater depths and a few months old, even for sample depths of 20 cm (Galley et al., 2015; Garnett et al., 2019; Marks et al., 2017). . If the desire is to achieve salinities of a similar range, a lower starting salinity for the solution should be used. Indeed, it would be useful to perform a study of the measured in-ice salinity over a range of starting solution salinities in order to establish a model that allows for the calculation of the required initial solution salinity for the desired average in-ice salinity.

The salinity of the top layer (11 g kg^{-1}) does display the maximum normally experienced in sea ice. Rather, a single low value is measured at the top surface, with the proceeding points displaying a profile more consistent with the expected c-shaped profile. It was theorised that the decreasing ice at the surface could have affected the in-ice salinity, with the initial high salinity layer melting and migrating downwards at a rate greater than what the usual brine drainage occurs at. There was a large variation between the samples (2-3 g kg^{-1}), leading to the average profile displaying large error bars at each depth. Cottier and Wadhams (1999) addressed the in-ice salinity variations observed within samples located very close together. This is observed in natural sea ice as well, indeed, on a far greater scale (Maykut, 1986). Considering the level of variation found in previous artificial sea ice set-ups as well as natural sea ice it was deemed that the variation was within the normal range and could be said to be consistent enough for application to mechanical testing, as long as the number of samples was sufficient to ensure statistical accuracy. Mechanical samples do require consistent crystallographic properties however, so the cause of the extended granular and transition layer seen in Figure 5.34 would need to be identified and solved before use of the system for the growth of samples for mechanical testing.

The solution was seeded when the solution temperature was found to be at the freezing point at 20 hours into the experiment. Before seeding, the solution was completely ice-free. After the addition of the ice crystals, the concentration of ice crystals on the solution surface was seen to increase, and the temperature probe at a depth of 1 cm showed a negative deviation from the freezing point (Figure 5.27), indicating ice formation at this depth. Figure 5.27 showed that the temperature probe at 3 cm also experienced this decrease in temperature indicative of ice formation. However, visual inspection of the tank surface showed that the ice layer was still flexible, and a cohesive layer had not yet formed, confirming the presence of an extended granular ice layer. This created a difficulty with the fan used to increase the convective heat transfer rate at the solution interface. The fan could not be switched on until a cohesive layer formed. If a cohesive layer had not first formed, the ice crystals would be forced to the side, creating a discrepancy in distribution of ice across the tank surface. This effect was also experienced by Roscoe et al. (2011). It is due to the inverse relationship of solution density with temperature (Chaplin, 2018). As the solution cools, its density increases which causes an overturning of solution. Therefore it is not solely the uppermost layer that exists at the freezing point of the solution, but a much deeper layer. The overturning continues during ice formation, causing the formation of ice crystals within a deeper layer than at the atmosphere-solution interface. This phenomenon is similarly seen in natural sea ice, where the depths of this mixed layer can be between 10 – 40 m (Weeks, 2010).

Forty hours after the commencement of the experiment, the ice layer was found to be cohesive enough to resist the force of the air flow. Thus, the fan could be switched on. This was seen to have a drastic effect on the cooling rate, with the average temperatures within the ice displaying a sharp and almost immediate decrease of 6 °C (Figure 5.27). Despite the insulation being deemed as successful in promoting uni-axial, top-down cooling, it can be seen that there was a difference in temperature profiles between each of the two temperature probe strings (Figures 5.29 and 5.30). The location of the two temperature probe strings are seen in Figure 4.3. Temperature string 1 (TS1) was located on the side of the tank nearest to the fan while Temperature string 2 (TS2) was located nearest the chiller unit. From 0 to 40 hours, TS2, which was located closest to the chiller, displayed a lower average temperature of 0.5 °C than TS1 . This indicated a higher rate of cooling. After 40 hours, the ice had formed a cohesive layer which meant the fan could be switched on. This resulted in a reversal of the trend, with TS1 located closest to the fan displaying a lower average temperature. Analysis of Figure 5.29 showed that the temperature difference occurred primarily in the ice.

Considering the conditions under which the difference in temperature between TS1 and TS2 was observed, the possibility of it stemming from heat loss through the tank side walls was disregarded for several reasons. Both TS1 and TS2 displayed a linear, top-down in-ice temperature profile. The fan was directed over the ice surface, with the effect of trend reversal between TS1 and TS2 only seen after the fan was switched on. Additionally, the air flow will not have had as much of an effect on the the cooling rate through the side walls since heat transfer through the side walls is primarily conductive. Conductive heat transfer is not affected by an increase in air flow rate.

A consequence of the different cooling rates observed between TS1 and TS2 is a corresponding difference in the ice depths measured at the positions of the two probe strings. Ice thickness variation has been observed in previous artificial sea ice set-ups, where both Garnett et al. (2019) and Wiese (2012) measured a greater thickness of ice nearer the cooling units. While sea ice thickness variation is also observed in natural sea ice under real oceanic conditions (Maykut, 1986), this discrepancy in ice thickness is not desired in an artificial sea ice system. One of the main aims of such set-ups is to create ice with uniform properties throughout the tank so that multiple samples can be collected from a single tank and be tested with a high accuracy and repeatability (Haas, 1999).

The use of a fan has been used extensively within artificial sea-ice set-ups to increase the convective cooling heat flux at the surface and promote a more even distribution of cooling (Roscoe et al., 2011; Wiese, 2012). However, the use of a fan within the tank system of this project was not found to create this desired even cooling distribution. Rather, it just resulted in the switch of the side experiencing a greater degree of cooling from the side where the chiller was located to the side where the fan was located. In light of these difficulties attributed to the use of the fan (prevention of the formation of a cohesive ice layer during seeding, possible sublimation of the ice surface, and a differential cooling rate), the location of the fan and generated air flow rate should be further investigated. The fan should be located close enough to enable an increased air flow above the tank to increase the convective heat transfer and thus an increased ice growth

rate, but far away enough to negate the undesired effects observed within this study.

The differences in temperature measurements observed between TS1 and TS2 demonstrated that while there may be unidirectional cooling, the assumption that there were no temperature gradients in the horizontal direction, as assumed in the HeatGen program, was therefore not valid. With only TS1 and TS2 providing measurements, there were only two measurements within the horizontal plane at each depth increment to indicate the difference in temperature. It is not possible to fully describe a temperature gradient with only two data points. Considering the limited number of temperature probes available for measurement, it was not possible in this study, where the focus is placed on measuring the vertical temperature profile, to spare more probes for the measurement of the horizontal temperature profile. However, the two measured data points did give some indication of the variation and was still used within the population of the temperature matrix within the Heatgen program to generate the tank temperature heatmaps. The population of this matrix would not have been possible if this assumption was discarded.

Lastly, a rather unexpected phenomenon occurred during the 28 g kg^{-1} ice growth experiment. Visual observation of the ice surface showed the presence of a liquid layer which Roscoe et al. (2011) stated was indicative of inadequate pressure relief. However, while free-floating ice could not be accomplished, the pressure relief pipe was found to relieve the pressure built up in the solution under the ice adequately. It was therefore not thought to be the cause of the liquid layer of water on the surface of the ice. Moreover, it was observed that the ice surface level dropped during the experiment, with the temperature probes initially located at 1 cm clearly visible above the ice surface by the end of the experiment (Appendix A.4). This was also reflected in the temperature profiles, where the temperature at 1 cm depth was found to be as cold as -18 °C, which was very close to the ambient temperature of -20 °C. If the ice had been free-floating, the loss of some of the underlying solution could have resulted in a lowering of the surface level. However, the ice was found to be firmly fixed to the vessel walls. In addition, the temperature probes were frozen within the ice and had been attached from the top of the tank, meaning that these should have moved down with the ice if the entire ice puck had shifted downwards. It has been shown that the salinity levels of the ice surface are normally relatively high at over 20 g kg^{-1} (Nakawo and Sinha, 1981). It was therefore theorised that the increased ambient temperature during the defrost cycles, which could be as high as 0 °C, could have melted some of the high-salinity ice at the surface. Some of this melted ice water could have drained downwards through the ice into the solution. Additionally, the high air flow rate could also have caused ice sublimation (Das et al., 2013). The cause of this phenomenon was not established, and it is suggested that the first avenue of investigation is to adjust the fan position and speed.

In summary, the ice grown within the designed small-scale system for the growth of artificial sea ice had the majority of the properties that classified it as artificial columnar S2 sea ice. This was namely, a vertical, linear temperature profile, with a parabolic ice depth profile over time. The CT scan showed that the ice crystal morphology at the bottom of the sample consisted of vertically elongated ice crystals, with c-axes located within the horizontal plane. The c-axes orientation within the horizontal plane seemed to be random, thereby classifying the bottom section as “S2”.

The CT scan also showed the location of brine inclusions as vertically orientated, contained within the intracrystalline planes. The crystal planes were measured to have spacings of 1 ± 0.3 mm. However, the presence of an extended granular layer and transition zone is cause for concern, since these samples cannot be used for mechanical testing. The cause of this phenomenon would need to be identified and solved, with further analysis of the crystal structure carried out using cross-polarised light on a universal stage.

Lastly, the salinity profile of the ice was observed to fit the c-shaped profile seen within literature with the exception of a lower salinity measured at the ice surface. The salinity values were within range of that measured in young sea ice by Nakawo and Sinha (1981) and in laboratory studies by Wiese et al. (2015), but it may be beneficial to establish the required starting solution salinity to create artificial sea ice with salinities in range of 4-8 g kg^{-1} (Galley et al., 2015; Garnett et al., 2019; Marks et al., 2017; Schulson et al., 2015). However, by fulfilling these key properties, the proof of design concept experiment validated the tank system design with regards to its ability to accurately replicate the metocean conditions necessary to grow artificial columnar S2 sea ice. Therefore, the design objectives of the study have been met.

7 Conclusions and Recommendations

7.1 Conclusions

The aim of this thesis was to design a small-scale system for the growth of artificial sea ice. The system will be used for method development of testing protocols for the Antarctic sea ice. It will also enable controlled studies of specific sea ice properties, studied in isolation under repeatable conditions. Given that this thesis is mainly design-oriented, the conclusions consist of deliverables rather than confirmation of hypotheses. However, all the conclusions drawn from this work are presented below.

A small-scale system capable of growing artificial sea ice was designed. The key questions were answered, and the lower section of the ice grown within the tank fulfilled the requirements to be termed "artificial columnar S2 sea ice" namely, vertically elongated ice crystals with a c-axis located randomly within the horizontal plane. There were concerns over the extended granular and transition layer experienced in the ice, and this would need to be addressed before the samples could be used for mechanical testing. The measured ice depth displayed a $\sqrt{x}$ profile over time. The brine inclusions were located in vertically orientated, contained within the intracrystalline planes. The crystal planes were measured to have spacings of 0.5 ± 0.2 mm. Lastly, the salinity profile of the ice was observed to fit the c-shaped profile with exception of a surface anomaly.

By fulfilling the aim of the proof of the ice growth experiment used as a proof of design concept, the ability of the small-scale system to accurately replicate the metocean conditions necessary to grow artificial columnar S2 sea ice was partially validated. The primary and secondary system design objectives of the design is that the system is large enough with low enough sample variation to be able to produce samples of artificial columnar S2 sea ice of the correct size and number to be used for mechanical testing. At present, it fulfils all of these requirements with the exception of consistent, continuous columnar S2 ice. Some further work is required on the system to identify the cause of the extended granular and transition layer before the system can produce sea ice solely of columnar S2 nature. Through assessment of the initial design choices for each of the modules and their respective components the secondary objectives of being cost-effective, portable and simple were fulfilled.

This study produced a small-scale system design for the growth of artificial sea ice which succeeds in replicating many of the standard metocean conditions. With some refinement, this system can provide the necessary test samples for method development for the mechanical testing of sea ice samples collected from the Antarctic MIZ. Following on from this initial design, additional design implementations can be undertaken to accomplish the growth of sea ice that more closely resembles the ice found in the Antarctic MIZ, and these are stated below.

7.2 Recommendations and Future Studies

While the designed system was deemed to be largely successful, it is in the nature of design that the first iteration of a product will have some points where it can be improved upon. Thus, the following recommendations for improvement to the design are made.

- Identify the cause of the extended granular and transition layer of ice morphology seen within the artificial sea ice grown in this tank. It is suggested that the possible causes of this anomaly and thus a good starting point for the investigation would be the pump flow rates and the cooling rate through adjustment of the fan.

- Perform a study of the measured in-ice salinity over a range of starting solution salinities in order to establish a model that allows for the calculation of the required initial solution salinity for the desired average in-ice salinity so as to achieve ice salinities in the range of 4 - 9 g kg^{-1}

- All connectors for temperature probes should be mounted outside of control centre, with this connector plate connected to data logger with a ribbon cable, making connection of the probes easier and reducing the need to open the control center. The data logger is also capable of recording NTC thermistor probes and it is recommended that the probes are switched to these if they can be procured. Thermistors are advantageous since they respond quicker to temperature change, are less susceptible to change in accuracy from bumps or knocks, and should be of similar price but last longer and are same if not more accurate.

- With a relatively simple circuit, it should be possible to increase the number of temperature probes that the datalogger can measure. The additional probes would allow greater resolution of tank temperature, specifically the in-ice temperatures, which would assist in the accuracy of the temperature derived ice depth measurement.

- A top-down metal cooling plate with circulating coolant as used by Schulson et al. (2015) is recommended in that it will create more consistent cooling temperatures and remove the effect of the temperature fluctuations created by the defrost cycles of the laboratory. This cooling method is favoured by set-ups growing ice for the purpose of mechanical testing.

Following on from the successful design of a small scale system for the growth of artificial sea ice, a number of future studies can be recommended. Firstly, the tank was designed in order to produce artificial sea ice samples for the purpose of mechanical testing. Therefore a future study is to grow artificial sea ice for the method development of mechanical testing protocols for the mechanical testing of Antarctic sea ice. As well as investigating the variation of the mechanical properties of sea ice as function of variables such as ocean salinity, ambient temperature ocean heat flux, wind speed. In addition, it is recommended that initial design work is carried out so as to enable the tank to produce artificial sea ice that resembles that found in the Antarctic. The biggest addition required for this would be a wave-making system, where the required rate and intensity of agitation to produce frazil and pancake ice will need to be investigated.

There is also further development and validation of both the temperature derived ice depth model,

as well as the temperature derived solution salinity models that can be carried out. This would involve the implementation of other methods of measurement to compare these systems to, and for many more validation experiments to be carried out to improve upon the statistical assessment of the model accuracy. The parameter of the ice depth measurement model used to differentiate between the transition point of in-ice temperature gradient and underlying solution temperatures could be further tested and adjusted, to assess whether it is truly independent of solution salinity. The optimum probe layout for ice-depth accuracy could also be further explored.

References

Allison, I. A. N. 1979. Sea Level, Ice, and Climatic Change: Antarctic sea ice growth and oceanic heat flux. In *Sea Level, Ice and Climate Change*, number 131, pages 1–10, Canberra, Australia.

Anderson, D. L. 1961. Growth Rate of Sea Ice. *Journal of Glaciology*, 3(30):1170–1172.

Arakawa, K. 1954. Studies of the Freezing of Water (II): Formation of Disc Crystals. *J Faculty Sci Hokkaido University*, II(4):311–339.

Ashton, G. D. 1989. Thin ice growth. *Water Resources Research*, 25(3):564–566.

Assur, A. 1960. Composition of Sea Ice and its Tensile Strength. *SIPRE Research Report*, 44:54.

Aussillous, P., Sederman, A. J., Gladden, L. F., Huppert, H. E., and Grae Worster, M. 2006. Magnetic resonance imaging of structure and convection in solidifying mushy layers. *Journal of Fluid Mechanics*, 552:99–125.

Barber, D. G., Ehn, J. K., Pućko, M., Rysgaard, S., Deming, J. W., Bowman, J. S., Papakyriakou, T., Galley, R. J., and Søgaard, D. H. 2014. Frost flowers on young Arctic sea ice: The climatic, chemical, and microbial significance of an emerging ice type. *Journal of Geophysical Research*, 119(20):11593–11612.

Barrette, P. D. 2001. Triaxial Testing of Ice: a Survey of Previous Investigations. *Port and Ocean Engineering under Arctic Conditions*, pages 1375–1380.

Barrette, P. D. and Jordaan, I. 2001. Compressive Behaviour of Confined Polycrystalline Ice. Technical report, Memorial University of Newfoundland, St John's.

Buist, I., Potter, S., Nedwed, T., and Mullin, J. 2011. Herding surfactants to contract and thicken oil spills in pack ice for in situ burning. *Cold Regions Science and Technology*, 67(1-2):3–23.

Butler, B. M. and Kennedy, H. 2015. An investigation of mineral dynamics in frozen seawater brines by direct measurement with synchrotron X-ray powder diffraction. *Journal of Geophysical Research: Oceans*, 120(8):5686–5697.

Butler, B. M., Papadimitriou, S., Santoro, A., and Kennedy, H. 2016. Mirabilite solubility in equilibrium sea ice brines. *Geochimica et Cosmochimica Acta*, 182:40 – 54.

Campbell Scientific. 2006. CR5000 Measurement and Control System User Manual. Technical report, Logan, Utah.

Carns, R. C., Brandt, R. E., and Warren, S. G. 2015. Salt precipitation in sea ice and its effect on albedo, with application to Snowball Earth. *Journal of Geophysical Research: Oceans*, 120 (11):7400–7412.

Celera Motion. 2019. Accuracy, Resolution, Repeatability. Available: https://www.celeramotion.com/zettlex/support/technical-papers/accuracy-resolution-repeatability/. [Accessed on: 2019-

12-12].

Chaplin, M. 2018. Water on Earth. Available: http://www1.lsbu.ac.uk/water/water{_}on{_}earth.html. [Accessed on: 2019-09-02].

Cottier, F. and Wadhams, P. 1999. Linkages between Salinity and Brine Channel Distribution. *Polar Research*, 104:859–871.

Cox, G. F. N. and Weeks, W. F. 1975. Brine Drainage and Initial Salt Entrapment in Sodium Chloride Ice Cold Regions Research and Engineering Laboratory. (345).

Cox, G. F. N. and Weeks, W. F. 1983. Equations for determining the gas and brine volumes in sea-ice samples. *Journal of Glaciology*, 29(102):306–316.

Cox, G. and Weeks, W. 1986. Changes in the Salinity and Porosity of Sea Ice Samples during Shipping and Restorage. *Journal of Glaciology*, 32(112):371–375.

Crabeck, O., Galley, R., Delille, B., Else, B., Geilfus, N. X., Lemes, M., Roches, M. D., Francus, P., Tison, J. L., and Rysgaard, S. 2016. Imaging air volume fraction in sea ice using non-destructive X-ray tomography. *Cryosphere*, 10(3):1125–1145.

Das, I., Bell, R. E., Scambos, T. A., Wolovick, M., Creyts, T. T., Studinger, M., Frearson, N., Nicolas, J. P., Lenaerts, J. T., and Van Den Broeke, M. R. 2013. Influence of persistent wind scour on the surface mass balance of Antarctica. *Nature Geoscience*, 6(5):367–371.

DeFranco, S. J. and Dempsey, J. P. 1991. Crack Growth Stability in Saline Ice. In *Mechanics of Creep Brittle Materials 2*, volume 42, pages 25–36. Springer Netherlands, Dordrecht.

Doble, M. J., Coon, M., and Wadhams, P. 2003. Pancake ice formation in the Weddell Sea. *Journal of Geophysical Research*, 108(C7):3209.

Eatas, A. and Jones, J. C. 1993. *The Engineering Design Process*. John Wiley & Sons, Chichester, second edi edition.

Eicken, H., Lange, M. A., and Dieckmann, G. S. 1991. Spatial variability of sea-ice properties in the northwestern Weddell Sea. *Journal of Geophysical Research*, 96:10603–10615.

Eicken, H., Bock, C., Wittig, R., Miller, H., and Poertner, H. O. 2000. Magnetic resonance imaging of sea-ice pore fluids: Methods and thermal evolution of pore microstructure. *Cold Regions Science and Technology*, 31(3):207–225.

Eicken, H., Gradinger, R., Salganek, M., Shirasawa, K., Perovich, D., and Leppäranta, M. 2010. *Field Techniques for Sea-Ice Research*.

Eicken, H. 1992. Salinity profiles of Antarctic sea ice: Field data and model results. *Journal of Geophysical Research*, 97(C10):15545.

Eicken, H. and Lange, M. A. 1989. Development and properties of sea ice in the coastal regime of the southeastern Weddell Sea. *Journal of Geophysical Research*, 94(C6):8193.

Eide, L. I. and Martin, S. 1975. The Formation of Brine Drainage Features in Young Sea Ice. *Journal of Glaciology*, 14(70):137–154.

Feltham, D. L., Untersteiner, N., Wettlaufer, J. S., and Grae Worster, M. 2006. Sea ice is a mushy layer. *Geophysical Research Letters*, 33(14):4–7.

Fernicola, V. C. and Iacomini, L. 2008. Approximating the ITS-90 Temperature Scale with Industrial Platinum Resistance Thermometers. *International Journal of Thermophysics*, 29(5): 1817–1827.

Frankenstein, G. and Garner, R. 1967. Equations for Determining the Brine Volume of Sea Ice from 0.5 to -22.9C. *Journal of Glaciology*, 6(48):943–944.

Fransson, L. 2009. *Ice Handbook for Engineers*.

Freitag, J. 1999. The hydraulic properties of Arctic sea ice: Implications for the small-scale particle transport (in German),. *Ber. Polarforsch*, 325(ISSN 0176 5027):150.

Galley, R. J., Else, B. G. T., Geilfus, N. X., Hare, A. A., Isleifson, D., Barber, D. G., and Rysgaard, S. 2015. Imaged brine inclusions in young sea ice-Shape, distribution and formation timing. *Cold Regions Science and Technology*, 111:39–48.

Garnett, J., Halsall, C., Thomas, M., France, J., Kaiser, J., Graf, C., Leeson, A., and Wynn, P. 2019. Mechanistic insight into the uptake and fate of persistent organic pollutants in sea ice. *Environmental Science & Technology*, 53(2):6757–6764.

Geilfus, N.-X., Galley, R. J., Cooper, M., Halden, N., Hare, A., Wang, F., Søgaard, D. H., and Rysgaard, S. 2013. Gypsum crystals observed in experimental and natural sea ice. *Geophysical Research Letters*, 40(24):6362–6367.

Gitterman, K. E. 1937. Thermal Analysis of Seawater. Technical report, USA Cold Reg.Res. Eng. Lab, USA Cold Reg.Res. Eng. Lab, Hanover, N. H.

Gold, L. B. 1977. Engineering Properties of Fresh-Water Ice. *Journal of Glaciology*, 19(81): 197–212.

Golden, K. M., Ackley, S. F., and Lytle, V. I. 1998. The percolation phase transition in sea ice. *Science*, 282(5397):2238–2241.

Golden, K. M., Eicken, H., Heaton, A. L., Miner, J., Pringle, D. J., and Zhu, J. 2007. Thermal evolution of permeability and microstructure in sea ice. *Geophysical Research Letters*, 34(16): 2–7.

Golding, N., Snyder, S. A., Schulson, E. M., and Renshaw, C. E. 2014. Plastic faulting in saltwater

ice. *Journal of Glaciology*, 60(221):447–452.

Grae Worster, M. and Rees Jones, D. W. 2015. Sea-ice thermodynamics and brine drainage. *Philosophical transaction s. Series A, Mathematical, physical, and engineering sciences*, 373 (2045):20140166.

Gratz, E. T. and Schulson, E. M. 1997. Brittle failure of columnar saline ice under triaxial compression. *Journal of Geophysical Research: Solid Earth*, 102(B3):5091–5107.

Griewank, P. J. and Notz, D. 2015. A 1-D modelling study of Arctic sea-ice salinity. *Cryosphere*, 9(1):305–329.

Haas, C. 1999. Ice tank investigations of the microstructure of artificial sea ice grown under different boundary conditions during INTERICE II. In Evers, K. U., Grüne, J., and van Os, A., editors, *Proc. Of HYDRALAB workshop in Hannover, Germanyth-19th February 1999*, volume 17, pages 107–113.

Hare, A. A., Wang, F., Barber, D., Geilfus, N. X., Galley, R. J., and Rysgaard, S. 2013. PH evolution in sea ice grown at an outdoor experimental facility. *Marine Chemistry*, 154:46–54.

IPCC. 2007. *Climate change 2007: The Physical Science Basis. Contributions of Working Group I to the Fourth Assessment Report of the Intergovernmental Panel on the Climate Change*. Cambridge University Press, Cambridge, United Kingdom and New York, NY, USA.

Jeffries, M., Weeks, W., Shaw, R., and Morris, K. 1993. Structural characteristics of congelation and platelet ice and their role in the development of antarctic land-fast sea ice. *Journal of Glaciology*, 39:223–238.

Jones, S. 1997. High Strain-Rate Compression Tests on Ice. *The Journal of Physical Chemistry B*, 101(32):6099–6101.

Kawamura, T., Ishikawa, M., Takatsuka, T., Kojima, S., and Shirasawa, K. 2006. Measurements of Permeability of Sea Ice. *Arctic*, pages 105–112.

Kim, J. H., Choi, K. S., and Seo, Y. K. 2006. Standardization of Laboratory Experimental Techniques With a Cold Room in Korea. *Journal of Ocean Engineering and Technology*, 21: 60–66.

Kotovitch, M., Moreau, S., Zhou, J., Vancoppenolle, M., Dieckmann, G. S., Evers, K.-U., Van der Linden, F., Thomas, D. N., Tison, J.-L., and Delille, B. 2016. Air-ice carbon pathways inferred from a sea ice tank experiment. *Elementa: Science of the Anthropocene*, 4:000112.

Kovacs, A. 1996. Sea Ice: Part II. Estimating the Full-Scale Tensile, Flexural and Compressive Strength of First-Year Ice. *Cold Regions Research & Engineering Laboratory*, 11:2047–2054.

Krembs, C. and Deming, J. 2011. Sea Ice: A refuge for life in polar seas? Available: https://www.pmel.noaa.gov/arctic-zone/essay{_}krembsdeming.html. [Accessed on: 2017-08-14].

Lake, R. A. and Lewis, E. L. 1970. Salt rejection by sea ice during growth. *Journal of Geophysical Research*, 75(3):583–597.

Lange, M. A., Ackley, S. F., Wadhams, P., Dieckmann, G., and Eicken, H. 1989. Development of Sea Ice in the Weddell Sea. *Annals of Glaciology*, 12:92–96.

Langhorne, P. J. and Robinson, W. 1986. Alignment of crystals in sea ice due to fluid motion. *Cold Regions Science and Technology*, 12(3):197–214.

Lekang, O.-I., editor. 2013. *Aquaculture Engineering*. John Wiley & Sons, Oxford.

Lepparanta, M. 1993. A review of analytical models of sea-ice growth. *Atmosphere - Ocean*, 31 (1):123–138.

Lewis, E. L. and Perkin, R. G. 1981. The practical salinity scale 1978: conversion of existing data. *Deep Sea Research Part A. Oceanographic Research Papers*, 28(4):307–328.

Li, Z. and Riska, K. 2002. Index for Estimating Physical and Mechanical Parameters of Model Ice. *Journal of Cold Regions Engineering*, 16(2):72–82.

Light, B., Maykut, G. A., and Grenfell, T. C. 2003. Effects Of Temperature On The Microstructure Of First-Year Arctic Sea Ice. *Journal of Geophysical Research: Oceans*, 108(C2).

Light, B., Brandt, R. E., and Warren, S. G. 2009. Hydrohalite in cold sea ice: Laboratory observations of single crystals, surface accumulations, and migration rates under a temperature gradient, with application to "snowball earth". *Journal of Geophysical Research: Oceans*, 114 (C7).

Light, B., Carns, R. C., and Warren, S. G. 2015. "Albedo dome": a method for measuring spectral flux-reflectance in a laboratory for media with long optical paths. *Applied Optics*, 54(17):5260.

Lofgren, G. and Weeks, W. F. 1969. Effect of Growth Parameters on Substructure Spacing in NaCl Ice Crystals. *Journal of Glaciology*, 8(52):153–164.

Loose, B., McGillis, W. R., Schlosser, P., Perovich, D., and Takahashi, T. 2009. Effects of freezing, growth, and ice cover on gas transport processes in laboratory seawater experiments. *Geophysical Research Letters*, 36(5):1–5.

Marion, G. M., Mironenko, M. V., and Roberts, M. W. 2010. FREZCHEM: A Geochemical Model for Cold Aqueous Solutions. *Comput. Geosci.*, 36:10–15.

Marks, A. A., Lamare, M. L., and King, M. D. 2017. Optical properties of laboratory grown sea ice doped with light absorbing impurities (black carbon). *The Cryosphere Discussions*, pages 1–26.

Maus, S. and De La Rosa, S. 2012. Salinity and solid fraction of frazil and grease ice. *Journal of Glaciology*, 58(209):594–612.

Maykut, G. A., Grenfell, T. C., and Weeks, W. F. 1992. On estimating spatial and temporal variations in the properties of ice in the polar oceans. *Journal of Marine Systems*, 3(1-2):41–72.

Maykut, G. A. 1986. *The Surface Heat and Mass Balance*, pages 395–463. Springer US, Boston, MA.

Maykut, G. A. and Untersteiner, N. 1971. Some results from a time-dependent thermodynamic model of sea ice. *Journal of Geophysical Research*, 76(6):1550–1575.

Middleton, C. A., Thomas, C., De Wit, A., and Tison, J.-L. 2016. Visualizing brine channel development and convective processes during artificial sea-ice growth using Schlieren optical methods. *Journal of Glaciology*, 62(231):1–17.

Millero, F. J., Feistel, R., Wright, D. G., and McDougall, T. J. 2008. The composition of standard seawater and the definition of the reference-composition salinity scale. *Deep Sea Research Part I: Oceanographic Research Papers*, 55(1):50 – 72.

Moreau, S., Kaartokallio, H., Vancoppenolle, M., Zhou, J., Kotovitch, M., Dieckmann, G. S., Thomas, D., Tison, J.-L., and Delille, B. 2015. Assessing the O2 budget under sea ice: An experimental and modelling approach. *Elementa: Science of the Anthropocene*, 3:000080.

Nakawo, M. and Sinha, N. K. 1981. Growth Rate and Salinity Profile of First-Year Sea Ice in the High Arctic. *Journal of Glaciology*, 27(96):315–330.

Naumann, A. K., Notz, D., Hävik, L., and Sirevaag, A. 2012. Laboratory study of initial sea-ice growth: Properties of grease ice and nilas. *Cryosphere*, 6(4):729–741.

Nelson, K. H. and Thompson, T. G. 1954. Deposition of Salts from Sea Water by Frigid Concentration. *Journal of Marine Research*, 13(2):166–182.

Newyear, K. and Martin, S. 1997. A comparison of theory and laboratory measurements of wave propagation and attenuation in grease ice. *Journal of Geophysical Research: Oceans*, 102(C11): 25091–25099.

Niedrauer, T. M. and Martin, S. 1979. An experimental study of brine drainage and convection in Young Sea ice. *Journal of Geophysical Research*, 84(C3):1176.

NIOSH. 1998. Worker Deaths by Electrocution: A Summary of NIOSH Surveillance and Investigative Findings. Technical Report May 1998, DHHS (NIOSH).

Nomura, D., Yoshikawa-Inoue, H., and Toyota, T. 2006. The effect of sea-ice growth on air–sea CO 2 flux in a tank experiment. *Tellus B: Chemical and Physical Meteorology*, 58(5):418–426.

Notz, D. 2005. Thermodynamic and fluid-dynamical processes in sea ice. *University of Cambridge*, (January 2005):238.

Notz, D. and Grae Worster, M. 2008. In situ measurements of the evolution of young sea ice.

Journal of Geophysical Research: Oceans, 113(3).

Notz, D. and Grae Worster, M. 2009. Desalination processes of sea ice revisited. *Journal of Geophysical Research: Oceans*, 114(5):1–10.

Notz, D., Wettlaufer, J. S., and Grae Worster, M. 2005. Instruments and Methods A non-destructive method for measuring the salinity and solid fraction of growing sea ice in situ. *Journal of Glaciology*, 51(172):159–166.

Omega. 2019. Temperature Probes: How to choose the right temperature sensor type? Available: https://www.omega.co.uk/temperature/z/thermocouple-rtd.html. [Accessed on: 10/12/2019].

Pahl, G., Beitz, W., Feldhusen, J., and Grote, K.-H. 2007. *Engineering Design: A Systematic Approach*. Springer London, London, fourth edi edition.

Papadimitriou, S., Kennedy, H., Kattner, G., Dieckmann, G. S., and Thomas, D. N. 2004. Experimental evidence for carbonate precipitation and CO2 degassing during sea ice formation. *Geochimica et Cosmochimica Acta*, 68(8):1749–1761.

Pearce, J. 2014. *Open-Source Lab: How to Build Your Own Hardware and Reduce Research Costs*. Elsevier.

Perovich, D. K. and Grenfell, T. C. 1981. Laboratory studies of the optical properties of young sea ice. *Journal of Glaciology*, 27(96):329–344.

Perovich, D. K. and Gow, A. J. 1996. A quantitative description of sea ice inclusions. *Journal of Geophysical Research: Oceans*, 101(C8):18327–18343.

Petrich, C. and Eicken, H. 2010. Growth, Structure and Properties of Sea Ice. In Thomas, D. N. and Dieckmann, G., editors, *Sea Ice: Second Edition*, chapter 3, pages 23–77. Wiley-Blackwell, second edi edition.

Pringle, D. J., Miner, J. E., Eicken, H., and Golden, K. M. 2009. Pore space percolation in sea ice single crystals. *Journal of Geophysical Research: Oceans*, 114(12):1–14.

Rabault, J., Sutherland, G., Jensen, A., Christensen, K. H., and Marchenko, A. 2019. Experiments on wave propagation in grease ice: combined wave gauges and particle image velocimetry measurements. *Journal of Fluid Mechanics*, 864:876–898.

Randall, D., Nathoo, J., and Lewis, A. 2009. Seeding for selective salt recovery during eutectic freeze crystallization. In *International Mine Water Conference*, pages 639–646, Pretoria, South Africa.

Rinke, A., Maslowski, W., Dethloff, K., and Clement, J. 2006. Influence of sea ice on the atmosphere: A study with an Arctic atmospheric regional climate model. *Journal of Geophysical Research Atmospheres*, 111(16):1–14.

Roscoe, H. K., Brooks, B., Jackson, A. V., Smith, M. H., Walker, S. J., Obbard, R. W., and Wolff, E. W. 2011. Frost flowers in the laboratory: Growth, characteristics, aerosol, and the underlying sea ice. *Journal of Geophysical Research Atmospheres*, 116(12):1–12.

Salomon, M. L., Arntsen, M., Phuong, N. D., Maus, S., O'Sadnick, M., Petrich, C., Schneebeli, M., and Wiese, M. 2017. Experimental and Micro-CT study on the Oil Distribution in laboratory grown Sea Ice. In *Port and Ocean Engineering under Arctic Conditions*, Busan, Korea.

Schulson, E. M., Renshaw, C. E., and Snyder, S. A. 2015. Effect of Deformation Damage on the Mechanical Behavior of Sea Ice: Ductile-Brittle Transition, Elastic Modulus and Brittle Compressive Strength. Final Repo(July):1–218.

Schwarz, J. and Weeks, W. 1977. Engineering Properties of Sea Ice. *Journal of Glaciology*, 19 (81):499–529.

Schwarz, J., Frederking, R., Gavrillo, V., Petro, I., Hirayama, K., Mellor, M., Tryde, P., and Vaudrey, K. 1981. Standardized Testing Methods for Measuring Mechanical Properties of Ice.pdf. *Cold Regions Science and Technology*, (4):245–253.

Shaw, M. D., Carpenter, L. J., Baeza-Romero, M. T., and Jackson, A. V. 2011. Thermal evolution of diffusive transport of atmospheric halocarbons through artificial sea-ice. *Atmospheric Environment*, 45(35):6393–6402.

Shazly, M., Prakash, V., and Lerch, B. 2009. High Strain-Rate Behavior of Ice under Uniaxial Compression. *International Journal of Solids and Structures*, 46(6):1499–1515.

Shokr, M., Asmus, K., and Agnew, T. A. 2009. Microwave emission observations from artificial thin sea ice: The ice-tank experiment. *IEEE Transactions on Geoscience and Remote Sensing*, 47(1):325–338.

Sinha, N. 1986. Young Arctic Frazil Sea Ice: Field and Laboratory Strength Tests. *Journal of Materials Science*, 21(5):1533–1546.

Siren, K., Rosén, G., Vad, J., and Nielsen, P. V. 2001. Experimental Techniques. In *Industrial Ventilation Design Guidebook*, pages 1105–1195. Elsevier.

Stander, E. and Michel, B. 1989. The effect of fluid flow on the development of preferred orientations in sea ice: Laboratory experiments. *Cold Regions Science and Technology*, 17 (2):153–161.

Style, R. W. and Grae Worster, M. 2009. Frost flower formation on sea ice and lake ice. *Geophysical Research Letters*, 36(11):20–23.

Talley, L. D. 2002. Salinity Patterns in the Ocean. In MacCracken, M. C. and Perry, J. S., editors, *Encyclopedia of Global Environmental Change*, volume 1, pages 629–640. John Wiley & Sons, Chichester.

Texas Instruments. 2019. The Engineer's Guide to Temperature Sensing. Technical report.

Thomas, M., France, J., Crabeck, O., Hall, B., Hof, V., Notz, D., Rampai, T., Riemenschneider, L., Tooth, O., Tranter, M., and Kaiser, J. 2020. The Roland von Glasow Air-Sea-Ice Chamber (RvG-ASIC): an experimental facility for studying ocean/sea-ice/atmosphere interactions. *Atmospheric Measurement Techniques Discussions*, 1(2):1–30.

Timco, G. and Frederking, R. 1996. A Review of Sea Ice Density. *Cold Regions Science and Technology*, 24(1):1–6.

Timco, G. and Weeks, W. 2010. A Review of the Engineering Properties of Sea Ice. *Cold Regions Science and Technology*, 60(2):107–129.

Timmons, M. B., Summerfelt, S. T., and Vinci, B. J. 1998. Review of circular tank technology and management. *Aquacultural Engineering*, 18(1):51–69.

TU Delft. 2016. Ice Physics. Technical report, Delft University of Technology.

Tucker III, W., Gow, A., and Weeks, W. 1987. Physical Properties of Summer Sea Ice in the Fram Strait. *Journal of Geophysical Research*, 92(C7):PP.–6787–6803.

van den Broeke, M., Reijemer, C., and van de Wal, R. 2004. Surface radiation balance in Antarctica as measured with automatic weather stations. *Journal of Geophysical Research D: Atmospheres*, 109(9):1–17.

Vancoppenolle, M., Madec, G., Thomas, M., and McDougall, T. J. 2019. Thermodynamics of sea ice phase composition revisited. *Journal of Geophysical Research: Oceans*, 124(1):615–634.

Wadhams, P. and Wilkinson, J. 1999. The Physical Properties of Sea Ice in the Odden Ice Tongue. *Deep-Sea Research Part II: Topical Studies in Oceanography*, 46(6-7):1275–1300.

Wadhams, P., Comiso, J., Prussen, E., Wells, S., Brandon, M., Aldworth, E., Viehoff, T., Allegrino, R., and Crane, D. 1996. The Development of the Odden Ice Tongue in the Greenland Sea during Winter 1993 from Remote Sensing and Field Observations. *Journal of Geophysical Research: Oceans*, 101(C8):18213–18235.

Weeks, W. F. 1962. Tensile Strength of NaCl Ice. *Journal of Glaciology*, 4(31):25–52.

Weeks, W. F. 2010. *On Sea Ice*. University of Alaska Press, Fairbanks.

Weeks, W. F. and Ackley, S. F. 1986. The Growth, Structure, and Properties of Sea Ice. In *The Geophysics of Sea Ice*, pages 9–164. Springer US, Boston, MA.

Weeks, W. and Assur, A. 1967. The Mechanical Properties of Sea Ice. *Cold Regions Research & Engineering Laboratory*, (September):96.

Weeks, W. and Cox, G. 1974. Laboratory Preparation of Artificial Sea and Salt Ice. Technical

report, Hanover, N.H.

Weissenberger, J. 1998. Arctic Sea ice biota: Design and evaluation of a mesocosm experiment. *Polar Biology*, Volume 19(Issue 3):151–159.

Weissenberger, J., Dieckmann, G., Gradinger, R., and Spindler, M. 1992. Sea ice: A cast technique to examine and analyze brine pockets and channel structure. *Limnology and Oceanography*, 37 (1):179–183.

Wettlaufer, J. S., Grae Worster, M., and Huppert, H. E. 1997. Natural Convection during Solidification of an Alloy from above with Application to the Evolution of Sea Ice. *Journal of Fluid Mechanics*, 344:291–316.

Wiese, M., Griewank, P., and Notz, D. 2015. On the thermodynamics of melting sea ice versus melting freshwater ice. *Annals of Glaciology*, 56(69):191–199.

Wiese, M. 2012. *Laboratory experiments on the thermodynamics of melting sea ice*. Master's thesis, University of Hamburg.

Williams, G. P. 1963. Heat transfer coefficients for natural water surfaces. *International Association of Scientific Hydrology. Bulletin*, 62:203–212.

Zhang, P., Tian, L., Zhang, Z. P., Shao, G., and Li, J. C. 2012. Investigation of the hydrogen bonding in ice Ih by first-principles density function methods. *The Journal of Chemical Physics*, 137(4):044504.

A Appendix

A.1 Control Centre System Design

Figure A.1: Insulated box used to house control centre

A.1.1 Temperature Measurement

CR5000 Specifications

Electrical specifications are valid over a -25° to +50°C range unless otherwise specified; non-condensing environment required. To maintain electrical specifications, Campbell Scientific recommends recalibrating dataloggers every two years. We recommend that you confirm system configuration and critical specifications with Campbell Scientific before purchase.

PROGRAM EXECUTION RATE

The CR500X can measure one channel and store the result in 500 µs; all 40 single-ended (SE) channels can be measured in 3 ms (5 kHz aggregate rate).

ANALOG INPUTS

20 differential (DF) or 40 single-ended (SE) individually configured. Channel expansion provided by AM16/32B and AM25T multiplexers.

RANGES, RESOLUTION, AND TYPICAL INPUT NOISE: Basic Resolution (Basic Res) is the A/D resolution of a single conversion. Resolution of DF with input reversal is half the Basic Res. Noise values are for DF with input reversal; noise is greater with SE.

Input Reg (mV)	Basic Res (µV)	0 Int. (µV RMS)	250 µs Int (µV RMS)	20/16.7 ms Int (µV RMS)
±5000	167	70	60	30
±1000	33.3	30	12	6
±200	6.67	8	2.4	1.2
±50	1.67	3.8	0.8	0.3
±20	0.67	1.8	0.5	0.2

ACCURACY[1]:
±(0.05% of reading + offset), 0° to 40°C
±(0.075% of reading + offset), -25° to 50°C
±(0.10% of reading + offset), -40° to 85°C (-XT only)

[1]The sensor and measurement noise is not included and the offsets are the following:
Offset for DF without reversal = Basic Res + 1.0 µV
Offset for DF with input reversal = 2Basic Res + 2.0 µV
Offset for SE = 2Basic Res + 10 µV

MINIMUM TIME BETWEEN VOLTAGE MEASUREMENTS:

Zero Integration:	125 µs
250 µs Integration	475 µs
16.7 ms Integration:	19.9 ms
20 ms Integration:	23.2 ms

INPUT LIMITS: ±5 V

DC COMMON MODE REJECTION: >100 dB with input reversal (>80 dB without input reversal)

NORMAL MODE REJECTION: 70 dB @ 60 Hz when using 60 Hz rejection

SUSTAINED INPUT VOLTAGE W/O DAMAGE: ±16 Vdc

INPUT CURRENT: ±2 nA typ., ±10 nA max. @ 50°C

INPUT RESISTANCE: 20 Gohms typical

ACCURACY OF BUILT-IN REFERENCE JUNCTION THERMISTOR (for thermocouple measurements):
±0.25°C, 0° to 40°C
±0.5°C, -25° to 50°C
±0.7°C, -40° to 85°C (-XT only)

ANALOG OUTPUTS

4 switched voltage; 4 switched current; 2 continuous voltage; switched outputs active only during measurements, one at a time.

RANGE: Voltage outputs programmable between ±5 V; current outputs programmable between ±2.5 mA

RESOLUTION: 1.2 mV for voltage outputs; 0.6 µA for current outputs

ACCURACY: ±10 mV for voltage outputs; ±10 µA for current outputs

CURRENT SOURCING: 50 mA for switched voltage; 15 mA for continuous

CURRENT SINKING: 50 mA for switched voltage; 5 mA for continuous (15 mA w/selectable option)

COMPLIANCE VOLTAGE: ±5 V for switched current excitation

RESISTANCE MEASUREMENTS

Provides voltage ratio measurements of 4- and 6-wire full bridges, and 2-, 3-, 4-wire half bridges. Direct resistance measurements available with current excitation. Dual-polarity excitation is recommended.

VOLTAGE RATIO ACCURACY[2]: Assumes input and excitation reversal and an excitation voltage of at least 2000 mV

±(0.04% Reading + Basic Res/4) 0° to 40°C
±(0.05% Reading + Basic Res/4) -25° to 50°C
±(0.06% Reading + Basic Res/4) -40° to 85°C (-XT)

ACCURACY[2] WITH CURRENT EXCITATION: Assumes input and excitation reversal, and an excitation current, I_x, of at least 1 mA.

±(0.075% Reading + Basic Res/2I_x) 0° to 40°C
±(0.10% Reading + Basic Res/2I_x) -25° to 50°C
±(0.12% Reading + Basic Res/2I_x) -40° to 85°C (-XT)

[2]The sensor and measurement noise is not included.

PERIOD AVERAGING MEASUREMENTS

The average period for a single cycle is determined by measuring the duration of a specified number of cycles. Any of the 40 SE analog inputs can be used; signal attenuation and ac coupling may be required.

INPUT FREQUENCY RANGE:

Input Range	Signal (peak to peak) Min.	Max[3]	Min. Pulse Wi.	Max Freq.
±5000	600 mV	10 V	2.5 µs	200 kHz
±1000	100 mV	2.0 V	5.0 µs	100 kHz
±200	4 mV	2.0 V	25 µs	20 kHz

[3]Maximum signal must be centered around datalogger ground.

RESOLUTION: 70 ns/number of cycles measured

ACCURACY: ±(0.03% of Reading + Resolution)

PULSE COUNTERS

Two 16-bit inputs selectable for switch closure, high frequency pulse, or low-level ac.

MAXIMUM COUNT: 4 x 10⁹

SWITCH CLOSURE MODE:
Minimum Switch Closed Time: 5 ms
Minimum Switch Open Time: 6 ms
Max Bounce Time: 1 ms open w/o being counted

HIGH-FREQUENCY PULSE MODE:
Maximum Input Frequency: 400 kHz
Maximum Input Voltage: ±20 V
Voltage Thresholds: Count upon transition from below 1.5 V to above 3.5 V at low frequencies. Larger input transitions are required at high frequencies because of 1.2 µs time constant filter.

LOW-LEVEL AC MODE: Internal ac coupling removes dc offsets up to ±0.5 V

Input Hysteresis: 15 mV
Maximum ac Input Voltage: ±20 V
Minimum ac Input Voltage:

Sine wave (mV RMS)	Range (Hz)
20	1.0 to 1000
200	0.5 to 10,000
1000	0.3 to 16,000

DIGITAL I/O PORTS

8 ports selectable as binary inputs or control outputs.

OUTPUT VOLTAGES (no load): high 5.0 V ±0.1 V; low < 0.1 V

OUTPUT RESISTANCE: 330 ohms

INPUT STATE: high 3.0 to 5.3 V; low -0.3 to 0.8 V

INPUT RESISTANCE: 100 kohms

SWITCHED 12 V

Two independent 12 V unregulated sources switched on and off under program control. Thermal fuse hold current = 900 mA @ 20°C, 650 mA @ 50°C, 360 mA @ 85°C.

EMI and ESD PROTECTION

The CR5000 is encased in metal and incorporates EMI filtering on all inputs and outputs. Gas discharge tubes provide robust ESD protection on all terminal/base inputs and outputs. The following European CE standards apply:

EMC tested and conforms to BS EN61326:1998.

Details of performance criteria applied are available upon request.

Warning: This is a Class A product. In a domestic environment this product may cause radio interference in which case the user may be required to correct the interference at the user's own expense.

CPU AND INTERFACE

PROCESSOR: Hitachi SH7034

MEMORY: Battery-backed SRAM provides 2 Mbytes for data and operating system use with 128 kbytes reserved for program storage. Expanded data storage with PCMCIA type I, type II, or type III card, or CF card (requires an adapter).

DISPLAY: 8-line-by-21 character alphanumeric or 128 x 64 pixel graphic LCD display w/backlight.

SERIAL INTERFACES: Optically isolated RS-232 9-pin DCE port for computer or non-CSI modem connection. CS I/O 9-pin port for Campbell Scientific peripherals.

BAUD RATES: Selectable from 1,200 to 115,200 bps. ASCII protocol is eight data bits, one start bit, one stop bit, no parity.

CLOCK ACCURACY: ±1 minute per month, -25° to +50°C; ±2 minute per month, -40° to +85°C

SYSTEM POWER REQUIREMENTS

VOLTAGE: 11 to 16 Vdc

TYPICAL CURRENT DRAIN: 400 µA software power off; 1.5 mA sleep mode; 4.5 mA at 1 Hz (200 mA at 5 kHz) sample rate.

INTERNAL BATTERIES: 7 Ah rechargeable base (optional); 1650 mAh lithium battery for clock and SRAM backup, 10 years of service typical, less at high temperatures.

EXTERNAL BATTERIES: 11 to 16 Vdc; reverse polarity protected.

PHYSICAL SPECIFICATIONS

SIZE: 9.8" x 8.3" x 4.6" (24.7 cm x 21.0 cm x 11.4 cm). Terminal strips extend 0.4" (1.0 cm).

WEIGHT: 4.5 lbs (2.0 kg) with low-profile base; 12.2 lbs (5.5 kg) with rechargeable base.

WARRANTY

3 years against defects in materials and workmanship.

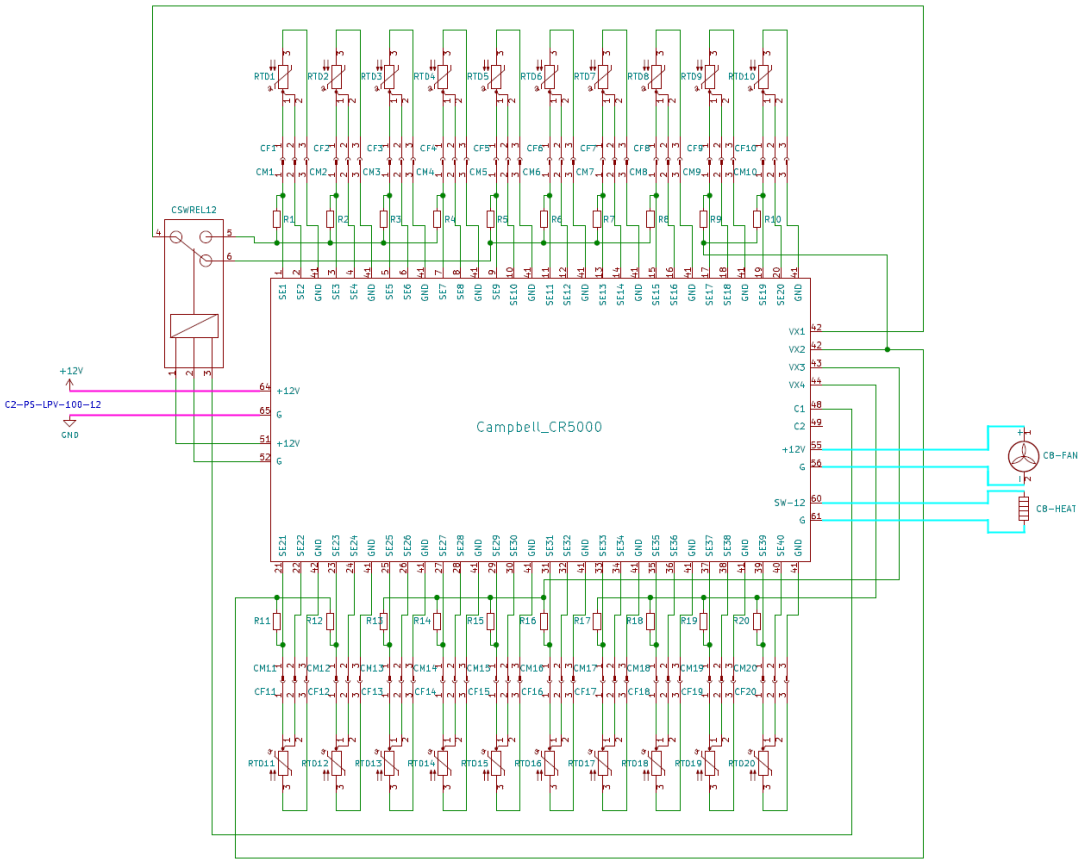

Figure A.2: Circuit Diagram for additional PT100 Temperature Measurement Circuitry for Campbell Logger

A.1.2 Tank Control

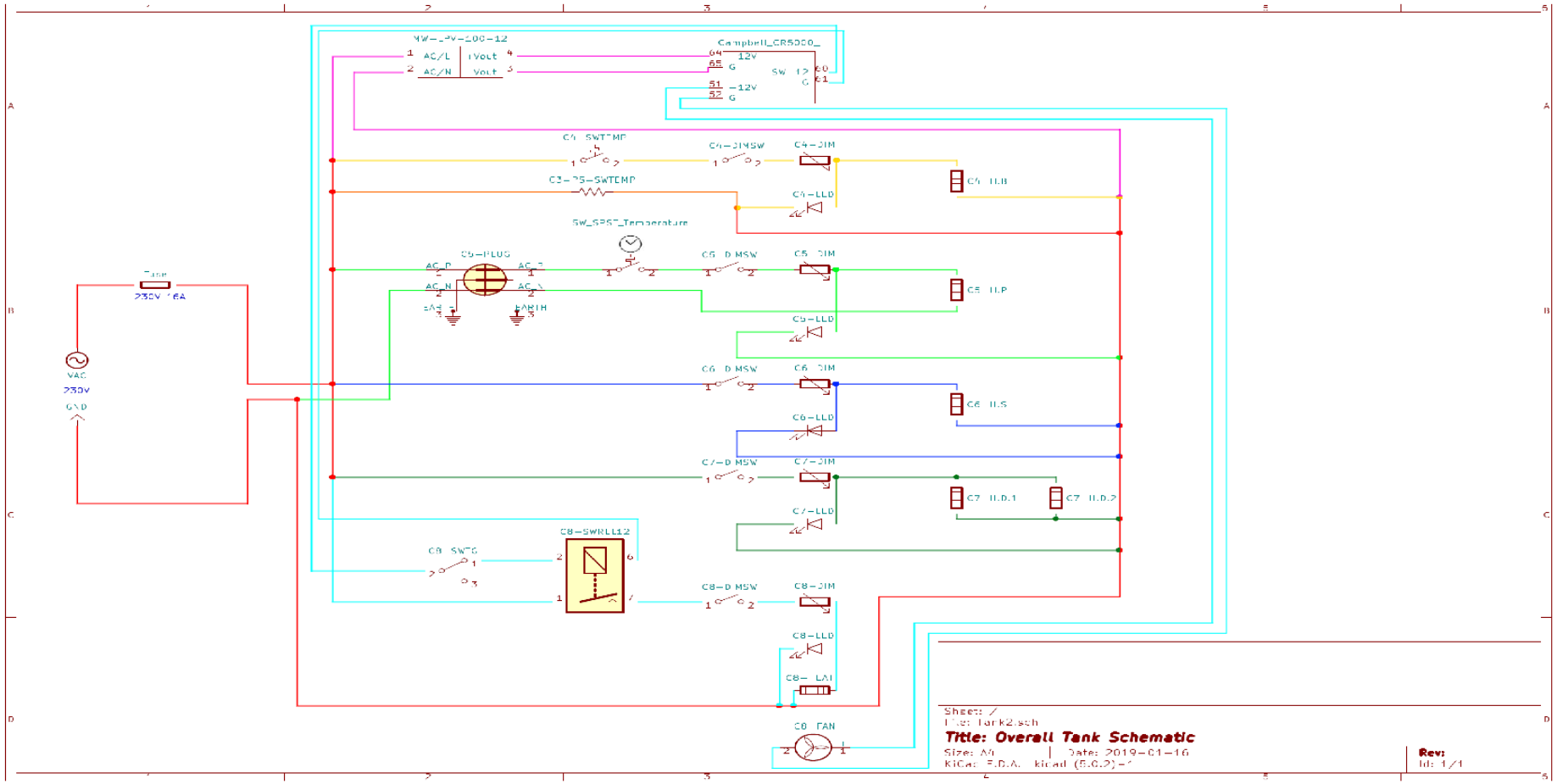

Figure A.3: Tank System Circuit Diagram

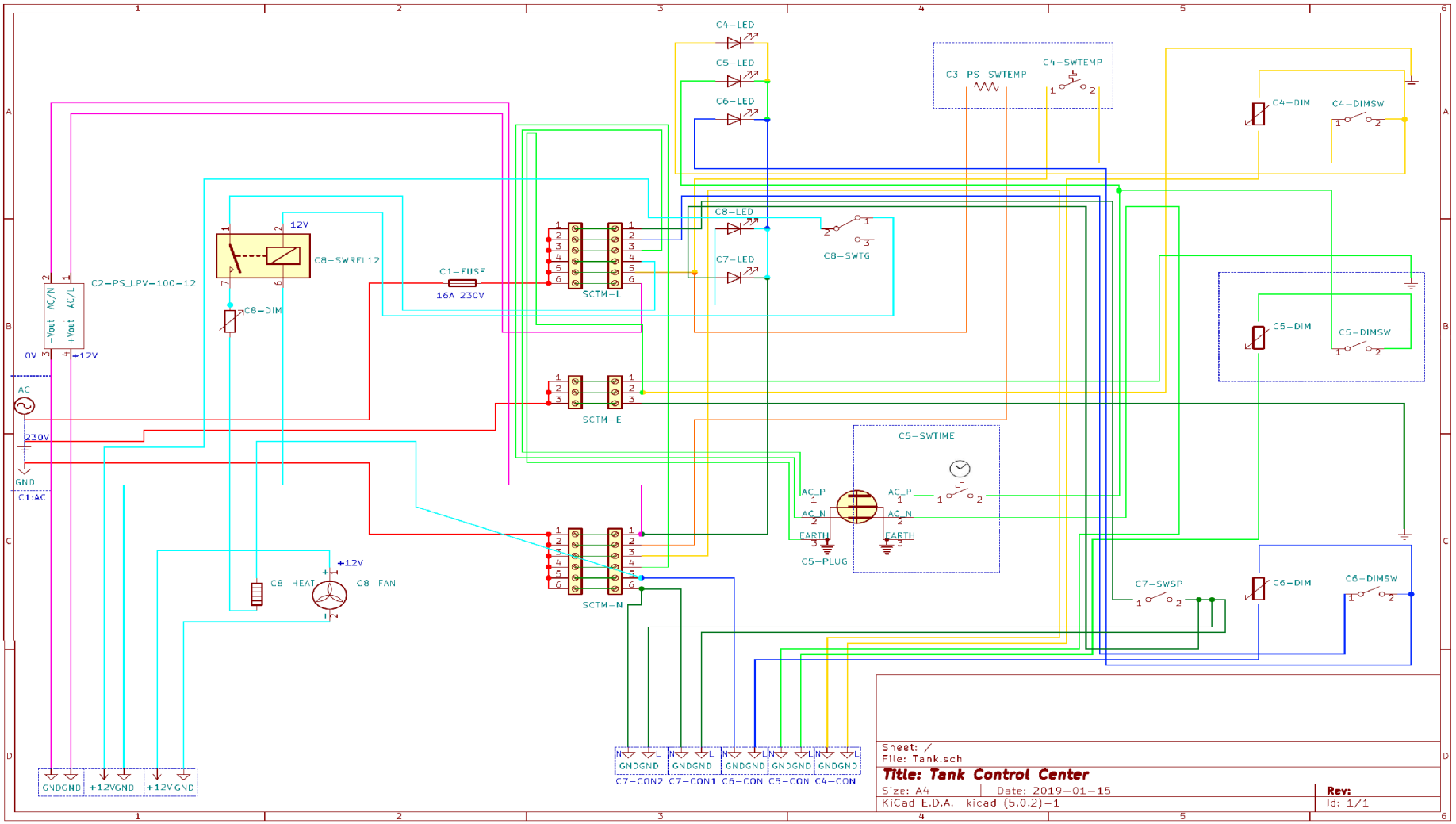

Figure A.4: Control Center Circuit Diagram

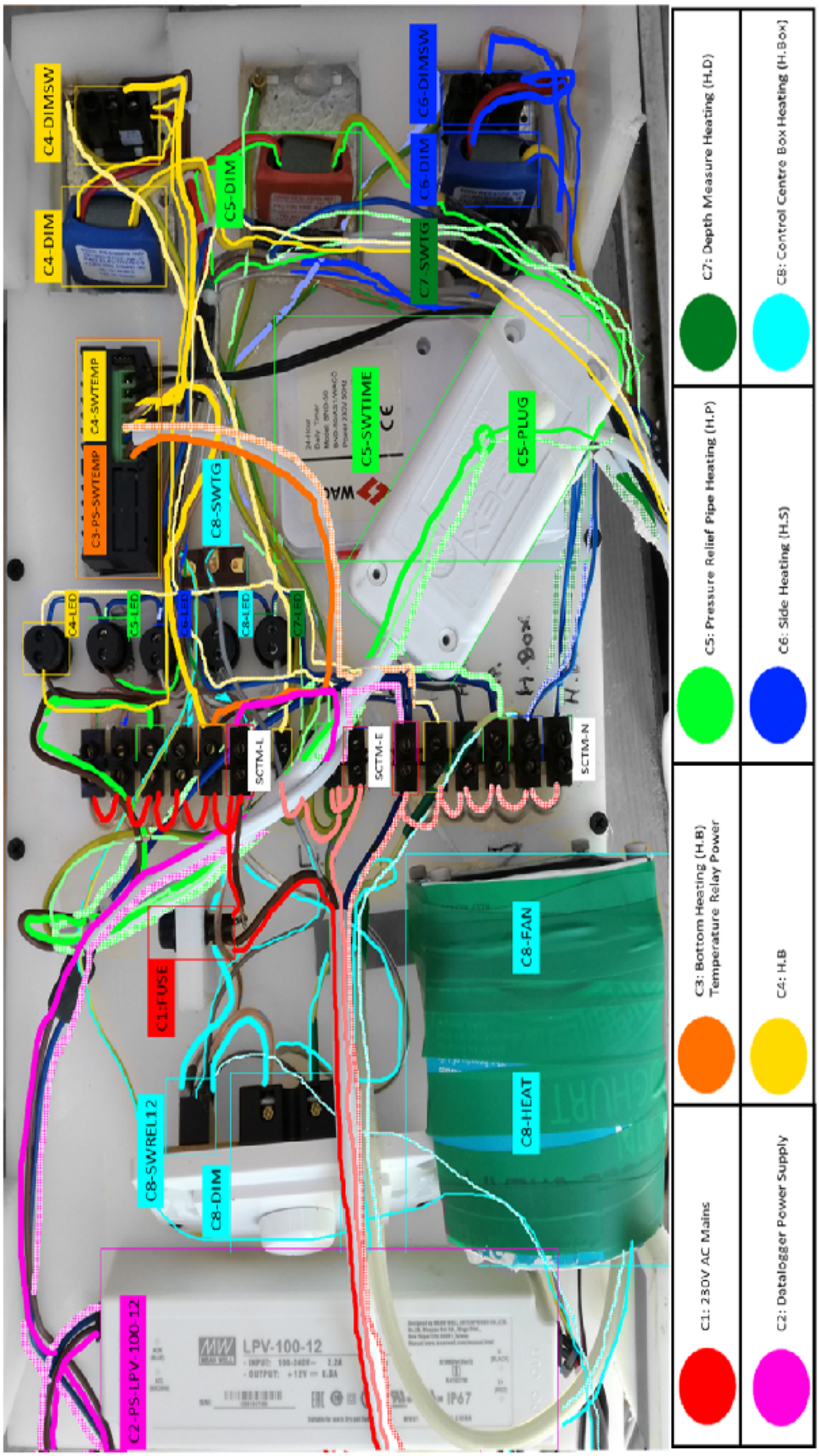

Figure A.5: Control Center Rear with Schematic Overlay

A.2 HeatGen Method Development

A.2.1 Temperature Smoothing

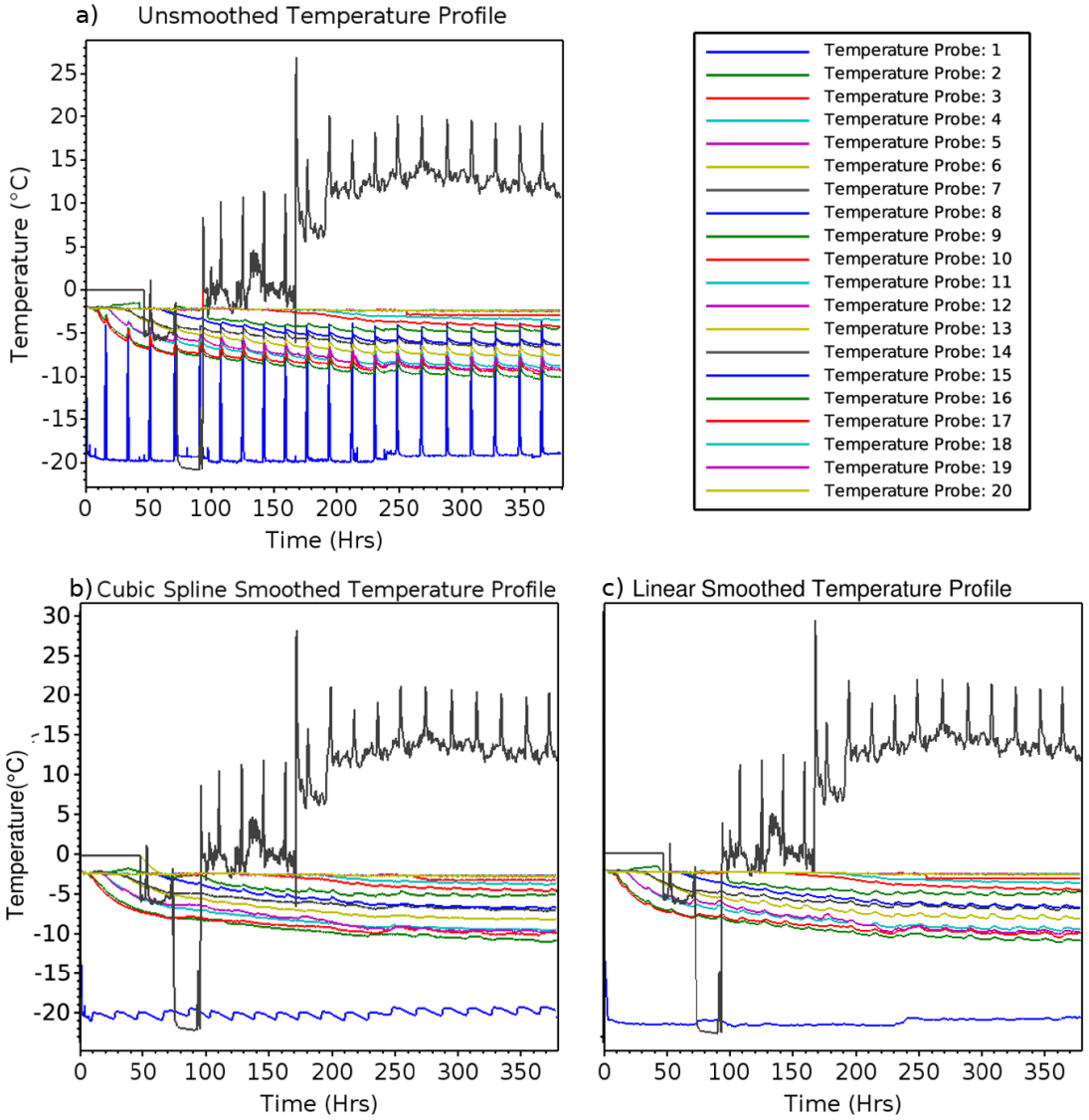

Figure A.6: Comparison of smoothing methods where a) shows unsmoothed temperature profiles, b) shows the cubic spline method and c) shows the linear smoothed temperature profile

Scilab function for linear smoothing of raw temperature data

```
    for i=5:length(Dat2(:,1))-3
        for j=1:length(Dat2(1,:))
            if abs(mean(Dat2(i-2:i+2,j))-Dat2(i,j))>1.5 then
                Dat2(i,j)=(mean(Dat2(i-2:i-1,j))+mean(Dat2(i+1:i+2,j)))/2;
            end
        end
    end
    ////////////////////////////////SMOOTHING//////////////////////////////////////
    global Probes
    for i=2:length(Dat2(:,1))
        for z=1:length(Dat2(1,:))
            chk=find(Probes==z);
            if chk<>[] then
                j=z;
                    if Dat2(i,j)-Dat2(i-1,j)>0.003 & Dat2(i,j)<0 then
                        for k=1:30
                            if i+k<length(Dat2(:,1)) then
                                if Dat2(i+k,j)<(Dat2(i-1,j)+1) then
                                    for l=1:k
                                        Dat2(i+l-1,j)=Dat2(i-1,j)-((Dat2(i-1,j)-Dat2(i+k,j))/k)*l;
                                    end
                                    k=30;
                                elseif k==30
                                    for l=1:30
                                        Dat2(i+l-1,j)=Dat2(i-1,j);
                                    end
                                end
                            else
                                for l=1:(length(Dat2(:,1)) i)
                                    Dat2(i+l-1,j)=Dat2(i-1,j);
                                end
                            end
                        end
                    end
            end
        end
        waitbar((i/length(Dat2(:,1))),winID5);
    end
```

A.2.2 Procedure for Temperature Grid Population

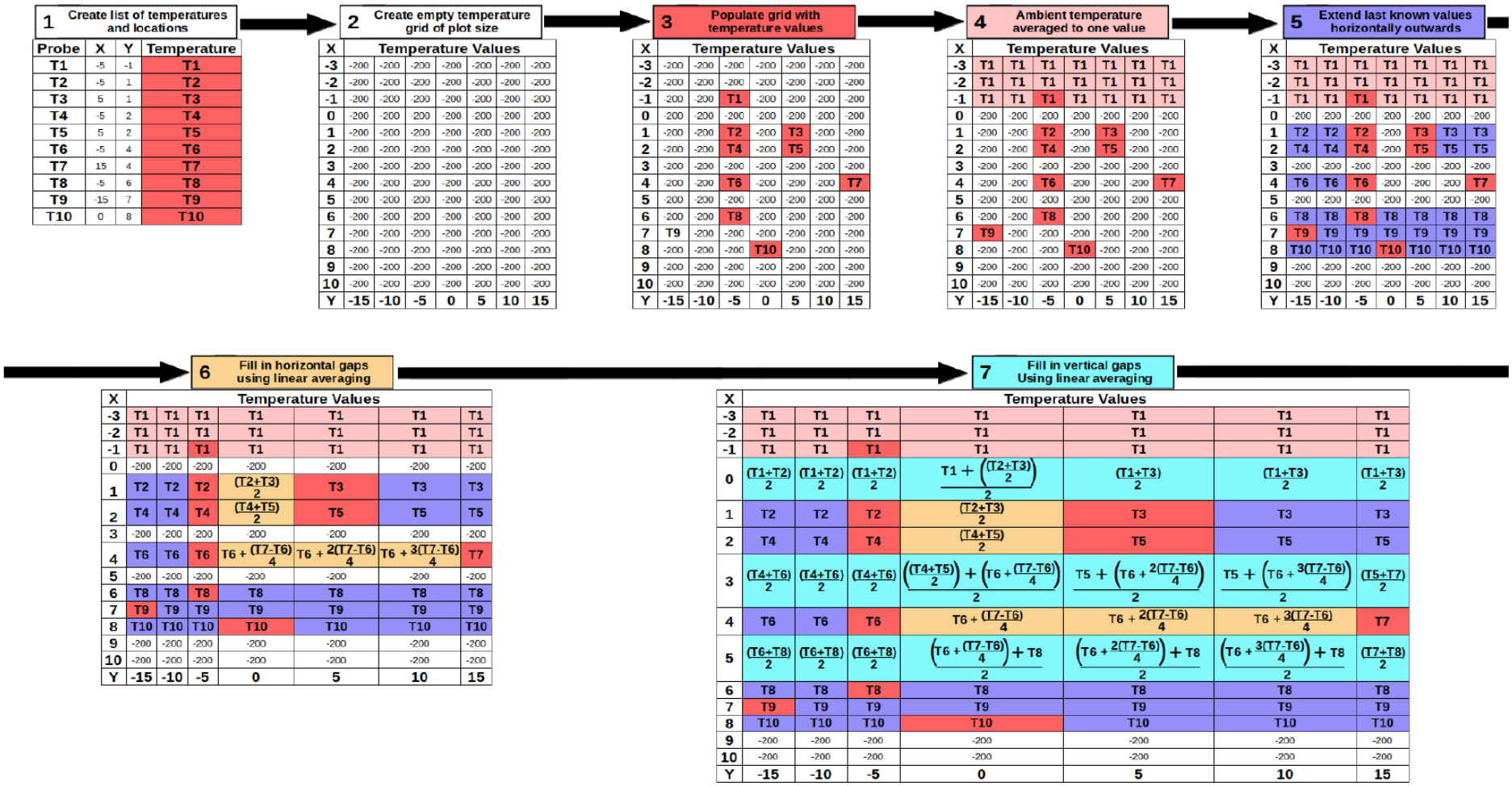

Probe	X	Y	Temperature
T1	-5	-1	T1
T2	-5	1	T2
T3	5	1	T3
T4	-5	2	T4
T5	5	2	T5
T6	-5	4	T6
T7	15	4	T7
T8	-5	6	T8
T9	-15	7	T9
T10	0	8	T10

X	Temperature Values						
-3	-200	-200	-200	-200	-200	-200	-200
-2	-200	-200	-200	-200	-200	-200	-200
-1	-200	-200	-200	-200	-200	-200	-200
0	-200	-200	-200	-200	-200	-200	-200
1	-200	-200	-200	-200	-200	-200	-200
2	-200	-200	-200	-200	-200	-200	-200
3	-200	-200	-200	-200	-200	-200	-200
4	-200	-200	-200	-200	-200	-200	-200
5	-200	-200	-200	-200	-200	-200	-200
6	-200	-200	-200	-200	-200	-200	-200
7	-200	-200	-200	-200	-200	-200	-200
8	-200	-200	-200	-200	-200	-200	-200
9	-200	-200	-200	-200	-200	-200	-200
10	-200	-200	-200	-200	-200	-200	-200
Y	-15	-10	-5	0	5	10	15

X	Temperature Values						
-3	-200	-200	-200	-200	-200	-200	-200
-2	-200	-200	-200	-200	-200	-200	-200
-1	-200	-200	T1	-200	-200	-200	-200
0	-200	-200	-200	-200	-200	-200	-200
1	-200	-200	T2	-200	T3	-200	-200
2	-200	-200	T4	-200	T5	-200	-200
3	-200	-200	-200	-200	-200	-200	-200
4	-200	-200	T6	-200	-200	-200	T7
5	-200	-200	-200	-200	-200	-200	-200
6	-200	-200	T8	-200	-200	-200	-200
7	T9	-200	-200	-200	-200	-200	-200
8	-200	-200	-200	T10	-200	-200	-200
9	-200	-200	-200	-200	-200	-200	-200
10	-200	-200	-200	-200	-200	-200	-200
Y	-15	-10	-5	0	5	10	15

X	Temperature Values						
-3	T1	T1	T1	T1	T1	T1	T1
-2	T1	T1	T1	T1	T1	T1	T1
-1	T1	T1	T1	T1	T1	T1	T1
0	-200	-200	-200	-200	-200	-200	-200
1	-200	-200	T2	-200	T3	-200	-200
2	-200	-200	T4	-200	T5	-200	-200
3	-200	-200	-200	-200	-200	-200	-200
4	-200	-200	T6	-200	-200	-200	T7
5	-200	-200	-200	-200	-200	-200	-200
6	-200	-200	T8	-200	-200	-200	-200
7	T9	-200	-200	-200	-200	-200	-200
8	-200	-200	-200	T10	-200	-200	-200
9	-200	-200	-200	-200	-200	-200	-200
10	-200	-200	-200	-200	-200	-200	-200
Y	-15	-10	-5	0	5	10	15

X	Temperature Values						
-3	T1	T1	T1	T1	T1	T1	T1
-2	T1	T1	T1	T1	T1	T1	T1
-1	T1	T1	T1	T1	T1	T1	T1
0	-200	-200	-200	-200	-200	-200	-200
1	T2	T2	T2	-200	T3	T3	T3
2	T4	T4	T4	-200	T5	T5	T5
3	-200	-200	-200	-200	-200	-200	-200
4	T6	T6	T6	-200	-200	-200	T7
5	-200	-200	-200	-200	-200	-200	-200
6	T8	T8	T8	T8	T8	T8	T8
7	T9	T9	T9	T9	T9	T9	T9
8	T10	T10	T10	T10	T10	T10	T10
9	-200	-200	-200	-200	-200	-200	-200
10	-200	-200	-200	-200	-200	-200	-200
Y	-15	-10	-5	0	5	10	15

X	Temperature Values						
-3	T1	T1	T1	T1	T1	T1	T1
-2	T1	T1	T1	T1	T1	T1	T1
-1	T1	T1	T1	T1	T1	T1	T1
0	-200	-200	-200	-200	-200	-200	-200
1	T2	T2	T2	-200	T3	T3	T3
2	T4	T4	T4	-200	T5	T5	T5
3	-200	-200	-200	-200	-200	-200	-200
4	T6	T6	T6	-200	-200	-200	T7
5	-200	-200	-200	-200	-200	-200	-200
6	T8	T8	T8	T8	T8	T8	T8
7	T9	T9	T9	T9	T9	T9	T9
8	T10	T10	T10	T10	T10	T10	T10
9	-200	-200	-200	-200	-200	-200	-200
10	-200	-200	-200	-200	-200	-200	-200
Y	-15	-10	-5	0	5	10	15

X	Temperature Values						
-3	T1	T1	T1	T1	T1	T1	T1
-2	T1	T1	T1	T1	T1	T1	T1
-1	T1	T1	T1	T1	T1	T1	T1
0	-200	-200	-200	-200	-200	-200	-200
1	T2	T2	T2	-200	T3	T3	T3
2	T4	T4	T4	-200	T5	T5	T5
3	T4	T4	T4	T5	T5	T5	T5
4	T6	T6	T6	T6	T6	T6	T7
5	T6	T6	T6	T7	T7	T7	T7
6	T8	T8	T8	T8	T8	T8	T8
7	T9	T9	T9	T9	T9	T9	T9
8	T10	T10	T10	T10	T10	T10	T10
9	-200	-200	-200	-200	-200	-200	-200
10	-200	-200	-200	-200	-200	-200	-200
Y	-15	-10	-5	0	5	10	15

X	Temperature Values						
-3	T1	T1	T1	T1	T1	T1	T1
-2	T1	T1	T1	T1	T1	T1	T1
-1	T1	T1	T1	T1	T1	T1	T1
0	$\frac{(T1+T2)}{2}$	$\frac{(T1+T2)}{2}$	$\frac{(T1+T2)}{2}$	$T1 + \frac{\left(\frac{(T2+T3)}{2}\right)}{2}$	$\frac{(T1+T3)}{2}$	$\frac{(T1+T3)}{2}$	$\frac{(T1+T3)}{2}$
1	T2	T2	T2	$\frac{(T2+T3)}{2}$	T3	T3	T3
2	T4	T4	T4	$\frac{(T4+T5)}{2}$	T5	T5	T5
3	$\frac{(T4+T6)}{2}$	$\frac{(T4+T6)}{2}$	$\frac{(T4+T6)}{2}$	$\frac{\left(\frac{(T4+T5)}{2}\right) + \left(T6 + \frac{(T7-T6)}{4}\right)}{2}$	$\frac{T5 + \left(T6 + \frac{2(T7-T6)}{4}\right)}{2}$	$\frac{T5 + \left(T6 + \frac{3(T7-T6)}{4}\right)}{2}$	$\frac{(T5+T7)}{2}$
4	T6	T6	T6	$T6 + \frac{(T7-T6)}{4}$	$T6 + \frac{2(T7-T6)}{4}$	$T6 + \frac{3(T7-T6)}{4}$	T7
5	$\frac{(T6+T8)}{2}$	$\frac{(T6+T8)}{2}$	$\frac{(T6+T8)}{2}$	$\frac{\left(T6 + \frac{(T7-T6)}{4}\right) + T8}{2}$	$\frac{\left(T6 + \frac{2(T7-T6)}{4}\right) + T8}{2}$	$\frac{\left(T6 + \frac{3(T7-T6)}{4}\right) + T8}{2}$	$\frac{(T7+T8)}{2}$
6	T8	T8	T8	T8	T8	T8	T8
7	T9	T9	T9	T9	T9	T9	T9
8	T10	T10	T10	T10	T10	T10	T10
9	-200	-200	-200	-200	-200	-200	-200
10	-200	-200	-200	-200	-200	-200	-200
Y	-15	-10	-5	0	5	10	15

Figure A.7: Calculation steps for population of example temperature grid for Heatmap generation

X	Temperature Values						
-3	T1	T1	T1	T1	T1	T1	T1
-2	T1	T1	T1	T1	T1	T1	T1
-1	T1	T1	T1	T1	T1	T1	T1
0	$\frac{(T1+T2)}{2}$	$\frac{(T1+T2)}{2}$	$\frac{(T1+T2)}{2}$	$\frac{T1+\left(\frac{(T2+T3)}{2}\right)}{2}$	$\frac{(T1+T3)}{2}$	$\frac{(T1+T3)}{2}$	$\frac{(T1+T3)}{2}$
1	T2	T2	T2	$\frac{(T2+T3)}{2}$	T3	T3	T3
2	T4	T4	T4	$\frac{(T4+T5)}{2}$	T5	T5	T5
3	$\frac{(T4+T6)}{2}$	$\frac{(T4+T6)}{2}$	$\frac{(T4+T6)}{2}$	$\frac{\left(\frac{(T4+T5)}{2}\right)+\left(T6+\frac{(T7-T6)}{4}\right)}{2}$	$\frac{T5+\left(T6+\frac{2(T7-T6)}{4}\right)}{2}$	$\frac{T5+\left(T6+\frac{3(T7-T6)}{4}\right)}{2}$	$\frac{(T5+T7)}{2}$
4	T6	T6	T6	$T6+\frac{(T7-T6)}{4}$	$T6+\frac{2(T7-T6)}{4}$	$T6+\frac{3(T7-T6)}{4}$	T7
5	$\frac{(T6+T8)}{2}$	$\frac{(T6+T8)}{2}$	$\frac{(T6+T8)}{2}$	$\frac{\left(T6+\frac{(T7-T6)}{4}\right)+T8}{2}$	$\frac{\left(T6+\frac{2(T7-T6)}{4}\right)+T8}{2}$	$\frac{\left(T6+\frac{3(T7-T6)}{4}\right)+T8}{2}$	$\frac{(T7+T8)}{2}$
6	T8	T8	T8	T8	T8	T8	T8
7	T9	T9	T9	T9	T9	T9	T9
8	T10	T10	T10	T10	T10	T10	T10
9	T10	T10	T10	T10	T10	T10	T10
10	T10	T10	T10	T10	T10	T10	T10
Y	-15	-10	-5	0	5	10	15

Figure A.8: Completed example temperature grid for Heatmap generation

A.3 Temperature Derived Depth Measurement

Table A.1: Example data showing the linear line fitting and associated error that provided cut-off point for ice depth. Last known point in ice shown by red line

Time (Hrs)	Depth	Temperature	m	c	Least Squares Error
41.67	1	-8.871	0	0	0
	3	-5.652	1.610	-10.480	1.104 x 10^(-15)
	5	-2.405	**1.617**	**-10.492**	0.000
	8	-1.627	1.046	-9.085	3.711
	13	-1.724	0.550	-7.355	13.181
	18	-1.706	0.346	-6.429	19.548
	25	-1.813	0.217	-5.662	25.883
	30	-1.837	0.159	-5.249	29.512
	45	-1.883	0.096	-4.630	35.399
	70	-1.817	0.052	-4.067	40.797
	Average Solution Temperature = **-1.772** °C				
	Estimated Ice Depth: (**-1.772** - (**-10.492**))/**1.617** = **5.393 cm**				
50.00	1	-12.564	0	0	0
	3	-9.813	1.376	-13.940	1.099 x 10^(-15)
	5	-6.639	1.481	-14.116	0.030
	8	-2.436	**1.457**	**-14.057**	0.036
	13	-1.793	0.926	-12.204	10.896
	18	-1.699	0.630	-10.861	24.274
	25	-1.881	0.413	-9.573	42.163
	30	-1.909	0.311	-8.844	53.493
	45	-1.956	0.192	-7.681	74.239
	70	-1.881	0.106	-6.572	95.217
	Average Solution Temperature = **-1.853** °C				
	Estimated Ice Depth: (**-1.853** - (**-14.057**))/**1.457** = **8.376 cm**				
100.00	1	-16.177	0	0	0
	3	-14.285	0.946	-17.122	1.094 x 10^(-15)
	5	-11.929	1.062	-17.316	0.036
	8	-9.702	0.938	-17.011	0.210
	13	-5.631	0.873	-16.784	0.373
	18	-2.081	**0.824**	**-16.563**	0.737
	25	-1.993	0.631	-15.411	15.015
	30	-2.023	0.511	-14.558	30.542
	45	-2.084	0.335	-12.834	76.140
	70	-2.005	0.193	-11.003	133.328
	Average Solution Temperature = **-2.026** °C				
	Estimated Ice Depth: (**-2.026** - (**-16.563**))/**0.824** = **17.642 cm**				

Scilab Code for Temperature Derived Depth Measurement Function

```
//Temperature Derived Ice Depth Function

gap2=1


function y=FF(x,p)
  y=p(1)*x+p(2)
endfunction

//The criterion function
function e=G(p, z),
  y=z(1),x=z(2);
  e=y-FF(x,p);
endfunction


num_data_points = size(Ice,1)-1;

Freeze=zeros(num_data_points,4);
winID7=waitbar("Estimating Ice Thickness")
for q=2:gap2:num_data_points
//hjk=figure(q);
//clf(hjk);
        Y1=[];
        X1=[];
        Y1(1,:)=Ice(q,2:$);
        X1(1,:)=Ice(1,2:$);
        Fits=[X1(1) Y1(1) 0 0 0];
//        Fig11()
//        Ledg3=[]
    for i=2:length(Y1)
        X=X1(1:i);
        Y=Y1(1:i);

    //X=y;
    //Y=k';
        Z=[Y;X];

        //Solve the problem
        p0=[0.01;0];
        [p,err]=datafit(G,Z,p0);

        Fits = resize_matrix(Fits, (size(Fits)(1)+1),-1);
        Fits(i,:)=[X(i) Y(i) p(1) p(2) err];

    end
    Tsol=[];
    IDepth=[];
    for j=1:size(Fits)(1)
        if Fits(j,5)>2
            //disp(j)
            Tsol=mean(Fits(j:$,2));
            c=Fits((j-1),4);
            m=Fits((j-1),3);
            IDepth=(Tsol-c)/m;
            if IDepth<mean(Freeze(q-5:q-1,4))-0.3 & IDepth>10
                Freeze(q,:)=[q Fits((j-1),1) Tsol Freeze(q-1,4)];
                break
            else
                Freeze(q,:)=[q Fits((j-1),1) Tsol IDepth];
                break
            end
        end
    end
    if Freeze(q,:)==[0 0 0 0] then
            Tsol=mean(Fits(:,2));
            Freeze(q,:)=[q 0 Tsol 0];
    end
    if Freeze(q,2)==0 then
        Y2=Ice(q,2:$);
        X2(1,:)=Ice(1,2:$);
        for f=size(Y2)(2)-1:-1:1
            Y2m=mean(Y2(f:$));
            if Y2(f)<Y2m-0.2
                Tsol=mean(Fits(f+1:$,2));
                if f>1 then
                    T2=Fits(f,2);
                    T1=Fits(1,2);
                    x2=Fits(f,1);
                    x1=Fits(1,1);
                    m1=(T2-T1)/(x2-x1);
                    c1=T1-m1*x1;
                    IDepth=(Tsol-c1)/m1;
                    Freeze(q,:)=[q X2(f) Tsol IDepth];
                    break
```

file:///tmp/tmp0n8n_m.html

```
                    else
                        Freeze(q,:)=[q X2(f) Tsol X2(f)];
                        break
                    end
                end
            end
        end

        cntl=[];
        for n=1:size(X2(1,:))(2)
            if find(Freeze(1:q,2)==X2(n))<>[] then
                cntl(n)=X2(n);
            end
        end
        if size(cntl)(1)<>0 then
                s=size(cntl)(1);
                if sum(cntl(1:s))<>sum(X2(1,1:s))
                    Y2=Ice(q,2:$);
                    X2(1,:)=Ice(1,2:$);
                    for f=size(Y2)(2)-1:-1:1
                        Y2m=mean(Y2(f:$));
                        if Y2(f)<Y2m-0.2
                            Tsol=Y2m;
                            if f>1 then
                                T2=Fits(f,2);
                                T1=Fits(1,2);
                                x2=Fits(f,1);
                                x1=Fits(1,1);
                                m1=(T2-T1)/(x2-x1);
                                c1=T1-m1*x1;
                                IDepth=(Tsol-c1)/m1;
                                Freeze(q,:)=[q X2(f) Tsol IDepth];
                                break
                            else
                                Freeze(q,:)=[q X2(f) Tsol X2(f)];
                                break
                            end
                        end
                    end
                end
            end
        end
        frac=((q-1)/num_data_points);
        waitbar(frac,winID7);
    end
    close(winID7)

    [row, column] = find(Freeze==0)
    Freeze(row, column) =[]
    Fr1=[Freeze(1,1)-1 0 0 0]
    Freeze=[Fr1;Freeze]
```

A.4 Proof of Concept: Artificial Sea Ice Growth Experiment

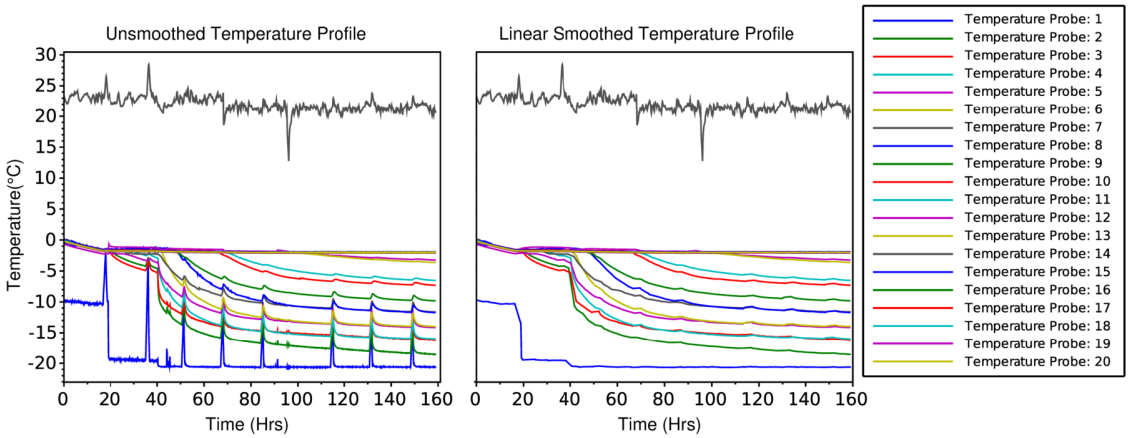

Figure A.9: 28 ppt Experimental Run: Smoothing of Temperature Profiles

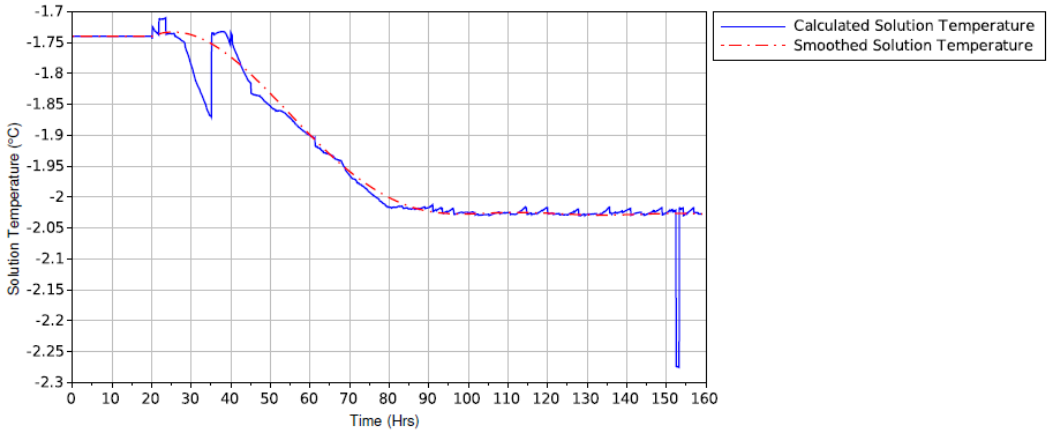

Figure A.10: 28 ppt Experimental Run: Solution Temperature Profile

SAMPLE 1		
Sample Length: 22cm		
Sample Section (cm)	Temperature (℃)	Salinity (g kg^{-1})
0-2	-9.21	12.5246
2-4	-8.35	15.7658
4-6	-7.54	15.6523
6-8	-7.1	14.3716
8-10	-6.39	13.8721
10-12	-5.99	12.4799
12-14	-5.42	10.9113
14-16	-5.28	8.72895
16-18	-4.63	10.5942
18-20	-4.27	10.5942
20-22	-4.12	
SAMPLE 2		
Sample Length: 21cm		
Sample Section (cm)	Temperature (℃)	Salinity (g kg^{-1})
0-3	-8.05	11.3192
3-5	-8.09	14.5453
5-7	-7.71	13.9473
7-9	-6.87	13.594
9-11	-6.05	11.9062
11-13	-5.51	10.9113
13-15	-4.93	9.01655
15-17	-4.27	6.8172
17-19	-3.92	10.3384
19-21	-3.33	
SAMPLE 3		
Sample Length: 23cm		
Sample Section (cm)	Temperature (℃)	Salinity (g kg^{-1})
0-3	-7.76	11.2513
3-5	-7.96	13.9735
5-7	-7.74	13.3514
7-9	-7.54	12.1396
9-11	-6.73	11.1381
11-13	-5.72	10.9755
13-15	-5.25	10.8103
15-17	-4.72	9.3115
17-19	-4.23	9.23768
19-21	-4.11	11.7962
21-23	-3.36	

Figure A.11: 28 ppt Experimental Run: Temperature and Salinity Data from 3 Samples used for Salinity Trend Calculation

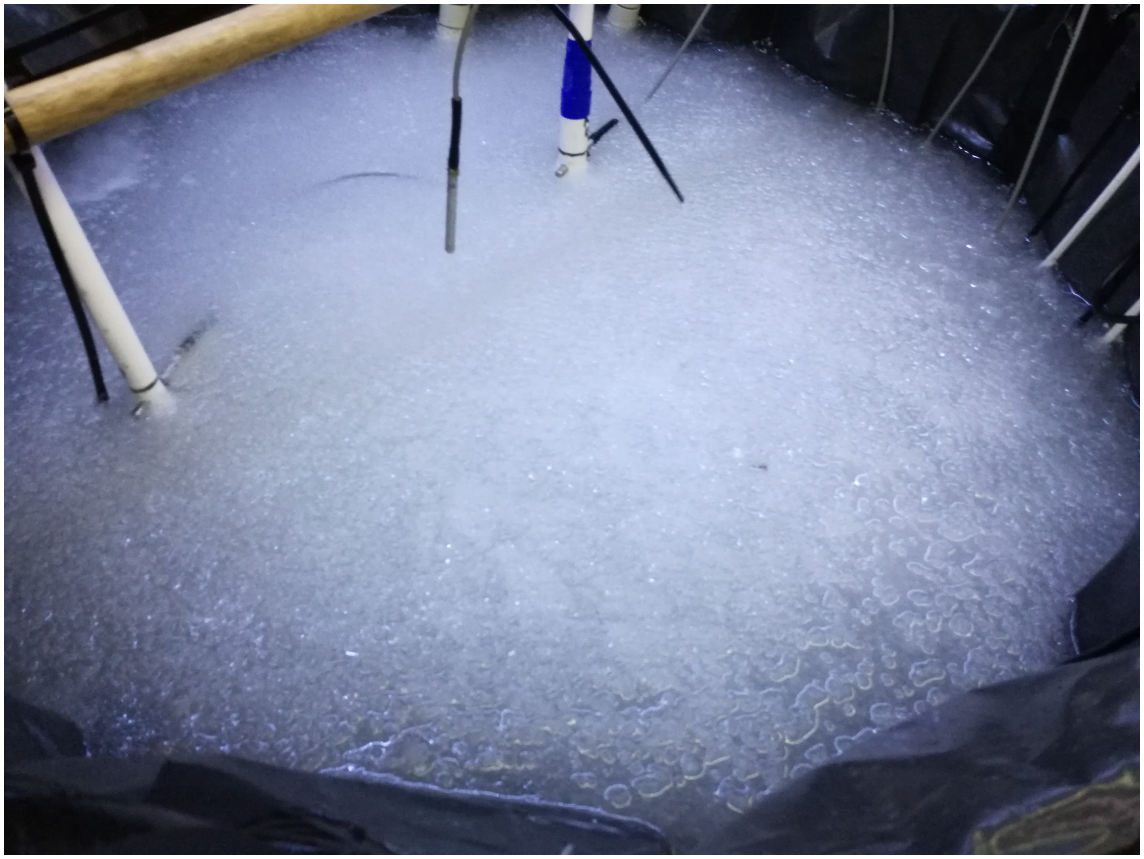

Figure A.12: 28 ppt Experimental Run: Ice Melting and Subsequent Brine Drainage Due to Defrost Cycles